MICROCOPY CHART

AFGL-TR-85-0159

A CUMULUS PARAMETERIZATION STUDY WITH SPECIAL ATTENTION
TO THE ARAKAWA-SCHUBERT SCHEME

Chin-Yue J. Kao[1] and Yoshi Ogura

University of Illinois
Department of Atmospheric Sciences
Urbana, IL 61801

AD-A166 801

June 1985

Scientific Report No. 1

AIR FORCE GEOPHYSICS LABORATORY
AIR FORCE SYSTEMS COMMAND
UNITED STATES AIR FORCE
HANSCOM AIR FORCE BASE, MASSACHUSETTS 01731
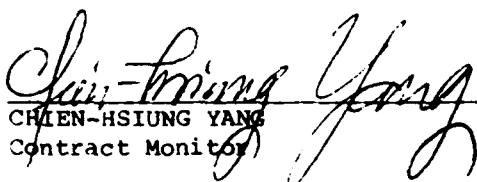
[1]Present affiliation: Earth and Space Science Division, Los Alamos
National Laboratory, Los Alamos, NM 87545

"This technical report has been reviewed and is approved for publication"

CHIEN-HSIUNG YANG
Contract Monitor

H. STUART MUENCH, Acting Chief
Atmospheric Prediction Branch

FOR THE COMMANDER

KENNETH R. HARDY, Acting Director
Atmospheric Sciences Division

AD-A166801

REPORT DOCUMENTATION PAGE

1a. REPORT SECURITY CLASSIFICATION	1b. RESTRICTIVE MARKINGS
Unclassified	

2a. SECURITY CLASSIFICATION AUTHORITY	3. DISTRIBUTION/AVAILABILITY OF REPORT
	Approved for public release;
2b. DECLASSIFICATION/DOWNGRADING SCHEDULE	Distribution unlimited.

4. PERFORMING ORGANIZATION REPORT NUMBER(S)	5. MONITORING ORGANIZATION REPORT NUMBER(S)
	AFGL-TR-85-0159

6a. NAME OF PERFORMING ORGANIZATION	6b. OFFICE SYMBOL (If applicable)	7a. NAME OF MONITORING ORGANIZATION
University of Illinois		Air Force Geophysics Laboratory

6c. ADDRESS (City, State and ZIP Code)	7b. ADDRESS (City, State and ZIP Code)
Department of Atmospheric Sciences	Hanscom AFB
Urbana, IL 61801	Massachusetts 01731

8a. NAME OF FUNDING/SPONSORING ORGANIZATION	8b. OFFICE SYMBOL (If applicable)	9. PROCUREMENT INSTRUMENT IDENTIFICATION NUMBER
		F19628-82-K-0030

8c. ADDRESS (City, State and ZIP Code)	10. SOURCE OF FUNDING NOS.			
	PROGRAM ELEMENT NO.	PROJECT NO.	TASK NO.	WORK UNIT NO.
	61102F	2310	G7	AC

11. TITLE (Include Security Classification) A Cumulus Parameterization Study With Special Attention to the Arakawa-Schubert Scheme

12. PERSONAL AUTHOR(S) Chih-Yue J. Kao and Yoshi Ogura

13a. TYPE OF REPORT	13b. TIME COVERED	14. DATE OF REPORT (Yr., Mo., Day)	15. PAGE COUNT
Scientific #1	FROM _____ TO _____	1985 June	224

16. SUPPLEMENTARY NOTATION

17.	COSATI CODES		18. SUBJECT TERMS (Continue on reverse if necessary and identify by block number)
FIELD	GROUP	SUB. GR.	Cumulus parameterization, Semi-prognostic studies
			the Arakawa-Schubert scheme Meso-scale model
			Cloud work function Sensitivity tests

19. ABSTRACT (Continue on reverse if necessary and identify by block number)

Arakawa and Schubert (1974) developed a cumulus parameterization scheme in a framework that conceptually divides the mutual interaction of the cumulus convection and large-scale disturbance into the categories of large-scale budget requirements and the quasi-equilibrium assumption of cloud work function. We have applied the A-S scheme through a semi-prognostic approach to two different data sets: one is for an intense tropical cloud band event; the other is for tropical composite easterly wave disturbances. Both were observed in GATE. The cloud heating and drying effects predicted by the

20. DISTRIBUTION/AVAILABILITY OF ABSTRACT	21. ABSTRACT SECURITY CLASSIFICATION
UNCLASSIFIED/UNLIMITED ☐ SAME AS RPT. ☐ DTIC USERS ☐	Unclassified

22a. NAME OF RESPONSIBLE INDIVIDUAL	22b. TELEPHONE NUMBER (Include Area Code)	22c. OFFICE SYMBOL
Chien-Hsiung Yang	(617) 861-3913	AFGL/LYP

DD FORM 1473, 83 APR   EDITION OF 1 JAN 73 IS OBSOLETE.

Block 19, Abstract, continued:

Arakawa-Schubert scheme are found to agree rather well with the observations. However, it is also found that the Arakawa-Schubert scheme underestimates both condensation and evaporation rates substantially when compared with the cumulus ensemble model results (Soong and Tao, 1980; Tao, 1983). An inclusion of the downdraft effects, as formulated by Johnson (1976), appears to alleviate this deficiency.

In order to examine how the Arakawa-Schubert scheme works in a fully prognostic problem, a simulation of the evolution and structure of the tropical cloud band, mentioned above, under the influence of an imposed large-scale low-level forcing has been made, using a two-dimensional hydrostatic model with the inclusion of the Arakawa-Schubert scheme. Basically, the model result indicates that the meso-scale convective system is driven by the excess of the convective heating derived from the Arakawa-Schubert scheme over the adiabatic cooling due to the imposed large-scale lifting and induced meso-scale upward motion. However, as the convective system develops, the adiabatic warming due to the subsidence outside the cloud cluster gradually accumulates into a secondary temperature anomaly which subsequently reduces the original temperature contrast and inhibits the further development of the convective system. A 24 hour integration shows that the model is capable of simulating many important features such as the life cycle, intensity of circulation, and rainfall rates.

TABLE OF CONTENTS

ABSTRACT

Arakawa and Schubert (1974) developed a cumulus parameterization scheme in a framework that conceptually divides the mutual interaction between the cumulus convection and large-scale disturbance into the categories of large-scale budget requirements and the quasi-equilibrium assumption of cloud work function. We have applied the Arakawa-Schubert scheme through a semi-prognostic approach to two different data sets: one is for an intense tropical cloud band event; the other is for tropical composite easterly wave disturbances. Both were observed in GARP (Global Atmospheric Research Program) Atlantic Tropical Experiment (GATE). The cloud heating and drying effects predicted by the Arakawa-Schubert scheme are found to agree rather well with the observations. However, it is also found that the Arakawa-Schubert scheme underestimates both condensation and evaporation rates substantially when compared with the cumulus ensemble model results (Soong and Tao, 1980; Tao, 1983). An inclusion of the downdraft effects, as formulated by Johnson (1976), appears to alleviate this deficiency.

In order to examine how the Arakawa-Schubert scheme works in a fully prognostic problem, a simulation of the evolution and structure of the tropical cloud band mentioned above under the influence of an imposed large-scale, low-level lifting was made by using a two-dimensional hydrostatic model with the inclusion of the Arakawa-Schubert scheme. Basically, the model result indicates that the mesoscale convective system is driven by the excess of the convective heating derived from the Arakawa-Schubert scheme over the adiabatic cooling due to the imposed large-scale lifting and induced mesoscale upward motion. However, as the convective system develops, the adiabatic warming due to the subsidence outside the cloud system gradually accumulates into a

secondary temperature anomaly which subsequently reduces the original temperature contrast and inhibits the further development of the convective system. A 24-hour integration shows that the model is capable of simulating many important features, such as the life cycle, the intensity of circulation, and rainfall rates.

CHAPTER I

INTRODUCTION

The importance of the vertical transports of heat, moisture, vorticity, and momentum by cumulus clouds has long been recognized not only in the numerical predictions of weather and climate but also in the simulation studies on mesoscale circulations such as tropical convective systems, mid-latitude frontogenesis, and the sea-land breeze. However, it is impractical to resolve those individual cumulus clouds because of the distinct scale difference between them and larger-scale circulations. In the past two decades, there have been numerous attempts to relate subgrid-scale cumulus convection to large-scale fields by specifying the cumulus activity as a function of large-scale variables, which is now commonly referred to as "cumulus parameterization". The goal of cumulus parameterization is to predict the change of large-scale disturbances due to cumulus convection by describing not each of the many individual clouds, but only their collective effects.

The first attempts to parameterize cumulus convection have been known as Conditional Instability of the Second Kind (CISK) by Charney and Eliassen (1964) and Ooyama (1964). The concept of CISK, which was particularly designed to explain the growth of tropical cyclones, can be summarized as follows: the release of latent heat generated by cumulus cloud drives the cyclone and, in turn, the cyclone provides the moisture which maintains the cumulus clouds. Later, many studies extended the concept of CISK in investigating tropical wave disturbances through normal-mode linear analysis, which is commonly called the

Wave-CISK theory. The study by Lindzen (1974) is representative of the state of the art. However, Ooyama (1982) recently made a thorough review of the validity and limitations of CISK and pointed out that many arguments about "preferred scales" in the linear theory were irrelevant to the tropical cyclones, especially to their mature stages where the nonlinear processes are dominant.

Since the emergence of CISK theory, a great number of methods or "schemes" dealing with the interaction of cumulus convection with the large-scale disturbances have been developed. Each involves different specific formulations based on the model's needs and the author's intuitive idealizations of cumulus convection. To date, there are three major kinds of cumulus parameterization schemes which have been more generally employed in large-scale and mesoscale numerical models. These are: (1) Convective adjustment scheme (Manabe et al., 1965); (2) Kuo's Scheme (Kuo, 1965, 1974); and (3) the Arakawa-Schubert scheme (Arakawa and Schubert, 1974).

The concept of the convective adjustment scheme is rather simple and implicit. Whenever the atmosphere is super-saturated and the temperature stratification is unstable with respect to the moist adiabatic lapse rate, the scheme assumes that cumulus clouds form and redistribute the temperature and moisture profiles so that the total moist enthalpy is conserved and the lapse rate is moist adiabatic. This scheme has been extensively used in the general circulation model (GCM) at the Geophysical Fluid Dynamics Laboratory (GFDL). This method was also adopted by the National Center for Atmospheric Research (NCAR) for its Community Climate Model (CCM). In addition, Kurihara (1973) and

Kurihara and Tuleya (1974) applied a modified version of this adjustment scheme to hurricane modeling studies.

Kuo's scheme (1965) parameterizes the release of latent heat by relating the convective activity to the large-scale moisture convergence into a conditionally unstable atmospheric column. The adjustment of the large-scale temperature and moisture fields due to clouds can be determined from the large-scale horizontal convergence of moisture and the profiles of excess temperature and mixing ratio inside the cloud. Kuo (1974) modified his scheme by separating the total convergence of moisture into two parts: one (denoted by $b \times M_t$) for increasing the humidity of the air; the other (denoted by $(1-b) \times M_t$) for warming the air by the release of latent heat. There have been quite a few studies which attempted to estimate the value of b (Cho, 1976; Krishnamurti et al., 1980, etc.), but no satisfactory theoretical determination for b is available yet. Kuo's 1965 scheme has been extensively used at the National Meteorological Center (NMC) for various operational and research models. The European Center for Medium Range Forecasts is currently using Kuo's 1974 Scheme. Theoretically speaking, both the convective adjustment scheme and Kuo's scheme are highly empirical, neglecting many of the physical processes involved in the mutual interaction between clouds and the environment. Consequently, these two schemes are not able to provide detailed information about the properties of cumulus ensembles such as cloud mass flux, liquid water detrainment, condensation and evaporation rates and vertical eddy transports of heat and moisture. Hence, from the academic point of view, the convective adjustment scheme and Kuo's scheme do not serve the whole purpose of cumulus parameterization.

Ooyama (1971) first proposed a theory taking into account the coexistence of a spectrum of clouds which were represented by independent entraining buoyant elements dispatched from the mixed layer. However, this theory was not closed since the determination of the dispatcher function was left to future consideration. Based on the concept of Ooyama's spectral clouds and the earlier works of Arakawa (1969, 1972), a theory of the interaction between a cumulus ensemble and the large-scale environment has been developed by Arakawa and Schubert (1974). In essence, the Arakawa-Schubert scheme divides the cumulus ensemble into one-dimensional, steady-state, entraining sub-ensemble clouds; and, more importantly, the scheme is closed by a physically well-defined hypothesis. This scheme can be partitioned into two parts: (1) the budget requirements for the large-scale disturbances, which describe that the cumulus convection affects the temperature and moisture fields through cumulus-induced subsidence, detrainment of saturated air, and evaporation of detrained liquid water; (2) the assumption of quasi-equilibrium for the cloud work function, which describes how the clouds stabilize the atmosphere while the large-scale motion generates moist convective instability.

The "quasi-equilibrium assumption" permits the determination of the cloud mass flux at cloud base (a unique unknown variable in the scheme) so that the large-scale budget equations can be used in a prognostic sense. Meanwhile, the vertical distributions of cloud mass flux, cloud detrainment, condensation and evaporation rates, and eddy transports of heat and moisture can be also determined. Besides, the quasi-equilibrium assumption involves the significance of the interaction between clouds. Thus, as far as the physical processes are concerned, the Arakawa-Schubert scheme has been considered the most complete cumulus parameterization scheme. This report will focus on the

Arakawa-Schubert scheme (hereafter referred to as the A-S scheme) not only because it contains more sophisticated physical processes but also because it has been explored less frequently in the past when compared with the convective adjustment scheme and Kuo's scheme.

Investigations with the use of the A-S scheme in linear Wave-CISK models have been conducted by Stuart (1976), Shukla (1978), and Crum and Stevens (1983). Since the interaction between clouds and large-scale disturbances is inherently a nonlinear process and since the linear normal-mode concept can cause negative heating which is physically unrealistic, we believe that additional research on the role of the A-S scheme in the interaction between clouds and the environment should be carried out with a numerical prognostic model. Miyakoda and Sirutis (1977) compared the convective adjustment scheme in the GFDL GCM with the A-S scheme in the UCLA GCM. Basically, they found that the A-S scheme can produce deeper penetrative convective clouds. Also, the distribution of rainfall relative to the trough and ridge of tropical easterly waves is different between the two schemes. However, in this experiment, not only the cumulus parameterization schemes but also parameterization schemes for other processes are different. Consequently, it is not entirely possible to isolate the differences due to the different cumulus parameterizations. Krishnamurti et al. (1980) evaluated the rainfall rates produced by several different schemes with the GATE Phase III data in a semi-prognostic approach (i.e., one time-step integration). They concluded that Kuo's 1974 scheme and the A-S scheme provided the least root-mean-square error between the calculated and observed estimates. However, neither of these comparative studies enlightened readers on the intrinsic nature of the schemes themselves. In particular, the physical reasons behind the model results or

the skill scores derived from each scheme were not fully examined. Recently, a series of extensive studies evaluating the quasi-equilibrium assumption and testing the A-S scheme was conducted by Lord (1978, 1982), Lord and Arakawa (1980), and Lord et al. (1982) also on the basis of a semi-prognostic approach using the GATE (GARP (Global Atmospheric Research Program) Atlantic Tropical Experiment) Phase III data. The predicted rainfall rates by Lord are generally in good agreement with observations.

By "semi-prognostic" we mean that an instantaneous evaluation of tendency terms produced by the cumulus parameterization at a single grid point in response to a large-scale forcing is made and that the computation is terminated after only one time-step. The advantage of using the semi-prognostic approach to test the cumulus parameterization scheme is that we can make a prediction without the use of a large-scale prediction model. Moreover, since this is only a one time-step integration, the predicted results are free from numerical nonlinear errors and complicated physical feedback effects resulting from the interactions with the boundary layer and with radiation physics. We have also tested the A-S scheme semi-prognostically with a computational algorithm different from Lord's, using data gathered from an intense cloud band (cloud cluster) that developed over the GATE A/B scale ship array on 12 August 1974. A semi-prognostic study using the composite GATE Phase II and III data has also been made. In both of these studies, the cloud heating and drying effects predicted by the A-S scheme were found to agree well with observations. Investigations have been made not only on the net cloud heating and drying effects but also on their associated condensation, evaporation, and vertical transports of heat and moisture. Furthermore, we have modified the A-S scheme by including the convective-scale downdrafts to

explore how the cloud properties such as condensation, evaporation, and the convergence of heat and moisture fluxes can be altered due to the downdraft effects. For comparison purposes, the results derived from a cumulus ensemble model on the cloudband case by Soong and Tao (1980, 1984) were used.

Even though the applicability of the "quasi-equilibrium assumption" to the time and space scales of tropical convective systems is still under debate, Hack and Schubert (1980) and Hack et al. (1984) applied the A-S scheme to an axisymmetric hurricane model and demonstrated that the scheme has the inherent potential to establish a better understanding of the physical nature of the interaction between organized cumulus convection and the large-scale fields. Based on the encouraging results derived from our semi-prognostic studies mentioned above, we subsequently made another test on the A-S scheme using a fully prognostic mesoscale model. In order to examine the evolution and the structure of a tropical cloud cluster under the influence of a low-level, large-scale lifting, a two-dimensional hydrostatic model was developed with the inclusion of the A-S scheme. The model was applied to the same cloudband event mentioned previously. A time-independent, large-scale, low-level forcing was imposed on the model throughout the whole integration. The model results indicate that the mesoscale convective system is driven primarily by the horizontal temperature gradient resultsing from the latent heat release of the clouds. However, the adiabatic heating due to the subsidence outside the cloud cluster was found to contribute significantly to the evolution of the system. A 24-hour integration shows that the model is capable of simulating many important features such as the life cycle, the intensity of circulation, and rainfall rates. The sensitivity of the model was tested by including the vertical wind shear, deleting the large-scale forcing at the middle of the

integration, incorporating the cumulus downdrafts into the A-S scheme, and changing the mixed layer thermodynamic properties. Another important aspect is that, through this simulation study, we were able to observe the intrinsic nature of the A-S scheme as the convective system evolved. This is something which those previous studies did not emphasize. For comparison purposes, a run with the use of Kuo's 1974 scheme was made. It was found that Kuo's scheme seems unable to simulate any prominent features. We believe this is mainly due to the fact that only the highest clouds are allowed to develop in Kuo's scheme, thereby leading to the sudden introduction of a large amount of heating to the upper atmosphere. Combined with the cooling effect due to the large-scale lifting, the thermodynamic structure becomes unfavorable for the development of the cloud cluster. In passing, it should be mentioned that the vertical transport of horizontal momentum due to cumulus clouds is not included in the model.

The topics covered in this report range from the investigation of the A-S scheme itself to the applications of the scheme to semi-prognostic studies and a fully prognostic simulation. Chapter 2 reviews the A-S scheme and several related studies. Chapter 3 presents the results of the semi-prognostic studies, in which the computational algorithm and the procedure of modifying the A-S scheme by including the downdraft effects are also discussed. Chapter 4 describes the prognostic model for the simulation of a tropical mesoscale convective system. Chapter 5 presents the model results and sensitivity tests. Chapter 6 gives the conclusion of this report.

CHAPTER II

REVIEW OF THE ARAKAWA-SCHUBERT CUMULUS PARAMETERIZATION

In this chapter, we briefly present a review of the A-S scheme and several previous studies in which the A-S scheme was applied. The full details of the scheme have been discussed by Arakawa and Schubert (1974) and Lord (1978). The interested reader is referred to those original articles. The large-scale budget equations are reviewed in Section 2.1. The quasi-equilibrium assumption of the cloud work function is reviewed in Section 2.2

2.1 The large-scale budget equations:

To establish the relationship between the collective properties of the clouds and the large-scale variables, the heat and moisture budgets can be expressed in z-coordinates as:

$$\rho \frac{\partial \bar{s}}{\partial t} + \rho \vec{V} \cdot \nabla \bar{s} + \rho \bar{w} \frac{\partial \bar{s}}{\partial z} = Q_R + L(\bar{C} - \bar{e}) - \frac{\partial \rho \overline{w's'}}{\partial z} \qquad (2.1)$$

$$\rho \frac{\partial \bar{q}}{\partial t} + \rho \vec{V} \cdot \nabla \bar{q} + \rho \bar{w} \frac{\partial \bar{q}}{\partial z} = (\bar{e} - \bar{C}) - \frac{\partial \rho \overline{w'q'}}{\partial z} \qquad (2.2)$$

where the variables with the overbar define a large-scale system and the variables with the prime define a cloud-scale system, ρ is the air density, $s = c_p T + gz$ is the static energy, q is the mixing ratio of water vapor, L is the latent heat, Q_R is the radiative heating rate, C is the rate of

condensation, e is the rate of evaporation from liquid water, and $\dfrac{\partial \rho \overline{w's'}}{\partial z}$ and $\dfrac{\partial \rho \overline{w'q'}}{\partial z}$ respectively represent the convergence of vertical eddy transports of s′ and q′ with clouds.

Spectrally dividing the cumulus ensemble into sub-ensembles according to their fractional entrainment rate λ (this variable will be defined shortly), the vertical eddy transports of s′ and q′ are written as:

$$\rho \ \overline{w's'} = \int_0^{\lambda_D(z)} m(z,\lambda)\big(s_c(z,\lambda) - \bar{s}(z)\big)d\lambda \qquad (2.3)$$

$$\rho \ \overline{w'q'} = \int_0^{\lambda_D(z)} m(z,\lambda)\big(q_c(z,\lambda) - \bar{q}(z)\big)d\lambda \qquad (2.4)$$

where the subscript c denotes a cloud variable. The notations introduced in (2.3) and (2.4) will be explained shortly. Representing the sub-ensemble cloud by a one-dimensional steady-state entraining cloud model (the governing equations for the cloud variables are given in Appendix A), the vertical convergence of eddy transports of s′ and q′ can be expressed as:

$$\frac{\partial \rho \overline{w's'}}{\partial z} = L\bar{C} - M_c \frac{\partial \bar{s}}{\partial z} \qquad (2.5)$$

$$\frac{\partial \rho \overline{w'q'}}{\partial z} = D(\bar{q} - \bar{q}^*) - M_c \frac{\partial \bar{q}}{\partial z} - \bar{C} \qquad (2.6)$$

The detailed derivations of (2.3) through (2.6) are given in Arakawa and Schubert (1974). Substituting (2.5) and (2.6) into (2.1) and (2.2), respectively, we obtain:

$$\rho \frac{\partial \bar{s}}{\partial t} + \rho \vec{V} \cdot \nabla \bar{s} + \rho \bar{w} \frac{\partial \bar{s}}{\partial z} = - DL\hat{\ell} + M_c \frac{\partial \bar{s}}{\partial z} + Q_R \tag{2.7}$$

$$\rho \frac{\partial \bar{q}}{\partial t} + \rho \vec{V} \cdot \nabla \bar{q} + \rho \bar{w} \frac{\partial \bar{q}}{\partial z} = D(\bar{q}^* - \bar{q} + \hat{\ell}) + M_c \frac{\partial \bar{q}}{\partial z} \tag{2.8}$$

where the evaporation rate $\bar{e}$ in (2.1) and (2.2) has been replaced by $D\hat{\ell}$ whose physical meaning will be given shortly. Multiplying (2.8) by L and adding to (2.7) gives the budget equation for moist static energy (h):

$$\rho \frac{\partial \bar{h}}{\partial t} + \rho \vec{V} \cdot \nabla \bar{h} + \rho \bar{w} \frac{\partial \bar{h}}{\partial z} = DL(\bar{q}^* - \bar{q}) + M_c \frac{\partial \bar{h}}{\partial z} + Q_R \tag{2.9}$$

where $h = c_p T + gz + Lq$ and the asterisk denotes the value at saturation of the variable. The notations introduced in (2.3) to (2.9) are explained as follows:
(i) M_c, the total cloud mass flux, is expressed as:

$$M_c(z) = \int_0^{\lambda_D(z)} m(z,\lambda)d\lambda \tag{2.10}$$

where

$$\tag{2.11}$$

$$m(z,\lambda)d\lambda = \sum_{\lambda_i \in (\lambda, \lambda+d\lambda)} M_i(z)$$

is the sub-ensemble mass flux due to the clouds which have the parameter λ_i in the interval $(\lambda, \lambda+d\lambda)$. $\lambda_D(z)$, introduced in (2.3), (2.4) and (2.10), represents the fractional entrainment rate of the sub-ensemble which detrains at the cloud top at the level z. It is customary in diagnostic and prognostic

studies of cumulus ensembles to divide the area averaged vertical mass flux $(\bar{M})$, which can be expressed as $\rho\bar{w}$, into:

$$\bar{M} = M_c + \tilde{M} \qquad (2.12)$$

where $\tilde{M}$ is the mass flux averaged over the cloud-free area.

Each individual cumulus cloud is considered to have a characteristic fractional entrainment rate λ which uniquely determines the cloud depth. Assuming that λ is a constant with height for each cloud, we define λ as:

$$\frac{1}{m(z,\lambda)} \frac{\partial m(z,\lambda)}{\partial z} = \lambda \qquad (2.13)$$

It should be noted that the total cumulus population is described by a continuum of cloud entrainment rates. The procedure to determine λ is given in Appendix A. Solving (2.13), we have

$$m(z,\lambda) = m_B(\lambda) \exp \{\lambda(z - z_B)\} \qquad (2.14)$$

where $m_B(\lambda)$ is the cloud mass flux at cloud base and z_B is the cloud base height. Here, we assume that z_B coincides with the condensation level z_c. From (2.14), we define:

$$\eta(z,\lambda) = \begin{cases} \exp \{\lambda(z-z_B)\} \ , \ z_B \leqslant z \leqslant z_D(\lambda) \\ \\ 0 \qquad\qquad\quad , \ z > z_D(\lambda) \end{cases} \qquad (2.15)$$

as the normalized cloud mass flux.

(ii) D(z), the detrainment of cloud mass which is assumed to take place only at the cloud top, is expressed as:

$$D(z) = -m(z,\lambda_D(z)) \frac{d\lambda_D(z)}{dz} \qquad (2.16)$$

where $\lambda_D(z)$ denotes the entrainment rate of the cloud sub-ensemble which detrains at level z.

(iii) $\hat{\ell}(z)$ is the detrained liquid water which spreads at the cloud top of each sub-ensemble and evaporates to cool the environment. $\hat{\ell}(z)$ is determined from the one-dimensional cloud model, as shown in Appendix A.

The physical interpretations of the cloud terms in (2.7) and (2.8) are described as follows:

(i) $M_c \frac{\partial \bar{s}}{\partial z}$ and $M_c \frac{\partial \bar{q}}{\partial z}$ are respectively the cloud heating and drying effects through the forms of "cumulus-induced subsidence." Looking into (2.5) and (2.6), it is seen that the real physical meanings of $M_c \frac{\partial \bar{s}}{\partial z}$ and $M_c \frac{\partial \bar{q}}{\partial z}$ are in terms of condensation, convergence of eddy transports, and the detrainment of water vapor. The last process is related to $M_c \frac{\partial \bar{q}}{\partial z}$ only.

(ii) $D\hat{\ell}$ is the evaporation rate from the detrained liquid water at the cloud top. Without the evaporation from falling precipitation associated with convective downdrafts, $D\hat{\ell}$ is identical to $\bar{e}$ in (2.1) and (2.2).

(iii) $D(\bar{q}^*-\bar{q})$ is the detrainment of saturated cloud air into the environment.

It is customary to describe (2.7) and (2.8) by:

$$Q_1 \equiv \rho\left(\frac{\partial \bar{s}}{\partial t} + \vec{V}\cdot\nabla\bar{s} + \bar{w}\frac{\partial \bar{s}}{\partial z}\right) = -DL\hat{\ell} + M_c \frac{\partial \bar{s}}{\partial z} + Q_R \qquad (2.17)$$

$$Q_2 \equiv -L\left(\frac{\partial \bar{q}}{\partial t} + \vec{V}\cdot\nabla\bar{q} + \bar{w}\frac{\partial \bar{q}}{\partial z}\right) = -LD(\bar{q}^* - \bar{q} + \hat{\ell}) - LM_c \frac{\partial \bar{q}}{\partial z} \qquad (2.18)$$

where Q_1 and Q_2 are respectively interpreted as the "apparent heat source" and "apparent moisture sink" (Yanai et al., 1973). Yanai et al. (1973) first proposed the concept that the heating and drying effects due to a cloud ensemble in a unit area, which is large enough to contain the ensemble but small enough to cover only a fraction of the large-scale disturbance, can be indirectly computed from large-scale observational data. Since the emergence of this idea, the Q_1 and Q_2 profiles have appeared widely in numerous literatures in discussion of the interaction between the cumulus clouds and their environment.

To complete the large-scale budgets, the governing equations for the sub-cloud mixed layer of variable depth are given by Arakawa and Schubert (1974) as:

$$\rho_M \frac{\partial s_M}{\partial t} = -(\rho\vec{V})_M\cdot\nabla s_m + \frac{1}{z_B}\left[(F_s)_0 + k\frac{\Delta s}{\Delta s_v}(F_{sv})_0\right] + (Q_R)_M \qquad (2.19)$$

$$\rho_M \frac{\partial q_M}{\partial t} = -(\rho\vec{V})_M\cdot\nabla q_M + \frac{1}{z_B}\left[(F_q)_0 + k\frac{\Delta q}{\Delta s_v}(F_{sv})_0\right] \qquad (2.20)$$

$$\rho_B \frac{Dz_B}{Dt} = -(M_B - \rho_B \bar{w}_B) + \frac{k}{\Delta s_v} (F_{sv})_0 \qquad (2.21)$$

Equation (2.21) describes the time change of the depth of mixed layer (z_B), which implies that the cloud base is at the top of the mixed layer. Equations (2.19) and (2.20) give:

$$\rho_M \frac{\partial h_M}{\partial t} = -(\rho \vec{V})_M \cdot \nabla h_M + \frac{1}{z_B}[(F_h)_0 + k \frac{\Delta h}{\Delta s_v} (F_{sv})_0] + (Q_R)_M \qquad (2.22)$$

where subscript M denotes the mixed layer values, subscript B denotes the cloud base values, and subscript 0 denotes the surface values. F_s, F_q, F_h, and F_{sv} are the vertical turbulent eddy fluxes of s, q, h, and s_v, respectively. The symbol Δ represents the jump of a particular property across the top of the sub-cloud mixed layer. The parameter k is an empirical constant which is the ratio between the turbulent eddy flux at the surface and the value at the top of the mixed layer. The quantity M_B is the total cloud mass flux at the cloud base and w_B is the large-scale vertical velocity at the cloud base. Fig. 2.1 is a schematic diagram of the sub-cloud layer thermodynamic variables. Arakawa and Schubert proposed that the cumulus clouds originated from the mixed layer with the thermodynamic values of s_M and q_M. A consequence of this assumption is that, as seen from (2.19) and (2.20), the cumulus convection does not directly change s_M and q_M. However, s_M and q_M can be indirectly modified by cumulus convection through the change of the depth of the mixed layer (see (2.21); Ogura and Cho, 1974; and Albrecht et al., 1979). An extensive investigation of the coupling processes between the planetary boundary layer (PBL) parameterization and the A-S cumulus parameterization in a GCM is given

in Suarez et al. (1983). A detailed discussion along this line will be presented in Chapter 4, where we develop a sub-cloud layer parameterization for a mesoscale model.

The analysis up to this point can be referred to as the first part of the A-S scheme. Once the large-scale variables, including $\frac{\partial \bar{s}}{\partial t}$ and $\frac{\partial \bar{q}}{\partial t}$, are given from observation, (2.17) and (2.18) can be used to diagnostically determine the cloud properties such as $m_B(\lambda)$, $D(z)$, and $\hat{\ell}(z)$. Ogura and Cho (1973) first demonstrated the properties of the cumulus population by applying the A-S scheme to the mean summertime conditions over the Marshall Islands. Their results indicated a bimodal distribution of the cloud base mass flux in terms of the height of the cloud top: one group of clouds penetrated up to the 200-300 mb level and another group stayed below the 600 mb level, while relatively few clouds lay between 400 and 600 mb. Later, Cho and Ogura (1974) applied the same method to the averaged easterly wave disturbances in the western Pacific based on Reed and Recker's data set (Reed and Recker, 1971). Bimodal distributions are also present in the region near trough axis while only shallow clouds dominate in the ridge area. Another finding is that there appears to be a linear correlation between the cloud base mass flux of deep clouds and large-scale, low-level mass convergence. It suggests that high cloud activities are mostly controlled by the low-level, large-scale lifting.

Nitta (1975) diagnostically determined the cloud mass flux distributions and cloud detrainment from observational data over the tropical Atlantic Ocean during the BOMEX (Barbados Oceanographic and Meteorological Experiment) Phase III (22-30 June 1969). He found that only shallow clouds were dominant and that the total cloud mass flux was confined below the inversion during the
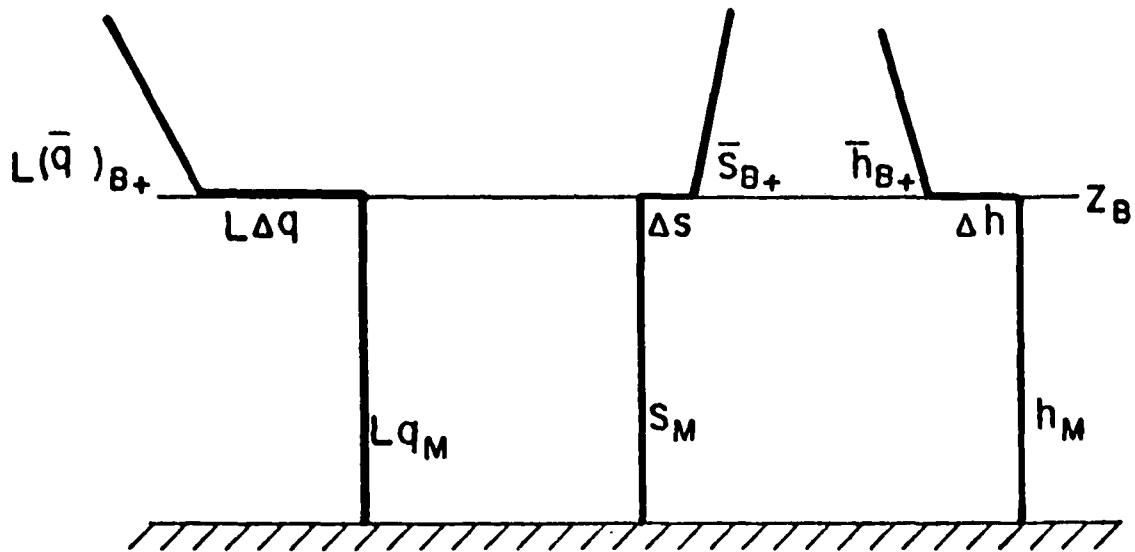
Fig. 2.1 A schematic diagram of the sub-cloud layer thermodynamic variables. s_M and q_M are the mixed layer dry static energy and mixing ratio and are assumed constant with height. h_M is given by $h_M = s_M + Lq_m$. $(\ )_B$ indicates a value in the free atmosphere immediately above the PBL top at $z = {}^+z_B$. There is an infinitely thin transition layer between z_B and z_{B_+} with the jump conditions Δq, Δs, and Δh.

typical trade inversion period. The cooling and moistening effects due to the detrainment of liquid water and water vapor appear to be very crucial in the large-scale heat and moisture budgets over the tropical trade wind region. Based on the framework of the A-S scheme, Johnson (1976) included convective-scale downdrafts in a diagnostic model to determine the cloud population and their associated properties. Basically, he found that cumulus downdrafts contributed significantly to the total convective mass transport in the lower atmosphere. Johnson concluded that the neglect of cumulus downdrafts and their associated rainfall evaporation led to the diagnosis of an extensively large population of shallow clouds in highly convective situations. Johnson's downdraft model will be discussed in detail in the next chapter, where we incorporate his model into the A-S scheme in a prognostic study. Later, Johnson (1980) modified his diagnostic model by including mesoscale downdrafts to study anvil-type mesoscale convective systems. An entraining plume model with a spectrum distribution of clouds for convective-scale elements was still employed as before, while mesoscale downdrafts were formulated through a bulk cloud model. He concluded that the mesoscale downdrafts are equally important in contributing to the budgets of heat and moisture.

Undoubtedly, using the A-S scheme to diagnostically determine cloud properties under various topical weather conditions has contributed to an understanding of the interaction between cumulus convection and large-scale disturbances. Nevertheless, the ultimate purpose of the A-S scheme is a prognostic one, and the tendency terms $\frac{\partial \bar{s}}{\partial t}$ and $\frac{\partial \bar{q}}{\partial t}$ are the unknown variables to be determined from the large-scale variables. This problem will be discussed in the next section. In passing, it is worthwhile to mention a physically

unrealistic aspect which may be encountered when using the A-S scheme in a diagnostic study. With the use of (2.10) and (2.14), it can be recognized that (2.17) and (2.18) are a set of two Volterra integral equations of the second kind with two unknowns $\hat{\ell}(z)$ and $m_B(\lambda)$. They can be solved by a proper numerical approach (Nitta, 1975). However, the solutions of $\hat{\ell}(z)$ and $m_B(\lambda)$ cannot be guaranteed to be positive values, as shown by Cho and Ogura (1974) and Johnson (1976, 1978). Although the magnitudes of the negative solutions in their results are relatively small, the experience gained from our preliminary studies shows that the negative magnitudes of $\hat{\ell}(z)$ and $m_B(\lambda)$ can be extensively large in some cases and that these situations pose difficulties in interpreting the solutions.

2.2 Cloud work function and quasi-equilibrium assumption

We start with the time change of the kinetic energy of each sub-ensemble:

$$\frac{dK(\lambda)}{dt} = A(\lambda)m_B(\lambda) - D(\lambda) \qquad (2.23)$$

where $K(\lambda)$ and $D(\lambda)$ are the kinetic energy and its dissipation, respectively. $A(\lambda)$ is called the cloud work function and is a measure of buoyancy. The derivation of (2.23) is presented in Haltiner and Williams (1979). The cloud work function $A(\lambda)$ is given as:

$$A(\lambda) = \int_{z_B}^{z_D(\lambda)} \frac{g}{c_p \bar{T}(z)} \, \eta(z,\lambda)[s_c(z,\lambda) - \bar{s}(z)]dz \qquad (2.24)$$

where s_c is the static energy of the sub-ensemble λ. The time derivative of $A(\lambda)$ can be expressed as:

$$\frac{\partial A(\lambda)}{\partial t} = \frac{\partial h_M}{\partial t} \int_{z_B}^{z_D(\lambda)} \rho(z)\beta(z)dz + \int_{z_B}^{z_D(\lambda)} \rho(z)b(z,\lambda)\lambda\eta(z,\lambda)\frac{\partial \bar{h}}{\partial t} dz$$

$$(2.25)$$

$$- \int_{z_B}^{z_D(\lambda)} \rho(z)\alpha(z)\eta(z,\lambda)\frac{\partial \bar{s}}{\partial t} dz$$

Substituting the expressions of $\frac{\partial \bar{s}}{\partial t}$ and $\frac{\partial \bar{h}}{\partial t}$ from (2.7) and (2.9) into (2.25), we obtain:

$$\frac{\partial A(\lambda)}{\partial t} = F_M(\lambda) + \int_0^{\lambda_{max}} [K_V(\lambda,\lambda') + K_D(\lambda,\lambda')]m_B(\lambda')d\lambda' + F_c(\lambda)$$

$$(2.26)$$

where $F_c(\lambda) = \int_{z_B}^{z_D(\lambda)} \eta(z,\lambda)\{\lambda b(z,\lambda)[-\bar{w}\frac{\partial \bar{h}}{\partial z} - \vec{V}\cdot\nabla\bar{h} + Q_R]$

$$(2.27)$$

$$- \alpha(z)(- \bar{w}\frac{\partial \bar{s}}{\partial z} - \vec{V}\cdot\nabla\bar{s} + Q_R)\} \rho(z)dz$$

$$F_M(\lambda) = \frac{\partial h_M}{\partial t} \int_{z_B}^{z_D(\lambda)} \rho(z)\beta(z)dz$$

$$(2.28)$$

$$K_V(\lambda,\lambda') = \int_{z_B}^{z_D(\lambda)} \eta(z,\lambda)\eta(z,\lambda')\{\lambda b(z,\lambda)\frac{\partial \bar{h}}{\partial z} - \alpha(z)\frac{\partial \bar{s}}{\partial z}\} dz$$

$$(2.29)$$

$$K_D(\lambda,\lambda') = \eta(z_D',\lambda)\eta(z_D',\lambda')\{\lambda b(z_D',\lambda) \ L(\bar{q}^*(z_D') - \bar{q}(z_D')) + \alpha(Z_D')L\hat{\ell}(Z_D')\}(2.30)$$

where $\dfrac{\partial h_M}{\partial t}$ in (2.28) can be replaced by the right hand side of (2.22) or another expression derived from a different approach of the mixed layer parameterization (e.g., Suarez et al., 1983 or Johnson, 1976). The detailed derivations of (2.25) and (2.26) and the actual forms of $\alpha(z)$, $\beta(z)$, and $b(z,\lambda)$ are presented in Appendix B.

The differences between Equations (2.26) - (2.30) and their original expressions in Arakawa and Schubert (1974) are due to the following approximations that we introduced:

(i) The cloud base z_B coincides with the condensation level z_c.

(ii) The effects of water vapor and liquid water on the cloud work function are neglected in (2.24).

(iii) The top of the mixed layer is defined by a fixed z-coordinate surface. Namely, z_B is constant with time.

The first two approximations are adopted from Lord et al. (1982) for simplification purposes. The last approximation may not be valid in studying a GCM (Suarez et al., 1983) or synoptic-scale prediction model. However, for the semi-prognostic studies and mesoscale simulations, it appears to be acceptable (Lord, 1978, 1982; Hack et al., 1983).

The kernel $K_v(\lambda,\lambda')$ in (2.26) serves as a stabilization factor for cloud type λ due to the heating effect of cloud type λ' on the environment. Meanwhile, $F_c(\lambda)$ and $F_M(\lambda)$ in (2.26) serve as destabilization factors for cloud type λ due to large-scale forcing. $K_D(\lambda,\lambda')$ also serves as a destabilization factor for cloud type λ due to the cooling effect through the evaporation of

detrained liquid water and the moistening effect through the detrainment of water vapor of cloud type λ'. Arakawa and Schubert (1974) respectively defined F_c, F_M, K_v, and K_D as "cloud layer forcing," "mixed layer forcing," "vertical mass flux kernel," and "detrainment kernel." However, the major effects in (2.26) are through the F_c and K_v terms: F_c increases the cloud work function of the sub-ensemble λ primarily through the adiabatic cooling due to the large-scale upward motion, while K_v decreases the cloud work function of the sub-ensemble λ through adiabatic warming of the environment due to the induced subsidence of sub-ensemble λ'. Typically, F_M and K_D are respectively smaller than F_c and K_v by one to two orders of magnitude. However, when the lower atmosphere is extremely dry, K_D can be equally as important as K_v due to the large excess mixing ratio (see (2.30)). Based on the argument of the quasi-equilibrium assumption (Arakawa and Schubert, 1974; Lord and Arakawa, 1980), (2.26) can be expressed as:

$$\int_0^{\lambda max} K(\lambda,\lambda')m_B(\lambda')d\lambda' + F(\lambda) = 0, \text{ when } m_B(\lambda) > 0 \qquad (2.31a)$$

$$\int_0^{\lambda max} K(\lambda,\lambda')m_B(\lambda')d\lambda' + F(\lambda) < 0, \text{ when } m_B(\lambda) = 0 \qquad (2.31b)$$

Where $K(\lambda,\lambda') = K_v(\lambda,\lambda') + K_D(\lambda,\lambda')$; and $F(\lambda) = F_c(\lambda) + F_M(\lambda)$. The quasi-equilibrium assumption, which serves as a closure hypothesis, can be briefly interpreted as follows: if the adjustment time of clouds is small compared to the time scale of the large-scale disturbance, we assume that the cumulus ensemble follows a sequence of quasi-equilibrium states while the large-scale forcing changes; and the condition described by (2.31a) must be valid for each positive $m_B(\lambda)$; on the other hand, when the time derivative of $A(\lambda)$ becomes

negative, a sub-ensemble of such λ would not exist, thus requiring $m_B(\lambda) = 0$ as shown in (2.31b).

(2.31a) is a Fedholm integral equation of the first kind for the unknown $m_B(\lambda)$ subject to the condition of inequality by (2.31b). Solving (2.31) is not a trivial matter. A "simplex over-adjustment method" proposed by Silva-Dias and Schubert (1977) is found to be very efficient, which is based on a linear programming algorithm (Dantzig, 1963; Gass, 1975). By introducing some "slack" variables into (2.31a), this method is able to provide positive solutions for $m_B(\lambda)$ and meet the requirement of (2.31b). Generally speaking, the linear programming method restates the quasi-equilibrium hypothesis as an optimization problem. A detailed description of how to use the linear programming algorithm to solve (2.31) is given by Lord (1978) and Hack et al. (1984).

Once $m_B(\lambda)$ is determined, $M_c(z)$ can be readily obtained from (2.14) and (2.10) and $D(z)$ can be obtained from (2.16). Substituting M_c, D, and $\hat{\ell}$ into (2.7) and (2.8) with the given large-scale variables, $\frac{\partial \bar{s}}{\partial t}$ and $\frac{\partial \bar{q}}{\partial t}$ can be determined. In the mean time, rainfall rates can be calculated from (A.6).

A series of tests of the A-S scheme have been conducted by Lord (1978, 1982), Lord and Arakawa (1980), and Lord et al. (1982). First, Lord and Arakawa (1980) assembled several data sets over various areas in the tropics and showed the evidence that the cloud work function is a quasi-universal function of the detrainment level (i.e., the height of cloud top). Later, Lord (1982) applied the semi-prognostic approach to the observational data for the period 1-18 September 1974 over the GATE area to evaluate the A-S scheme. The predicted vertical profile of the time-averaged heating effects of clouds

agrees well with the observed one (Fig. 2.2a), while the drying effects of clouds show less satisfactory agreement (Fig. 2.2b). Also, the predicted rainfall rates agree quite well with the observations.

The algorithm which Lord (1982) used in his semi-prognostic study can be outlined in the following steps:

(i) From the large-scale variables T, q, w, u, v, and Q_R, cloud parameters λ, $n(z,\lambda)$, h_c, s_c, and q_c are computed for each sub-ensemble whose cloud top height is specified according to the vertical grid arrangement of the model atmosphere.

(ii) The cloud work function (2.24) is computed for each sub-ensemble.

(iii) The large-scale forcing in (2.31) for the ith sub-ensemble is computed by:

$$F(i) = \frac{A'(i) - A(i)}{\Delta t'} \qquad (2.32)$$

where $A(i)$ is calculated from the data at a given observation time t and $A'(t)$ is the cloud work function computed from bogus large-scale temperature and moisture fields which would result when the large-scale horizontal and vertical advection operated for a short period of time $\Delta t'$. Note that the fractional entrainment rate for the ith sub-ensemble in $A'(i)$ is different from that in $A(i)$ because the temperature and moisture profiles have been modified.

(iv) The kernel in (2.31) is computed by:

$$K(i,j) = \frac{A''(i) - A(i)}{m_B(j)\Delta t''} \qquad (2.33)$$

a

b
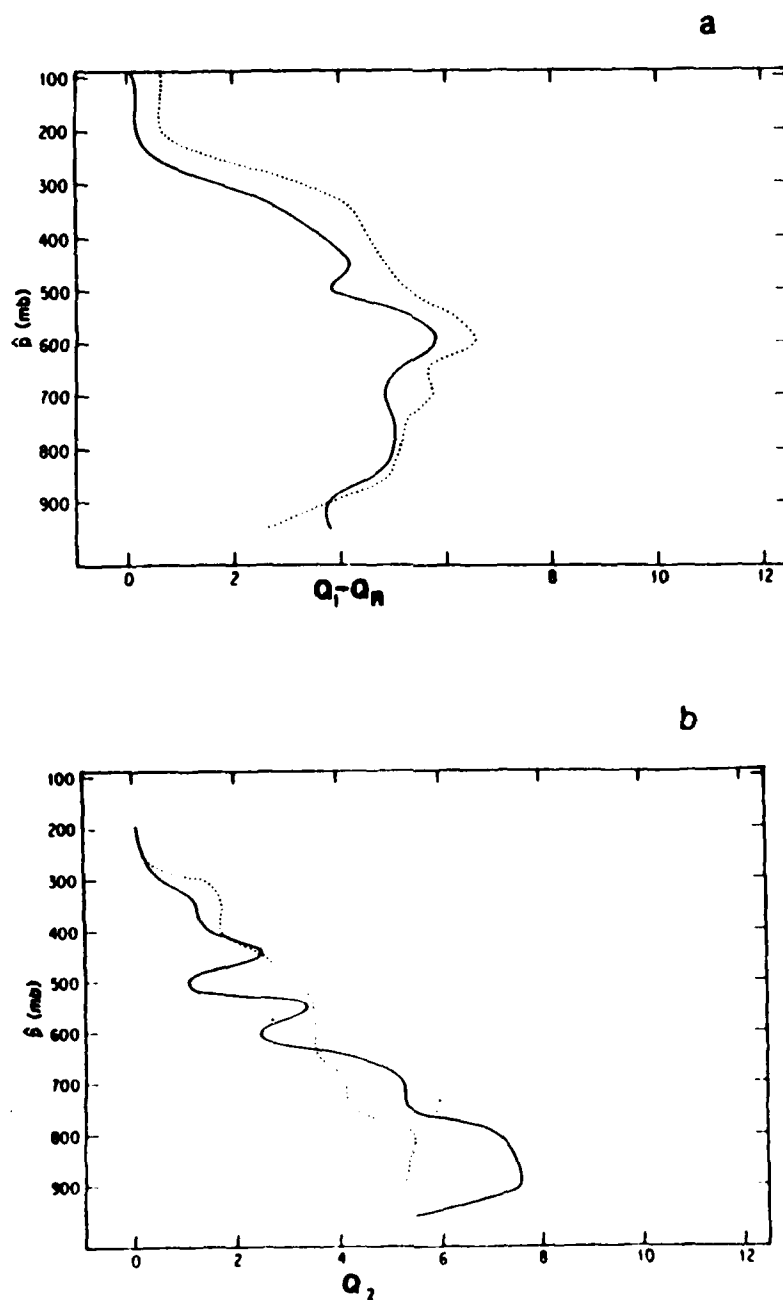
Fig. 2.2. (a) the time averaged vertical distributions of the apparent heat source due to clouds (Q_1-Q_R) and (b) The time averaged vertical distributions of the apparent moisture sink (Q_2). Both are in the units of C day^{-1}. The predicted values are indicated by solid lines and the observed values are indicated by dashed lines. (Adapted from Lord, 1982.)

where A"(i) is computed after the large-scale variables are modified by the jth sub-ensemble through its cloud effects in the time interval Δt". Again, the λ in A"(i) is different from the original one in A(i).

(v) Fredholm's integral equation (2.31) is now solved for $m_B(\lambda)$ by the "simplex over-adjustment method".

(vi) $\frac{\partial \bar{s}}{\partial t}$, $\frac{\partial \bar{q}}{\partial t}$ and rainfall rate are computed from (2.7), (2.8), and (A.6), respectively.

It is seen that Lord used finite difference approximations in steps (iii) and (iv) to calculate forcing and kernel terms instead of using their explicit forms stated in (2.27) to (2.30). Further discussion of Lord's algorithm is given in Chapter 3. Recently, Hack et al. (1984) modified the original A-S scheme into a flux form for computational convenience. They subsequently applied the scheme to a semi-prognostic study for the Marshall Islands data and a prognostic study of the development of an axisymmetric hurricane. However, they focused their attention primarily on the numerical aspects of the A-S scheme without much discussion of the model results. The only conclusion they presented about the physical aspects of their study is that the mass flux associated with deep clouds is controlled not only by vertical motion at the top of the mixed layer but also by large-scale vertical motion in the middle and upper troposphere.

CHAPTER III

THE SEMI-PROGNOSTIC STUDIES

In this chapter, we present the results of semi-prognostically applying the A-S scheme to two different data sets: one for an intense cloud band observed in GATE, and the other for wave composites of GATE Phase II and III. Section 3.1 presents the motivation of this study. Section 3.2 gives the computational algorithm. Section 3.3 presents the results. Section 3.4 describes an experiment which incorporates the convective-scale downdraft effects into the A-S scheme for prognostic purposes.

3.1 Introduction:

Although the series of studies by Lord (1978); Lord and Arakawa (1980), Lord (1982), and Lord et al. (1982) have been considered the most extensive approach to test the A-S scheme, we feel that, as far as measuring the success of the A-S scheme through a semi-prognostic approach is concerned, simply presenting the result averaged over the period of 18 days (1-18 September 1974 of GATE Phase III), as shown in Fig. 2.2, may not be an accurate assessment of the scheme. In order to examine the response of cumulus clouds to the large-scale forcing through the application of the A-S scheme to an "individual" tropical convective event, a semi-prognostic approach using the data for an intense cloud band observed from the GATE A/B scale ship array on 12 August 1974 was undertaken. Furthermore, in order to examine the general behavior of the A-S scheme in the mean weather conditions over the tropics, we applied the

scheme to the wave composites. The composite data of GATE Phase II and III were used for this purpose.

To date, all the studies on the A-S scheme have placed the emphasis on the net heating and drying effects of cumulus clouds, neglecting their associated individual components, such as condensation, evaporation, and vertical transports of heat and moisture, which, in fact, can be easily deduced from the A-S scheme. Soong and Tao (1980), Tao (1983), and Soong and Tao (1984) applied the "cloud ensemble model" developed by Soong and Ogura (1980) to the GATE cloudband case. Their results indicate that statistical properties of model clouds that develop under a given large-scale forcing agree well with the observations in many aspects. We shall compare not only the predicted cloud heating and drying effects with the observations but also the predicted rates of condensation, evaporation, and vertical transports of heat and moisture with those derived from Soong and Tao's cloud modeling study. This comparison enables us to further illustrate the physical details of the A-S scheme.

It has become increasingly evident that in regions of active convection the convective-scale downdrafts and their associated evaporation from precipitation are important not only during the life cycle of individual cumulus clouds but also in contributing to the budgets of large-scale disturbances. On the other hand, the comparative study mentioned before reveals that the A-S scheme underestimates both condensation and evaporation rates substantially when compared with the results form the cloud ensemble model. We believe that the inclusion of the convective-scale downdraft effects may alleviate this deficiency. As mentioned in Chapter 2, Johnson (1976) developed a method to diagnostically estimate the contribution to cloud

properties by convective-scale downdrafts. Based on Johnson's model, a formulation which incorporates the downdraft effects into the quasi-equilibrium assumption is developed and applied to the semi-prognostic study. The result shows that a substantial improvement of predicted condensation and evaporation is obtained.

3.2 The algorithm:

Because the cumulus parameterization is incorporated in a vertically discrete model atmosphere, the use of the fractional entrainment rate λ as the spectral parameter in the original theory of the A-S scheme may introduce computational difficulties. Namely, if we specify λ in time as an independent variable, then the detrainment level $z_D(\lambda)$ will be a function of time, which is not compatible with the fixed vertical coordinates. Thus, in the applications of the A-S scheme we may determine the cloud spectrum distributions with the use of cloud top height, denoted by $\hat{z}$, instead of using λ. $\hat{z}$ is associated with the pre-existing vertical grids and λ, which corresponds to each $\hat{z}$, is determined by an iterative method through the large-scale thermodynamic structure with the cloud top condition of zero buoyancy (see Appendix A). Hence, λ is no longer an independent variable. In this way, we can rewrite (2.31) as:

$$\int_{z_B}^{\hat{z}_{max}} K(\hat{z},\hat{z}')m_B(\hat{z}')d\hat{z}' + F(\hat{z}) = 0 \text{ , when } m_B(\hat{z}) > 0 \tag{3.1a}$$

$$\int_{z_B}^{\hat{z}_{max}} K(\hat{z},\hat{z}')m_B(\hat{z}')dz' + F(\hat{z}) < 0 \text{ , when } m_B(\hat{z}) = 0 \tag{3.1b}$$

where the expressions for $k(\hat{z}, \hat{z}')$, and $F(\hat{z})$ remain the same as shown in (2.27)

to (2.30). Note that the upper and lower limits of the integral equations have been changed according to the new spectral parameter. In transforming (2.31) to (3.1), all the terms associated with the time rate of change of λ $\left(\frac{\partial \lambda}{\partial t}\right)$ were neglected. As indicated by Hack et al. (1984), where the pressure at the cloud top $(\hat{p})$ was used to represent the cloud spectrum, this change in spectral parameter somewhat alters the quantitative details of quasi-equilibrium as originally formulated because of the negligence of $\frac{\partial \lambda}{\partial t}$ in deriving (3.1a) and (3.1b). Nonetheless, the qualitative aspects should remain unchanged, since the modifications of the kernel and forcing terms due to the time rate of change of λ is small (Schubert, 1973). A complete discussion of the use of the detrainment level $(\hat{z}$, or $\hat{p})$ as the cloud spectral parameter in the A-S scheme is given in Hack et al. (1984), where interested readers should be referred to. From now on, all the λs in the equations related to the A-S scheme are replaced by the new spectral parameter $\hat{z}$.

It was noticed in Section 2.2 that Lord used the finite difference approximations (2.32) and (2.33) to calculate the forcing and kernel terms instead of using the explicit forms as stated in (2.27) to (2.30). The advantage of Lord's approach is that the time rate of change of λ can be numerically determined with two bogus time intervals $\Delta t'$ and $\Delta t''$ and a bogus mass flux $m_B(j)$. In principle, $\Delta t'$ in (2.32) and $m_B(j)\Delta t''$ in (2.33) can be arbitrarily chosen (Lord, 1978). However, it was indicated by Lord that there are practical upper and lower bounds for the choices. So (1982) applied the A-S scheme using Lord's algorithm to the mid-latitude Baiu situation. He found that $A'' - A$ in (2.33) is not linear with the choice of $m_B(j)\Delta t''$ so that the kernel and, as a consequence, the cloud base mass flux (m_B) depend upon the choice of $m_B(j)\Delta t''$. Figs. 3.1 and 3.2, adapted from So (1982), indicate that
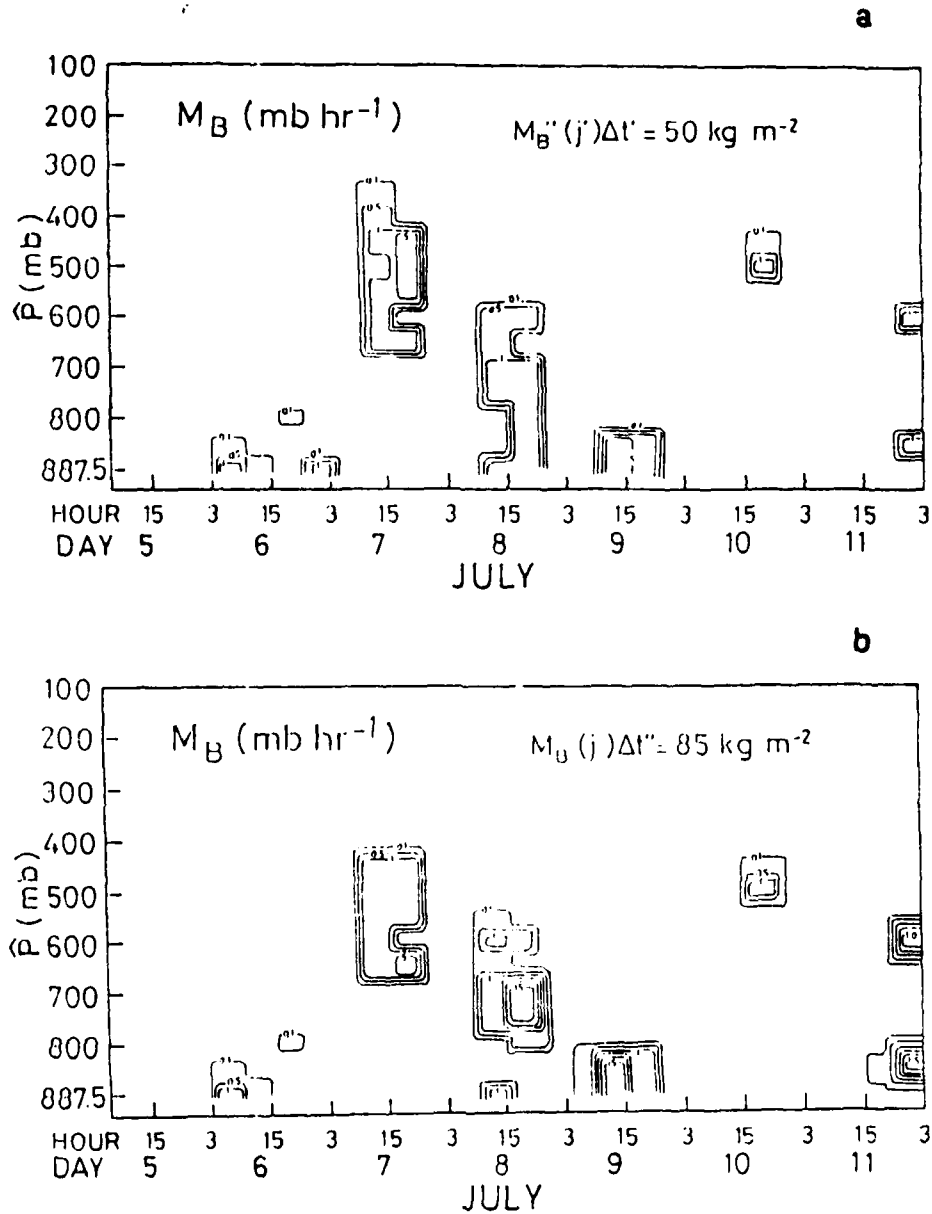
Fig. 3.1. The time series of cloud base mass fluxes in the units of mb hr-1 for (a) mb(j)Δt" = 50 Kg m^{-2} and (b) mb(j)Δt" = 85 Kg m^{-2}. The ordinates are the cloud top pressure p (mb). (Adapted from So, 1982.)
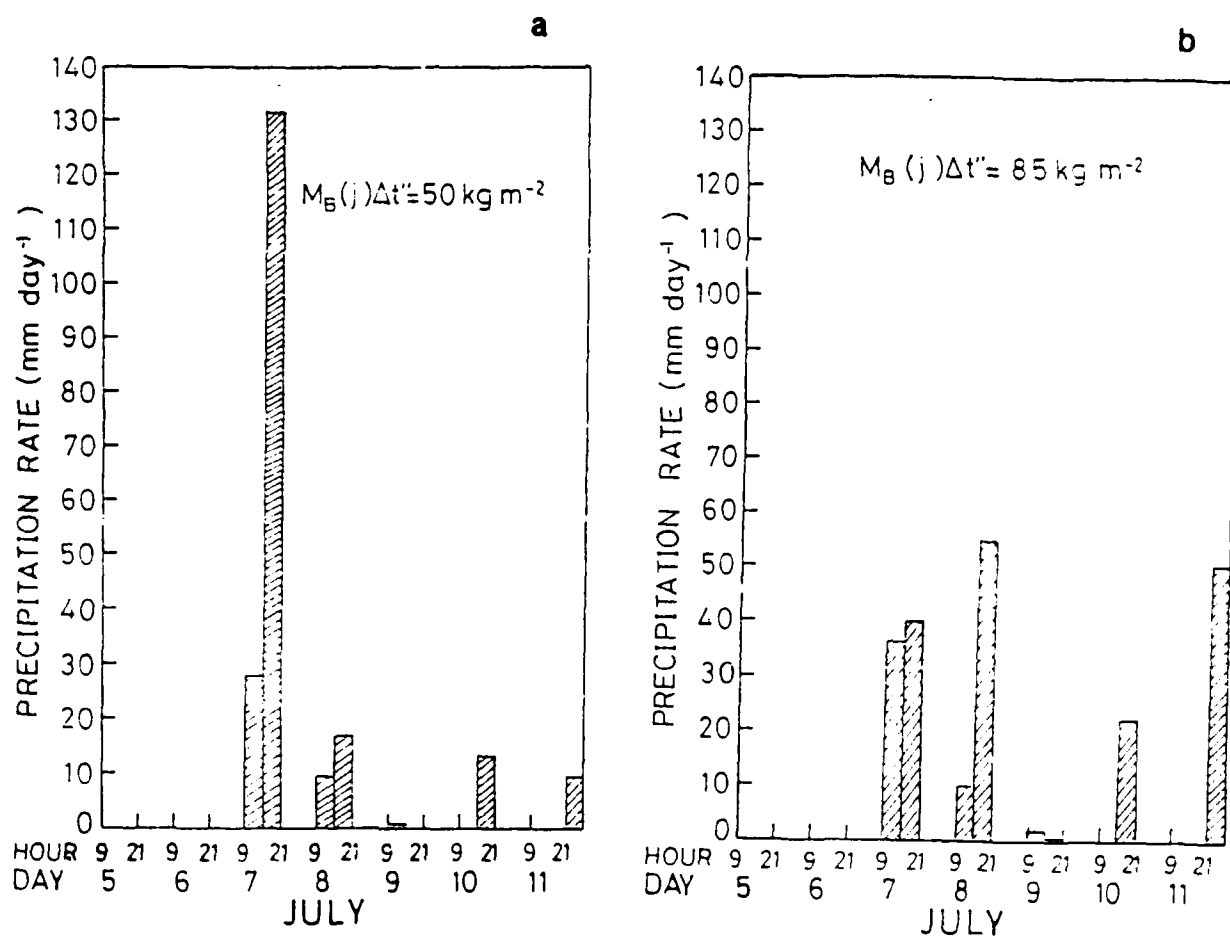
Fig. 3.2. The same as Fig. 3.1 except for the precipitation rate. (Adapted from So, 1982.)

there are substantial differences both in m_B and the precipitation rates when two different $m_B(j)\Delta t''$ are used. Our preliminary examination also reveals that the different choices of $\Delta t'$ and $m_B(j)\Delta t''$ result in different heating and drying profiles. Although the differences are not as dramatic as So showed, we feel that a more acceptable algorithm is required.

To avoid the undesirable sensitivities described above, we applied the A-S scheme by directly calculating the forcing and kernels from (2.26) to (2.29), but with the change of spectral parameter from λ to $\hat{z}$. As mentioned in Chapter 2, once $F(\hat{z})$ and $K(\hat{z}, \hat{z}')$ in (3.1) are determined, m_B can be obtained by solving an optimization problem. The explicit forms of this problem can be illustrated as follows:

Numerically using the summation to represent the integral, (3.1a) can be expanded as:

$$a(1,1)X(1) + a(1,2)X(2) + \ldots + a(1,I_{max})\, X(I_{max}) = b(1)$$

$$a(2,1)X(1) + a(2,2)X(2) + \ldots + a(2,I_{max})\, X(I_{max}) = b(2)$$

$$\ldots \qquad\qquad \ldots \qquad\qquad\qquad (3.2)$$

$$\ldots \qquad\qquad \ldots$$

$$a(I_{max},1)X(1) + a(I_{max},2)X(2) + \ldots + a(I_{max},\, I_{max})X(I_{max}) =$$

$$b(I_{max})$$

where I_{max} denotes the number of total sub-ensembles, $a(n,m) = -K(\hat{z}, \hat{z}')$, $b(n) = F(\hat{z})$ and $X(m) = m_B(\hat{z}')d\hat{z}'$ for $n, m = 1, 2, \ldots, I_{max}$.
Introducing the other I_{max} "slack" variables expressed as $X(I_{max}+1)$, $X(I_{max}+2)$ $\ldots$ $X(2 \times I_{max})$ into (3.2) with the negative signs in front of them, we have:

$$a(1,1)X(1) + a(1,2)X(2) + \ldots + a(1,I_{max})X(I_{max}) - X(I_{max} + 1) = b(1)$$

$$a(2,1)X(1) + a(2,2)X(2) + \ldots + a(2,I_{max})X(I_{max}) - X(I_{max} + 2) = b(2)$$

$$\ldots \qquad\qquad \ldots \qquad\qquad\qquad\qquad (3.3)$$

$$\ldots \qquad\qquad \ldots$$

$$a(I_{max},1)X(1) + a(I_{max},2)X(2) + \ldots + a(I_{max},\ I_{max})X(I_{max}) -$$

$$X(2xI_{max}) = b(I_{max})$$

Now, we can rewrite (3.3) into the form of the "Linear Programming Problem" (also known as an optimization problem) as follows: Solve the set of linear equations:

$$\sum_{m=1}^{2 \times I_{max}} a(n,m)\ X(m) = b(n),\ \text{for}\ n = 1, 2, \ldots\ I_{max} \qquad (3.4)$$

subject to the constraints of

$$X(m) > 0\ \text{for}\ m = 1, 2, \ldots\ 2xI_{max} \qquad (3.5)$$

and a minimized linear objective function Z, defined by:

$$Z = \sum_{m=1}^{2 \times I_{max}} c(m)X(m)\ \text{for}\ m = 1, 2, \ldots, 2xI_{max} \qquad (3.6)$$

where

$$c(m) = 0,\ \text{for}\ m = 1, 2, \ldots\ I_{max} \qquad (3.7a)$$

$$c(m) = 1,\ \text{for}\ m = I_{max}+1,\ I_{max}+2, \ldots 2 \times I_{max} \qquad (3.7b)$$

Extensive discussions of this linear programming problem are given in Lord (1978) and Hack et al. (1984). Our biggest concern has been to obtain a software package which can provide the most accurate solutions. It was found that a subroutine named ZX4LP, based on the work by Hanson and Wisniewski (1979), from the IMSL (International Mathematic and Statistical Library) computing package is very efficient and accurate enough for our purposes.

Our computational algorithm, shown in Fig. 3.3, is generally the same as Lord's described in Section 2.2 except that the calculations for the forcing and kernel terms are different. In this study, we use z-coordinates and divide the atmosphere vertically into 16 layers with the equal depth of 1 km. As stated in Section 2.2, F_M is in general much smaller than F_c (see Eqs. (2.26), (2.27), and (2.28)). Consequently, an additional assumption that h_M is independent of time (i.e., $\frac{\partial h_M}{\partial t} = 0$) is used in this semi-prognostic study for simplicity. We followed Lord's (1982) discrete analogues of the A-S scheme. Fig. 3.4 shows the vertical structure of the large-scale variables. The schematic diagrams for the arrangement of the cloud variables and the distribution of the cloud spectrum are respectively shown in Figs. A.1 and A.2.

3.3 The results:

3.3.1 The tropical cloud band study:

A complete data analysis for the intense cloud band that developed on 12 August 1974 over the GATE A/B scale ship array is given by Ogura et al. (1979). The radar photographs shown in Fig. 3.5 indicate that this system started developing around 00 GMT and reached its peak activity around 15 GMT.
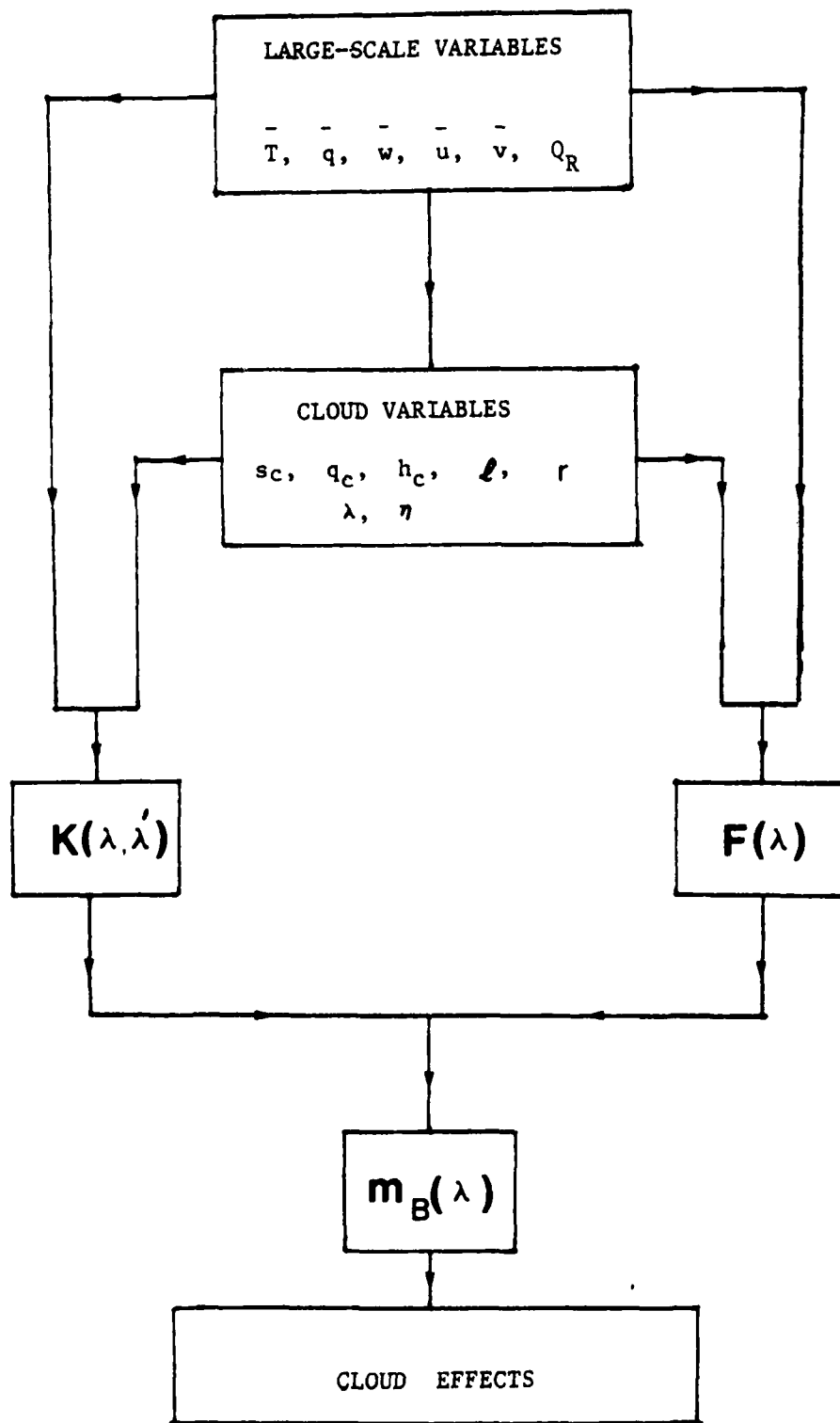
Fig. 3.3. The schematic diagram of the computational procedure of the A-S scheme in the semi-prognostic study.

LEVEL

—————————————— 16

————————————————— 15 1/2

—————————————— 15

$p(k-1/2)$ $\bar{w}(k-1/2)$ $\bar{T}(k-1/2)$ $\bar{q}_v(k-1/2)$ $k+1/2$

LAYER k

$p(k)$ $T(k)$ $\bar{q}_v(k)$ k

$p(k+1/2)$ $\bar{w}(k+1/2)$ $\bar{T}(k+1/2)$ $\bar{q}_v(k+1/2)$ $k-1/2$

—————————————— 2

Z_B

————— PBL ————— 1
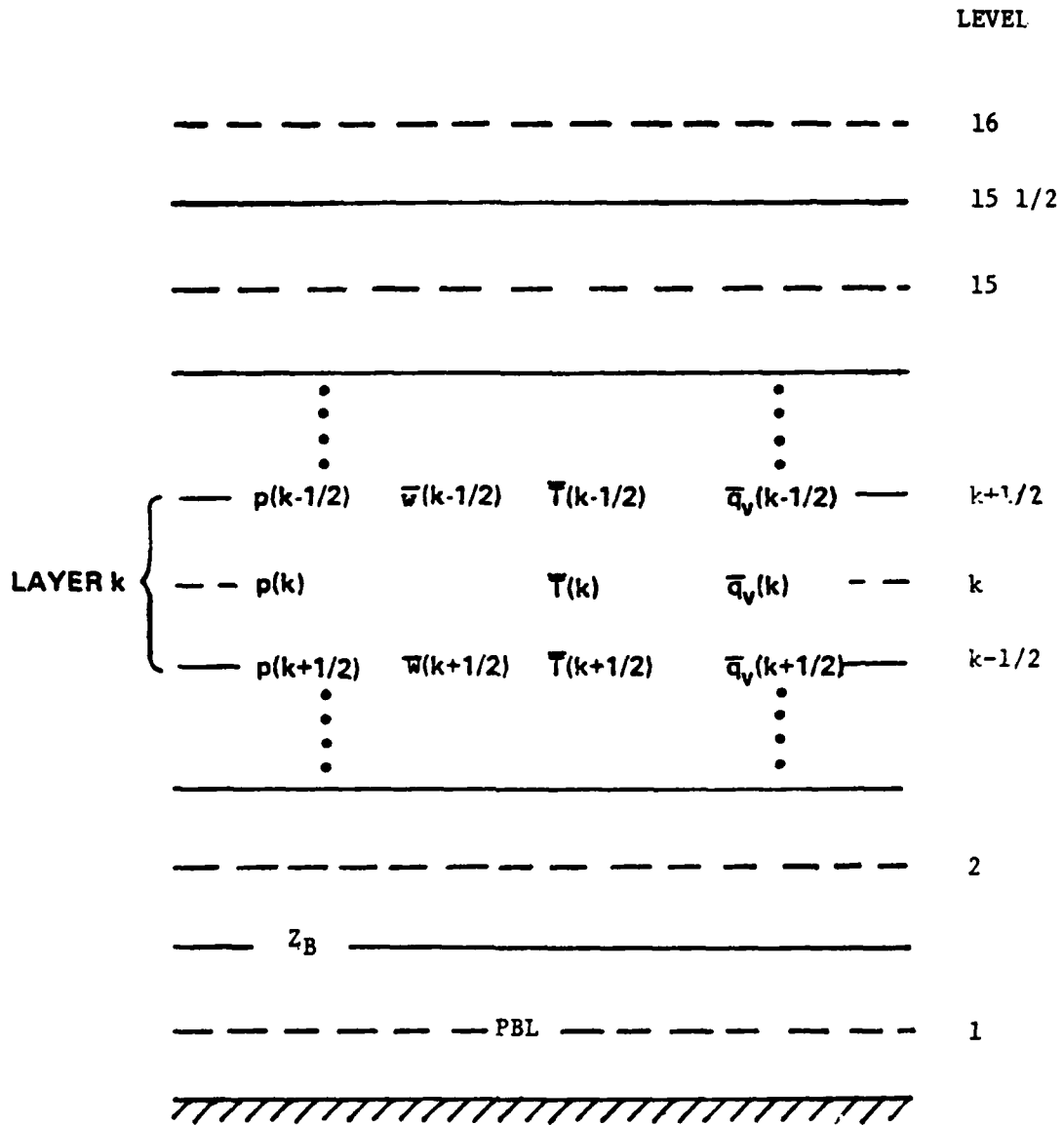
Fig. 3.4. The vertical structure of the large-scale model. Pressure (p) is provided at both integer and half-integer levels, temperature ($\bar{T}$) and mixing ratio ($\bar{q}$) are provided at integer levels, and vertical velocity ($\bar{w}$) is given at half-integer levels. The thermodynamic variables at half-integer levels $\bar{T}(k+1/2)$ and $\bar{q}(k+1/2)$ are the interpolated values from those at k+1 and k.
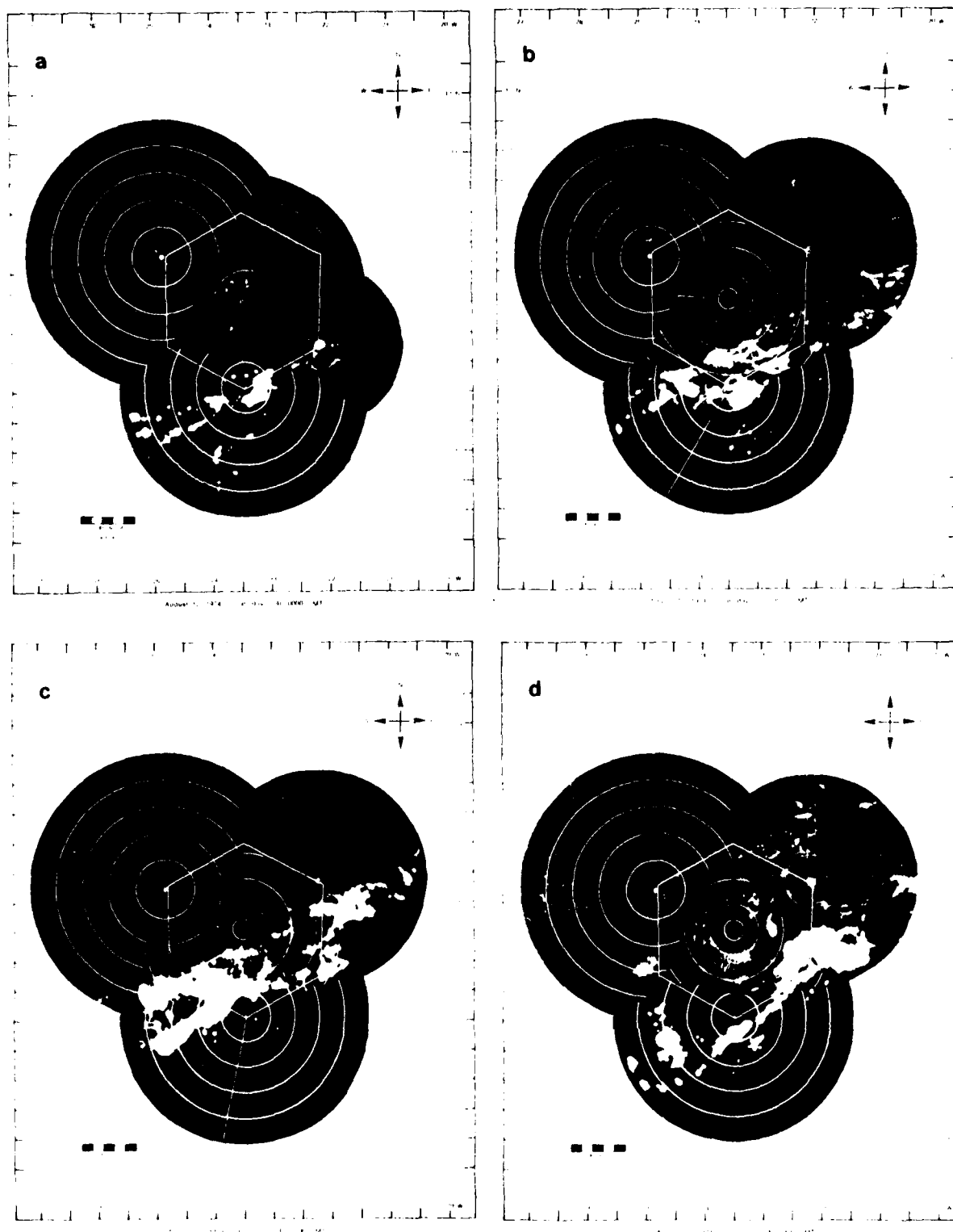
Fig. 3.5. Radar photographs at various convective stages at (a) 00 GMT, (b) 06 GMT, (c) 12 GMT, (d) 18 GMT, and (e) 24 GMT on 12 August 1974.
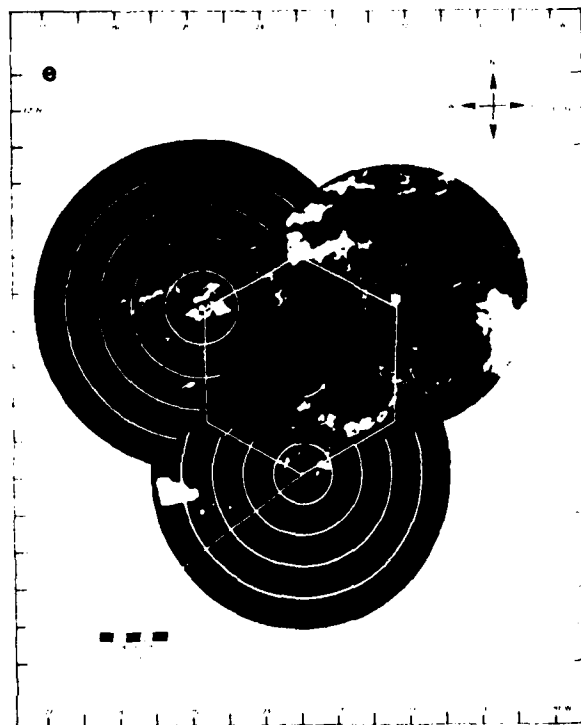
Fig. 3.5. (Continued)

Their results indicated that the formation of this convective system was preceded by mesoscale low-level convergence. Later, Soong and Tao (1980, 1984), and Tao (1983) used the cloud ensemble model (Soong and Ogura, 1980) to examine the response of the cloud band to the mesoscale lifting processes described by Ogura et al. (1979).

We have applied the A-S scheme to this tropical convective system using a semi-prognostic approach. Three-hourly rawinsonde observations and kinematically-computed vertical velocities were available for this event. The radiative cooling rate (Q_R) used in this study (shown in Fig. 3.6) is the climatological profile analyzed by Dopplick (1970). Figs. 3.7 and 3.8 show the results of predicted $Q_1 - Q_R$ and Q_2 respectively. By "predicted" $Q_1 - Q_R$ and Q_2, we mean those terms associated with cloud effects in the last members of (2.17) and (2.18). For comparison purposes, the profiles of $Q_1 - Q_R$ and Q_2 estimated from the observed large-scale heat and moisture budgets are also shown. Agreement between the predictions and observations is generally good, particularly for the heating profiles. We note that, in contrast to Fig. 2.2 which represents the results averaged over the period of 18 days, the predictions shown in Figs. 3.7 and 3.8 are for the observations of 3-hour intervals.

Fig. 3.9 shows the total mass flux ($\bar{M}$) (cf. (2.12)) as a function of time and height. The evolution of the system in terms of $\bar{M}$ is evident. It is seen that a low-level maximum is present during the period of 03 to 06 GMT, whereas a high-level maximum is present during 09 to 18 GMT. Fig. 3.10 shows the cloud mass flux (M_c) as a function of time and height. It is observed that the general feature of the evolution of M_c shown in Fig. 3.10 is very similar to
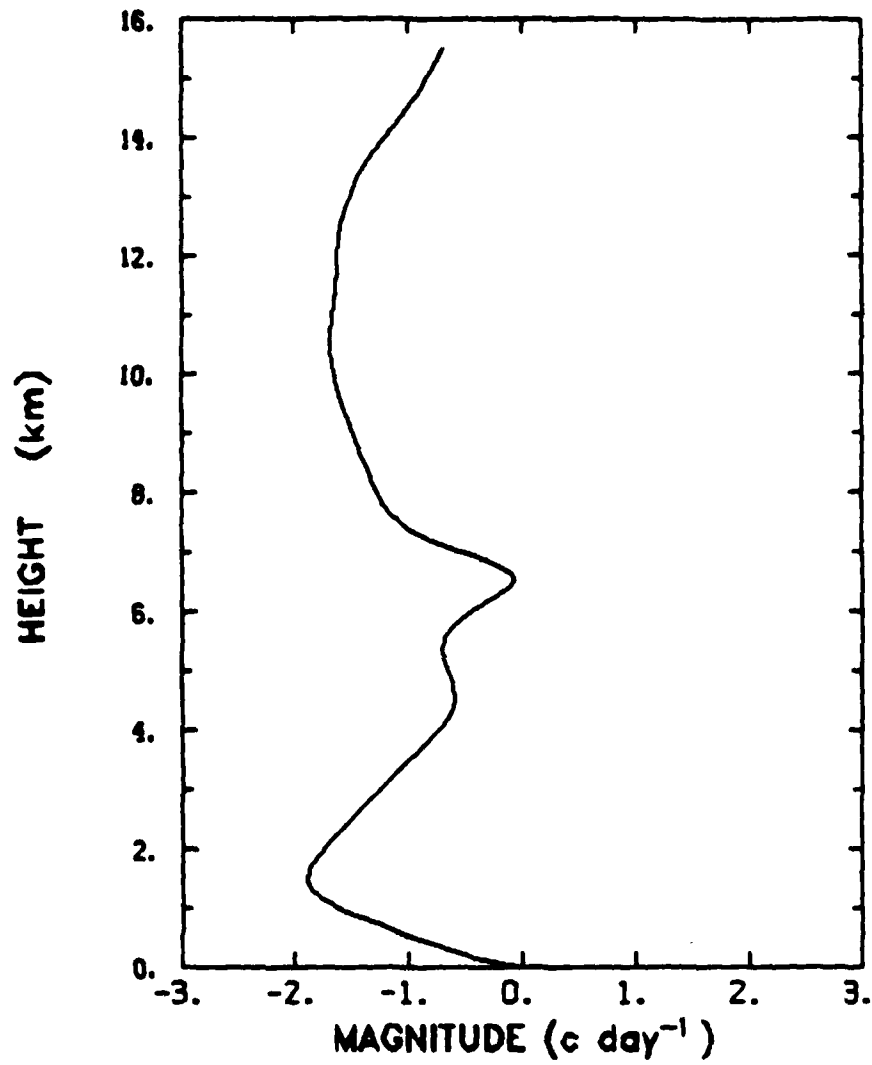
Fig. 3.6.   The radiative cooling rate used in the model.
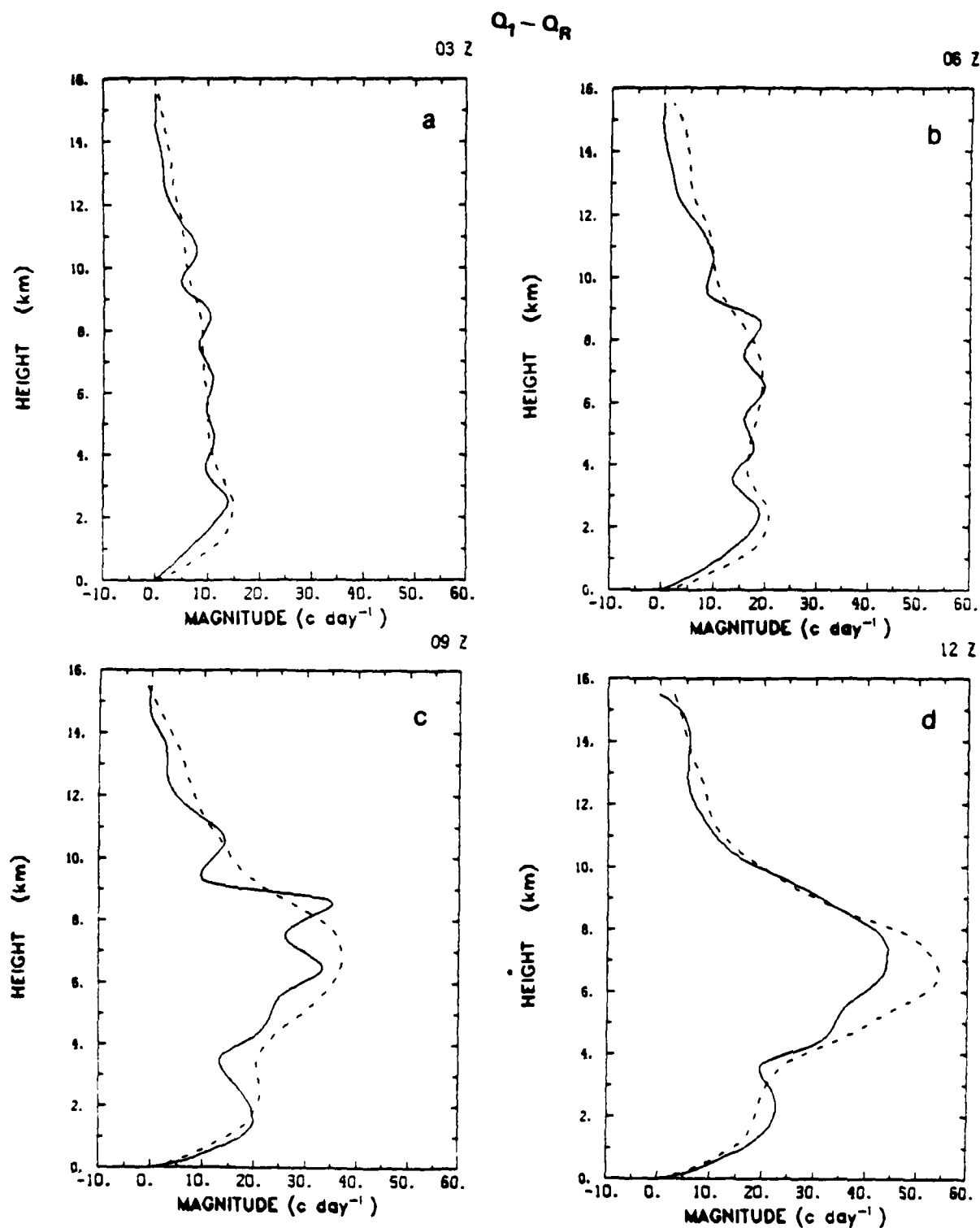
$$Q_1 - Q_R$$

Fig. 3.7. The vertical distributions of the apparent heat source due to clouds (Q_1-Q_R) at (a) 03 z, (b) 06 z, (c) 09 z, (d) 12 z, (e) 15 z, (f) 18 z, and (g) 21 z. The predicted values are indicated by solid lines, and the observed values are indicated by dashed values.
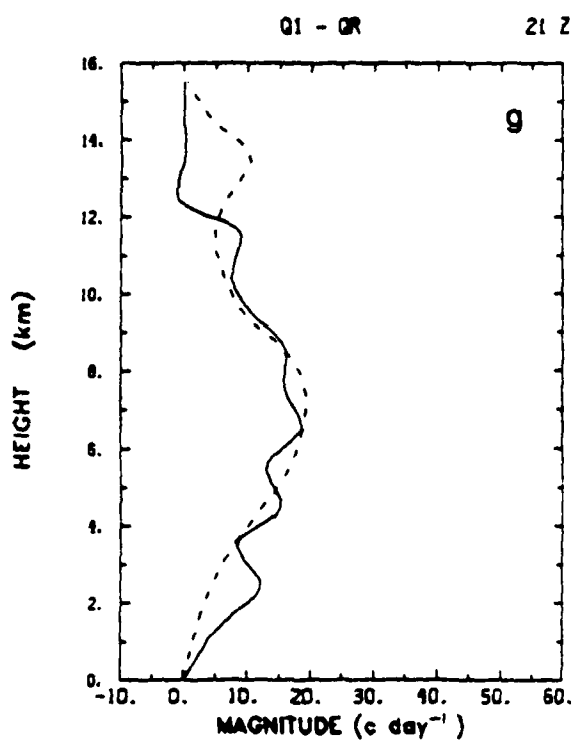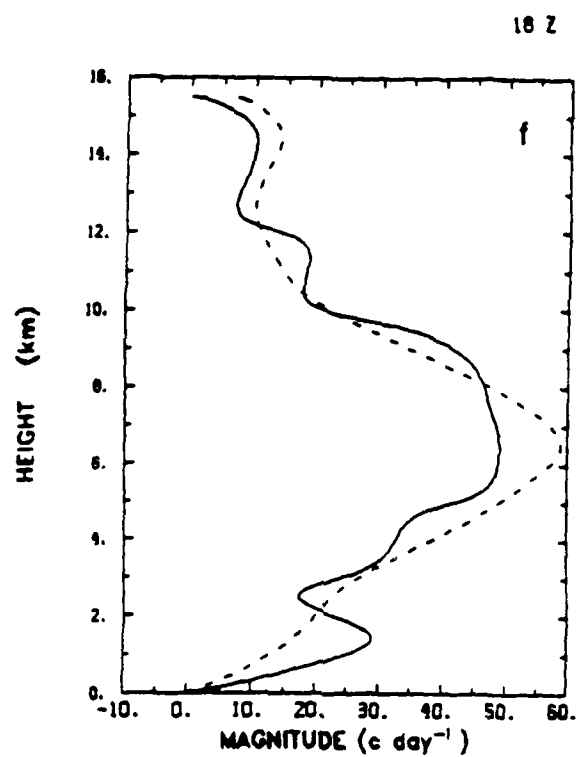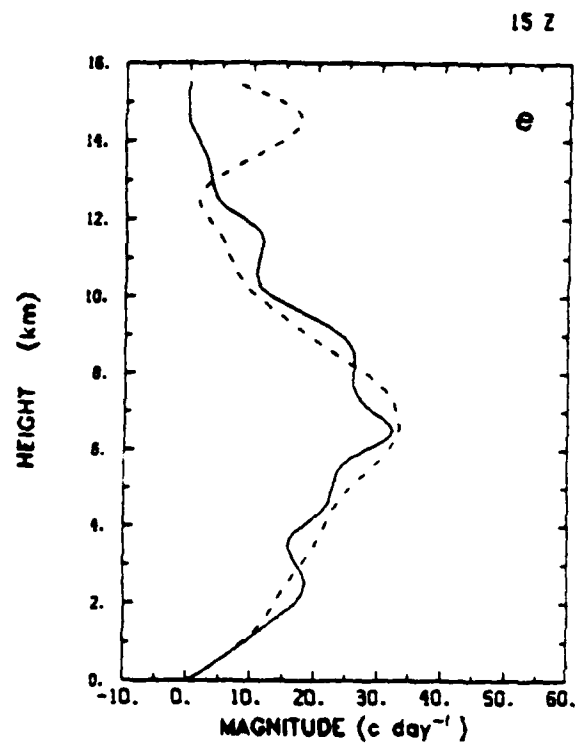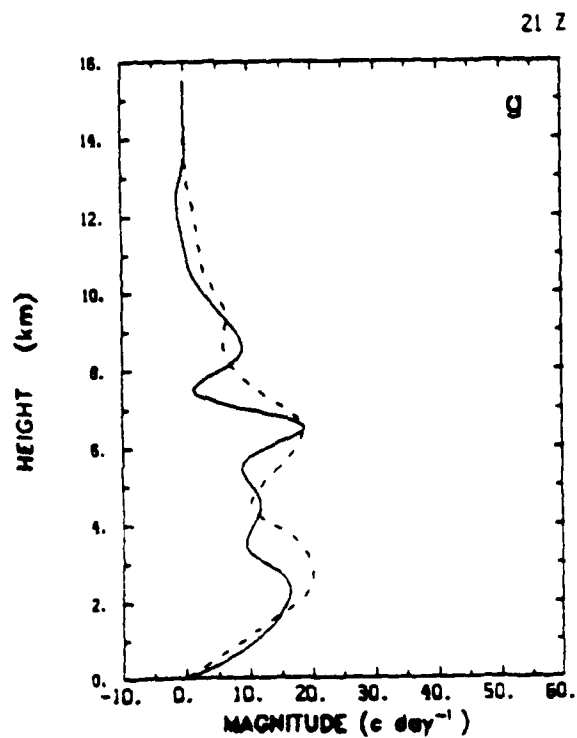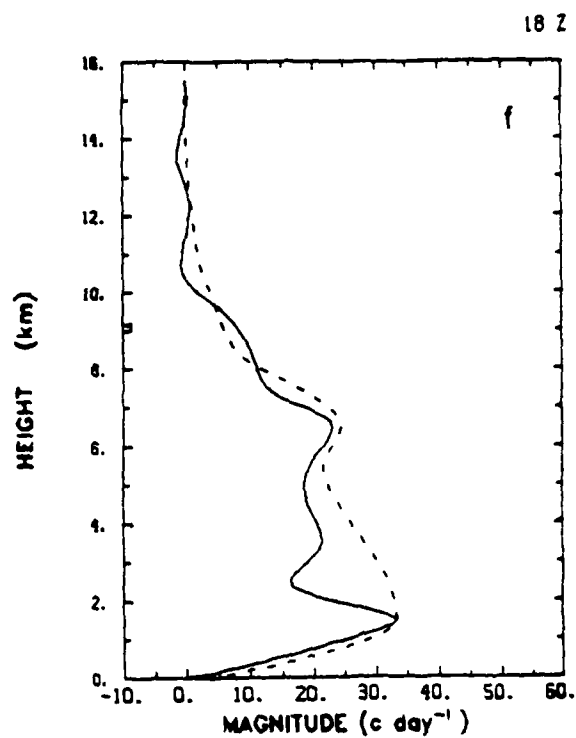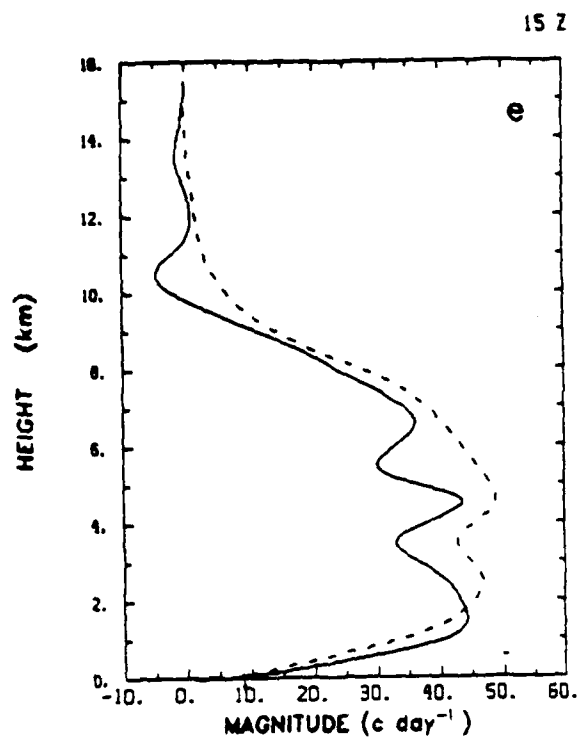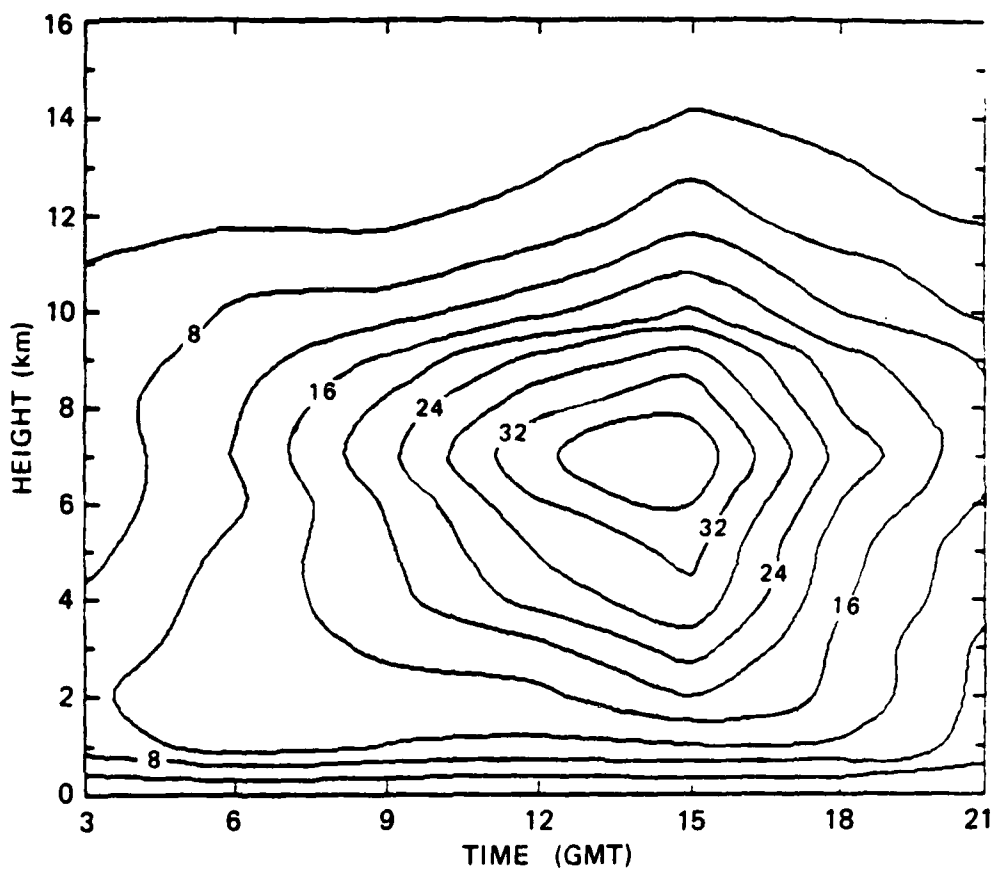
Fig. 3.7. (Continued)

Q_2
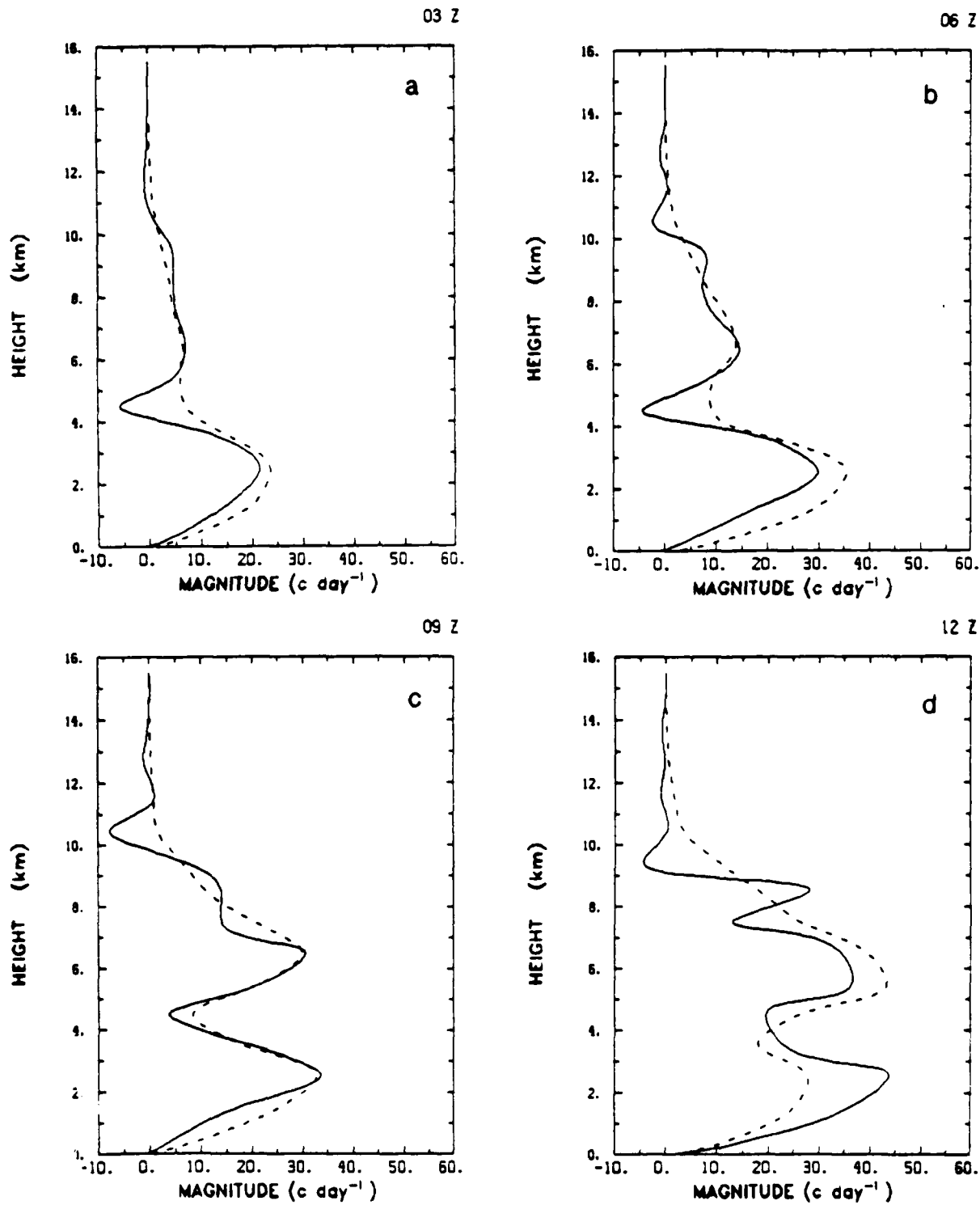
Fig. 3.8. The vertical distributions of the apparent moisture sink due to clouds (Q_2) at (a) 03 z, (b) 06 z, (c) 09 z, (d) 12 z, (e) 15 z, (f) 18 z, and (g) 21 z. The predicted values are indicated by solid lines, and the observed values are indicated by dashed lines.

Fig. 3.8. (Continued)

Fig. 3.9. The time series of total mass fluxes ($\bar{M}$) in the units of mb hr^{-1} as functions of height.
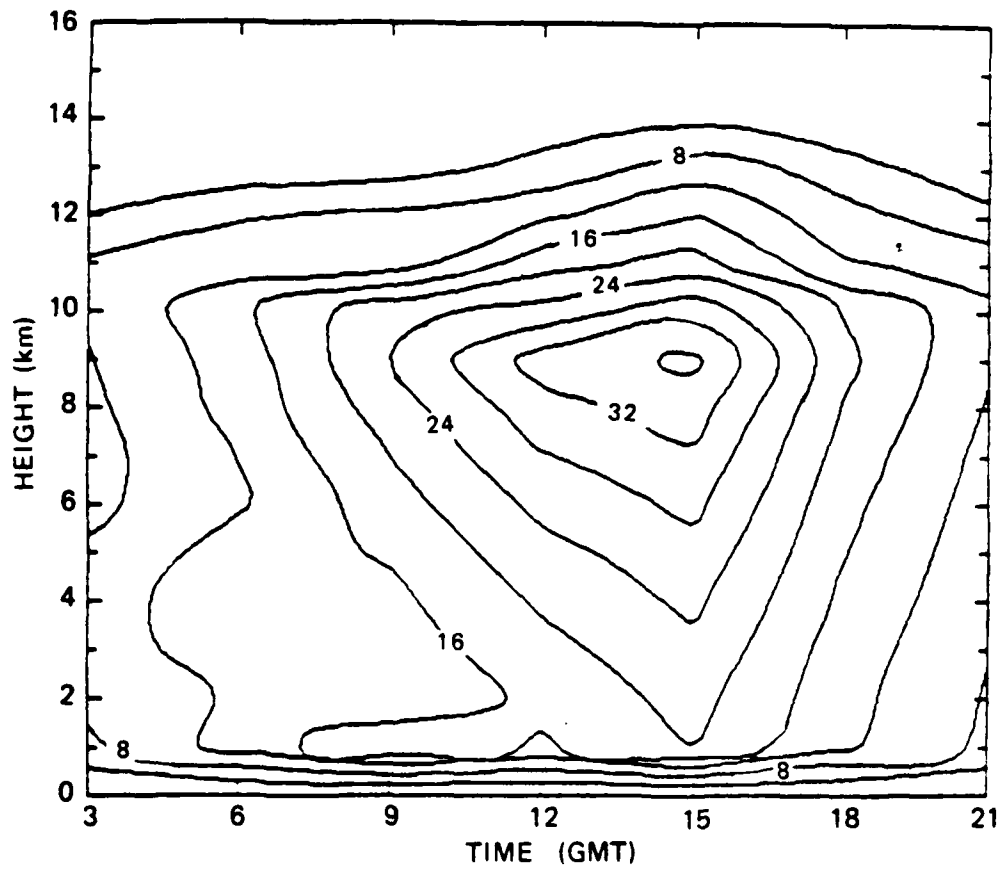
Fig. 3.10. The time series of cloud mass fluxes (M_c) in the units of mb hr^{-1} as functions of height.

that in Fig. 3.9 both qualitatively and quantitatively, implying that $\tilde{M}$ (cf. (2.12)) is negligibly small. This aspect is supported by the cloud model result simulated by Soong and Tao (1980, 1984), which will be discussed extensively in Section 3.3.3. Fig. 3.11 shows the cloud base mass flux (m_B) as a function of cloud top height and time. The results indicate that only deep clouds with cloud top height above 8 km (350 mb) prevailed over the mature and decaying periods, with the maximum around 12 to 15 GMT, while both shallow and deep clouds were present for the developing period from 03 to 09 GMT, making a bimodal distribution for this period. This implies that the shallow clouds are associated with the low-level maximum of the total mass flux $(\bar{M})$.

Figs. 3.12 and 3.13 show the vertical profiles of the contributions of individual components in the last members of (2.17) and (2.18) to the predicted $(Q_1 - Q_R)$ and Q_2 at 09 GMT. As expected, the effects of cumulus-induced subsidence are the dominant factors. However, at this particular time, it is noticed that the low-level detrainment of water vapor is also significant in contributing to the moisture budget. In general, this effect is significant when shallow clouds are abundant and the atmosphere is relatively dry at the lower levels. More discussion will be presented in Section 3.3.3 where we compute the cloud properties in terms of condensation, evaporation, and vertical eddy transports of heat and moisture and compare them against the results from the cloud ensemble model.

3.3.2 Easterly wave:

Chen and Ogura (1982) have prepared a composite of eight tropical wave disturbances that passed over the GATE A/B ship array. The filtered 700 mb meridional wind was analyzed and one of the eight wave categories was assigned
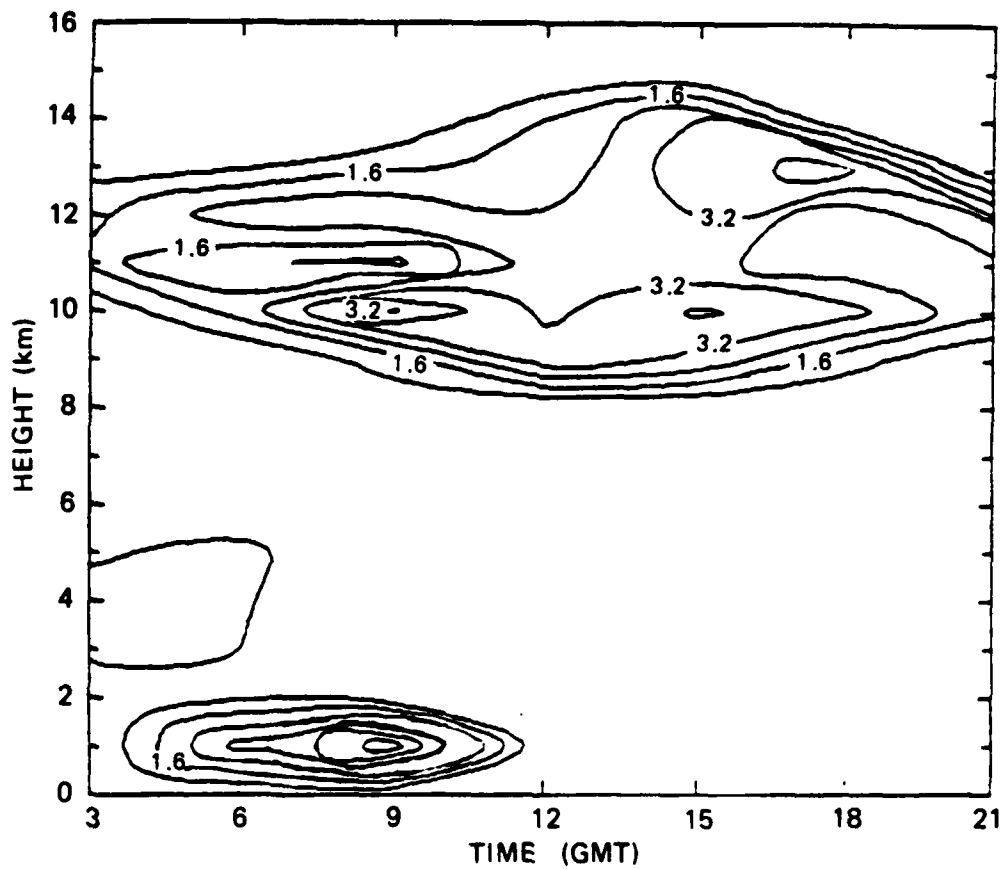
Fig. 3.11. The time series of cloud base mass fluxes (m_B) in the units of mb hr^{-1} as functions of cloud top height.
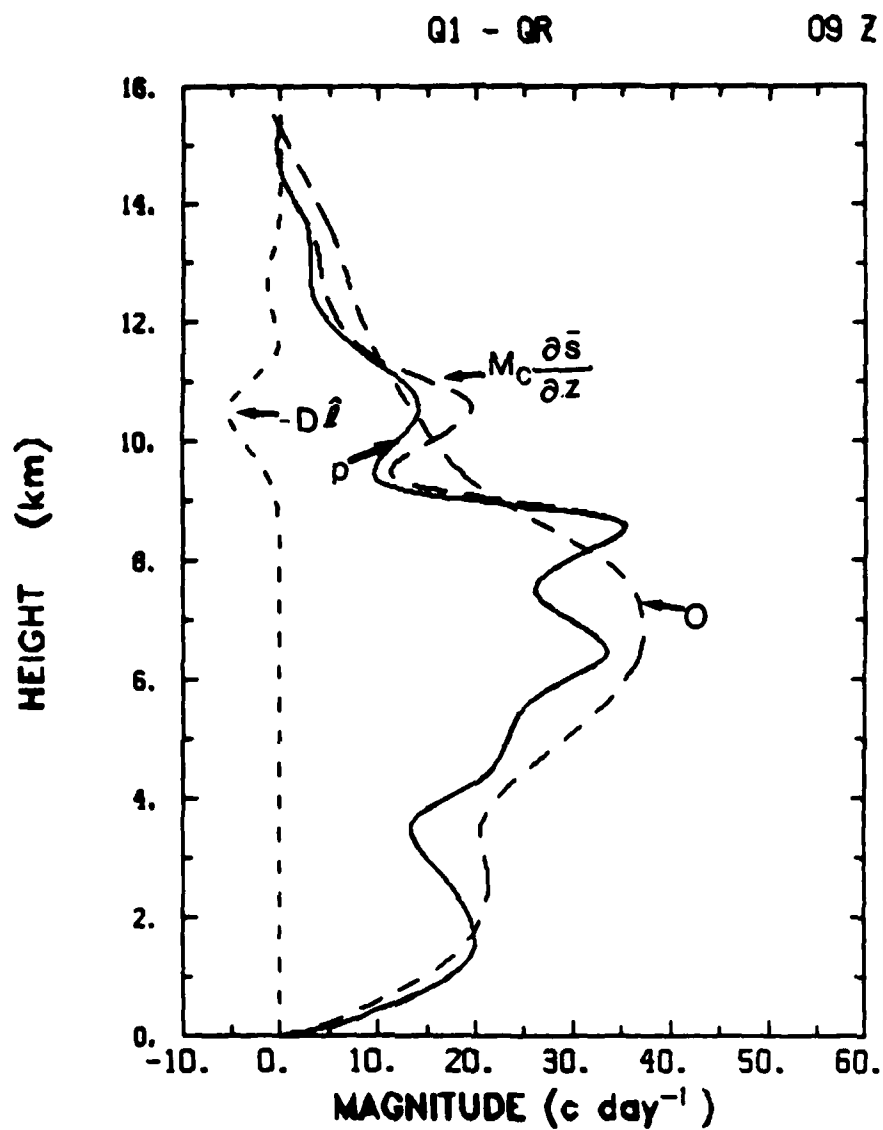
Fig. 3.12. The vertical distributions of the contributions due to cumulus-induced subsidence $(M_c\frac{\partial \bar{s}}{\partial z})$ and evaporation of the detrained liquid water $(-D\hat{\ell})$ to the predicted net heating rate indicated by "p". The net heating rate estimated from large-scale observations is indicated by "O".
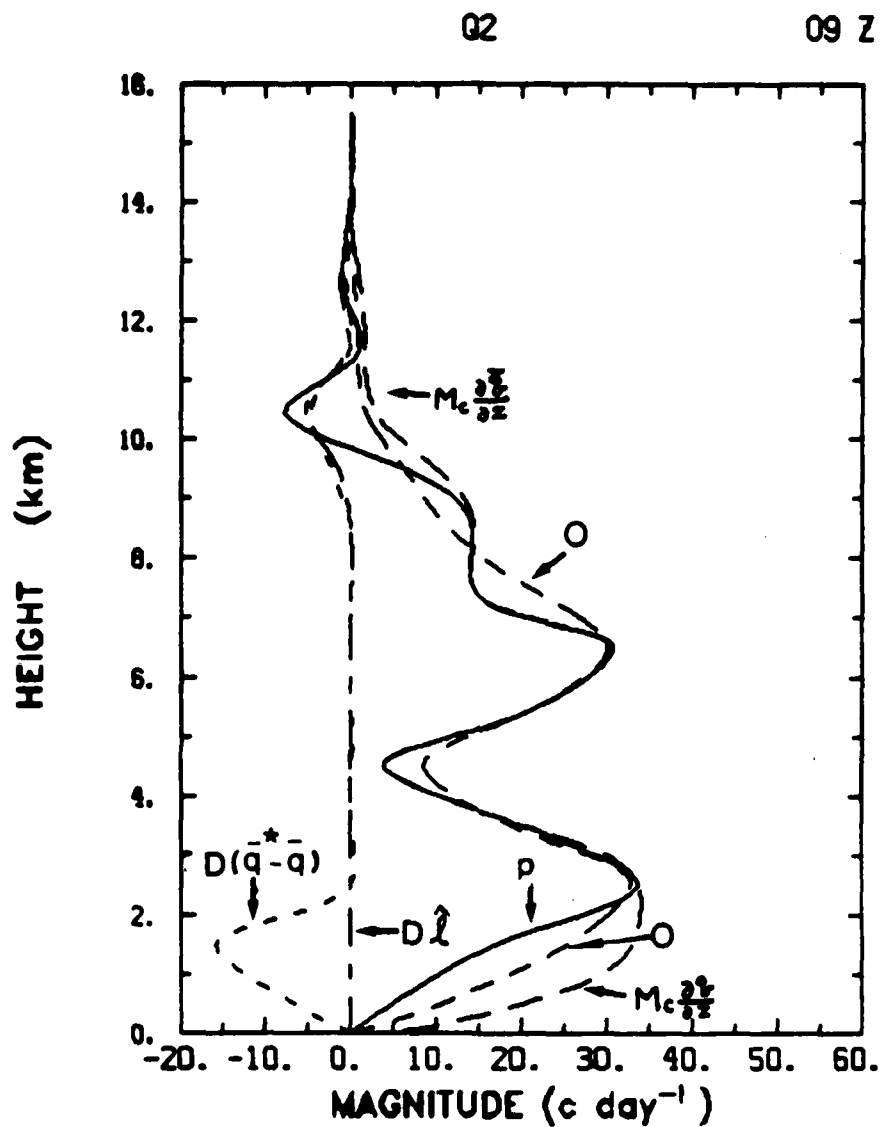
Fig. 3.13. The vertical distributions of the contributions due to cumulus-induced subsidence $(M_c \frac{\partial \bar{q}}{\partial z})$, detrainment of water vapor $(D(\bar{q}^* - \bar{q})$ and evaporation of detrained liquid water $(D\hat{\ell})$ to the predicted cloud drying effect indicated by "p". The net cloud drying effect estimated from large-scale observation is indicated by "O".

to each observation time at the center of the array (i.e., 23.5 W, 8.5 N) in three phases of GATE. The rawinsonde and surface data from the A/B- and B-array ships were then composited according to the wave categories. Wave phases or categories have been numbered 1 to 8, with category 2 centered on the region of maximum northerly wind, category 4 on the trough, category 6 on the region of maximum southerly wind and category 8 on the ridge. Categories 1, 3, 5 and 7 occupy intermediate positions.

In order to examine the general behavior of the A-S scheme in various weather conditions in the tropics, composited easterly wave data in Phase II and III were used in this semi-prognostic study. Phase I was not included, because it is not very reliable (Chen, private communication). The total mass flux ($\bar{M}$) is shown in Fig. 3.14. Significant features of $\bar{M}$ in Phase II are the middle level maxima around categories 2 and 3, low level maxima around categories 5 and 6,and relatively strong downward motion around categories 1 and 8. On the other hand, in Phase III, only low level maxima are present in categories 3, 4, and 5, whereas very weak low-level upward motion is present in categories 7 and 8. It is also seen that very weak downward motion is present around middle and upper levels in categories 7 and 8 in Phase III. Figs. 3.15 and 3.16 present the observed $Q_1 - Q_R$ and Q_2, respectively, whose general features are similar to those of $\bar{M}$. The predicted $Q_1 - Q_R$ and Q_2 are respectively shown in Figs 3.17 and 3.18. Comparing Figs. 3.17 and 3.18 with Figs. 3.15 and 3.16, respectively, it is found that the agreement between the prediction and observation is generally good. No cloud heating and drying effects exist in categories 1 and 8 in Phase II simply because of the presence of strong downward motion in those categories. The solutions for the cloud
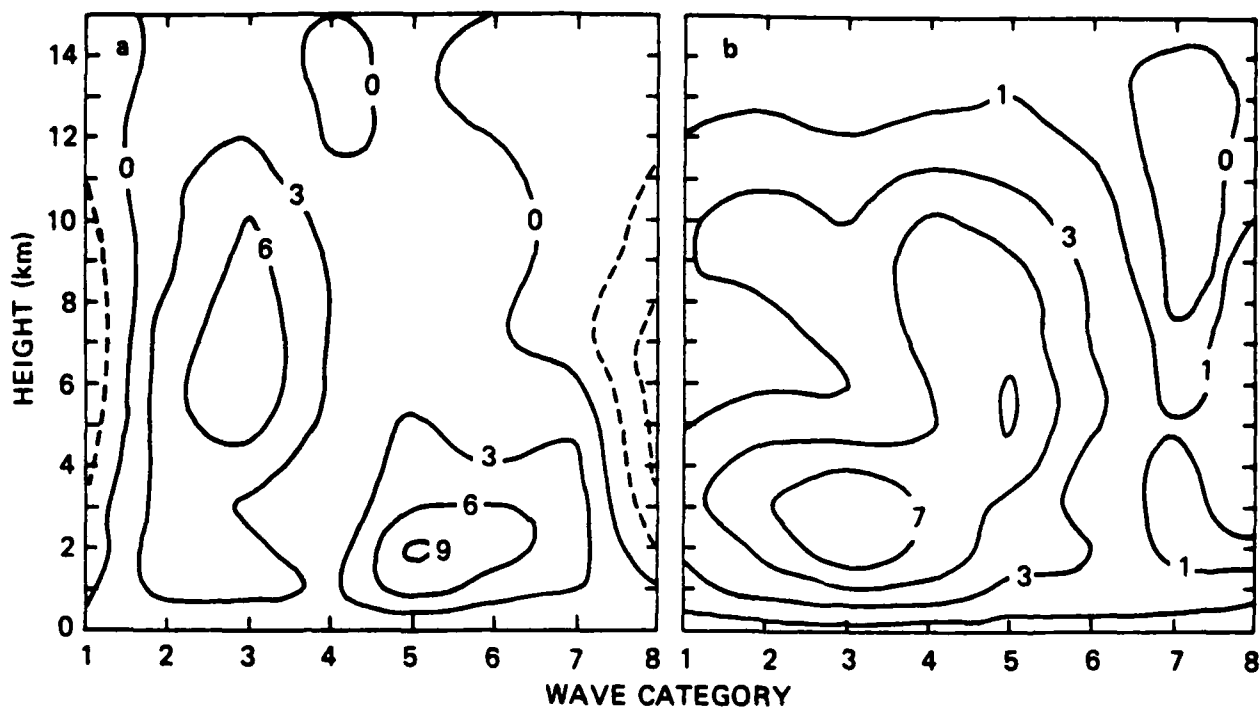
-53-

Fig. 3.14. The total mass fluxes ($\overline{M}$) in the units of mb hr^{-1} for the composite waves: (a) for Phase II and (b) for Phase III as functions of wave category and height.
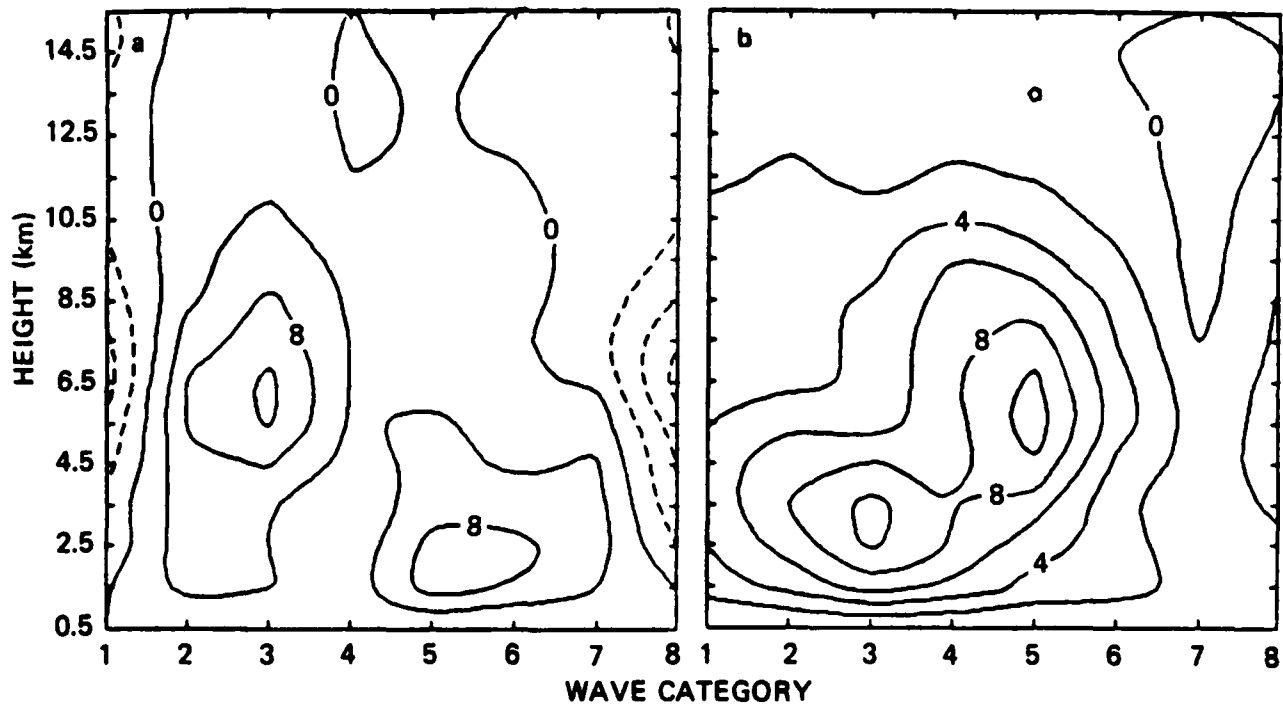
Fig. 3.15. The observed $Q_1 - Q_R$ in the units of C day^{-1} for the composite waves: (a) for Phase II and (b) for Phase III as functions of wave category and height.
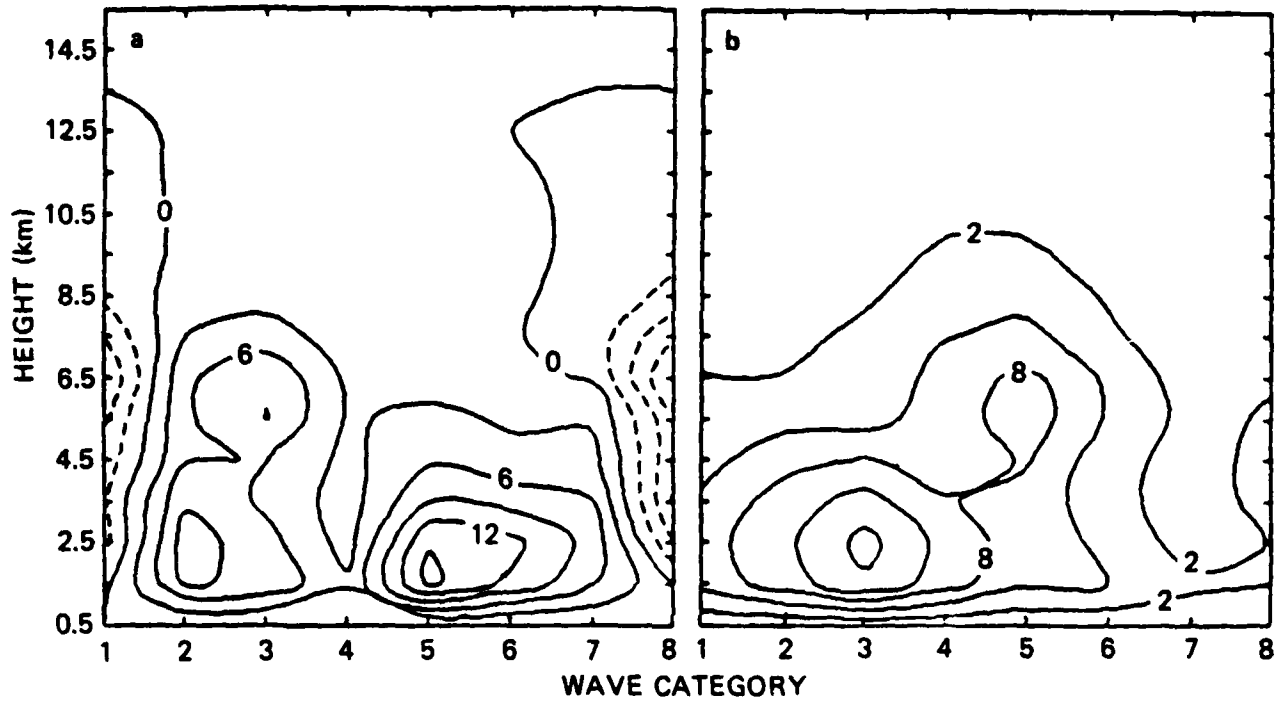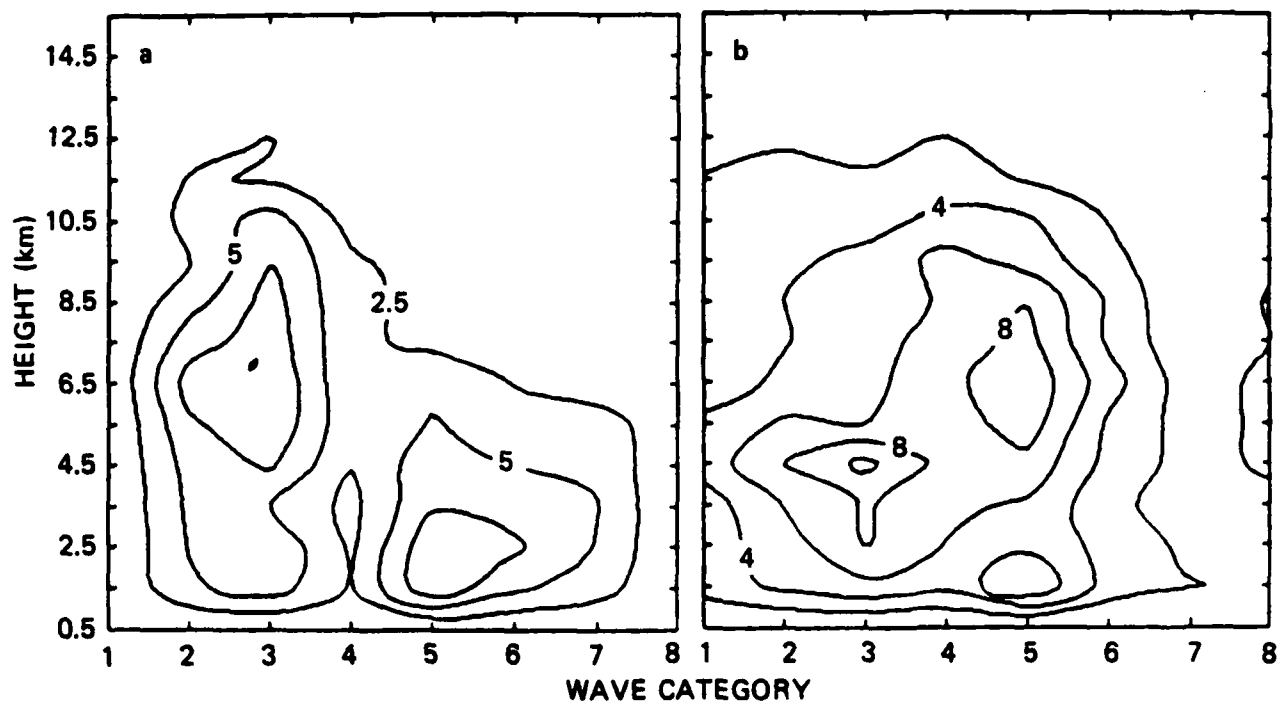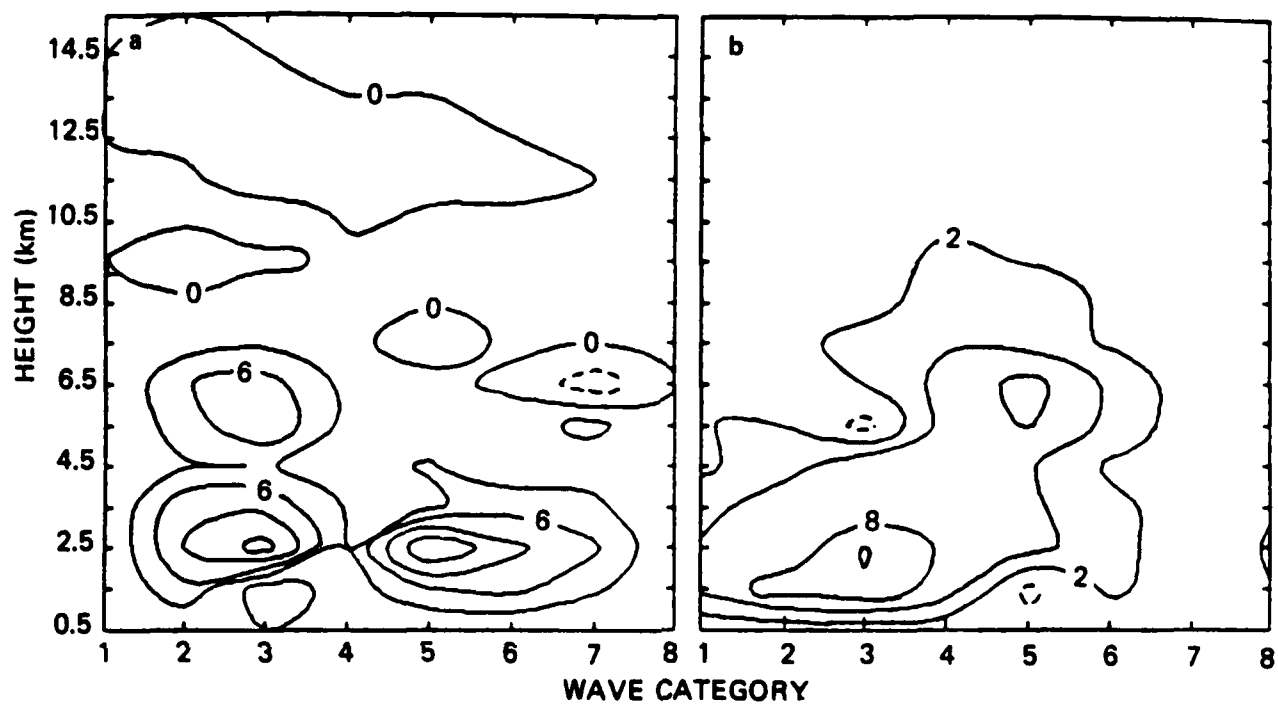
Fig. 3.16. The observed Q_2 in the units of C day^{-1} for the composite waves: (a) for Phase II and (b) for Phase III as functions of wave category and height.

Fig. 3.17. The predicted $Q_1 - Q_R$ in the units of C day^{-1} for the composite waves: (a) for Phase II and (b) for Phase III as functions of wave category and height.

Fig. 3.18. The predicted Q_2 in the units of C day^{-1} for the composite waves: (a) for Phase II and (b) for Phase III as functions of wave category and height.

base mass flux as functions of cloud top height and category are shown in Fig. 3.19. The bimodal distributions are clearly shown in categories 3, 4, and 5 for Phase II and in categories 4 and 5 for Phase III, where strong convective activities are present. This also reveals the relationship between the shallow clouds and the low-level maximum of $\bar{M}$ as described in the preceding section. On the other hand, only shallow clouds dominate around categories 7 and 8 for Phase III because upward motion is confined to below 6 km in those categories. The total cloud mass flux M_c is shown in Fig. 3.20. It is also seen that the general features and magnitudes of M_c are similar to those of $\bar{M}$, shown in Fig. 3.14.

We have presented the results of a semi-prognostic application of the A-S scheme to the various data sets over the GATE area. This semi-prognostic study is primarily intended to demonstrate the tractability and potential advantages of the quasi-equilibrium assumption, which is considered the core of the A-S scheme. We are encouraged by the fact that this scheme not only physically permits a highly interactive behavior between the large-scale disturbances and the cumulus ensemble, but also gives realistic predictions of the cloud heating and drying effects.

3.3.3 The comparison with the cloud modeling study

Soong and Ogura (1980) developed a "cumulus ensemble model". Basically, it is a nonhydrostatic, anelastic moist cloud model with parameterized cloud physics and turbulent processes. Using this model, one can study the statistical feedback effects of a group of cumulus clouds on the large-scale
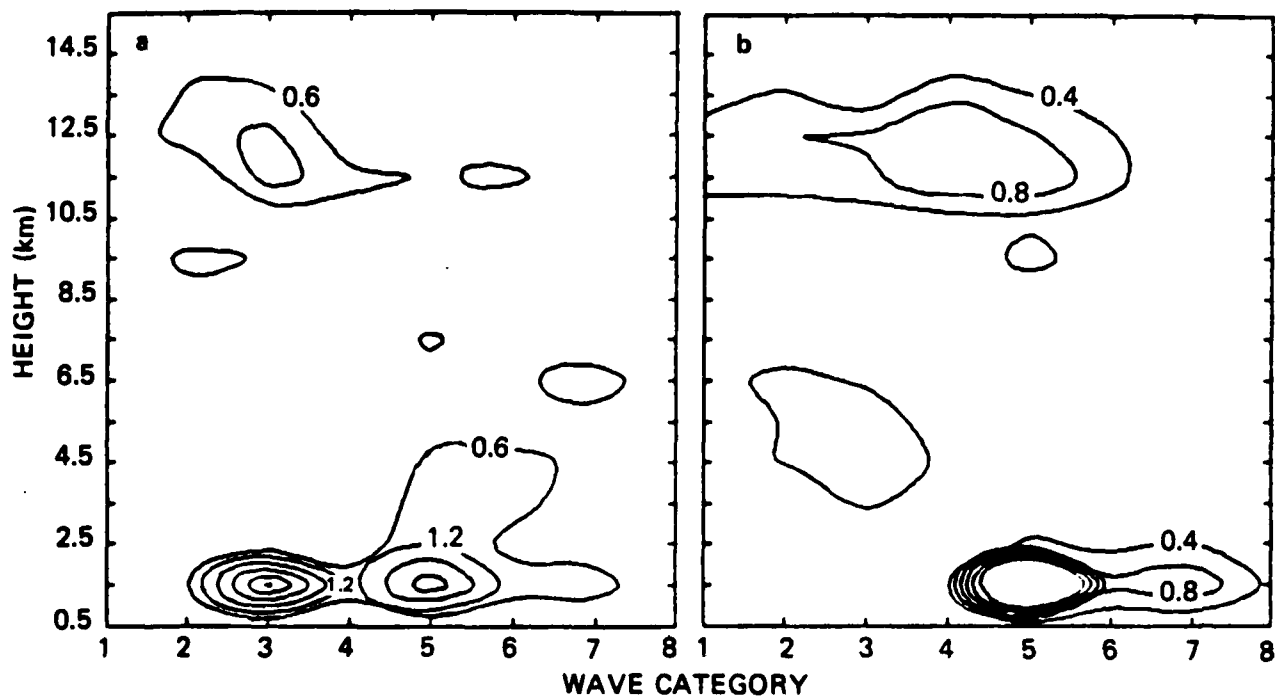
-59-

Fig. 3.19. The cloud base mass fluxes (m_B) in the units of mb hr^{-1} for composite waves: (a) for Phase II and (b) for Phase III as functions of wave category and height.
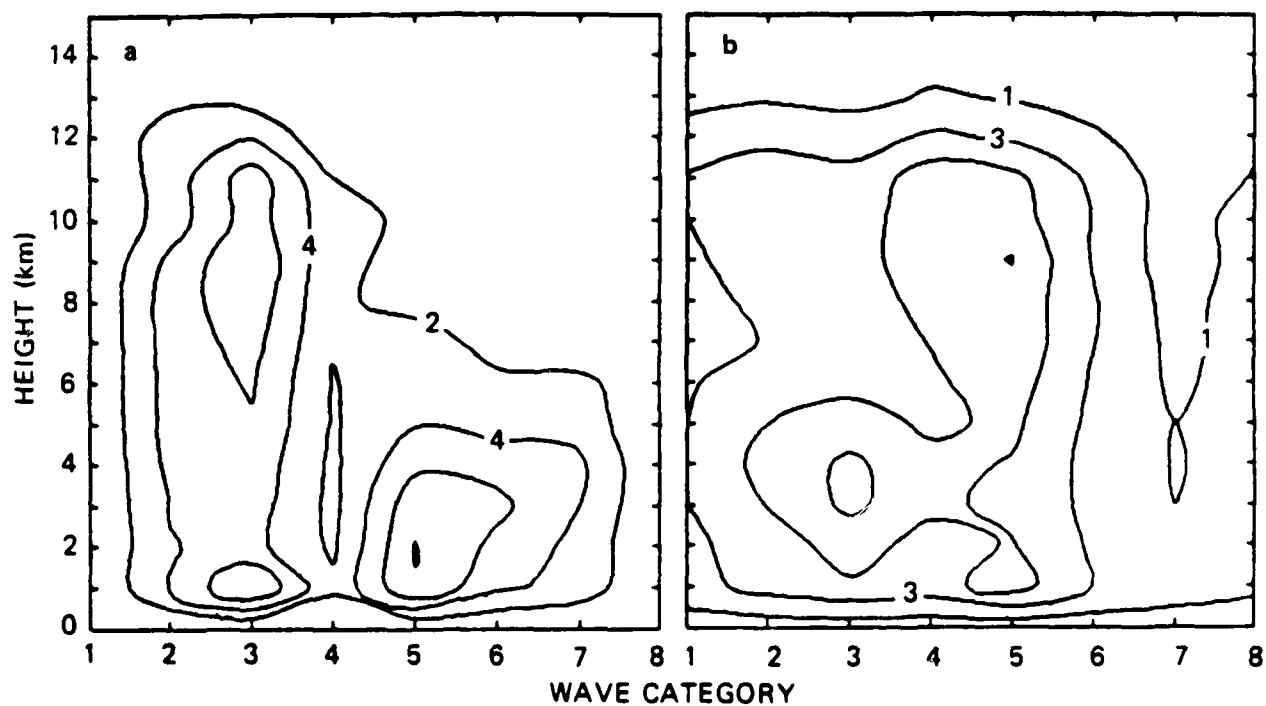
-60-

Fig. 3.20. The cloud mass fluxes (M_c) in the units of mb hr^{-1} for composite waves: (a) for Phase II and (b) for Phase III as functions of wave category and height.

environment in which a group of clouds is embedded. Soong and Tao (1980, 1984) and Tao (1983) have applied this model to the cloud band described previously. The thermodynamic feedback effects of cumulus clouds on the mesoscale temperature and mixing ratio profiles due to condensation, evaporation, and vertical eddy transports of heat and moisture with clouds were investigated. This experiment enables us to gain some insight into the underlying physical processes and quantitative aspects of the cloud properties which cannot be directly measured. On the other hand, this model may be categorized as a "quasi-prognostic" approach, since the large-scale advection of temperature and moisture in the model is prescribed from the observational data. Thus, the comparison between its results and those deduced from the semi-prognostic study described in Section 3.3.1 should be physically sound.

Adapted from Tao (1983), the profiles of simulated and observed cloud heating effects averaged in the period from 06 to 12 GMT, which was the developing stage of the cloud band, are shown in Fig. 3.21. The results from the semi-prognostic study at 09 GMT has been shown in Fig. 3.7c. Both results are encouraging in that the model cloud ensemble reaches a quasi-equilibrium state in which the heating and drying effects of clouds are almost balanced by the cooling and moistening effects due to large-scale advection and radiative cooling, as should be the case in the real atmosphere. One of the important conclusions derived by Soong and Tao (1980) and Tao (1983) is that M_c (the cloud mass flux) is very close to $\bar{M}$ (the total mass flux) as shown in Fig. 3.22. As already shown in Figs. 3.9 and 3.10, the M_c derived by the A-S scheme is also very close to $\bar{M}$.
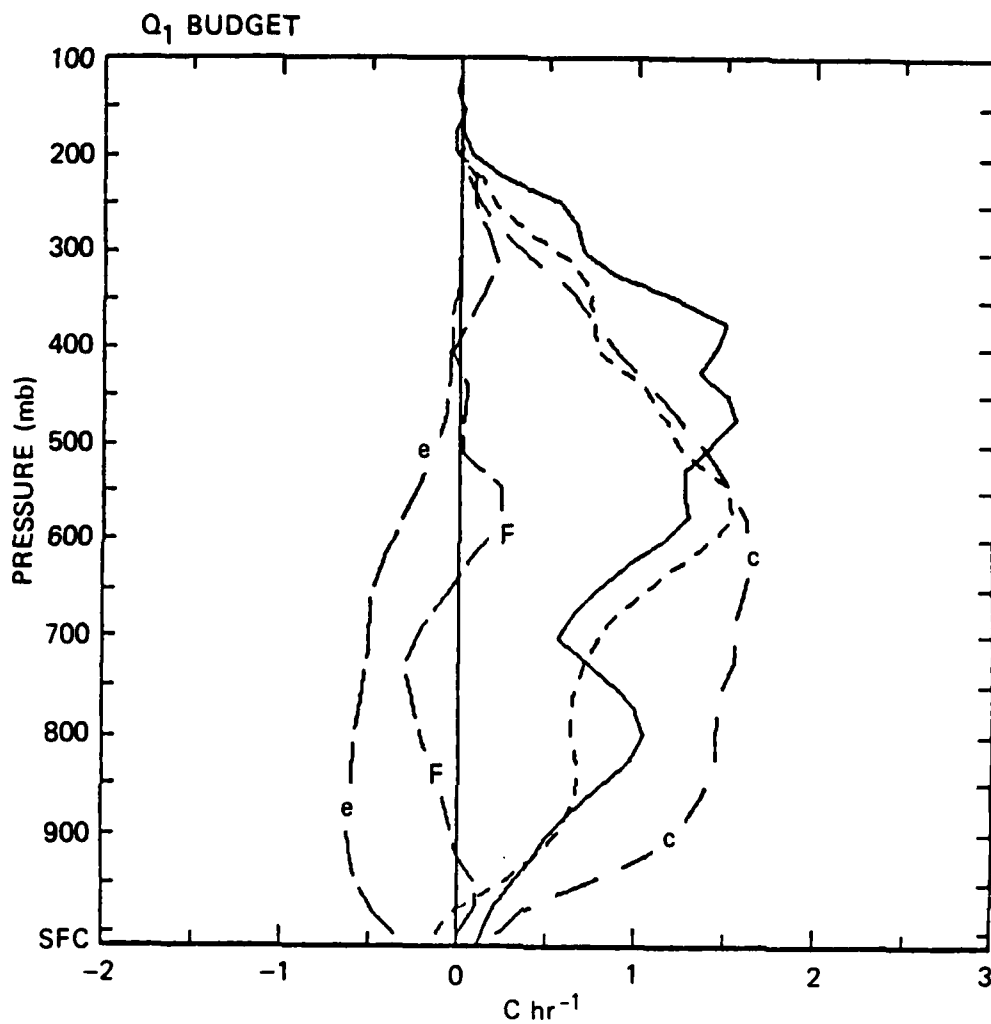
Fig. 3.21. The vertical profiles of the heating rate by condensation (C), evaporation (e), convergence of heat flux (F), the total heating rate by clouds (dashed line) and the heating rate estimated from large-scale observations $(Q_1 - Q_R)$ (solid line).
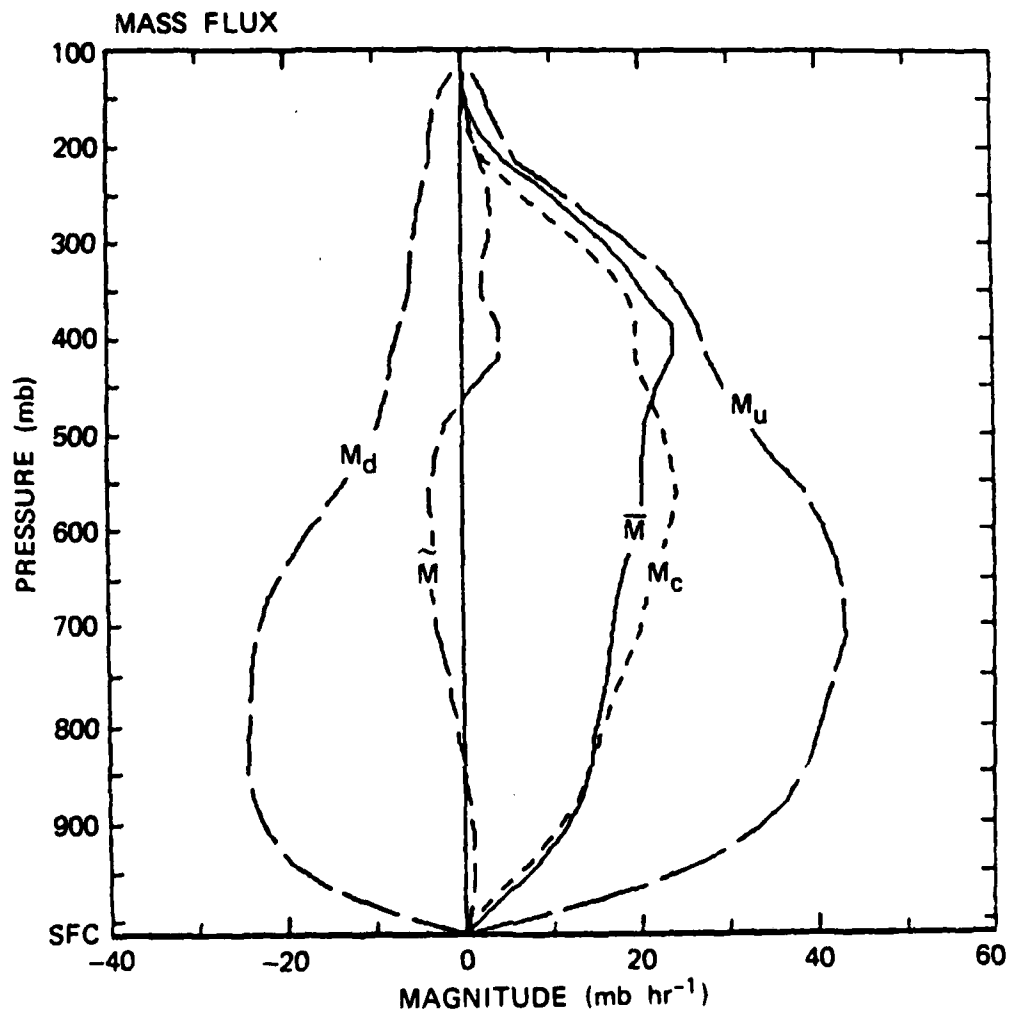
Fig. 3.22. The vertical profiles of total mass flux (M̄), updraft mass flux inside the clouds (M_u), downdraft mass flux inside clouds (M_d), net cloud mass flux (M_c), and mass flux in the clear area M̃ in the units of mb hr⁻¹.

In the A-S scheme the cloud effects due to condensation rate ($\overline{C}$) and vertical convergence of eddy transports of static energy and moisture ($\frac{\partial \rho \overline{w's'}}{\partial z}$ and $\frac{\partial \rho \overline{w'q'}}{\partial z}$) are implicitly included in the terms of cumulus-induced subsidence ($M_c \frac{\partial \overline{s}}{\partial s}$ and $M_c \frac{\partial \overline{q}}{\partial z}$). This can be verified by the relationship among (2.1), (2.5), and (2.7). Meanwhile, from (2.3) and (2.4), $\frac{\partial \rho \overline{w's'}}{\partial z}$ and $\frac{\partial \rho \overline{w'q'}}{\partial z}$ can be expressed by

$$\frac{\partial}{\partial z} \rho \overline{w's'} = \frac{\partial}{\partial z} \int_z^{\hat{z}_{max}} m(z,\hat{z})(s_c(z,\hat{z}) - \overline{s}(z))d\hat{z} \tag{3.8}$$

$$\frac{\partial}{\partial z} \rho \overline{w'q'} = \frac{\partial}{\partial z} \int_z^{\hat{z}_{max}} m(z,\hat{z})(q_c(z,\hat{z}) - \overline{q}(z))d\hat{z} \tag{3.9}$$

Hence, once $m_B(\hat{z})$ is known, $\frac{\partial \rho \overline{w's'}}{\partial z}$ and $\frac{\partial \rho \overline{w'q'}}{\partial z}$ can be obtained from (3.8) and (3.9), respectively. Then, we can calculate $\overline{C}$ either from (2.5) or (2.6). On the other hand, as indicated in Secton 2.1, the evaporation rate ($\overline{e}$) has the form expressed by $D\hat{\ell}$. In Section 3.3.1, we have shown that the A-S scheme can satisfactorily predict the net heating and drying rates due to cumulus clouds for the cloud band event. Now, the individual contributions due to the condensation, evaporation, and vertical transports of heat and moisture to the net heating and drying rates are examined and compared with Tao's (1983) results derived from the cumulus ensemble model.

Fig. 3.23 shows the distributions of heating effects due to each component at 09 GMT from the semi-prognostic results. For comparison purposes, the results were transformed into p-coordinates and in the units of C hr^{-1}. Apparently, condensation plays the dominant role in the net heating effect.
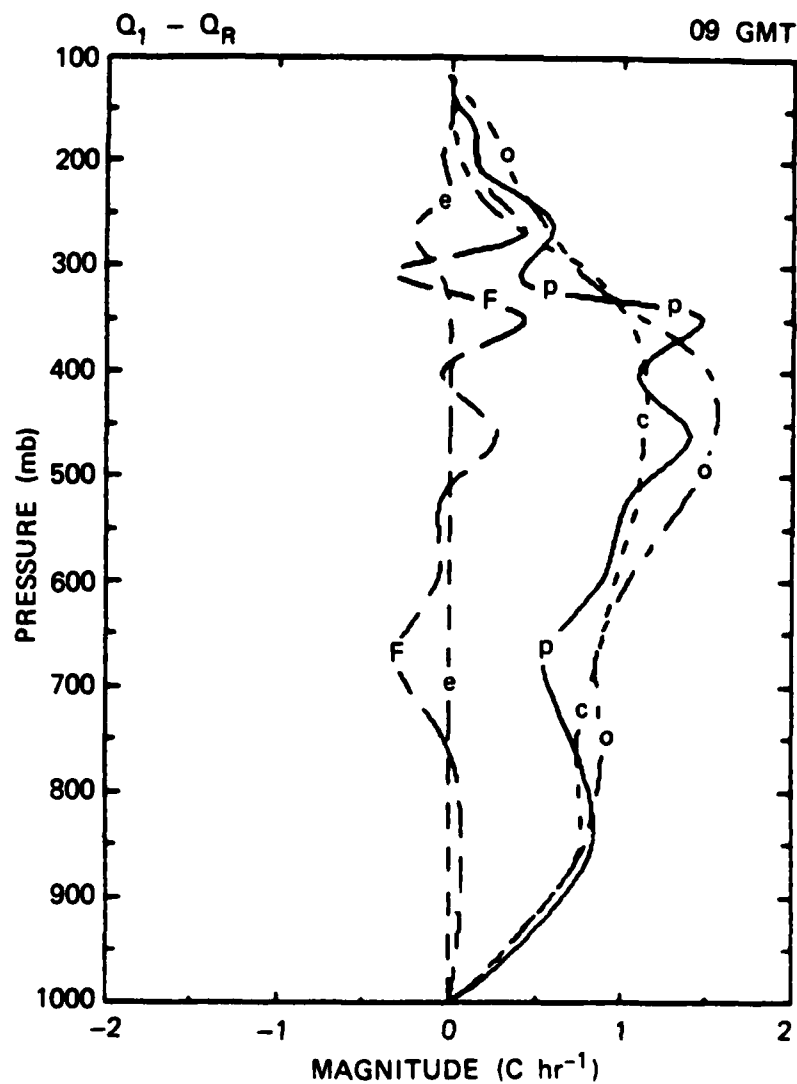
Fig. 3.23. The vertical profiles of heating rate by condensation (C), evaporation (e), and vertical convergence of heat flux (F). The net heating rate predicted by the A-S scheme is indicated by "p", and the net heating rate etimated from large-scale observations is indicated by "0".

Evaporation and the convergence of eddy heat transport are smaller by one order of magnitude. There is no evaporation at the low and middle levels because no cloud tops lie around those levels. Even though some extremely shallow clouds are present (see Fig. 3.11), there is still no evaporation because no detrained liquid water is produced by the model at that level. The corresponding results simulated by Tao using the three-dimensional version of the cumulus ensemble model have been shown in Fig. 3.21. It is seen that the A-S scheme underestimates the rate of evaporation by one order of magnitude. This is not surprising at all since the A-S scheme does not include the evaporation of rainwater and the evaporation of cloud water is assumed to take place only at the cloud tops. However, very interestingly, the A-S scheme also underestimates the rate of condensation by a factor of about 1.6. Hence, the net heating rate is about the same as that computed by Tao (1983). Finally, the magnitude of the convergence of vertical eddy transport is generally much smaller than the condensation in both cases.

To alleviate this deficiency, the inclusion of convective-scale downdrafts and their associated evaporation of falling precipitation into the scheme may be desirable. In the next section the results of an experiment incorporating the downdraft effects into the A-S scheme are presented.

3.4 Downdraft effects:

We do not intend to exaggerate the importance of downdraft effects by simply pointing out the deficiency encountered in the semi-prognostic study mentioned above. Actually, as far as a large-scale prediction model is

concerned, the importance of convective-scale downdrafts may lie in the interaction between the cumulus clouds and the boundary layer through the detrainment of the downdrafts into the boundary layer and their associated evaporation of the rainfall within the boundary layer. Simpson and Van Helvoirt (1980) discussed the interaction between the clouds and sub-cloud layer in GATE and postulated the cumulus downdrafts to be the main feedback mechanism. To translate this complicated physical process into a parameterization scheme is not a straightforward problem. First, we need to insure that the cumulus parameterization scheme with the inclusion of downdrafts will behave well. Secondly, we need to have a boundary layer parameterization which can resolve the cumulus downdraft effects well.

In this section, as a first attempt to study the downdraft effects in the cumulus parameterization, the semi-prognostic study is used to examine whether the accuracy obtained in the case without the downdrafts can be still maintained and the deficiency mentioned in the preceding section can be deleted. A mixed layer approach for the boundary layer parameterization with the downdraft effects will be reported in the next chapter, where a fully prognostic model is developed. The discussion of the interaction between the cumulus downdrafts and the sub-cloud layer will be presented in Chapter 5.

3.4.1 Formulation:

The downdraft model in this study is adopted from Johnson (1976). Basically, Johnson proposed that each updraft cumulus in the original A-S scheme be accompanied by a downdraft element, which is modeled as an "inverted"

one-dimensional, saturated, entraining plume that entrains the same environmental air as the updraft does. The physical interaction between the two drafts is neglected, except it is assumed that the updraft supplies the precipitation to the downdraft. Each downdraft is assumed to originate at a level given by three-fourths of the pressure-depth of the updraft and to detrain only below the cloud base. The model is closed by specifying the relative intensities between the updraft and the downdraft. Fig. 3.24 illustrates the fundamental features of this model. Generally speaking, the nature of this model is rather crude. However, in view of that the original A-S scheme is already so complicated, the crudity of the downdraft model may have its current necessity.

The details of applying this downdraft model to the A-S scheme for diagnostic purposes have been reported in Johnson (1976, 1980). Here, we shall consider its application to prognostic studies. The counterparts of Eqs. (2.1) and (2.2) for the downdraft case are now expressed by:

$$\rho\frac{\partial \bar{s}}{\partial t} + \rho \vec{V}\cdot\nabla\bar{s} + \rho\bar{w}\frac{\partial \bar{s}}{\partial z} = Q_R + L(\bar{C} - \bar{e}_u - \bar{e}_d) - \frac{\partial\rho\overline{w's'}}{\partial z} \qquad (3.10)$$

$$\rho\frac{\partial \bar{q}}{\partial t} + \rho \vec{V}\cdot\nabla\bar{q} + \rho\bar{w}\frac{\partial \bar{q}}{\partial z} = (\bar{e}_u + \bar{e}_d - \bar{C}) - \frac{\partial\rho\overline{w'q'}}{\partial z} \qquad (3.11)$$

where subscripts u and d denote updraft and downdraft, respectively, $\bar{e}_u$ is the evaporation rate of liquid water detrained from the updrafts, $\bar{e}_d$ is the evaporation rate of falling precipitation in the downdrafts, and $\bar{C}$ is the condensation rate, which only occurs in updrafts. Using the one-dimensional
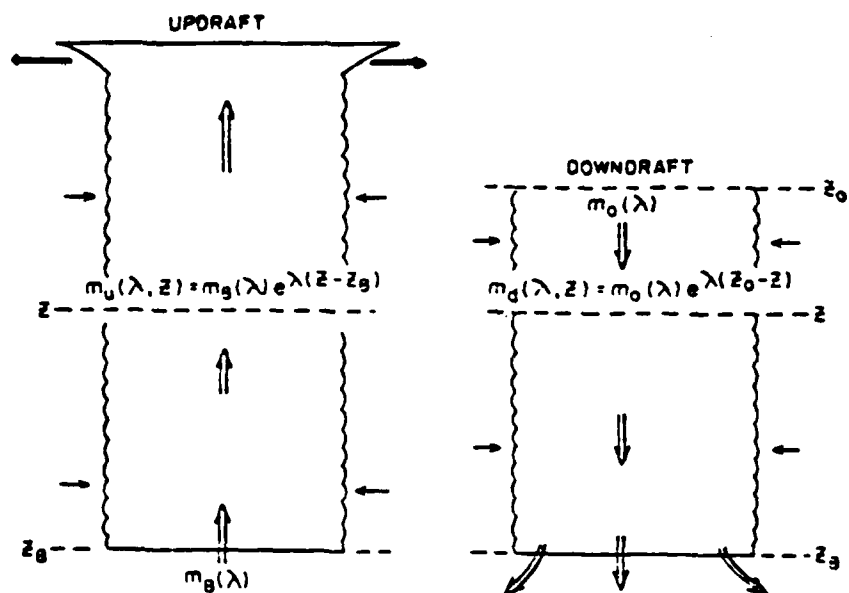
Fig. 3.24. The schematic diagram for the updraft and downdraft of cloud type
λ.

entraining cloud model for both the updrafts and downdrafts, the vertical eddy fluxes $\rho\overline{w's'}$ and $\rho\overline{w'q'}$ now include two parts expressed by (cf. Eqs. (2.3) and (2.4)):

$$\rho\,\overline{w'\alpha'} = \int_z^{\hat{z}_{max}} \{m_u(z,\hat{z})(\alpha_{cu}(z,\hat{z}) - \bar{\alpha}(z) + m_d(z,\hat{z})(\alpha_{cd}(z,\hat{z}) - \bar{\alpha}(z)\}d\hat{z} \tag{3.12}$$

where α = s, q, and h, α_{cu} and α_{cd} are the thermodynamic properties of the updraft and downdraft, respectively. The procedure of determining α_{cu} and α_{cd} is presented in Appendix A. The counterparts of (2.5) and (2.6) are respectively written as:

$$\frac{\partial\rho\overline{w's'}}{\partial z} \equiv \left(\frac{\partial\rho\overline{w's'}}{\partial z}\right)_u + \left(\frac{\partial\rho\overline{w's'}}{\partial z}\right)_d = L\bar{C} - M_u\frac{\partial\bar{s}}{\partial z}$$
$$- L\bar{e}_d - M_d\frac{\partial\bar{s}}{\partial z} \tag{3.13a}$$

where $\qquad \left(\frac{\partial\rho\overline{w's'}}{\partial z}\right)_u = L\bar{C} - M_u\frac{\partial\bar{s}}{\partial z} \tag{3.13b}$

and $\qquad \left(\frac{\partial\rho\overline{w's'}}{\partial z}\right)_d = - L\bar{e}_d - M_d\frac{\partial\bar{s}}{\partial z} \tag{3.13c}$

$$\frac{\partial \rho \overline{w' q'}}{\partial z} \equiv \left(\frac{\partial \rho \overline{w' q'}}{\partial z}\right)_u + \left(\frac{\partial \rho \overline{w' q'}}{\partial z}\right)_d = D(\bar{q} - \bar{q}^*) - M_u \frac{\partial \bar{q}}{\partial z}$$

$$- \bar{C} - M_d \frac{\partial \bar{q}}{\partial z} + \bar{e}_d \qquad (3.14a)$$

where $\qquad \left(\frac{\partial \rho \overline{w' q'}}{\partial z}\right)_u = D(\bar{q} - \bar{q}^*) - M_u \frac{\partial \bar{q}}{\partial z} - \bar{C} \qquad (3.14b)$

and $\qquad \left(\frac{\partial \rho \overline{w' q'}}{\partial z}\right)_d = - M_d \frac{\partial \bar{q}}{\partial z} + \bar{e}_d \qquad (3.14c)$

Here we define:

$$M_u(z) = \int_z^{\hat{z}_{max}} m_u(z,\hat{z}) d\hat{z} = \int_z^{\hat{z}_{max}} m_B(\hat{z}) \eta_u(z,\hat{z}) d\hat{z} \qquad (3.15)$$

$$M_d(z) = \int_z^{\hat{z}_{max}} m_d(z,\hat{z}) d\hat{z} = \int_z^{\hat{z}_{max}} m_0(\hat{z}) \eta_d(z,\hat{z}) d\hat{z} \qquad (3.16)$$

where $m_B(\hat{z})$ and $\eta_u(z,\hat{z})$ have the same definitions as in the no-downdraft case, $m_0(\hat{z})$ is the downdraft-originating-level mass flux, and $\eta_d(z,\hat{z})$ is the normalized mass flux of the downdraft defined by:

$$\eta_d(z,\hat{z}) = \begin{cases} \exp\{\lambda(z_0(\hat{z}) - z) & , \quad z_B \leq z \leq z_0(\hat{z}) \\ \\ 0 & , \quad z > z_0(\hat{z}) \end{cases} \qquad (3.17)$$

were $z_0(\hat{z})$ is the downdraft originating level (see Fig. 3.24). M_c, the net cloud mass flux, is given by

$$M_c = M_d + M_u \tag{3.18}$$

As mentioned above, in order to close the model, Johnson proposed a function $\varepsilon(\hat{z})$ specified by:

$$\varepsilon(\hat{z}) = \frac{m_0(\hat{z})}{m_B(\hat{z})} \tag{3.19}$$

From observational indications, Johnson proposed $\varepsilon = -0.2$ to -0.4. It should be noticed that the parameter ε does not imply any significance of the interaction between the updraft and downdraft but merely serves as a closure parameter. Respectively substituting (3.13a) and (3.14a) into (3.10) and (3.11) with $\bar{e}_u = -D\hat{\ell}$ as before, we obtain the counterparts of (2.7) and (2.8):

$$\rho \frac{\partial \bar{s}}{\partial t} + \rho \vec{V} \cdot \nabla \bar{s} + \rho \bar{w} \frac{\partial \bar{s}}{\partial z} = - DL\hat{\ell} + (M_u + M_d) \frac{\partial \bar{s}}{\partial z} + Q_R \tag{3.20}$$

$$\rho \frac{\partial \bar{q}}{\partial t} + \rho \vec{V} \cdot \nabla \bar{q} + \rho \bar{w} \frac{\partial \bar{q}}{\partial z} = D(\bar{q}^* - \bar{q} + \hat{\ell}) + (M_u + M_d) \frac{\partial \bar{q}}{\partial z} \tag{3.21}$$

Comparing (3.20) and (3.21) with (2.7) and (2.8), it is observed that the net effects on the temporal changes of the thermodynamic fields due to the downdrafts are through the cumulus-induced lifting processes $M_d \frac{\partial \bar{s}}{\partial z}$ and $M_d \frac{\partial \bar{q}}{\partial z}$. Mathematically, with the use of (3.19), (3.20) and (3.21) are still two

Volterra integral equations with two unknowns $m_B(\hat{z})$ and $\hat{\ell}(\hat{z})$ and they can be used in diagnostic studies (Johnson, 1976, 1978, and 1980).

For prognostic purposes, the next step is to apply the quasi-equilibrium assumption to each cloud sub-ensemble. To do so, we take the cloud work function for updraft $(A_u(\hat{z}))$ into consideration by defining:

$$A_u(\hat{z}) = \int_{z_B}^{\hat{z}} \frac{g}{c_p \bar{T}(z)} \eta_u(z,\hat{z}) \{s_{c_u}(z,\hat{z}) - \bar{s}(z)\} d\hat{z} \tag{3.22}$$

Then, the counterparts of (2.26) through (2.30) can be respectively written as:

$$\frac{\partial A_u(z)}{\partial t} = \int_{z_B}^{\hat{z}_{max}} \left(K_V(\hat{z},\hat{z}') + K_D(\hat{z},\hat{z}') \right) m_B(\hat{z}') d\hat{z}'$$

$$+ F_c(\hat{z}) + F_M(\hat{z}) + \left(\frac{\partial h_M}{\partial t}\right)_{cd} \int_{z_B}^{\hat{z}} \rho(z)\beta(z) dz \tag{3.23}$$

where $F_c(\hat{z}) = \int_{z_B}^{\hat{z}} \eta_u(z,\hat{z}) \{\lambda b(z,\hat{z}) \ (-w \frac{\partial \bar{h}}{\partial z} - \vec{V}\cdot\nabla\bar{h} + Q_R)$ (3.24)

$$- \alpha(z)(- \bar{w} \frac{\partial \bar{s}}{\partial z} - \vec{V}\cdot\nabla\bar{s} + Q_R)\}\rho(z) dz$$

$$F_M(\hat{z}) = \left(\frac{\partial h_M}{\partial t}\right)_{LS} \int_{z_B}^{\hat{z}} \rho(z)\beta(z) dz \tag{3.25}$$

$$K_v(\hat{z},\hat{z}') = \int_{z_B}^{\hat{z}} \eta_u(z,\hat{z})\eta_u(z,\hat{z}')\{\lambda b(z,\hat{z}) \frac{\partial \bar{h}}{\partial z} - \alpha(z) \frac{\partial \bar{s}}{\partial z}\} \, dz \qquad (3.26)$$

$$+ \epsilon \int_{z_B}^{\hat{z}} \eta_u(z,\hat{z})\eta_d(z,\hat{z}')\{\lambda b(z,\hat{z})\frac{\partial \bar{h}}{\partial z} - \alpha(z)\frac{\partial \bar{s}}{\partial z}\} \, dz$$

$$K_D(\hat{z},\hat{z}') = \eta_u(\hat{z}',\hat{z})\eta_u(\hat{z}',\hat{z}')\{\lambda b(\hat{z}',\hat{z})L(\bar{q}^*(\hat{z}') - \bar{q}(\hat{z}')) \qquad (3.27)$$

$$+ \alpha(\hat{z}') \, L\hat{\ell}\,(\hat{z}')\}$$

Comparing (3.23) to (3.27) with (2.26) to (2.30), the main difference between the two systems is the second integral term in (3.26), which increases the cloud work function of the updraft with time due to the induced lifting by downdrafts. It is also noticed from the last two terms in (3.23) that, since the inclusion of downdrafts can modify the thermodynamic properties of the mixed layer due to the detrainment of downdrafts, $\frac{\partial h_M}{\partial t}$ has been divided into two parts: $(\frac{\partial h_M}{\partial t})_{LS}$ and $(\frac{\partial h_M}{\partial t})_{cd}$. $(\frac{\partial h_M}{\partial t})_{LS}$ represents the time change of h_M due to large-scale horizontal advection and the turbulent eddy fluxes of heat and moisture at the surface and the top of the mixed layer (e.g., the right hand side of (2.21)). Meanwhile, $(\frac{\partial h_M}{\partial t})_{cd}$ represents the time change of h_M due to the detrainment of cumulus downdrafts. However, for the time being, the assumption that $\frac{\partial h_M}{\partial t} = 0$, as described in Section 3.2, is still employed in this semi-prognostic approach as a simplification, thus making the last two terms in (3.23) vanish. We shall derive a formulation for $(\frac{\partial h_M}{\partial t})_{cd}$ in Chapter 4, where a mixed layer parameterization is developed for a fully prognostic model.

Finally, applying the argument of the quasi-equilibrium assumption to (3.23) and using the algorithm described in Section 3.2, we can solve for m_B. Then, using (3.13a) and (3.13b), we can determine the condensation rate ($\bar{C}$) in updrafts and the evaporation rate due to precipitation ($\bar{e}_d$) in downdrafts.

3.4.2 The results:

We have extensively applied the method described in the previous section to the cloud band event. The value chosen for the ratio between the intensities of updraft and downdraft (ϵ) is -0.3. This value was experimentally determined based on the comparison between the result derived from the semi-prognostic study at 09 GMT and the averaged result from cloud model simulation for the period from 06 to 12 GMT by Soong and Tao (1980, 1984). Fig. 3.25 shows the net cloud mass flux (M_c) (cf. (3.18)) as a function of time and height. Comparing Fig. 3.25 with Fig. 3.9, it is found that the general structure and the magnitudes of M_c are similar to those of $\bar{M}$, which again indicates that the mass flux in the cloud-free area is negligibly small. Comparing Fig. 3.25 with Fig. 3.10, which is the M_c distribution for the no-downdraft case, it is observed that the inclusion of downdrafts would not largely influence the magnitudes of M_c. Fig. 3.26 shows the cloud base mass flux (m_B) as a function of cloud top height and time. Comparing Fig. 3.26 with Fig. 3.11, it is found that the general structures with and without downdrafts are quite similar. However, the maximum of m_B at the lower levels in Fig. 3.26 is about two times larger than that in Fig. 3.11, while the magnitudes at the higher levels of those two diagrams are about the same. This is not surprising, since the highest downdraft-originating-level in this model
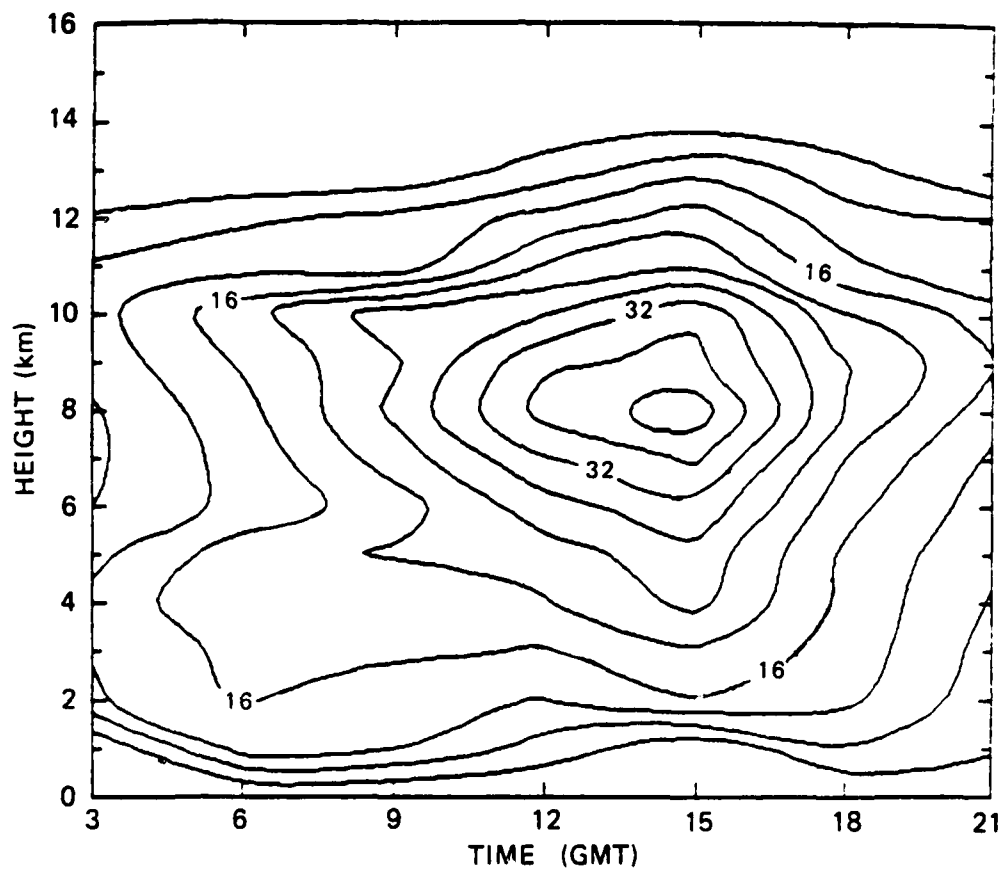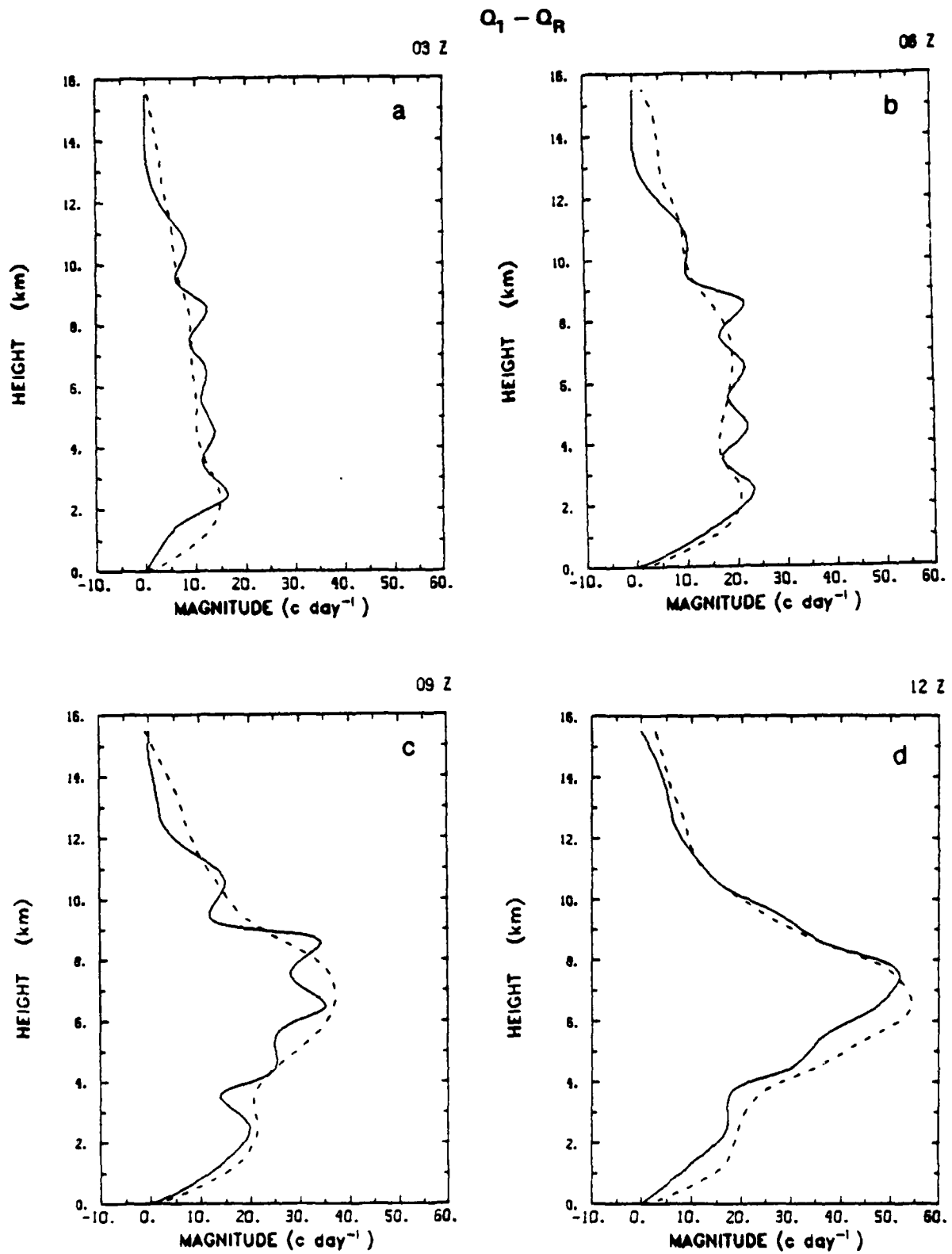
Fig. 3.25. The same as Fig. 3.10 except for the downdraft case with $\epsilon = -0.3$.
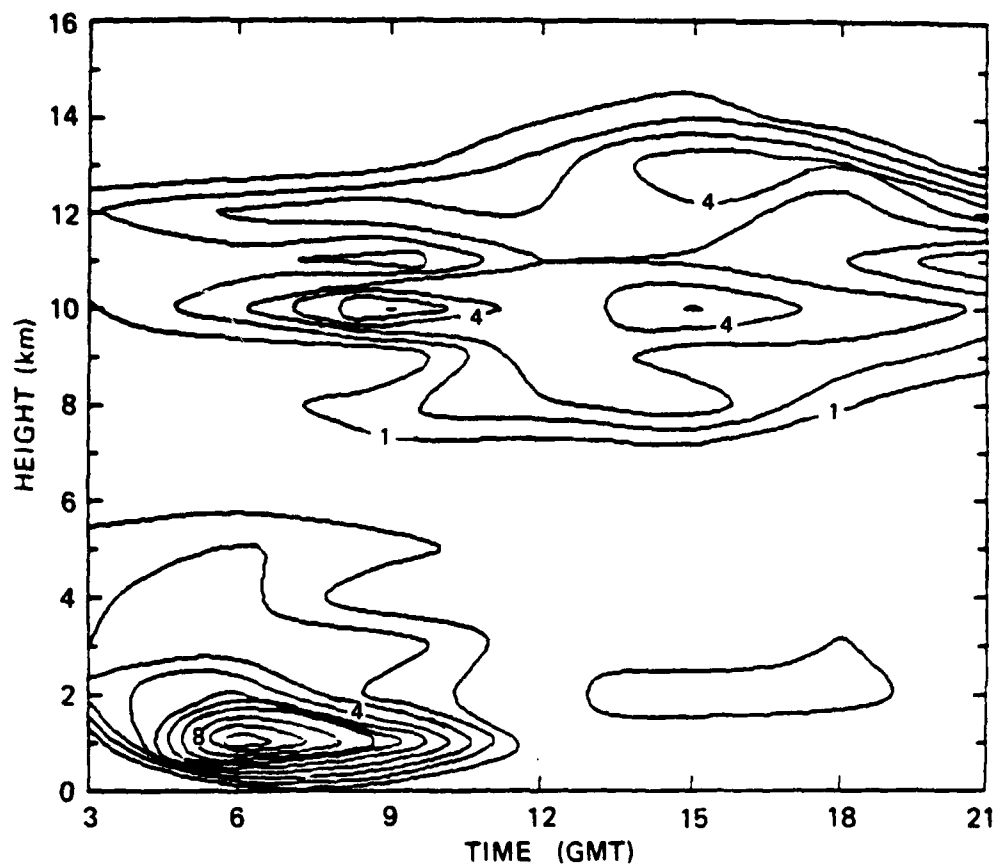
Fig. 3.26. The same as Fig. 3.11 except for the downdraft case with $\epsilon = -0.3$.

is about 8 km and, thus, all the downdraft effects are confined below that level. As discussed earlier, the downdrafts can introduce a cooling effect to the environment so that the population of shallow clouds increases. Note that the magnitudes of M_c with and without downdrafts are quite close, as shown in Figs. 3.25 and 3.10, simply because M_c also includes the component of M_d (cf. (3.18) and (3.16)).

Figs. 3.27 and 3.28, respectively, show the profiles of predicted $Q_1 - Q_R$ and Q_2 in contrast to the observed ones. It is found that the agreement between the predicted and observed $Q_1 - Q_R$ is generally as good as that shown in Fig. 3.7 for the no-downdraft case. However, in Fig. 3.28, less agreement between the predicted and observed Q_2 at the low levels is found for most cases which underestimate the cloud drying effects. These discrepancies can be expected because the inclusion of downdrafts increases shallow clouds, as described above, which would introduce an extra moistening effect by the entrainment of water vapor into the environment at the cloud tops (cf. Eq. (2.8) and Fig. 3.13)). However, it should be noted that the sensitivity of this moistening effect is also controlled by the relative humidity. Thus, if the lower atmosphere is extremely moist, this discrepancy would not take place.

Fig. 3.29 shows the results of the predicted condensation, evaporation, and vertical convergence of eddy heat flux in p-coordinates at 09 GMT. With the inclusion of downdrafts, it is clearly seen that both the condensation and evaporation are much larger than those without downdrafts, shown in Fig. 3.23, and quite close to the results derived from the cloud model, shown in Fig. 3.21. Fig. 3.30 shows the mass fluxes due to the updrafts and downdrafts.

$Q_1 - Q_R$

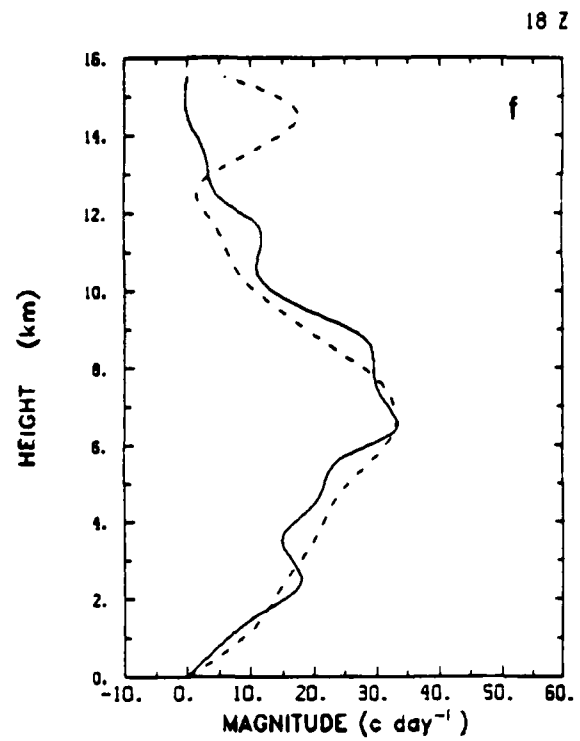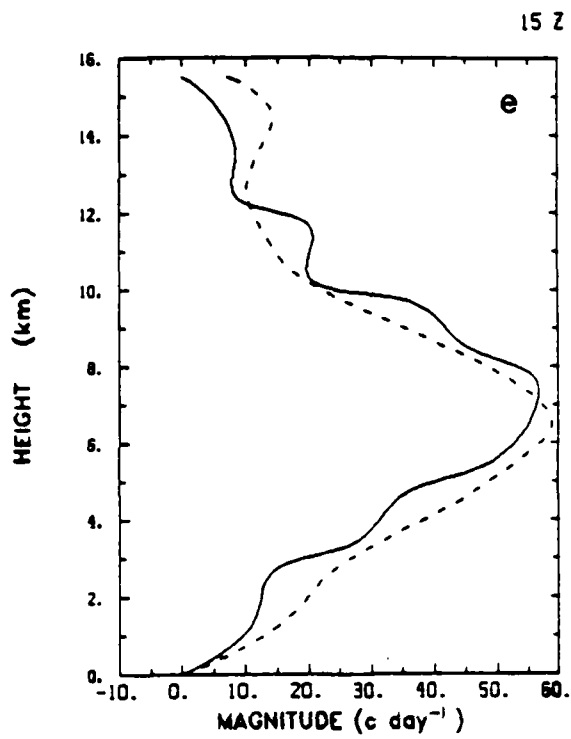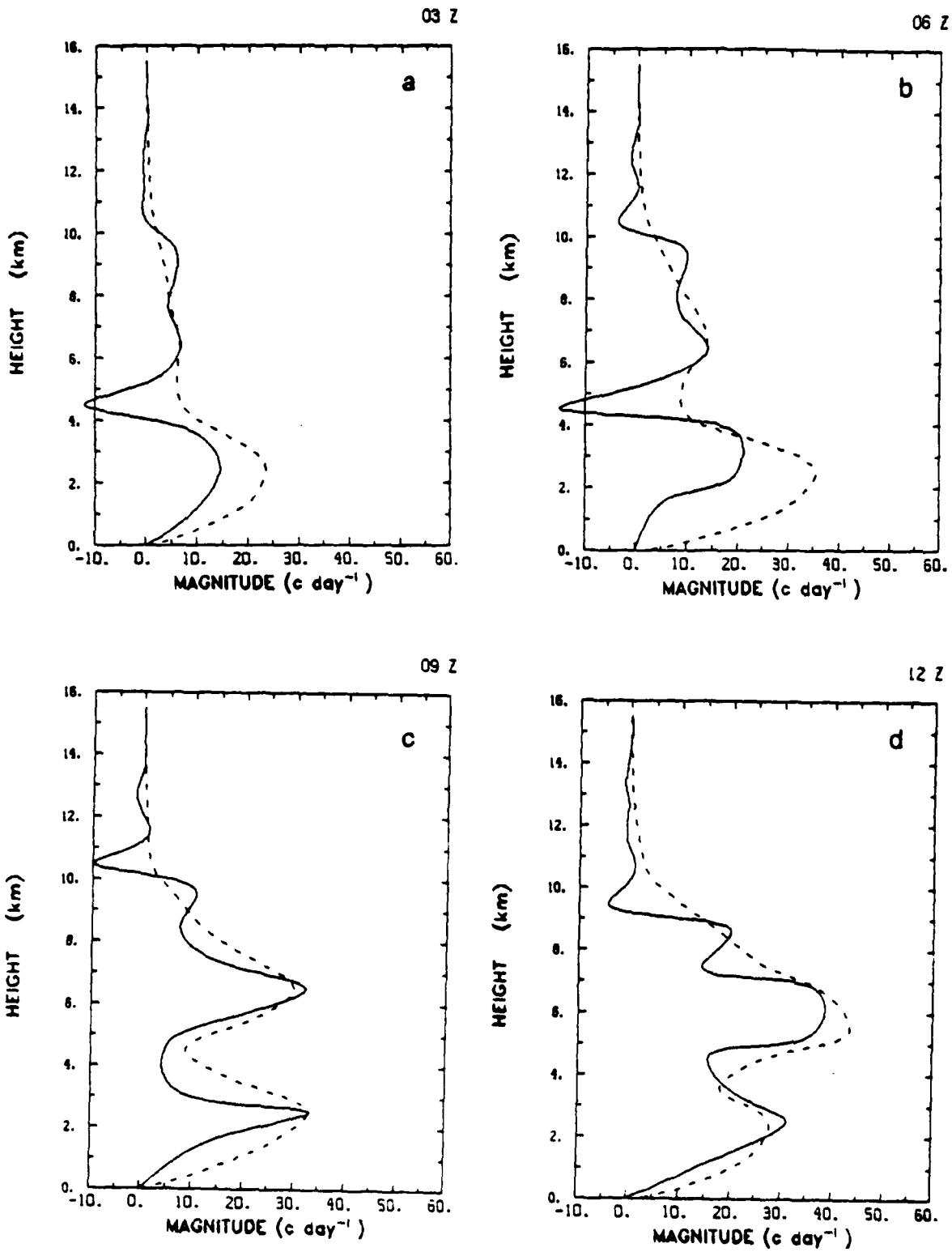Fig. 3.27. The same as Fig. 3.7 except for the downdraft case with ε = -0.3.
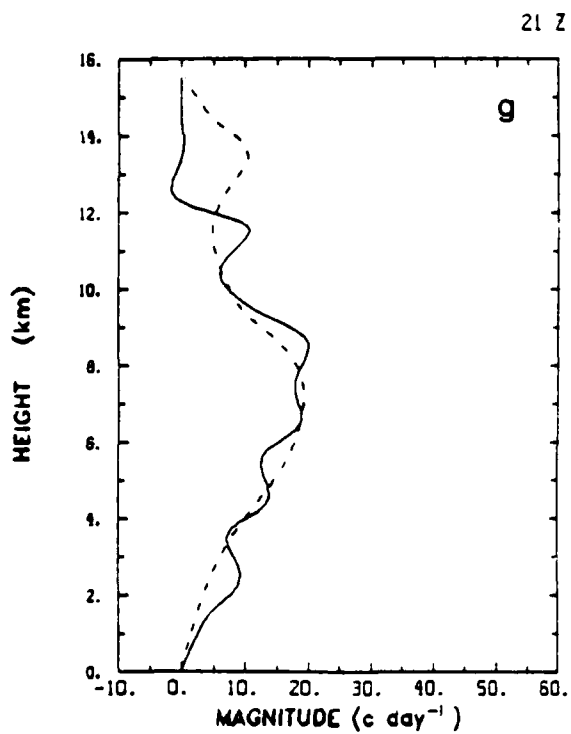
Fig. 3.27. (Continued)

Q_2

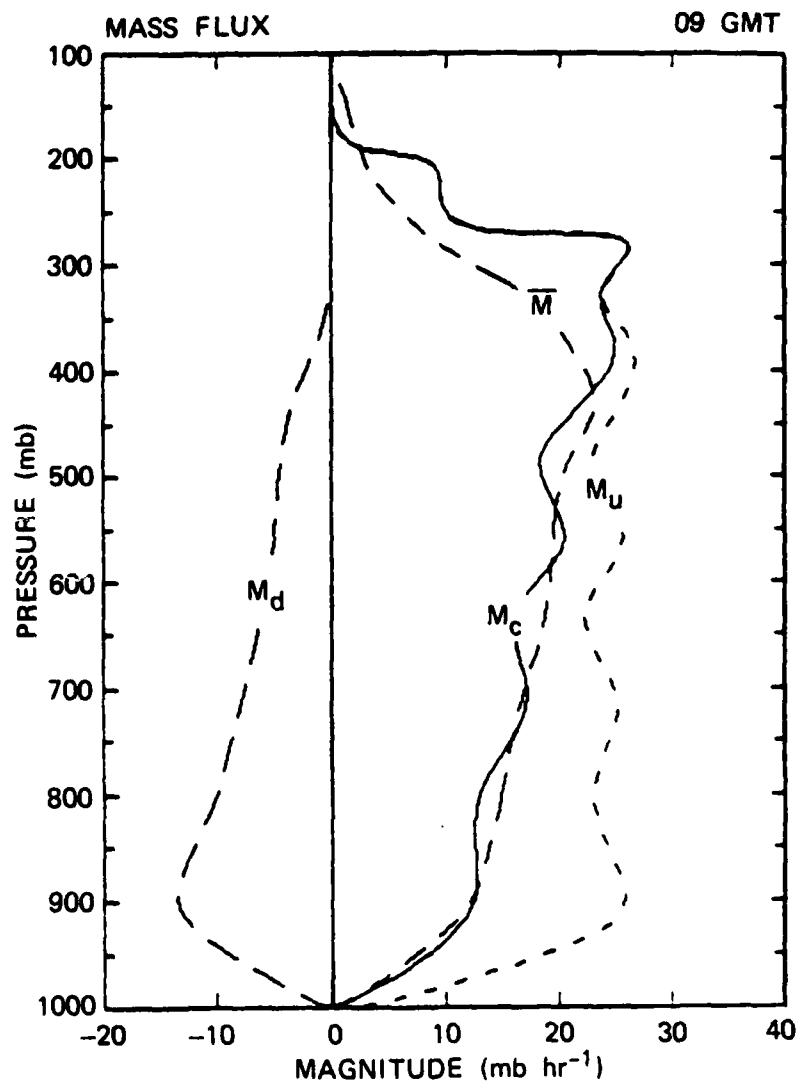Fig. 3.28. The same as Fig. 3.8 except for the downdraft case with ε = -0.3.

15 Z

e

HEIGHT (km)

MAGNITUDE (c day^{-1})

18 Z

f

HEIGHT (km)

MAGNITUDE (c day^{-1})

21 Z

g

HEIGHT (km)

MAGNITUDE (c day^{-1})
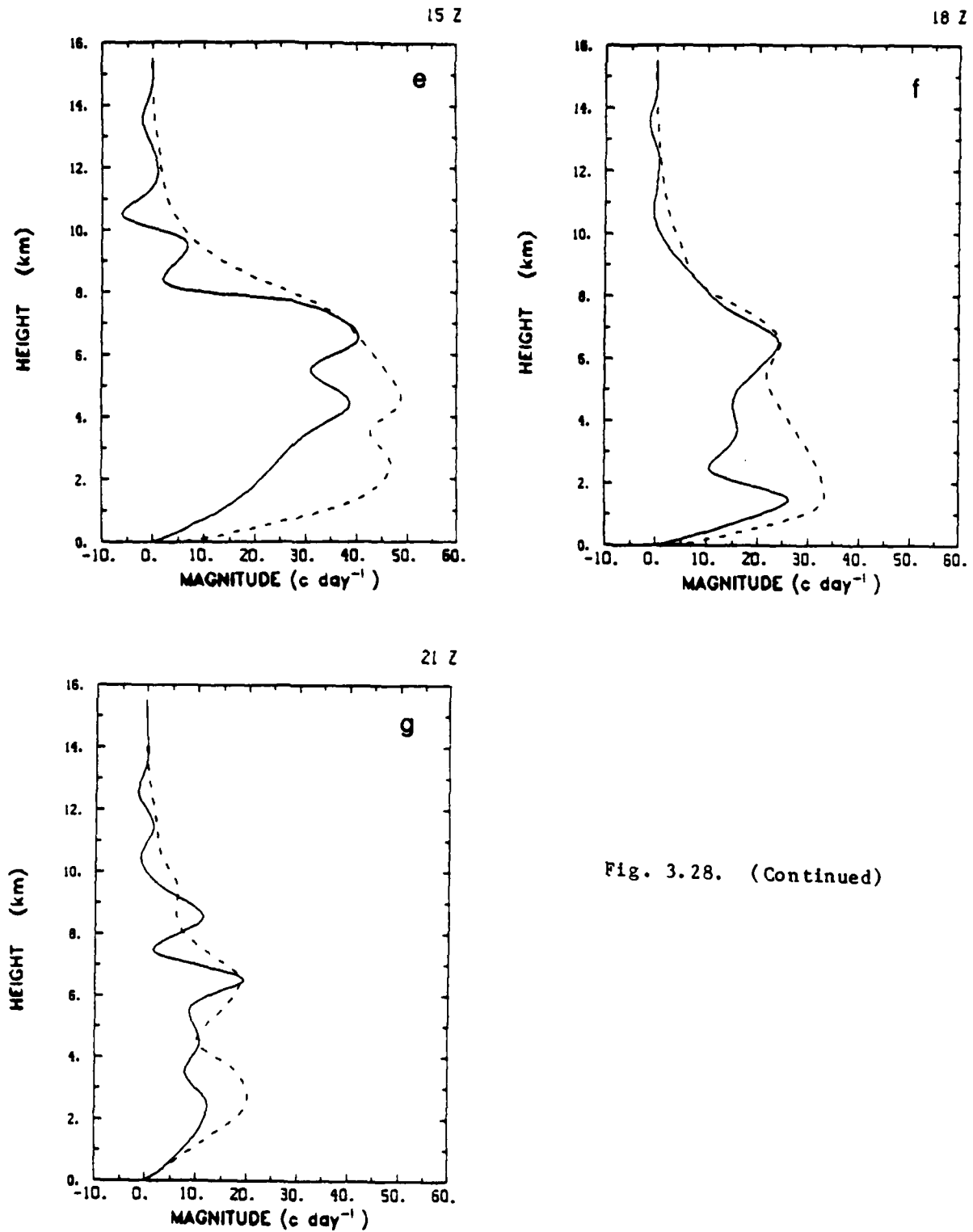
Fig. 3.28. (Continued)
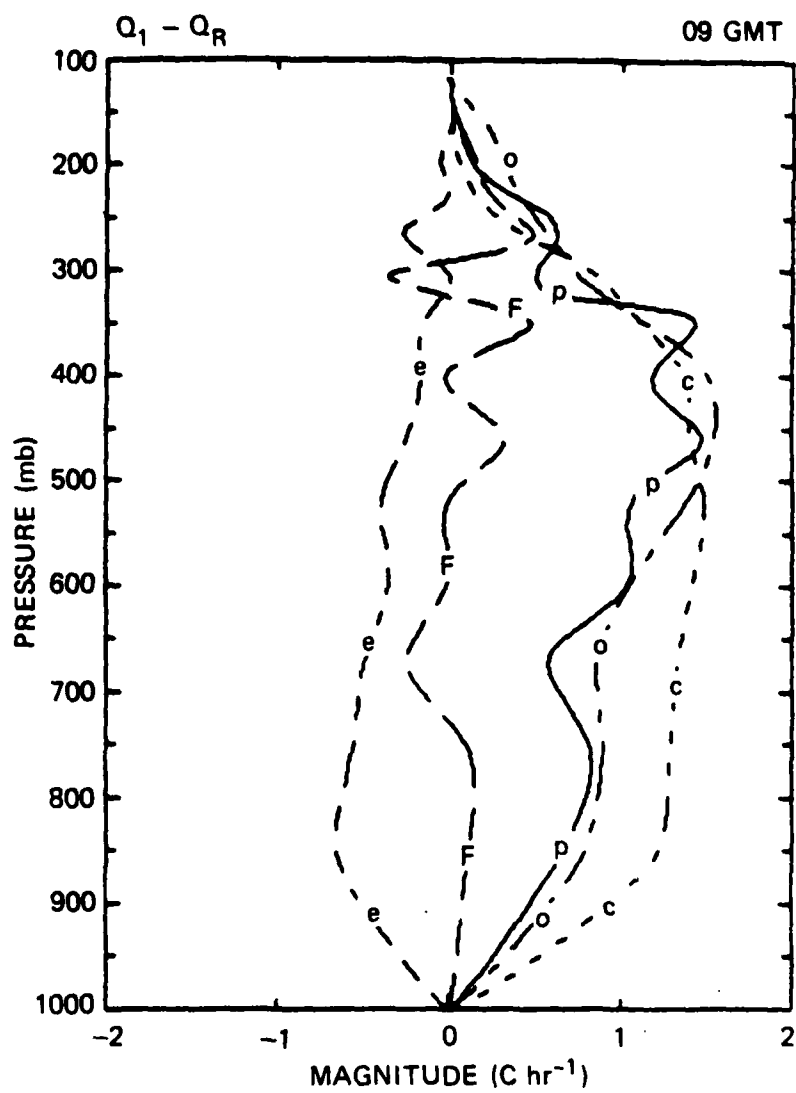
Fig. 3.29. The same as Fig. 3.23 except for the downdraft case with $\epsilon = -0.3$.

Fig. 3.30. The vertical profiles of total mass flux ($\overline{M}$), updraft mass flux (M_u), downdraft mass flux (M_d), and net cloud mass flux (M_c) in units of mb hr^{-1}.

Comparing Fig. 3.30 with Fig. 3.22, which shows the cloud model results, both the updraft and downdraft mass fluxes predicted by the A-S scheme are found to be smaller roughly by 25% for the former and by 35% for the later than those shown in Fig 3.22. One possible reason for this discrepancy may be due to the different definitions for the cloud area. The cloud area in the cloud model is defined as any area having a liquid water content of 10^{-2} g Kg^{-1} or more. This definition includes active and inactive clouds, the later including some shallow stratus clouds and anvil clouds. On the other hand, the cloud model used in the A-S scheme only considers active cumulus clouds. Nevertheless, the general agreement in the shape of the mass flux profiles between the two results is quite well.

In passing, it should be clarified that this downdraft model in the prognostic applications is still in an experimental stage simply because there has been no theoretical way to determine ϵ. The same method has been applied to the tropical composite waves. It was found that, in order to obtain reasonable cloud heating and drying effects, the lower limits of ϵ used for eight categories vary between 0 and -0.4. Thus, concerning the incorporation of this downdraft model into a large-scale prediction model, the problems become two-fold: what is the lower limit of ϵ for a specific weather condition? and what is the optimum ϵ between the lower limit and 0? First of all, it is felt that similar studies, as described in this section, with different data over different regions are required before attempting to analytically determine the optimum ϵ.

CHAPTER IV

THE MESOSCALE MODEL

In Chapter 3, we tested the A-S scheme using the semi-prognostic approach to examine the response of cumulus convection to the destabilization of the atmosphere by large-scale processes. The results indicate that the predicted cloud mass flux and its associated heating and drying effects by the A-S scheme are quite realistic, also bearing considerable resemblance to those obtained from a cloud modeling study. However, this close agreement between the predictions and observations in the semi-prognostic approach does not necessarily imply that the A-S scheme will have prognostic value in a fully prognostic model. This point should be clear, since, in a fully prognostic model, both the cloud properties and large-scale disturbances evolve in time and highly interact with each other.

In order to examine how the A-S scheme works in a complete prognostic problem, a two-dimensional hydrostatic model was developed with the inclusion of the A-S scheme to investigate the evolution and structure of the same tropical cloud band, discussed previously, under the influence of a low-level large-scale lifting. This chapter will describe the model. The model results will be represented in Chapter 5.

4.1 Governing equations

Although mesoscale dynamics is characteristically three-dimensional, as a first attempt to understand the response of a tropical mesoscale convective system to the large-scale forcing through the application of the A-S scheme, we assume that the predicted quantities do not depend on one of the horizontal Cartesian coordinates (namely y). In order to incorporate rotational effects, we retain the velocity component in the y direction. The mesoscale model presented here employs the "deep anelastic" equations (Ogura and Phillips, 1962) but with the hydrostatic assumption. The two-dimensional "hydrostatic version" of the anelastic system has been used by Orlanski and Ross (1977) with the replacements of the momentum equations by the vorticity equation in a frontal simulation. Rosenthal (1969, 1970) used this version but in an axisymmetric model to simulate the development of hurricanes.

The momentum equations in the x-z slab symmetric domain are:

$$\frac{\partial u}{\partial t} = - u \frac{\partial u}{\partial t} - w \frac{\partial u}{\partial z} + fv - c_p \theta \frac{\partial \pi}{\partial x} \qquad (4.1)$$

$$\frac{\partial v}{\partial t} = - u \frac{\partial v}{\partial t} - w \frac{\partial v}{\partial z} - f(u - u_g) \qquad (4.2)$$

where θ is the potential temperature, f is the Coriolis parameter with the value of 2.15×10^{-5} s^{-1}, u_g is the x-component of the geostrophic wind, which

is taken to be the constant value of the initial wind u throughout the integration, and π, the nondimensional pressure, is defined as:

$$\pi = \left(\frac{p}{P_0}\right)^{R/c_p} \tag{4.3}$$

where p is pressure, P_0 is the reference pressure (1000 mb), R is the gas constant of dry air, and c_p is the specific heat of dry air at constant pressure. The hydrostatic equation is:

$$c_p \theta_v \frac{\partial \pi}{\partial z} = -g \tag{4.4}$$

where g is the gravity and θ_v is the virtual potential temperature defined by:

$$\theta_v = \theta(1 + 0.61q) \tag{4.5}$$

The thermodynamic and moisture equations are:

$$\frac{\partial \theta}{\partial t} = -u \frac{\partial \theta}{\partial x} - w \frac{\partial \theta}{\partial z} - v \frac{\partial \theta_g}{\partial y} + Q_L \tag{4.6}$$

$$\frac{\partial q}{\partial t} = -u \frac{\partial q}{\partial x} - w \frac{\partial q}{\partial z} + P_v \tag{4.7}$$

where Q_L is the diabatic heating rate due to clouds, P_v is the production rate of water vapor due to clouds, and $\frac{\partial \theta_g}{\partial y}$ is related to u_g by the thermal wind relation:

$$\frac{\partial \theta_g}{\partial y} = - \frac{\theta_g f}{g} \frac{\partial u_g}{\partial z} \tag{4.8}$$

where θ_g can be specified from the initial soundings. It is noted that radiation effects are neglected in (4.6), assuming that they are not fundamental to the development of a tropical mesoscale convective system. The mass continuity equation is expressed in the anelastic form:

$$\frac{\partial u}{\partial x} + \frac{1}{\rho} \frac{\partial \rho w}{\partial z} = 0 \tag{4.9}$$

where ρ, the density, is a function of height only.

Respectively separating the variables θ, q, and π into the horizontal mean and its departure as:

$$A(x,z,t) = \bar{A}(z,t) + A'(x,z,t) \tag{4.10}$$

where $A = \theta$, q, and π, and subsequently substituting (4.10) into (4.1), (4.2), (4.4), (4.6), and (4.7), with the use of (4.9), we obtain a set of governing equations in flux form:

$$\frac{\partial u}{\partial t} = - \frac{\partial uu}{\partial x} - \frac{1}{\rho} \frac{\partial}{\partial z} (\rho uw) + fv - c_p \bar{\theta} \frac{\partial \pi'}{\partial x} \tag{4.11}$$

$$\frac{\partial v}{\partial t} = - \frac{\partial uv}{\partial x} - \frac{1}{\rho} \frac{\partial}{\partial z} (\rho vw) - f(u - u_g) \tag{4.12}$$
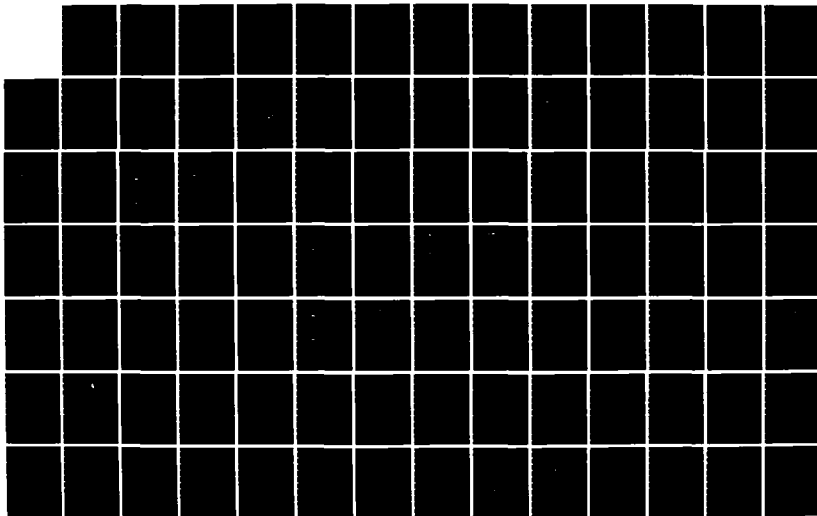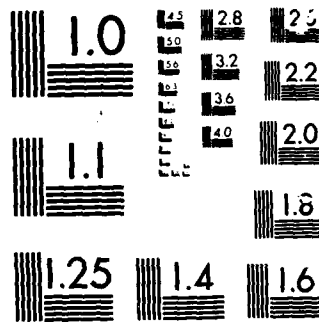
$$c_p \overline{\theta} \frac{\partial \pi'}{\partial z} = g\left(\frac{\theta'}{\overline{\theta}} + 0.61q'\right) \qquad (4.13)$$

$$\frac{\partial \theta}{\partial t} = -\frac{\partial}{\partial x}(u\theta') - \frac{1}{\rho}\frac{\partial}{\partial z}(\rho w\theta') - v\frac{\partial \theta_g}{\partial y} - w\frac{\partial \overline{\theta}}{\partial z} + Q_L \qquad (4.14)$$

$$\frac{\partial q}{\partial t} = -\frac{\partial}{\partial x}(uq') - \frac{1}{\rho}\frac{\partial}{\partial z}(\rho wq') - w\frac{\partial \overline{q}}{\partial z} + P_v \qquad (4.15)$$

In deriving (4.13), we assumed that the horizontal means satisfy the hydrostatic relation:

$$c_p \overline{\theta}_v \frac{\partial \overline{\pi}}{\partial z} = -g \qquad (4.16)$$

In deriving (4.11), θ in front of the pressure gradient term was approximated by $\overline{\theta}$.

Since this model is designed to examine the evolution of a mesoscale convective system under the influence of a weak large-scale lifting, a constantly imposed low-level circulation $[w_0, u_0]$, which satisfies the continuity equation, is now introduced into (4.11), (4.12), (4.14), and (4.15):

$$\frac{\partial u}{\partial t} = -\frac{\partial}{\partial x}(u+u_0)(u+u_0) - \frac{1}{\rho}\frac{\partial}{\partial z}[\rho(u+u_0)(w+w_0)]$$

$$+ fv - c_p \overline{\theta}\frac{\partial \pi'}{\partial x} \qquad (4.17)$$

$$\frac{\partial \theta}{\partial t} = -\frac{\partial}{\partial x}(u+u_0)v - \frac{1}{\rho}\frac{\partial}{\partial z}v(w+w_0) - f(u-u_g) \tag{4.18}$$

$$\frac{\partial \theta}{\partial t} = -\frac{\partial}{\partial x}(u+u_0)\theta' - \frac{1}{\rho}\frac{\partial}{\partial z}(w+w_0)\theta' - v\frac{\partial u_g}{\partial y}$$

$$-(w+w_0)\frac{\partial \bar{\theta}}{\partial z} + Q_L \tag{4.19}$$

$$\frac{\partial q}{\partial t} = -\frac{\partial}{\partial x}(u+u_0)q' - \frac{1}{\rho}\frac{\partial}{\partial z}(w+w_o)q' - (w+w_o)\frac{\partial \bar{q}}{\partial z} + P_v \tag{4.20}$$

The specifications for w_0 and u_0 are discussed in Section 4.3.2.

The final step is to replace the cloud terms represented by Q_L and P_v in (4.19) and (4.20) by the A-S parameterization. Using the notations introduced in Chapter 2, we have:

$$Q_L = \frac{1}{\rho c_p \bar{\pi}}\left[M_c\frac{\partial s}{\partial z} - DL\hat{\ell}\right] \tag{4.21}$$

$$P_v = \frac{1}{\rho}\left[M_c\frac{\partial q}{\partial z} + D(q^* - q) + D\hat{\ell}\right] \tag{4.22}$$

Since the thermodynamic equation in the A-S scheme was originally formulated in terms of the static energy (s), we need to convert θ into s, thus requiring the use of the nondimensional pressure π. In doing this, we adopt the

approximation that $\pi'/\bar{\pi}$ is an order of magnitude less than $\theta'/\bar{\theta}$, from Wilhelmson and Ogura (1972):

$$\frac{\pi'}{\bar{\pi}} << \frac{\theta'}{\bar{\theta}} \tag{4.23}$$

such that T is approximated by $T = \bar{\pi}\theta$ and s is approximated by $s = c_p\bar{\pi}\theta + gz$.

Now, the set of equations which govern the evolution of a mesoscale convective system under the influence of the large-scale lifting consists of (4.17) to (4.20) with the continuity equation (4.9) and hydrostatic equation (4.13).

4.2 Boundary layer parameterization:

A mixed layer approach (see Fig. 2.1) is employed with the assumption that the depth of the mixed layer is constant in time and space. The equations for θ_M and q_M are written as:

$$\rho \frac{\partial \theta_M}{\partial t} = - \rho \vec{V}_M \cdot \nabla \theta_M - \frac{\partial (\overline{\rho w'\theta'})}{\partial z} - \frac{\partial F_\theta}{\partial z} - Le \tag{4.24}$$

$$\rho \frac{\partial q_M}{\partial t} = - \rho \vec{V}_M \cdot \nabla q_M - \frac{\partial (\overline{\rho w'q'})}{\partial z} - \frac{\partial F_q}{\partial z} + e \tag{4.25}$$

where $\overline{\rho w'\theta'}$ and $\overline{\rho w'q'}$ represent the cumulus fluxes of heat and moisture, while

F_θ and F_q represent the vertical fluxes of heat and moisture due to all other turbulent eddies and e represents the evaporation rate of falling precipitation associated with downdrafts (Johnson, 1976). It is noted that $w \frac{\partial\theta}{\partial z}$ and $w \frac{\partial q}{\partial z}$ vanish in (4.24) and (4.25) because of our characterization of the mixed layer. Meanwhile, this mixed layer approximation is also applied to the momentum equations (Suarez et al., 1983) which are written as:

$$\rho \frac{\partial u_M}{\partial t} = - \rho \vec{V}_M \cdot \nabla u_M + \rho f v_M - \rho c_p \bar{\theta}_M \left(\frac{\partial \pi'}{\partial x}\right)_M - \frac{\partial F_u}{\partial z} \qquad (4.26)$$

$$\rho \frac{\partial v_M}{\partial t} = - \rho \vec{V}_M \cdot \nabla v_M - \rho f(u_M - u_{g_M}) - \frac{\partial F_v}{\partial z} \qquad (4.27)$$

where F_u and F_v represent the vertical momentum fluxes due to turbulent eddies.

Integrating (4.24) to (4.27) vertically from the surface to z_B, we obtain:

$$\rho_M \frac{\partial \theta_M}{\partial t} = - \rho_M \vec{V}_M \cdot \nabla \theta_M - \frac{(\rho\overline{w'\theta'})_B - (\rho\overline{w'q'})_0}{\Delta z} - \frac{(F_\theta)_B - (F_\theta)_0}{\Delta z} - Le_M \qquad (4.28)$$

$$\rho_M \frac{\partial q_M}{\partial t} = - \rho_M \vec{V}_M \cdot \nabla q_M - \frac{(\rho\overline{w'q'})_B - (\rho\overline{w'\theta'})_0}{\Delta z} - \frac{(F_q)_B - (F_q)_0}{\Delta z} + e_M \qquad (4.29)$$

$$\rho_M \frac{\partial u_M}{\partial t} = - \rho_M \vec{V}_M \cdot \nabla u_M + \rho_M f v_M + \rho_M c_p \bar{\theta}_M \left(\frac{\partial \pi'}{\partial x}\right)_M - \frac{(F_u)_B - (F_u)_0}{\Delta z} \qquad (4.30)$$

$$\rho_M \frac{\partial v_M}{\partial t} = - \rho_M \vec{V}_M \cdot \nabla v_M - \rho_M f(u_M - u_{g_M}) - \frac{(F_v)_B - (F_v)_0}{\Delta z} \qquad (4.31)$$

where

$$\rho_M = \frac{\int_0^{z_B} \rho \, dz}{\Delta z} \qquad (4.32)$$

$$e_M = \frac{\int_0^{z_B} e \, dz}{\Delta z} \qquad (4.33)$$

$\Delta z = z_B$, subscript B denotes the cloud base, and subscript 0 denotes the surface. It is assumed that the eddy momentum fluxes at the top of mixed layer and the cumulus fluxes at the surface vanish:

$$(F_u)_B = (F_v)_B = 0 \qquad (4.34)$$

$$(\rho \overline{w'\theta'})_0 = (\rho \overline{w'q'})_0 \qquad (4.35)$$

Using Deardoff's parameterization (1972), we can determine $(F_\theta)_0$, $(F_q)_0$, and $(F_v)_0$ by:

$$(F_\theta)_0 = \frac{(\theta_0 - \theta_M)(F_{\theta_v})_0}{\theta_{v_0} - \theta_{v_M}} \qquad (4.36)$$

$$(F_q)_0 = \frac{(q_0 - q_M)(F_{\theta_v})_0}{\theta_{v_0} - \theta_{v_M}} \qquad (4.37)$$

$$(F_{\vec{V}})_0 = \rho_0 c_u^2 |\vec{V}_M| \vec{V}_M \tag{4.38}$$

where $(F_\theta)_0$ is the eddy flux of virtual potential temperature at the surface and is given by:

$$(F_{\theta_v})_0 = \rho_0 c_\theta u_\star (\theta_{v_0} - \theta_{v_M}) \tag{4.39}$$

The notations introduced in (4.36) to (4.39) are explained as follows: ρ_0 is the air density at the surface, c_u the friction coefficient, c_θ the heat-transfer coefficient, and $u_\star$ the frictional velocity. $u_\star$ is determined by:

$$u_\star^2 = \frac{|(F_{\vec{V}})_0|}{\rho_0} \tag{4.40}$$

c_u and c_θ are determined through empirical formulas which are functions of the bulk Richardson number

$$R_{i_B} = \frac{g}{\theta_{v_M}} \frac{z_B(\theta_{v_M} - \theta_{v_0})}{|\vec{V}_M|^2} \tag{4.41}$$

Following Lilly (1968), we determine the turbulent eddy fluxes of heat and moisture at the top of the mixed layer by:

$$(F_\theta)_B = - k(F_\theta)_0 \tag{4.42}$$

$$(F_q)_B = k(F_q)_0 \tag{4.43}$$

where k is chosen to be 0.2.

The next step is to determine the cumulus fluxes of heat and moisture at the top of the mixed layer, which are respectively represented by $(\rho\overline{w'\theta'})_B$ and $(\rho\overline{w'q'})_B$ in (4.28) and (4.29). If following the Arakawa and Schubert's approach as stated in Sections 2.1, there would be no contributions to $(\rho\overline{w'\theta'})_B$ and $(\rho\overline{w'q})_B$ due to the updrafts. This can be shown by the relations (cf. (2.3)) and (2.4)):

$$(\rho\overline{w'\theta'})_{B_u} = \int_{z_B}^{\hat{z}_{max}} m_B(\hat{z}')\eta_u(z_B,\hat{z}')(\theta_{cu}(z_B,\hat{z}') - \overline{\theta}(z_B))d\hat{z} \qquad (4.44)$$

$$(\rho\overline{w'q'})_{B_u} = \int_{z_B}^{\hat{z}_{max}} m_B(\hat{z}')\eta_u(z_B,\hat{z}')(q_{cu}(z_B,\hat{z}') - \overline{q}(z_B))d\hat{z} \qquad (4.45)$$

where subscript u represents the updraft, and with $\theta_{cu}(z_B,\hat{z}) = \theta(z_B) = \theta_M$ and $q_{cu}(z_B,\hat{z}) = q(z_B) = q_M$. Thus, we obtain $(\rho\overline{w'\theta'})_{Bu} = (\rho\overline{w'q})_{Bu} = 0$. Hence, in this model, $(\rho\overline{w'\theta'})_B$ and $(\rho\overline{w'q'})_B$ are only associated with downdrafts and can be formulated by:

$$(\rho\overline{w'\alpha'})_B = \int_{z_B}^{\hat{z}_{max}} m_0(\hat{z})\eta_d(z_B,\hat{z}')(\alpha_{cd}(z_B,\hat{z}') - \overline{\alpha}(z_B+)))d\hat{z}' \qquad (4.46)$$

where $\alpha = \theta$ and q. $m_0(\hat{z})$ is the downdraft mass flux of sub-ensemble $\hat{z}$ at its downdraft originating level and $\eta_d(z_B,\hat{z})$ is the normalized mass flux for downdraft. $\alpha_{cd}(z_B,\hat{z})$ is the thermodynamic property of the cumulus downdraft of sub-ensemble $\hat{z}$ at the top of the mixed layer and $\alpha(z_B+)$ is the thermodynamic property of the environment at the level "immediately" above the top of the the mixed layer, assuming that an infinitesimally thin transition layer is above

the top of the the mixed layer (see Fig. 2.1). Referring to Fig. 3.4, the value of α at z_B+ is the one interpolated from levels 1 and 2. On the other hand, the value of α at z_B is the same as the one for level 1. This treatment of the cumulus downdraft fluxes at the top of the mixed layer is essentially the same as Johnson's (1976).

Applying (4.46) to the moist static energy (h), we have:

$$(\overline{\rho w'h'})_B = \int_{z_B}^{\hat{z}_{max}} m_0(\hat{z}')\eta_d(z_B,\hat{z}')(h_{cd}(z_B,\hat{z}') - h(z_B+))d\hat{z}' \qquad (4.47)$$

Now, referring back to (3.23), we can express $(\frac{\partial h_M}{\partial t})_{cd}$ by:

$$(\frac{\partial h_M}{\partial t})_{cd} = \frac{1}{\rho_M \Delta z} \int_{z_B}^{\hat{z}_{max}} m_0(\hat{z}')\eta_d(z_B,\hat{z}')(h_{cd}(z_B,\hat{z}') \qquad (4.48)$$

$$- \overline{h}(z_B+))d z'$$

With the uses of (4.48) and (3.19), the last term in (3.23) can be expressed as:

$$(\frac{\partial h_M}{\partial t})_{cd} \int_{z_B}^{\hat{z}} \rho(z)\beta(z)dz = \int_{z_B}^{\hat{z}_{max}} K_M(\hat{z},\hat{z}')m_B(\hat{z}')d\hat{z}' \qquad (4.49)$$

where

$$K_M(\hat{z}, \hat{z}') = - \frac{\epsilon}{\rho_{Mp\Delta z}} n_d(z_B, \hat{z}')(h_{cd}(z_B, \hat{z}') - \bar{h}(z_B+))$$

$$\cdot \int_{z_B}^{\hat{z}} \rho(z)\beta(z)dz \qquad (4.50)$$

Namely, we have introduced an extra kernel K_M into (3.23), which arises due to the presence of the downdrafts.

To determine the evaporation rate of falling precipitation in the sub-cloud layer (e_M) in (4.28) and (4.29), we simply take the interpolated value of e_d (see Eqs. (3.13c) and (3.14c)) from level 1 (see Fig. A.3) and the surface, where we assume that e_d vanishes.

4.3 Model design:

4.3.1 Model structure and finite difference schemes:

As shown in Fig. 4.1, this model has a horizontal domain of 1600 km, with 600 km of fine grids at the center part of the domain with a grid spacing of 20 km. On each side of the fine-grid area, there is an environmental area with 10 grid points stretched by a ratio of 1.2 to the preceding grid size. 17 grid points are located in the vertical z-coordinates with an even grid spacing of 900 m such that the top of the domain is at the level of 14.4 km, which is around 140 mb in p-coordinates. The mixed layer parameterization described in Section 4.2 is applied to the first layer of the model such that the cloud base height is fixed at 900 m. Since the convective system under investigation is
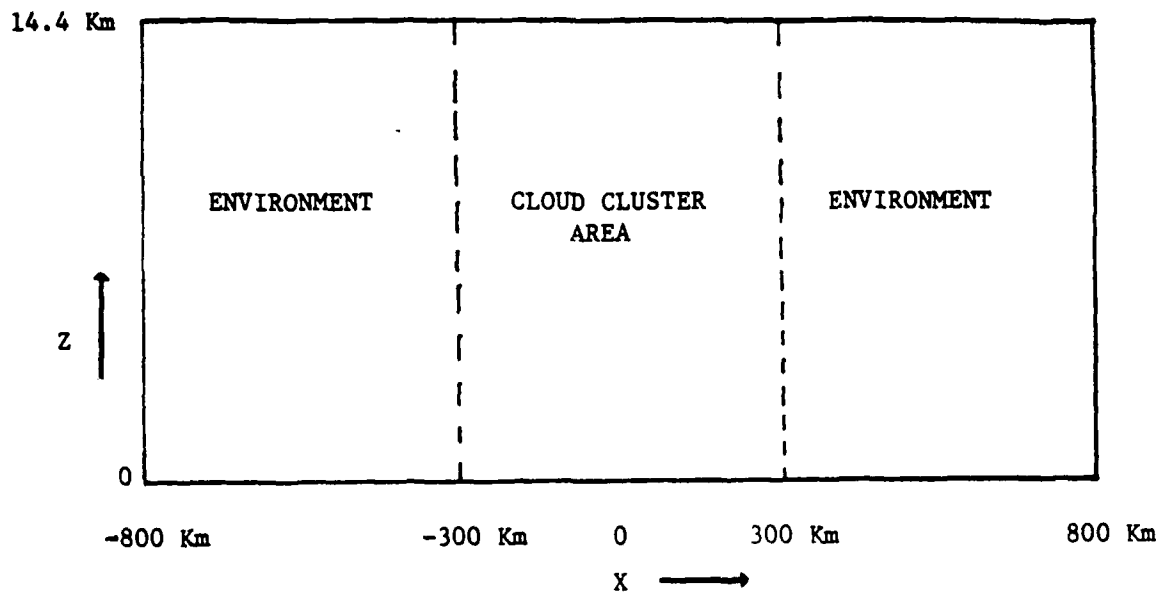
Fig. 4.1 The schematic diagram of model design.

in the form of a line structure, as shown in Fig. 3.5, the x-coordinates in the model are chosen in the direction normal to the cloud band with the positive x direction toward the NNW (Soong and Tao, 1980).

A leapfrog time integration and a second-order centered space difference are applied with a staggered grid arrangement, shown in Fig. 4.2. The finite difference equations corresponding to (4.9) and (4.17) through (4.20) are given in Appendix C. A time-smoothing scheme formulated by Robert (1966) is adopted in the integration to avoid the time splitting. The scheme is of the form:

$$u^{*n+1} = u^{n-1} + F^n \, 2\Delta t \tag{4.51a}$$

$$u^n = u^{*n} + \sigma(u^{*n+1} - 2u^{*n} + u^{n-1}) \tag{4.51b}$$

where superscript n denotes the time step, * denotes the unsmoothed value, F represents all the terms on the right hand side of the prognostic equation, and σ is the smoothing coefficient. A value of 0.1 is used for σ. The model also includes a horizontal fourth-order numerical smoother (Klemp and Wilhelmson, 1978; Bradley, 1985) which is applied to all of the prognostic fields. The smoother is of the form:

$$- \mu(\phi_{i+2} + \phi_{i-2} - 4(\phi_{i+1} + \phi_{i-1}) + 6\phi_i) \tag{4.52}$$

where the coefficient μ is 0.035. This horizontal smoother reduces the growth of nonlinear instabilities and filters out very short waves. The use of this fourth-order smoother makes the damping effects very selective by attenuating the short waves very effectively but leaving the longer waves almost unchanged.
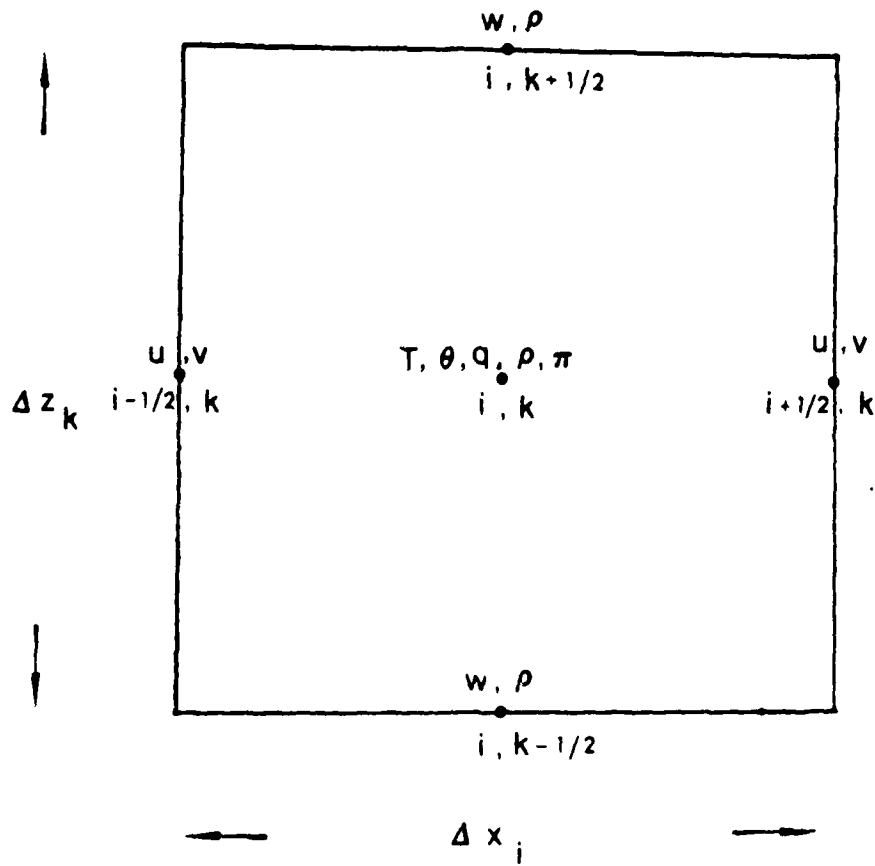
Fig. 4.2 The arrangement of model variables.

We apply a second-order smoother to those grid points adjacent to the lateral boundaries. In this model, no vertical smoothing is included. In addition to satisfying the Courant-Friedrichs-Levy (CFL) condition, the determination of the time step (Δt) in this kind of primitive mesoscale model requires caution, because of the behavior of gravity waves associated with the hydrostatic assumption (Tapp and White, 1976). In a non-hydrostatic atmosphere, the frequency of gravity waves is bounded by the Brunt-Väisälä frequency N. However, in a hydrostatic atmosphere, the frequency of the gravity waves goes to infinity as the wave number increases. Thus, all of the gravity waves with frequencies larger than N in a hydrostatic atmosphere should be regarded as high-frequency spurious waves that can introduce numerical instability if the choice of Δt is too large. Through the "local instability" analysis, the CFL condition for this model is:

$$\Delta t < \frac{1}{|\frac{u}{\Delta x}| + |\frac{w}{\Delta z}|} \tag{4.53}$$

From (4.53), the magnitude of Δt can be as large as 10^3 seconds. However, for the reason stated above, we choose Δt to be 90 seconds for the model integration.

4.3.2 Boundary and initial conditions:

Fixed upper and lower boundary conditions are applied for w, while zero-gradient lateral boundary conditions are applied for θ and q and open lateral boundary conditions for u and v:

$$w = 0 \qquad\qquad \text{at } z = 0, z_T \qquad\qquad (4.54)$$

$$
\left\{
\begin{aligned}
\frac{\partial u}{\partial t} &= -c_g \frac{\partial u}{\partial x} \\[2ex]
\frac{\partial v}{\partial t} &= -c_g \frac{\partial v}{\partial x} \qquad\qquad \text{at } x = -\ell, \ell \qquad\qquad (4.55) \\[2ex]
\frac{\partial \theta}{\partial x} &= \frac{\partial q}{\partial x} = 0
\end{aligned}
\right.
$$

where z_T represents the top of the domain, $-\ell$ and ℓ represent the left and right boundaries, respectively, and c_g represents a gravity-wave speed. A value of 10 m s^{-1} for c_g is used.

The soundings (shown in Fig. 4.3) taken from the ship Researcher at 00 GMT 12 August 1974 are used for the background initial conditions for θ and q. Fig. 4.4 shows the low-level vertical velocity at 00 GMT 12 August 1974 computed from the wind data over the GATE A/B array. It is seen that the maximum magnitude is about 1.7 cm s^{-1} around 850 mb. We double the magnitudes shown in Fig. 4.4 and multiply them by a sinusoidal function with the value of unity at the center of the domain and zero at the boundaries of the fine-grid area (see Fig. 4.1) to obtain the imposed vertical velocity $w_0(x,z)$ included in (4.17) to (4.20). The corresponding $u_0(x,z)$ is calculated from the continuity equation with the specification of $u_0 = 0$ at the center line of the model domain. This $[w_0, u_0]$ will be constantly imposed on the model as a time-independent, large-scale forcing. Fig. 4.5, adapted from Ogura et al. (1979), shows the surface wind and divergence calculated at the initial stage of the
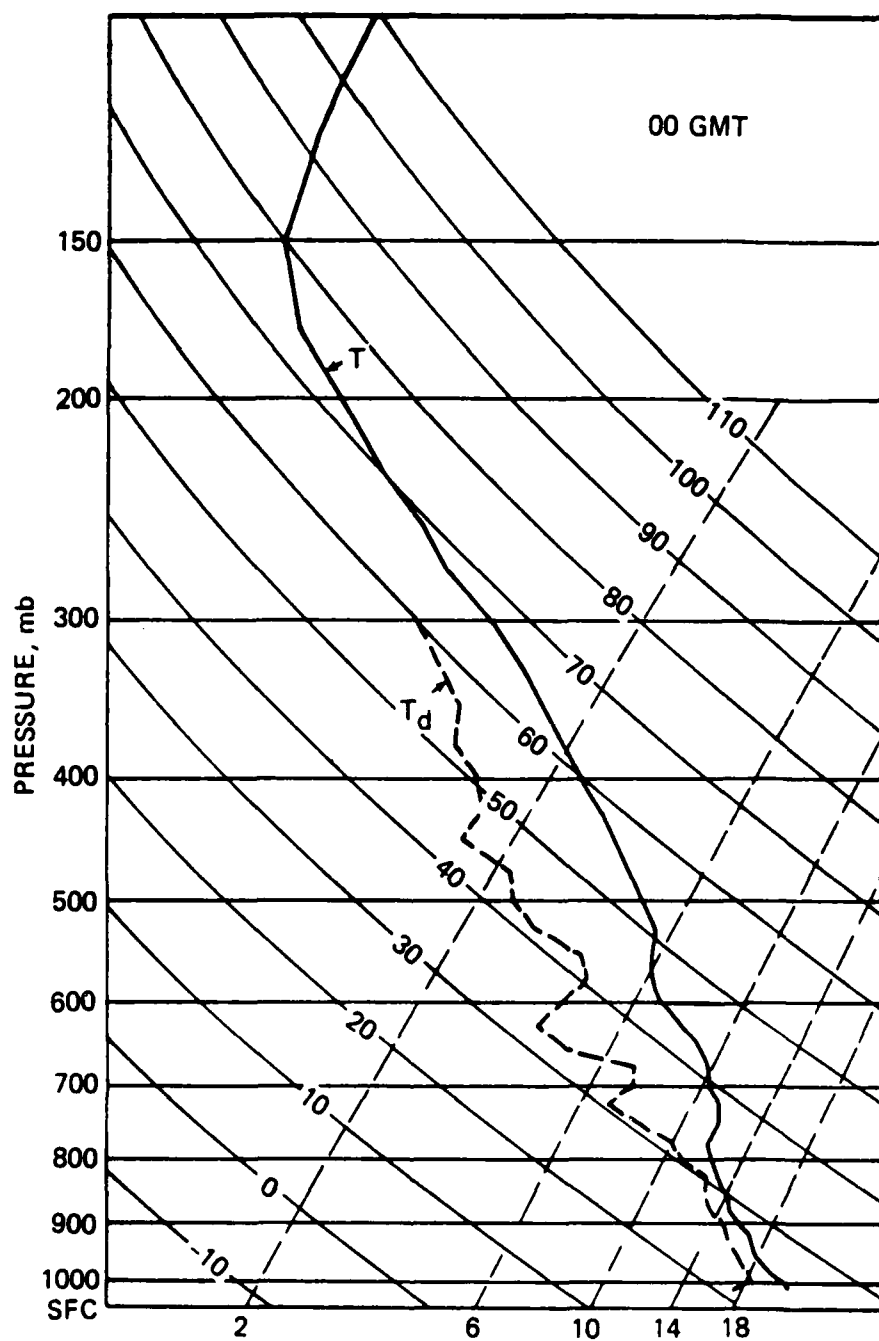
Fig. 4.3. The atmospheric soundings taken from the ship Researcher at
0000 GMT 12 August 1974.
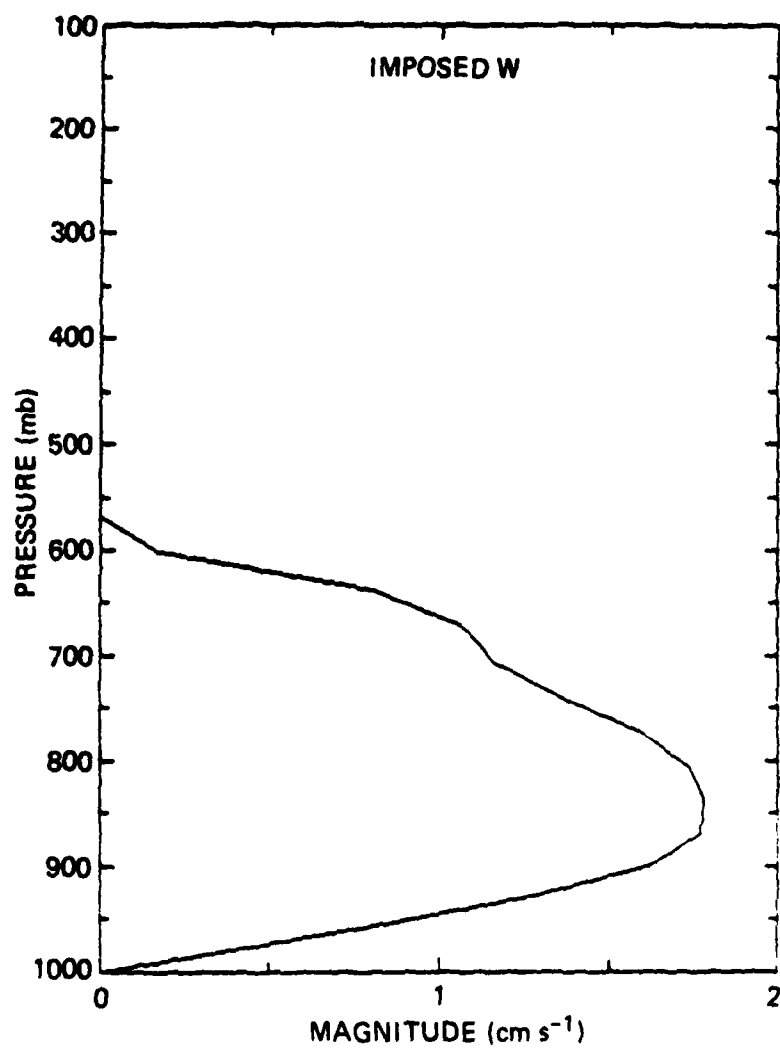
Fig. 4.4. The computed low-level vertical velocity at 0000 GMT 12 August 1974 at the ship Researcher.
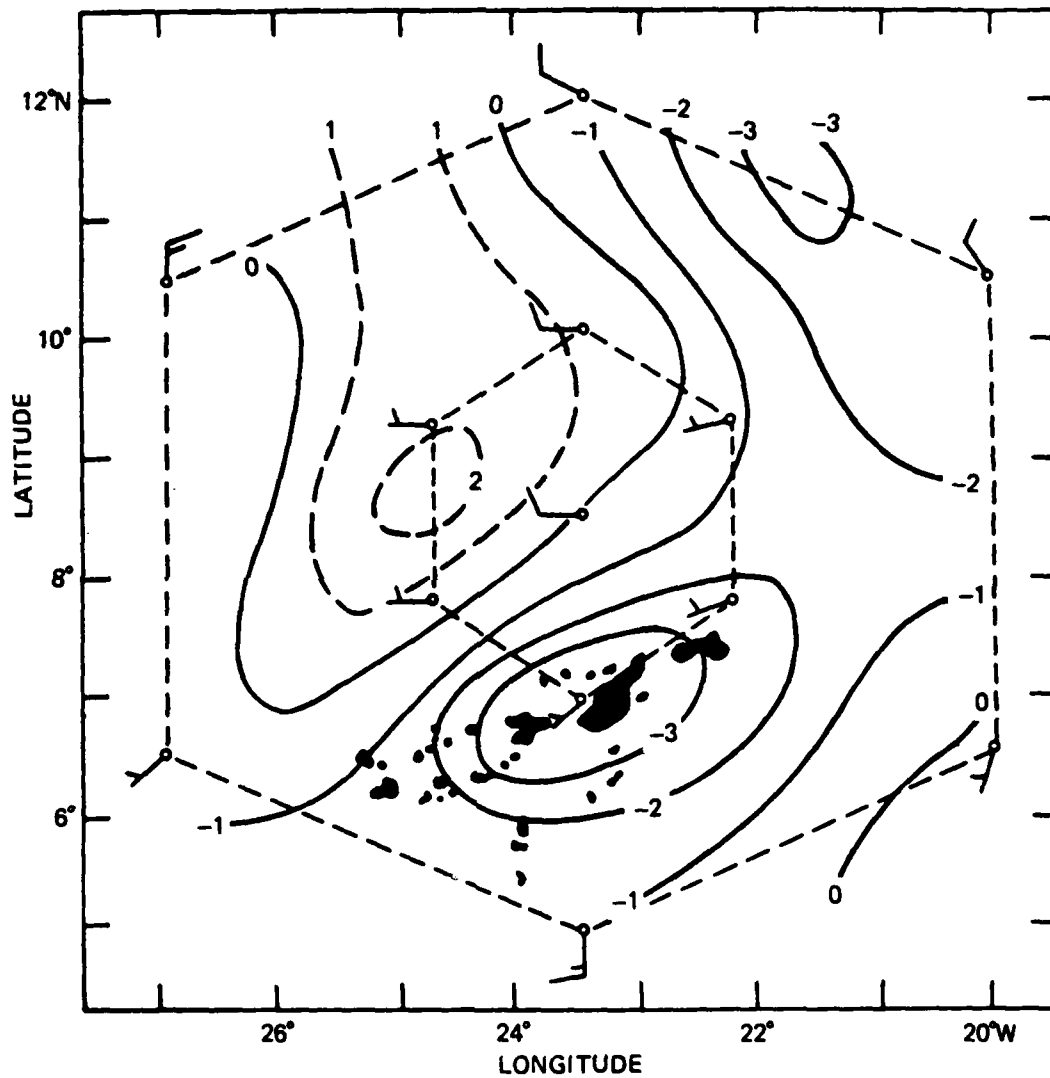
Fig. 4.5. The surface wind and divergence (in the units of 10^{-5} s^{-1}) along with radar echoes observed at 0000 GMT 12 August 1974. The outer hexagon indicates the GATE A/B scale ship array and the inner hexagon indicates B scale ship array. The full barb for wind is 5 m s^{-1} (Adapted from Ogura et al., 1979).

cloud band. It is evident that convective cells started developing in the area of the maximum surface convergence. Almost symmetric decreases of surface convergence are present on both sides of the cloud band. This indicates that our imposed circulation $[w_0, u_0]$ described above is fairly justifiable. The data analysis also shows that a 700 mb easterly wave was passing through the area during the period considered and that the A/B array was in category 3 when the development of the cloud band occurred. This implies that the large-scale, low-level lifting mechanism is associated with the passage of the easterly wave.

4.3.3 Computational procedure:

A computational cycle is outlined as follows:

(i) Compute the advection and Coriolis terms in momentum equations (4.17) and (4.18).

(ii) Compute the advection terms in thermodynamic and moisture equations (4.19) and (4.20).

(iii) Use the A-S scheme to compute the cloud effects. Since using the A-S scheme requires considerable computing time, the subroutine for the A-S scheme is called every 15 time steps. The values of the cloud effects within each 15 time steps are the ones calculated at the latest call of the A-S scheme. Once the cloud effects in (4.21) and (4.22) are determined, we can obtain θ and q for the next time step.

(iv) Use the boundary condition (4.54) and the mass continuity equation (4.9) to obtain the relation

$$\int_0^{z_T} \rho \, \frac{\partial u}{\partial t} \, dz = 0 \qquad\qquad (4.56)$$

Then, inserting (4.17) into (4.56) and using the hydrostatic equation (4.13), we can diagnostically determine $\frac{\partial \pi'}{\partial x}$.

(v) Use $\frac{\partial \pi'}{\partial x}$ obtained from (iv) and the values obtained from (i) to advance u and v for the next time step.

(vi) Apply the horizontal smoother to θ, q, u, and v.

(vii) Use u calculated from (vi) and the continuity equation to determine w for the next time step.

CHAPTER V

MODEL RESULTS OF MESOSCALE SIMULATION

In this chapter, the results of the response of the tropical mesoscale cloud band to the large-scale low-level lifting process through the applications of the A-S scheme are illustrated in terms of the following "circulation descriptors" defined by Kreitzberg and Perkey (1977): (i) the intensity of the mesoscale vertical motion, (ii) the time scale of the development of the mesoscale circulation, (iii) the time scale of the decay of the mesoscale circulation, (iv) the amount of surface precipitation, and (v) the horizontal width scale of the cloud band and its associated precipitation area. For verification purposes, the model results will be compared with the observed values deduced from data analysis. Furthermore, a detailed examination of the heating profiles under different mesoscale environmental conditions (primarily vertical velocity profiles) will be made to investigate the roles played by the convective heating, as represented by the A-S scheme, in the evolution of the mesoscale circulation.

Based on the model characteristics described in Chapter 4, the results of 5 runs are presented in this chapter. Run 1, which is hereafter referred to as the control run, excludes the initial horizontal wind (u_g) (see Eq. (4.2)) and the cumulus downdraft effects in the A-S scheme. The results of a 24-hour integration for the control run are discussed in Section 5.1. The other 4 sensitivity test runs are presented in Section 5.2. Note that only one factor

is changed in each subsequent run. In run 2, we performed an experiment by deleting the large-scale low-level, forcing $[w_0, u_0]$ at the time when the mesoscale circulation reaches its peak intensity in the control run. This experiment would reveal whether or not a well-defined mesoscale circulation can sustain itself for a considerable period of time without the large-scale, low-level lifting process. Run 3 presents an experiment with the inclusion of the initial sheared horizontal wind (u_g) since, based on various observational and simulation studies, the vertical wind shear has been considered very important to the development and movement of the mesoscale convective system. Run 4 presents an experiment with the inclusion of the cumulus downdraft effects into the A-S scheme. Emphasis here will be placed on the feedback mechanism between the cloud layer and the mixed layer due to the detrainment of the downdrafts. Finally, in run 5 we replaced the A-S scheme by Kuo's 1974 scheme for comparison purposes.

5.1 The control simulation:

5.1.1 Results of an early simulation:

The initial conditions shown in Fig. 4.3 are conditionally unstable except for a stable layer around 700 mb. There is no initial motion field except for the externally-imposed, time-independent, large-scale, low-level circulation $[u_0, w_0]$, as described in Section 4.3.2. The w_0 field is shown in Fig. 5.1. Since the model is symmetric about the center axis of the domain (see Fig. 4.1), hereafter all of the model results are presented only in the right half of the domain except for the run with vertical wind shear.
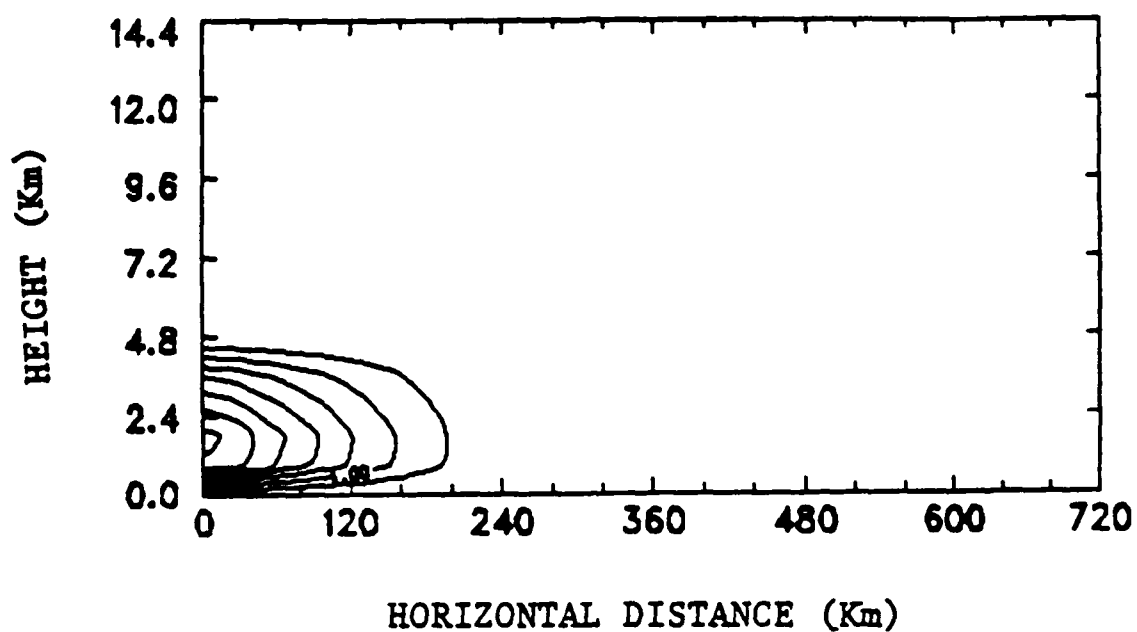
Fig. 5.1. Cross section of the imposed vertical velocity w_0 in units in cm s^{-1}. The contour interval is 0.5.

The mesoscale fields will evolve from the above initial conditions due to the horizontally-differential convective heating rates resulting from the applications of the A-S scheme. Fig. 5.2a shows the convective heating rates at 1 hr. Note that since the cloud base height is set at 900 m, no convective heating is observed below that level. It is clearly seen that significant convective heating concentrates in the central portion of the domain with a horizontally well-defined differential distribution because of the distribution of w_0, as shown in Fig. 5.1. Fig. 5.2b shows the model-predicted vertical velocity field (w) at 1 hr. Obviously, the concentration of w in the center part of the domain is due to the distribution of convective heating shown in Fig. 5.2a. The maximum of w is about 2 cm s^{-1} and occurs at the center and around 6 km in height. A broad area of weak downward motion is present away from the center. The deviation of the potential temperature (θ') from the initial state is shown in Fig. 5.2c. The maxima of positive anomalies located at 5 and 10 km in height at the center columns are obviously due to the strong convective heating. Negative anomalies are found at the low levels around the center because of the imposed w_0, which results in relatively stronger adiabatic cooling than the convective heating derived from the A-S scheme for the low levels. On the other hand, the weak positive anomalies between 120 and 200 km are caused by the adiabatic warming due to the downward motion. The temperature distributions shown in Fig. 5.2c are expected to generate a low-level mesolow around the central portion of the domain and to cause a circulation with the patterns of w and u, as shown in Figs. 5.2b and 5.3a, respectively. The fields of the ageostrophic wind (v_{ag}) defined by:
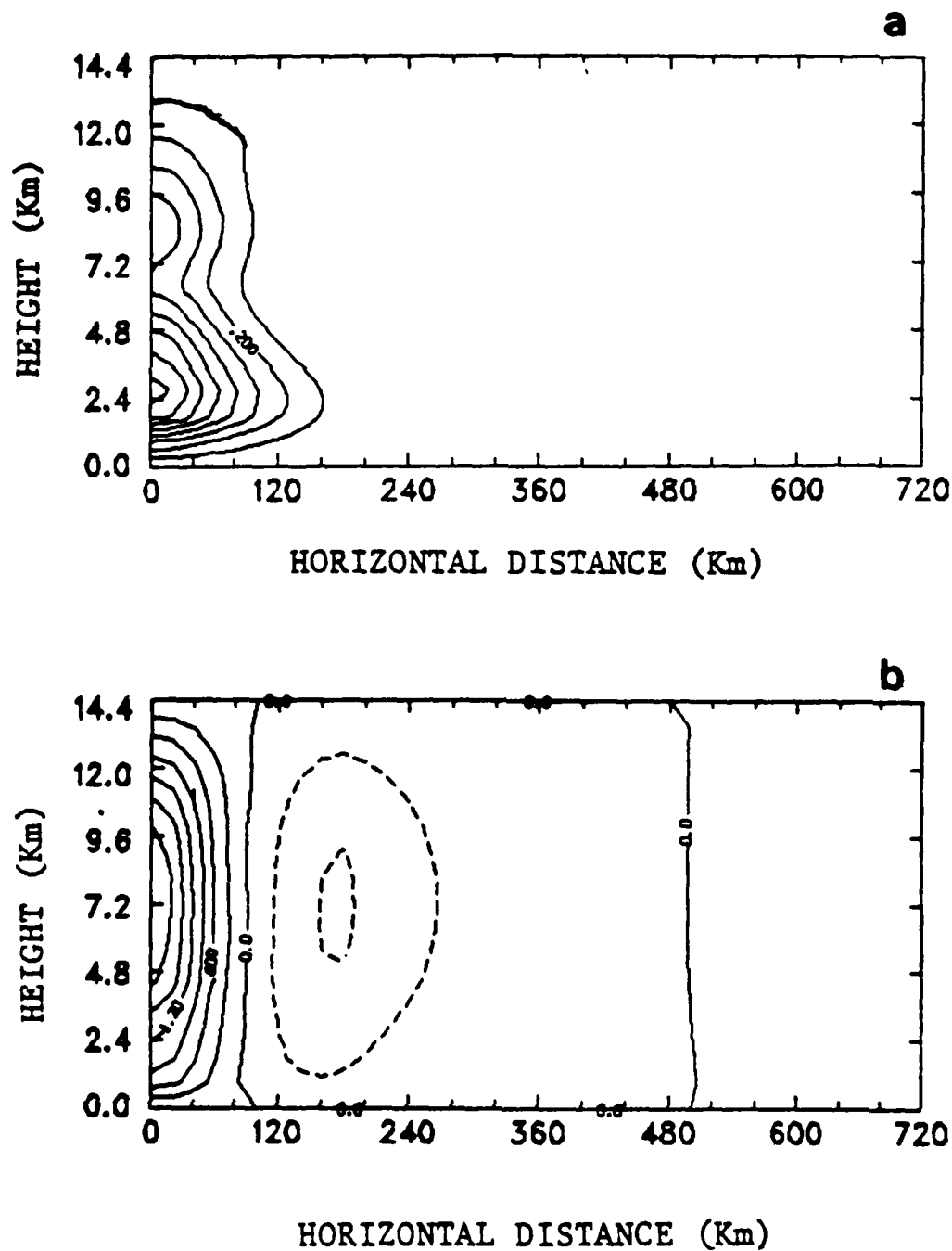
Fig. 5.2. Cross sections of simulation of the control run at 1 hr: (a) convective heating rate in units of K hr^{-1} with contour interval of 0.1, (b) vertical velocity in units of cm s^{-1} with contour interval of 0.3, and (c) deviation of potential temperature (θ') from the initial condition in units of K with contour interval of 0.03.

HORIZONTAL DISTANCE (Km)
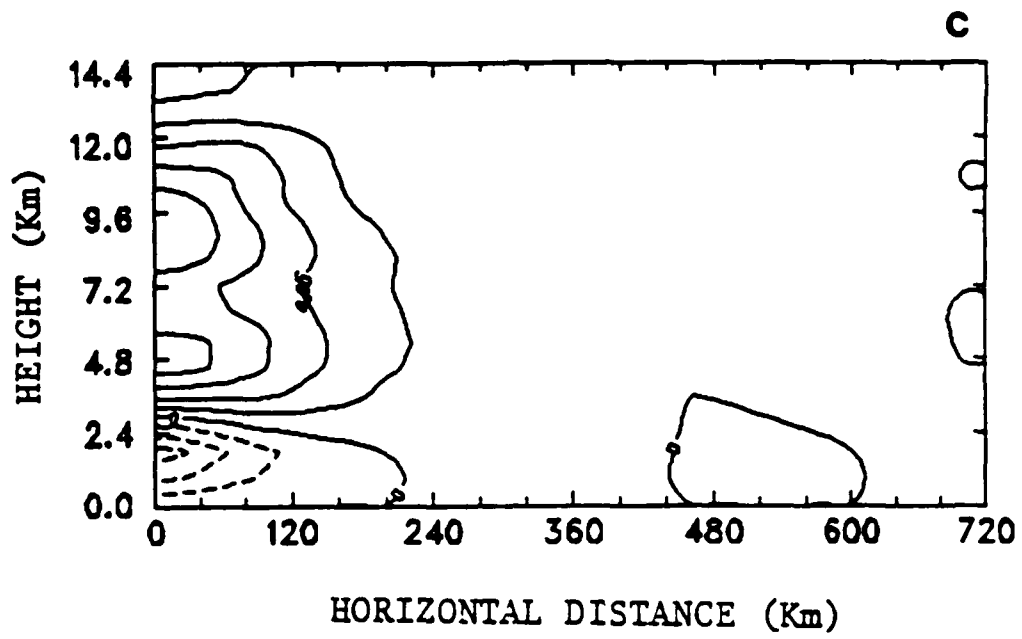
Fig. 5.2. (Continued)
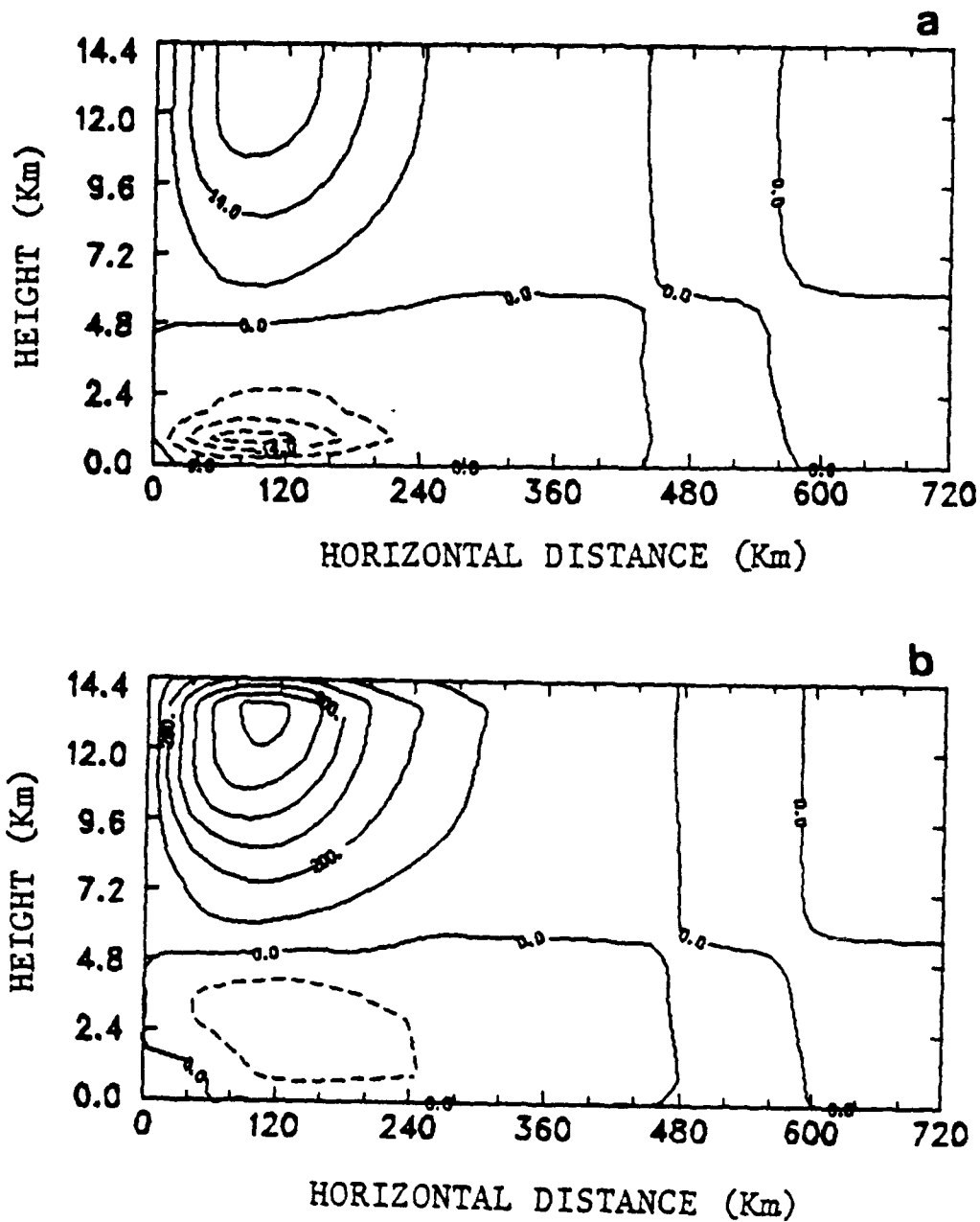
Fig. 5.3. Cross sections of simulation of the control run at 1 hr:
(a) x-component velocity in units of cm s^{-1} with contour interval of 7,
(b) y-component ageostrophic wind in units of cm s^{-1} with contour interval of
100, and (c) y-component velocity in units of cm s^{-1} with contour interval of
0.2.
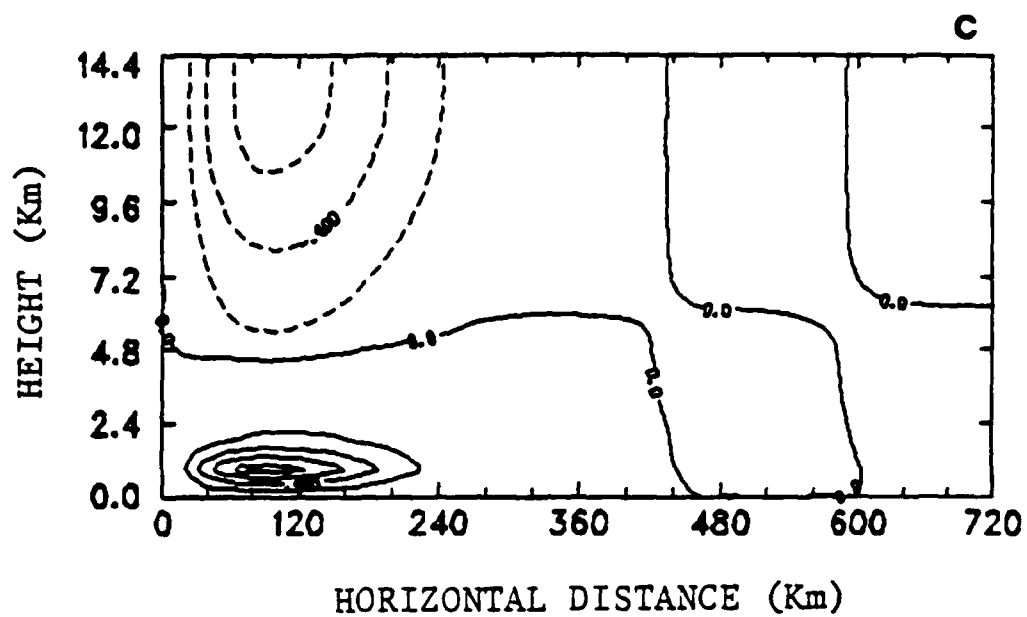
Fig. 5.3. (Continued)

$$v_{ag} = v - \frac{c_p \bar{\theta}}{f} \frac{\partial \pi'}{\partial x} \tag{5.1}$$

and the y-component velocity (v) are shown in Figs. 5.3b and 5.3c. Wherever v is sub-geostrophic ($v_{ag} < 0$), the air will accelerate to the left and cause convergence toward the center. Fig. 5.4a shows the cloud base mass fl x (m_B) distribution as a function of cloud top height and distance from the center at 1 hr. It is evident that the bimodal distributions with relatively weaker high clouds are present around the central columns, while only shallow clouds are present in the outer part of the domain. The corresponding cloud mass flux (M_c) is shown in Fig. 5.4b. The total mass flux ($\bar{M}$) is now defined by:

$$\bar{M} = \rho(w + w_0) \tag{5.2}$$

and shown in Fig. 5.4c. It is again found that the magnitudes of M_c and $\bar{M}$ are very close to each other, as indicated in the semi-prognostic studies.

The results of the early simulation at 1 hr have been discussed in the preceding paragraph. Since all of the fields evolving from the initial conditions are driven by the horizontally differential convective heating, which is computed from the A-S scheme, it is important to know how the A-S scheme responds to the imposed large-scale, low-level forcing at the very beginning. Fig. 5.5 shows the profiles of the adiabatic cooling rate due to the imposed w_0 and the convective heating rate deduced from the A-S scheme for the central column. It can be seen that the adiabatic cooling ceases at 500 mb because w_0 vanishes above that level while the convective heating takes place
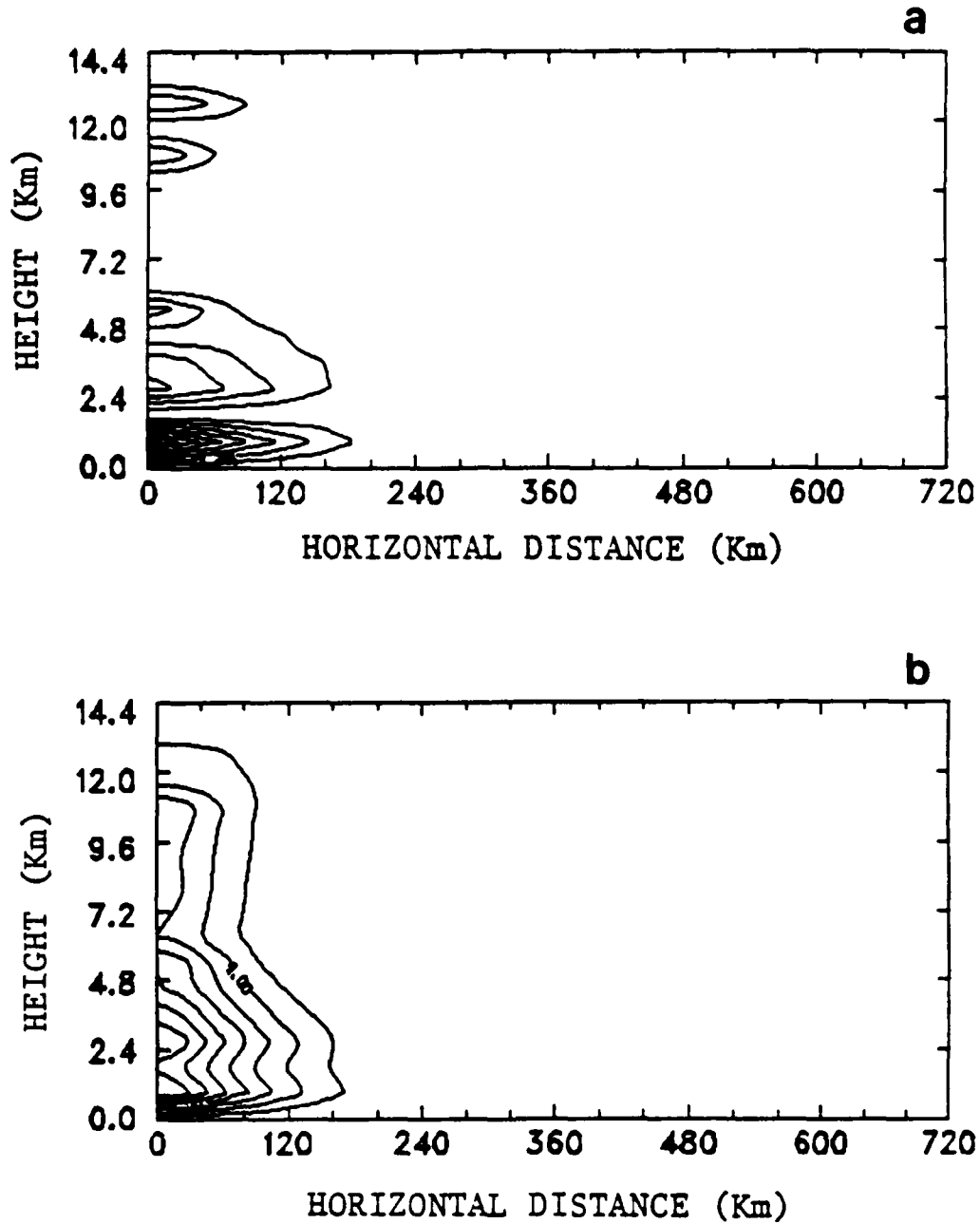
Fig. 5.4. Cross sections of simulation of the control run at 1 hr: (a) the cloud base mass flux (m_B) in units of mb hr^{-1} with the contour interval of 0.6, (b) the cloud mass flux (M_c) in units of mb hr^{-1} with the contour interval of 2.0, and (c) the total mass flux ($\bar{M}$) in units of mb hr^{-1} with contour interval of 2.0.
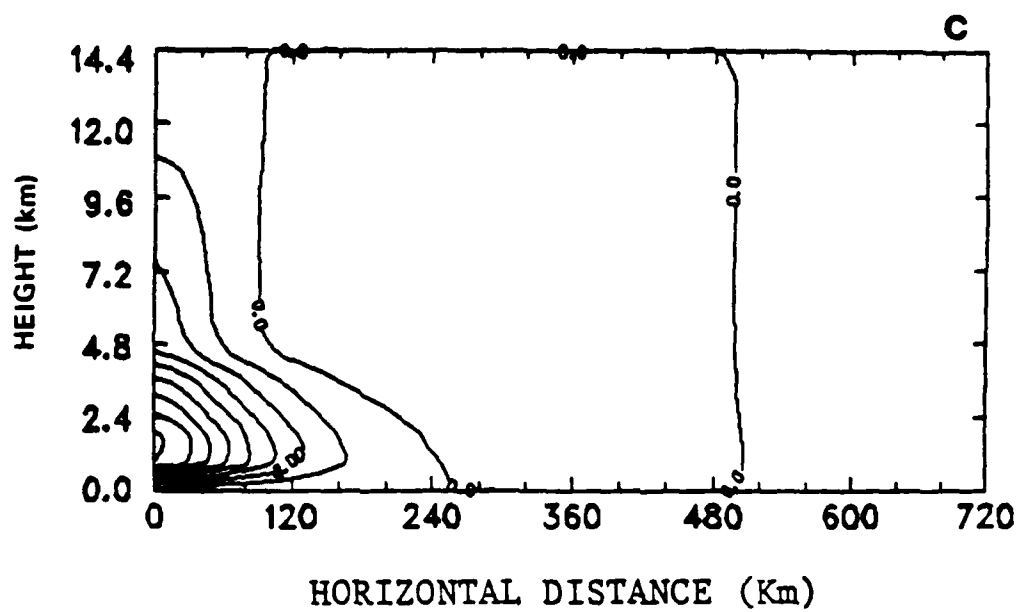
Fig. 5.4. (Continued)
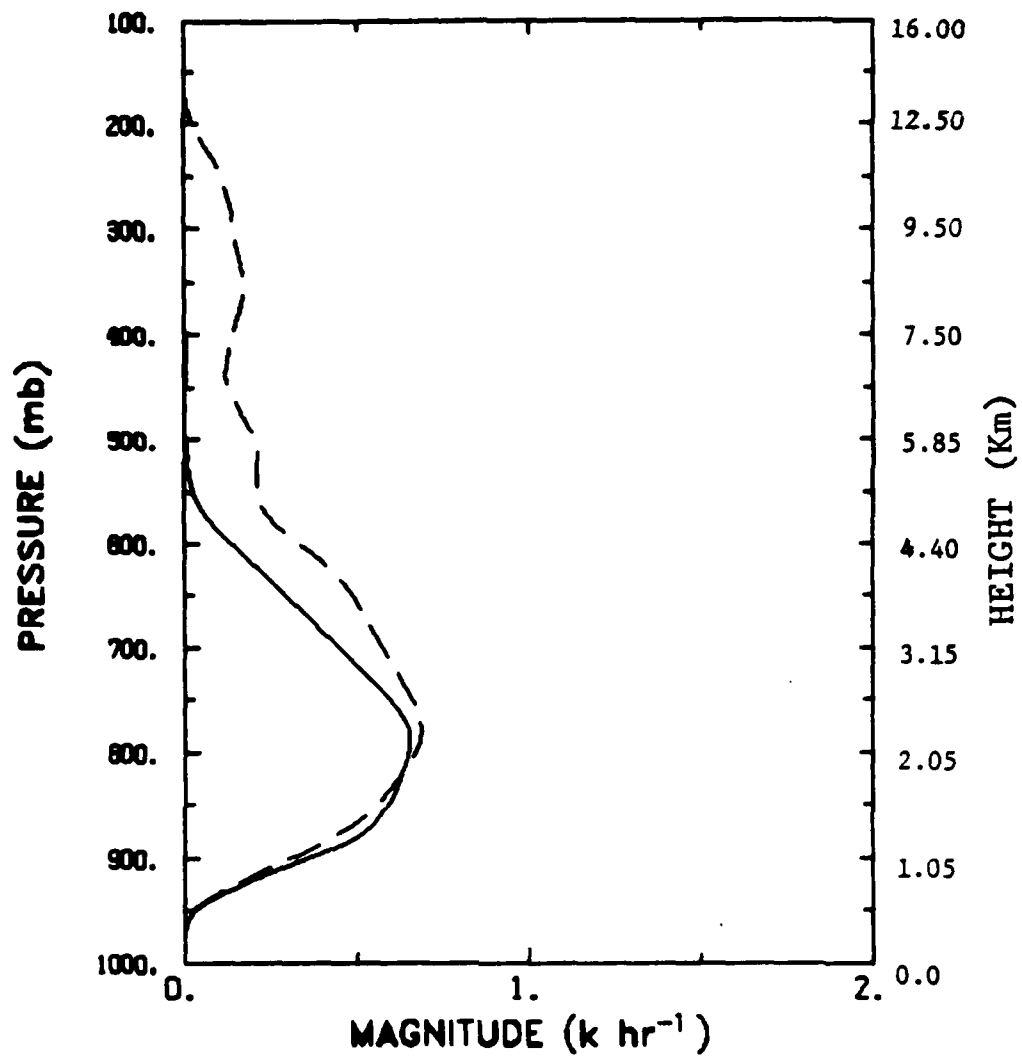
Fig. 5.5. Profiles of convective heating (dashed lines) in response to the imposed w_0 and adiabatic cooling (solid lines) due to the imposed w_0 in the control simulation.

from the cloud base up to 200 mb. The small differences between the two profiles from 825 mb to 200 mb introduce positive temperature tendencies and the small differences below 825 mb introduce negative tendencies. Meanwhile, the differences between the adiabatic cooling and convective heating rates gradually decrease outward from the center because of the distribution of w_0 so that a horizontal temperature gradient is generated. Note that, although the imposed low-level forcing is confined below 550 mb, high clouds are still present because the large-scale forcing for the clouds with cloud tops higher than 550 mb does exist (see 2.27)).

5.1.2 A 24-hour integration

Fig. 5.6 illustrates the evolution of the mesoscale circulation in the vector fields of [u, w]. The magnitudes of w have been enlarged by 10 times because of the scale difference between u and w, at 3, 9, and 17 hr, which can be respectively representative of developing, mature, and decaying stages based on their flow structures and intensity of vertical motion. The flow pattern, with inflows at low levels, upward motion at the central portion of the domain, and outflows at upper levels, is distinctly present in Figs. 5.6a and 5.6b. Fig. 5.7 shows the evolution of the vertical velocity at the different stages. It is seen that at 3 hr the magnitudes of w become much larger than those shown in Fig. 5.2b. However, the upward motion still concentrates around the center. Significant downward motion with magnitudes of about 2 to 3 cm s^{-1} is present beside the upward motion area. At 9 hr, the intensity of the upward motion reaches a magnitude of 17 cm s^{-1} and both the upward motion area and the significant downward motion area are more broad. At 17 hr, the system is
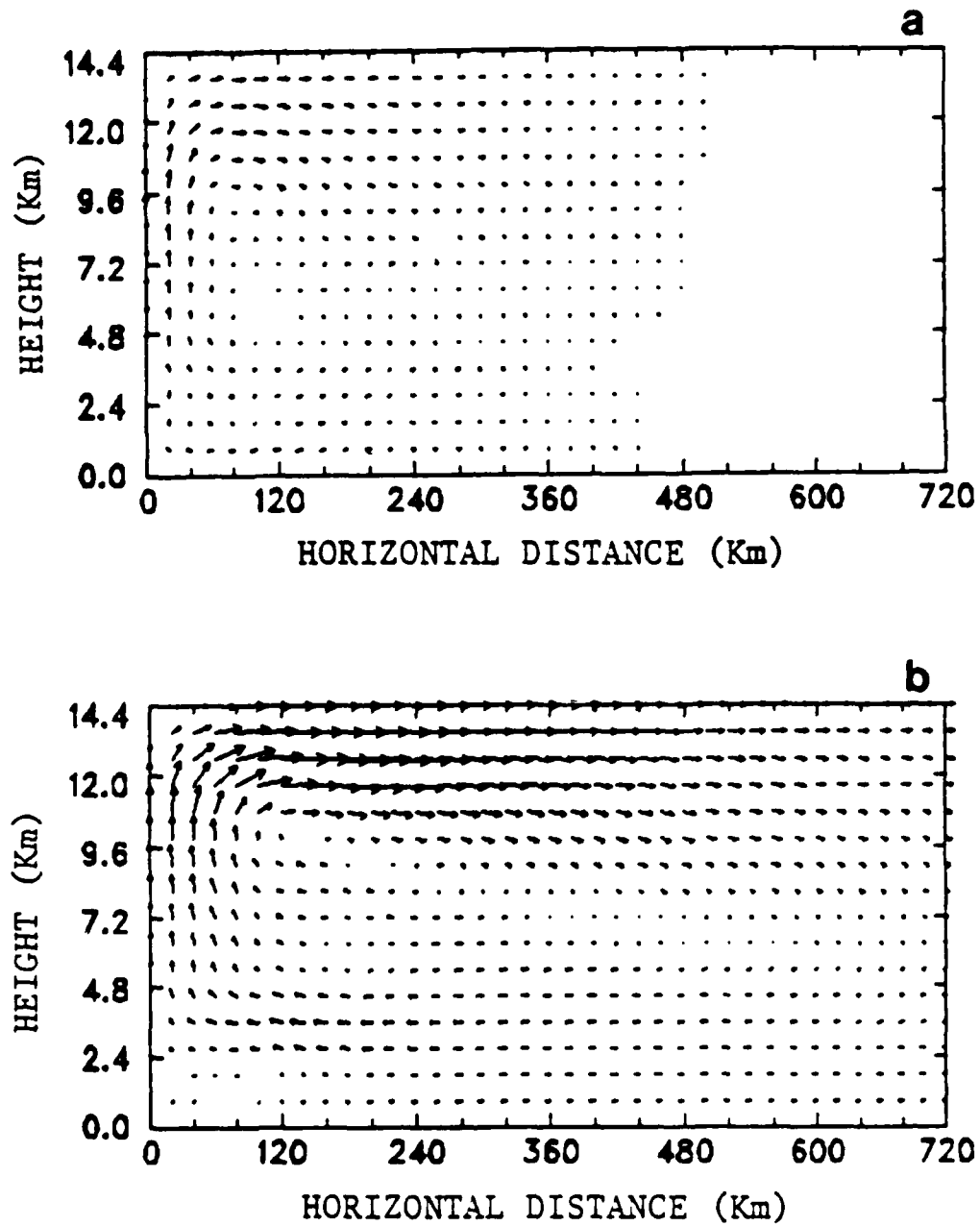
Fig. 5.6. Cross sections of vector field of [u,w] in the control run: (a) at 3 hr, (b) at 9 hr, and (c) at 17 hr. The magnitudes of w have been enlarged by 10 times.
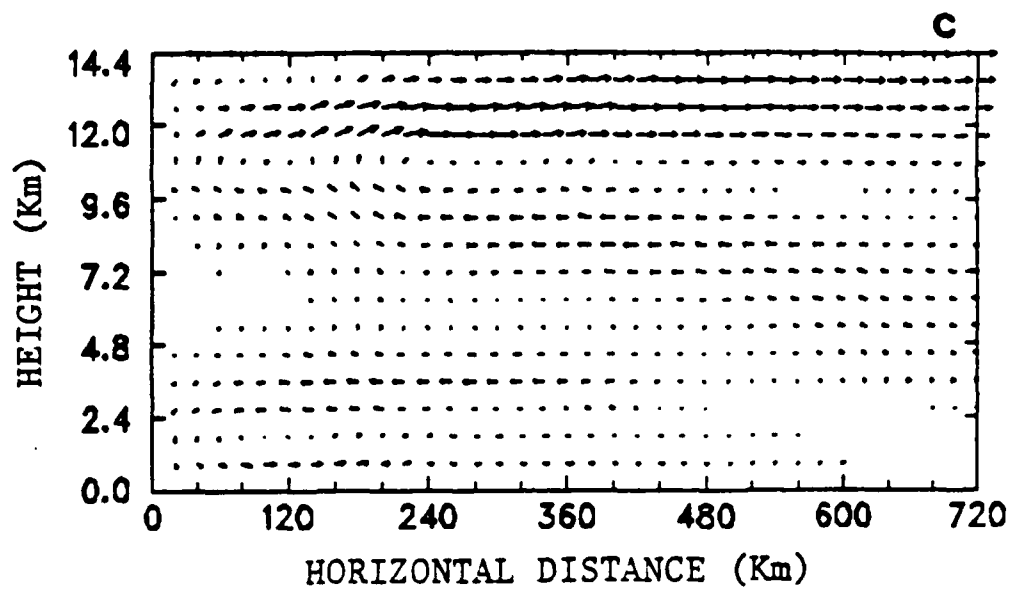
Fig. 5.6. (Continued)
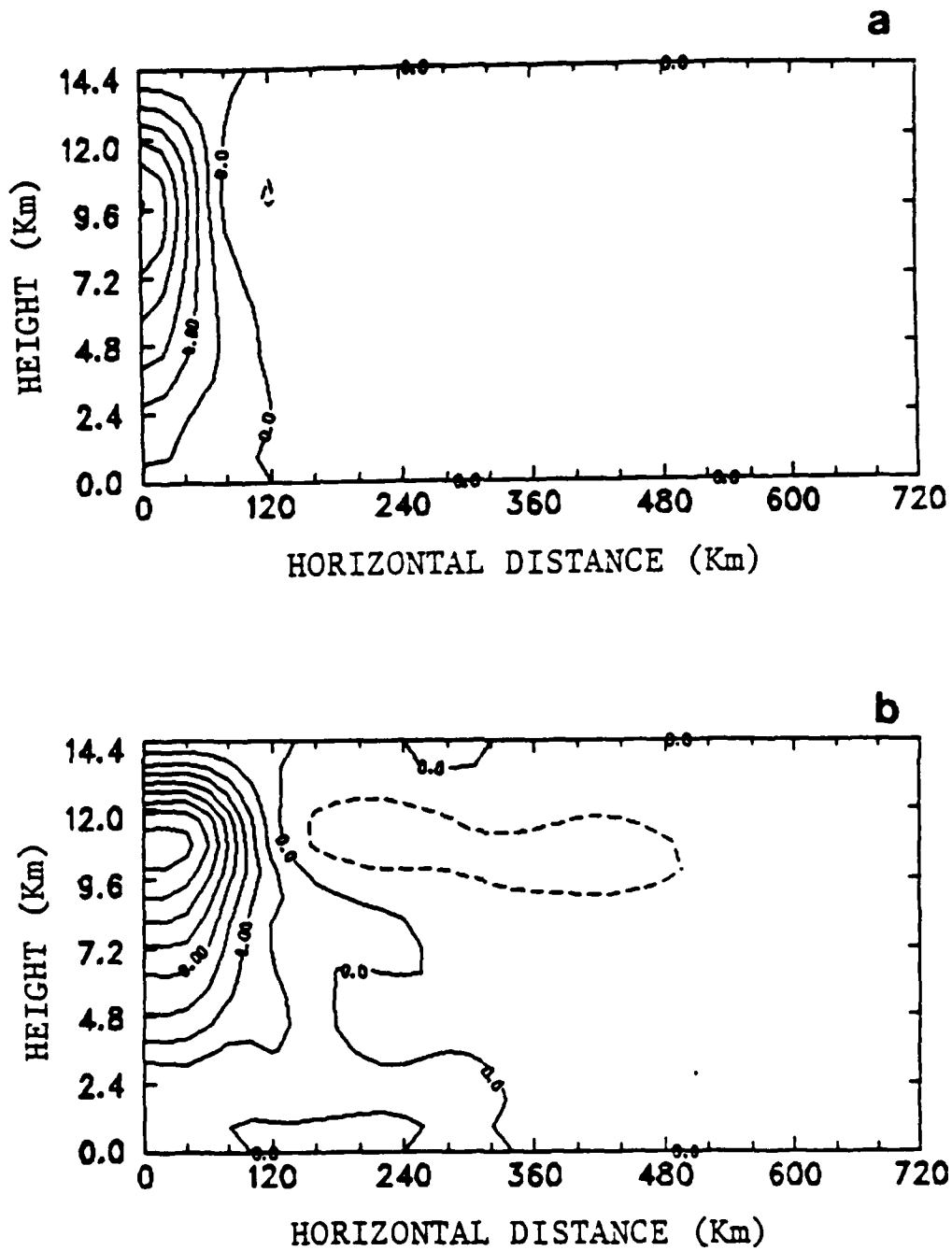
Fig. 5.7. Cross sections of vertical velocity (w) in units of cm s^{-1} in the control run: (a) at 3 hr with contour interval of 2.0, (b) at 9 hr with contour interval of 2.0, and (c) at 17 hr with contour interval of 1.0.

C

HORIZONTAL DISTANCE (Km)
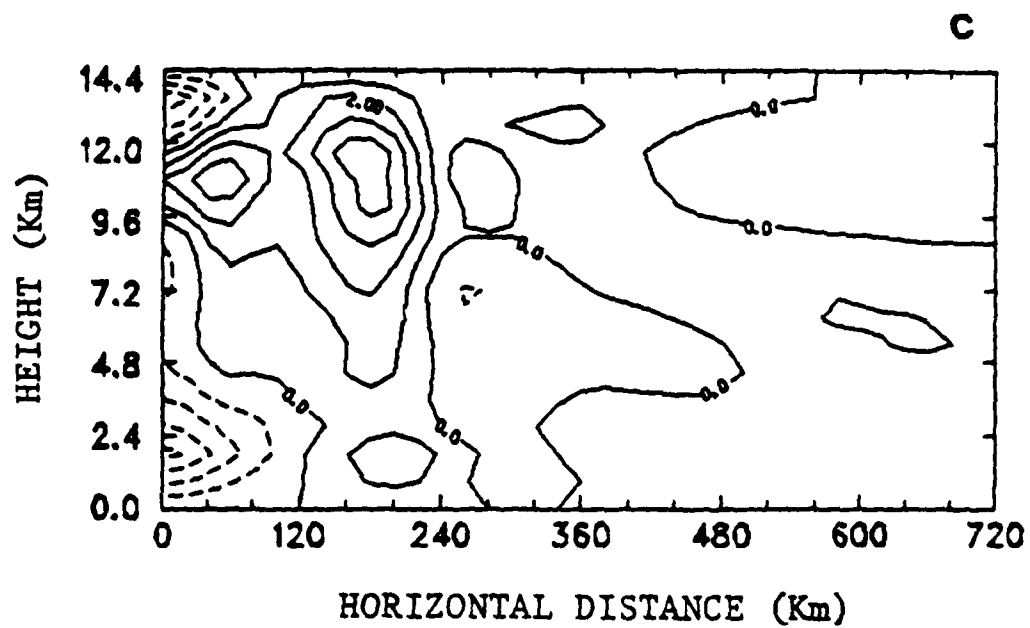
Fig. 5.7. (Continued)

obviously in its decaying stage with strong downward motion located at low levels around the center and weak upward motion at high levels away from the center. Note that all of the w fields presented in this chapter do not include the imposed w_0. The decaying situation is also indicated by Fig. 5.6c where a well-defined reverse circulation is present at the low levels. Fig. 5.8 shows the field of θ'. Examining the w field at 3 hr shown in Fig. 5.7a, it should be certain that the positive temperature anomalies at 3 hr in the area between 120 to 400 km are caused by the adiabatic warming due to the downward motion. It can be seen in Fig. 5.8b that after the 9-hour simulation the temperature increases about 1.9 K for the atmosphere at 11 km in height around the center. Meanwhile, the temperature decreases about 0.2 K for the atmosphere at low levels around the center. These features can be readily explained by Fig. 5.9a, which shows the profiles of the adiabatic cooling rate due to vertical and horizontal advection and the convective heating rate derived from the A-S scheme for the center column at 6 hr. As discussed earlier, the small difference between these two profiles is responsible for the temperature changes in the convective area. The double maximum distribution of the adiabatic cooling, shown in Fig. 5.9a, is due to the distribution of total vertical velocity $(w + w_0)$ shown in Fig. 5.9b. The lower maximum is apparently caused by the imposed low-level w_0. Generally speaking, the profile shown in Fig. 5.9b characterizes the situations of strong convection in the tropics.

The gradual accumulation of the adiabatic warming due to the downward motion, as noted above, results in a secondary maximum of the deviation of potential temperature about 300 km from the center and 11 km in height at 9 hr, as shown in Fig. 5.8b. Of great importance is that this secondary maximum of
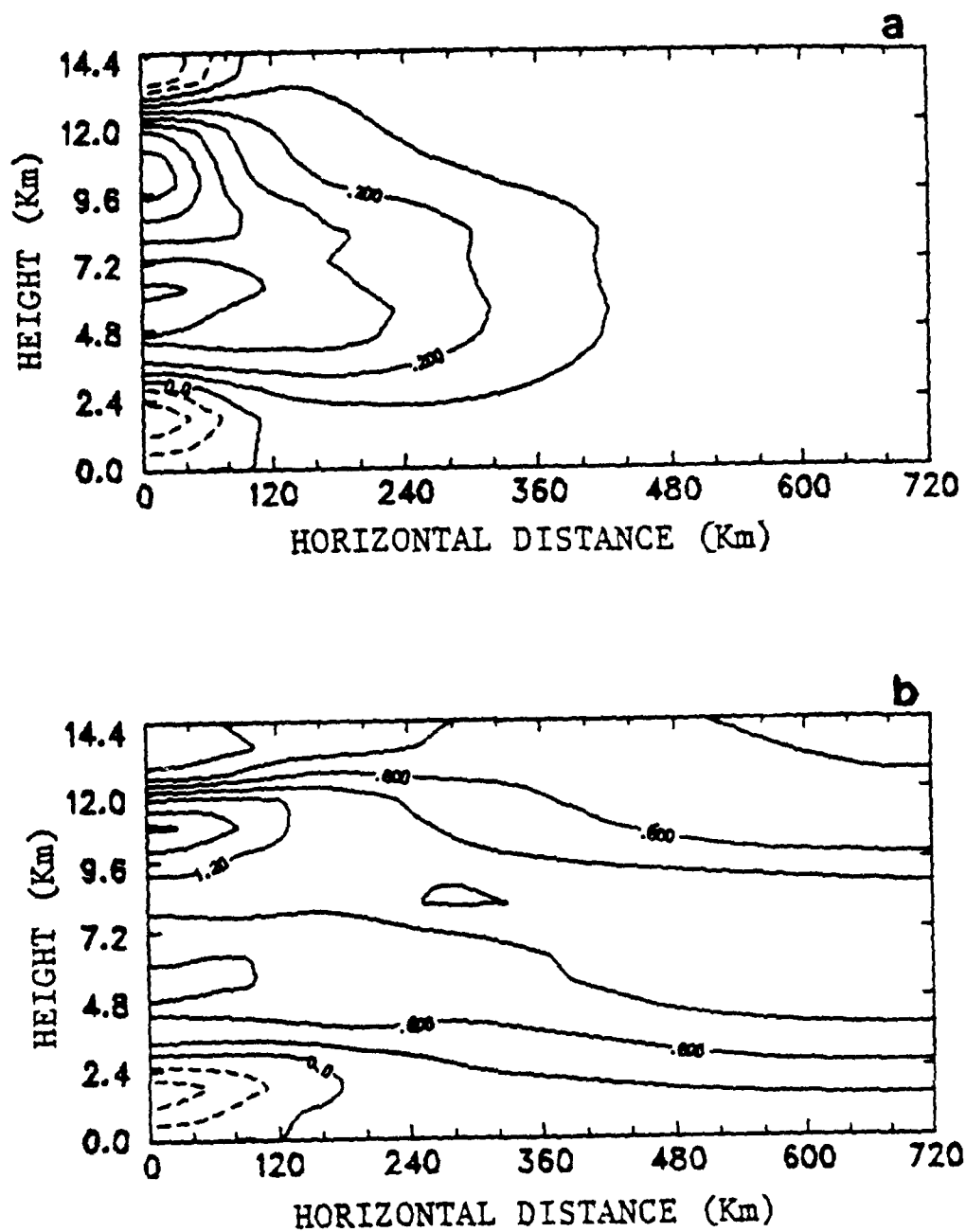
Fig. 5.8. Cross sections of the deviation of potential temperature (θ′) form the initial condition in units of K in the control run: (a) at 3 hr with contour interval of 0.1, (b) at 9 hr with conrour interval of 0.3, and (c) at 17 hr with contour interval of 0.3.
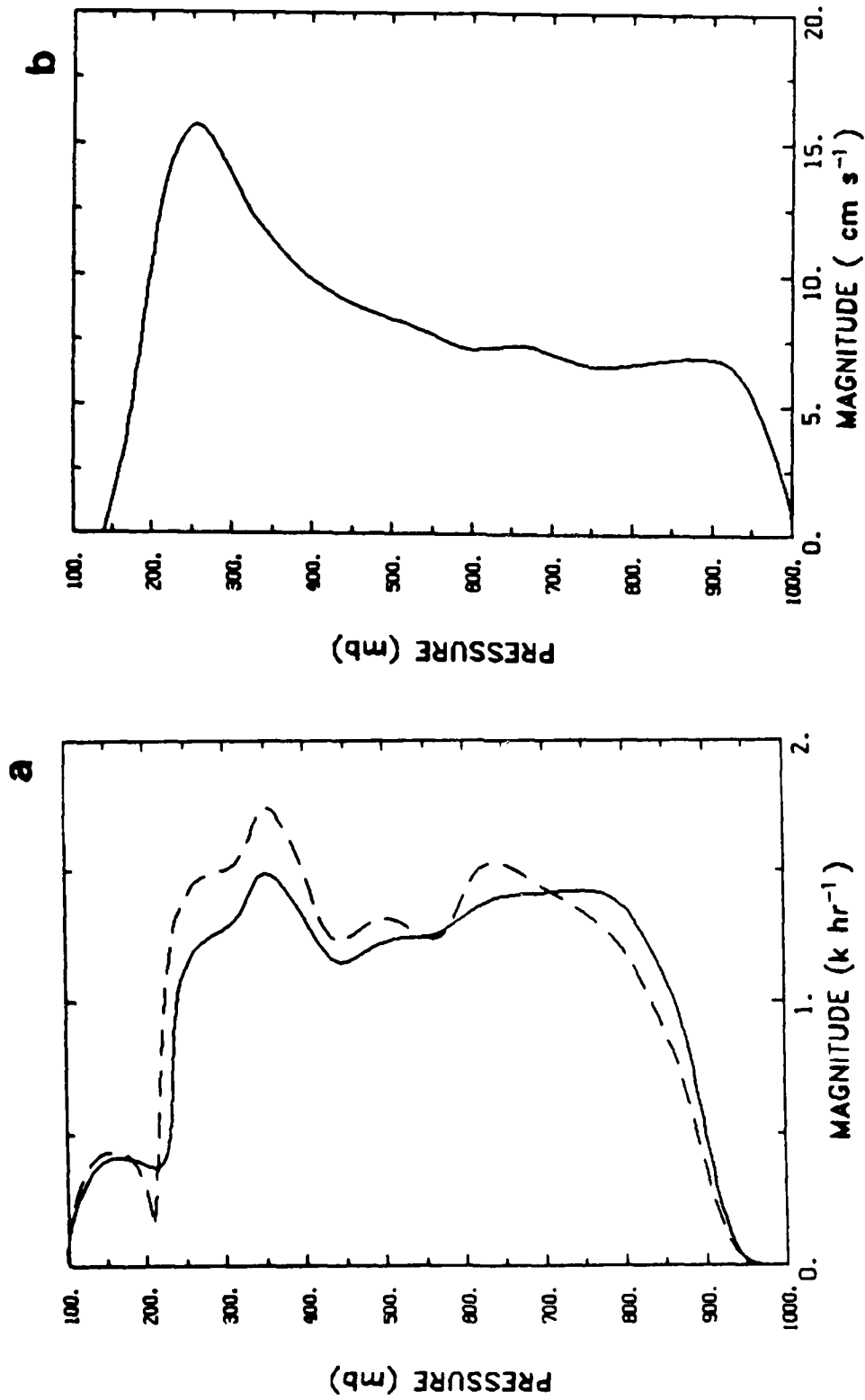
-128-
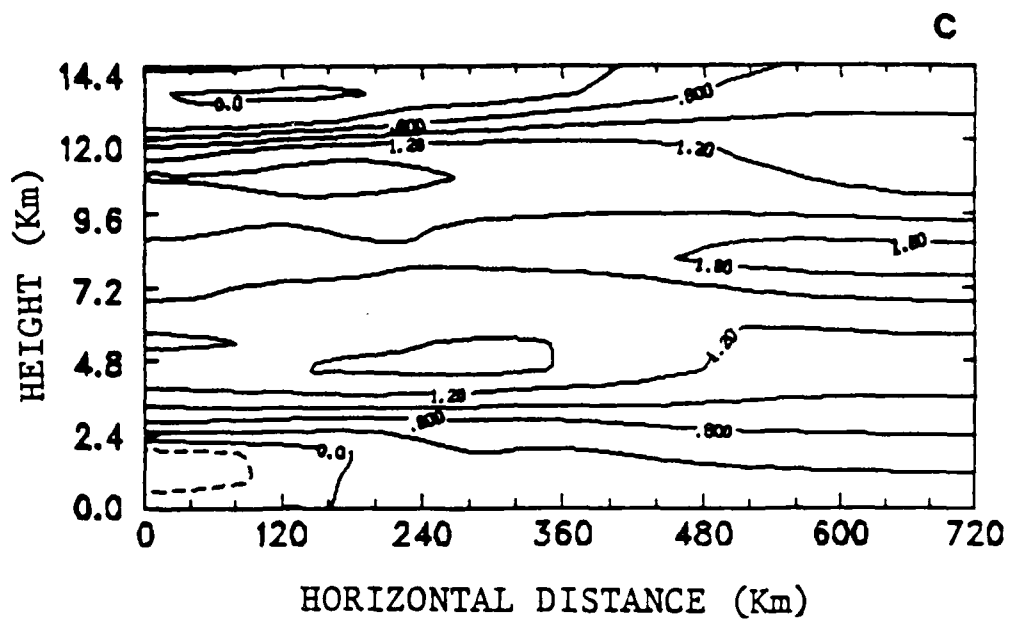
Fig. 5.8. (Continued)

Fig. 5.9. (a) Profiles of convective heating (dashed line) and adiabatic cooling (solid line) of the center column at 6 hr in the control run and (b) profile of the total vertical velocity $(w + w_0)$ of the center column at 6 hr in the control run.

θ' subsequently generates another activity center of a mesolow which results in the w field at 11, 13, and 15 hr, as shown in Fig. 5.10. In Fig. 5.10, two features are important: one is the downward motion below the upward motion area in the central portion of the domain (it is especially evident in Fig. 5.10c); another is the secondary maximum of upward motion beside the original upward motion area. The downward motion can reduce the heating ability of the A-S scheme for the upper atmosphere, as illustrated in Fig. 5.11a, which shows the profiles of the adiabatic cooling versus convective heating for the central column at 13 hr. It can be seen that the cooling rate exceeds the heating rate for the atmosphere above 350 mb so that the temperature would decrease afterwards above that level. This distribution is attributed to the total vertical velocity shown in Fig. 5.11b where no distinct lower maximum is found because of the downward motion induced by the model. Without sufficient low-level mass convergence, the activities of the high clouds are reduced. Another unfavorable factor in reducing the original convection around the center is that the secondary upward motion consumes most of the available moisture. On the other hand, it is found that the secondary upward motion area cannot develop into a well-defined convective system (see Fig. 5.7c). This nondevelopment can also be attributed to insufficient low-level mass convergence because the magnitudes of the imposed w_0 below the secondary upward motion are negligibly small (due to the property of the sinusoidal function).

Fig. 5.12 shows the moisture deviation from the initial state (q') at the different stages. The positive anomalies at 3 and 9 hr are mostly due to the detrainment of cloud air. The evaporation of detrained liquid water also contributes to moistening the atmosphere. It is seen in Fig. 5.12b that the
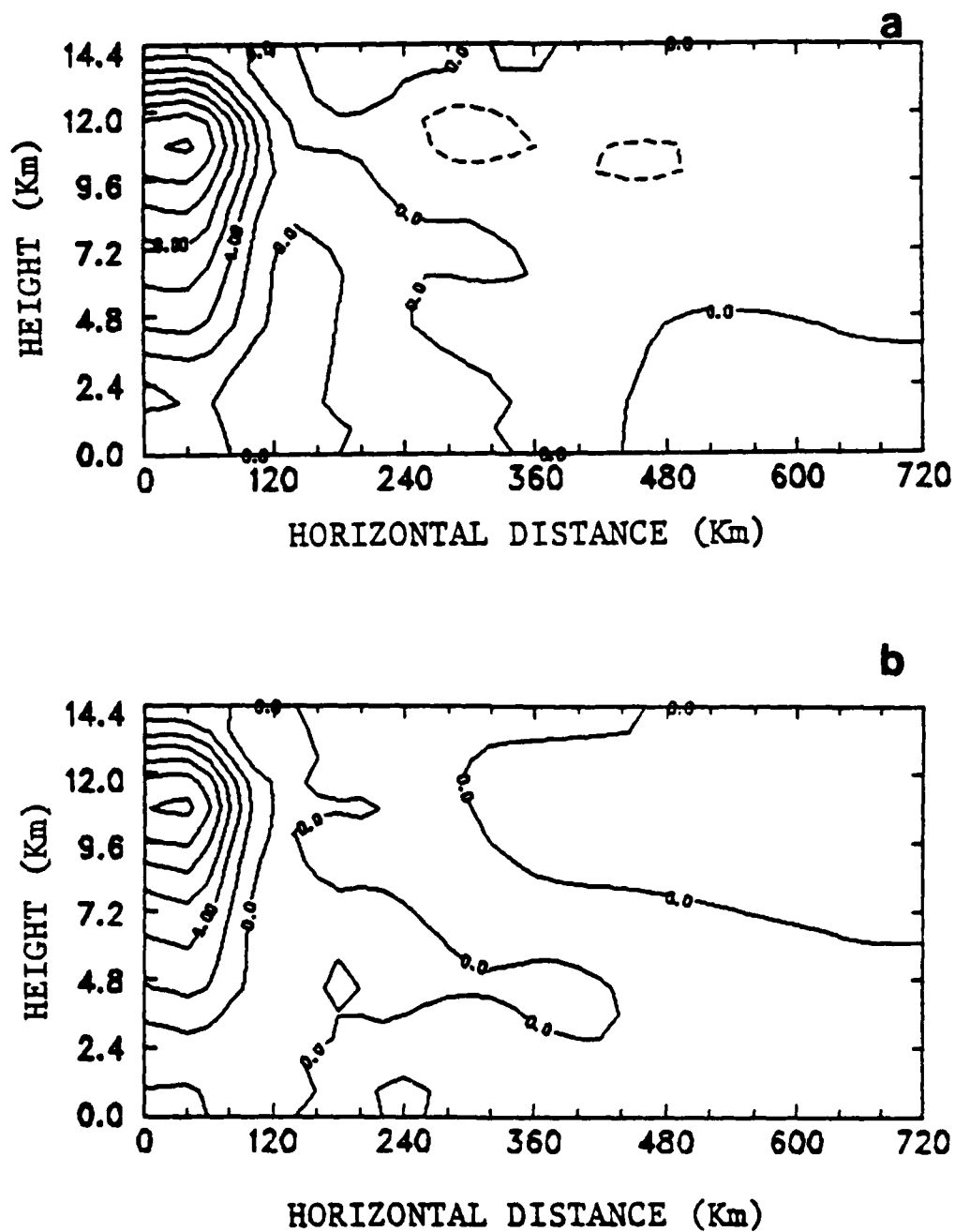
Fig. 5.10. Cross sections of vertical velocity (w) in units of cm s^{-1} in the control run: (a) at 11 hr with contour interval of 2.0, (b) at 13 hr with contour interval of 2.0, and (c) at 15 hr with contour interval of 1.0.
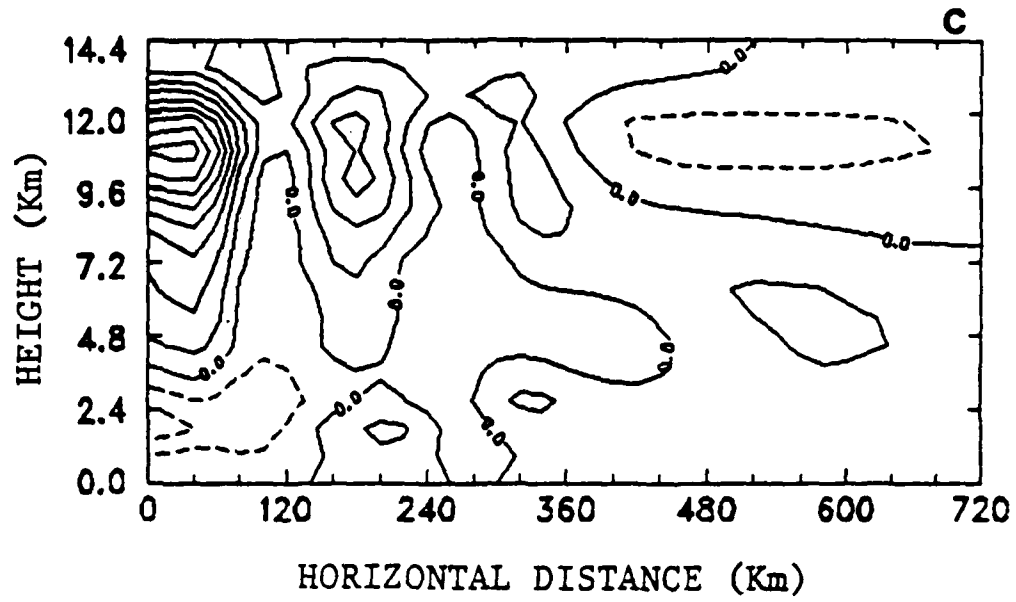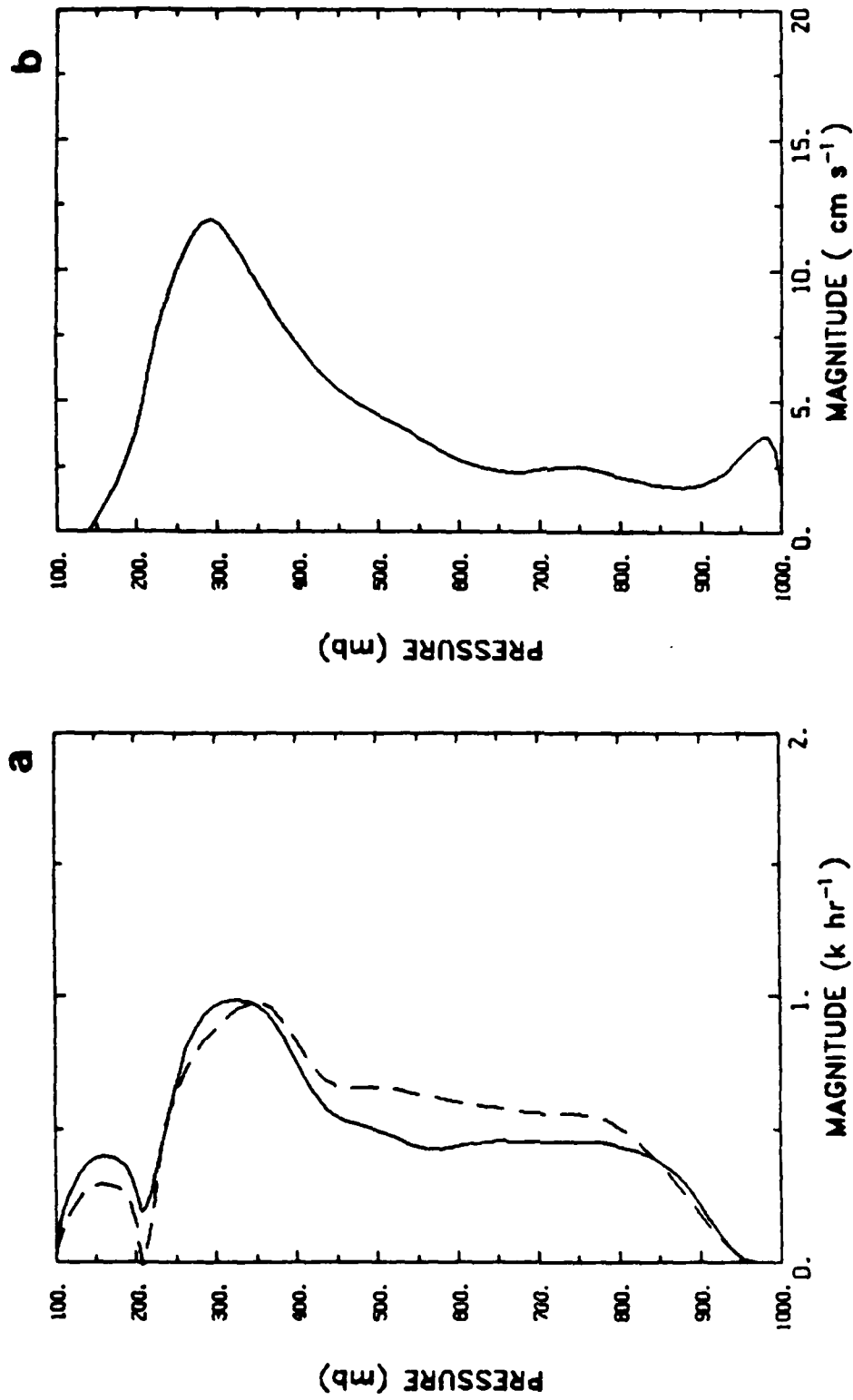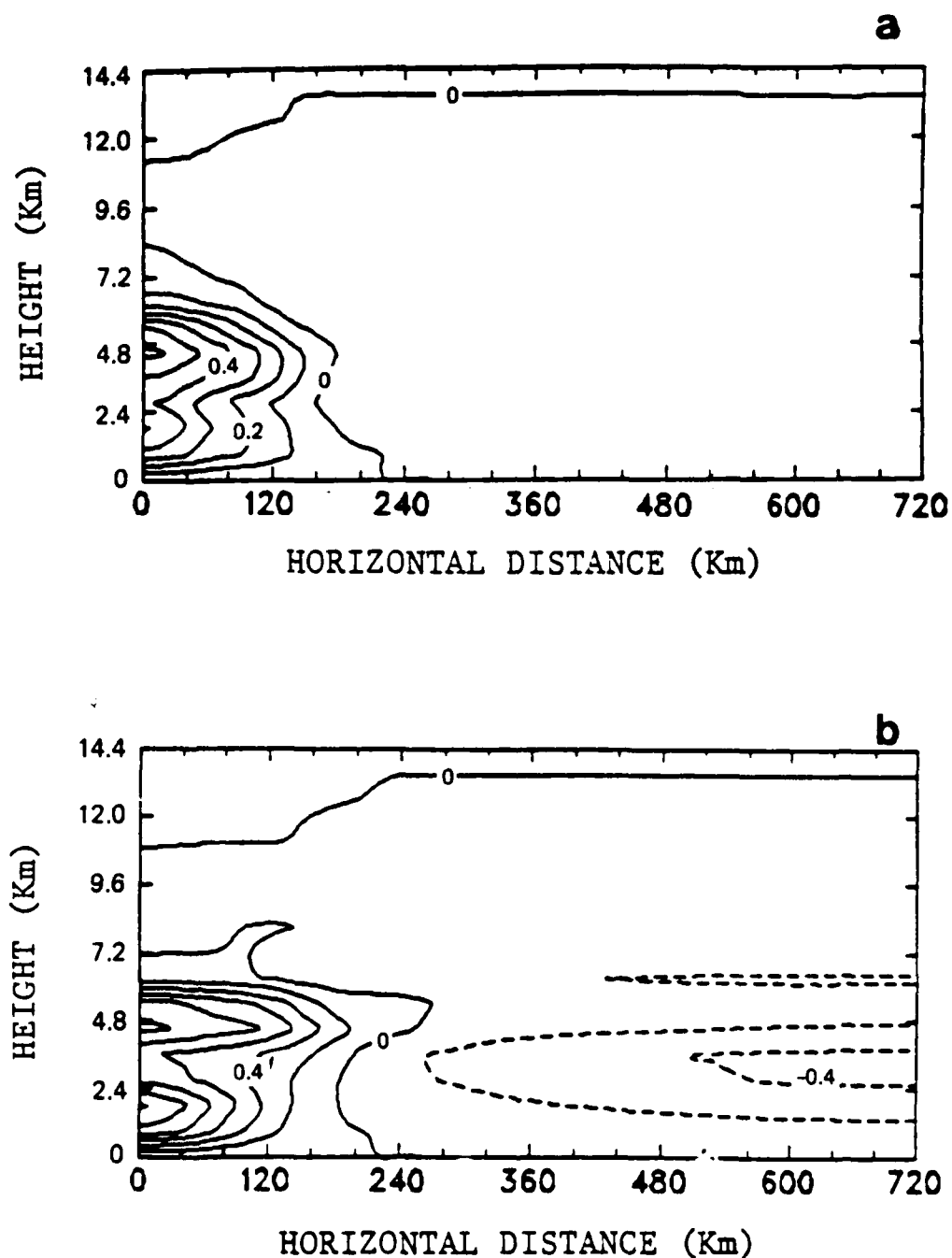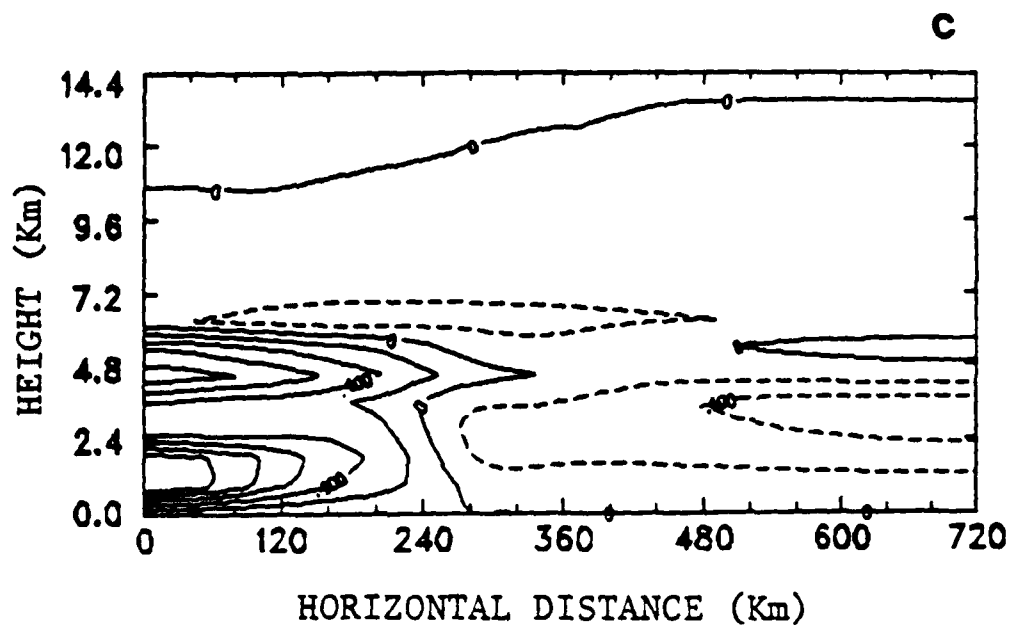
Fig. 5.10. (Continued)

Fig. 5.11. (a) Profiles of convective heating (dashed line) and adiabatic cooling (solid line) of the center column at 13 hr in the control run and (b) profile of the total vertical velocity $(w + w_0)$ of the center column at 13 hr in the control run.

Fig. 5.12. Cross sections of the deviation of mixing ratio (q') from the initial condition in units of g kg^{-1} in the control run: (a) at 3 hr with contour interval of 0.1, (b) at 9 hr with contour interval of 0.2, and (c) at 17 hr with contour interval of 0.2.

c

Fig. 5.12. (Continued)

net increase in the mixing ratio after the 9-hour simulation is rather small with the maximum about 1.3 g Kg^{-1}. The negative anomalies outside the convective area are undoubtedly due to the downward motion. The decrease in the positive anomalies around the lower center from 9 to 17 hr is also due to the downward motion. Fig. 5.13 shows the distributions of the cloud base mass fluxes (m_B) as functions of cloud top height and distance from the center at the different stages. At 3 hr, bimodal distributions are clearly present in the convective area. However, in the mature stage, only intense high clouds are found in the central portion of the domain. Finally, in the decaying stage, the cloud population becomes much less.

The evolution of the mesoscale fields in the period of 24 hours has been discussed in this section. The life cycle of this simulated convective system may be defined by categorizing the period from 0 to 5 hr as the developing stage, the one from 6 to 12 hr as the mature stage, and the one from 13 to 19 hr as the decaying stage. The period from 20 to 24 hr is practically in a steady state. In the next section, we shall compare the model results with the observational studies of this cloud band event.

5.1.3 Comparison with the observations:

Figure 5.14 adapted from Ogura et al. (1979) shows the vertical velocity (ω) at the center of the cloud band as a function of time and height, which is determined by the wind data from the observational network with a few hundred kilometers of station separation. The main features of this ω field are described as follows. Prior to and during the initial stage, low-level upward

HORIZONTAL DISTANCE (Km)
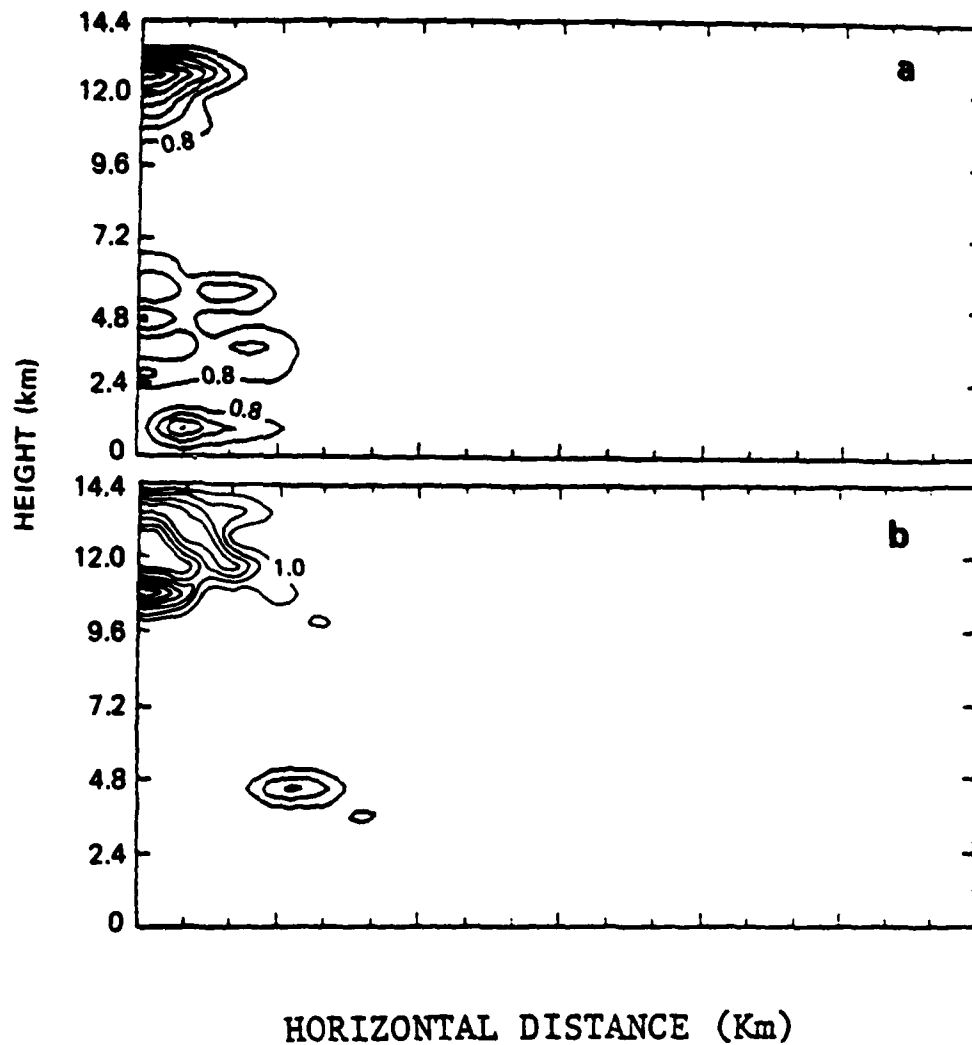
Fig. 5.13. Cross sections of the cloud base mass flux (m_B) in units in mb hr^{-1} in the control run: (a) at 3 hr with contour interval of 0.8, (b) at 9 hr with contour interval of 1.0, and (c) at 17 hr with contour interval of 0.4.
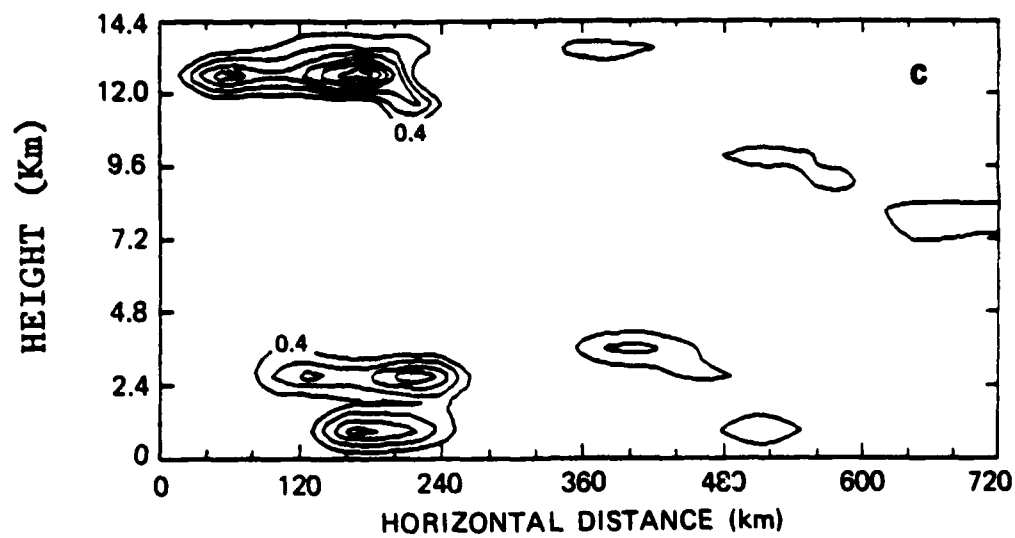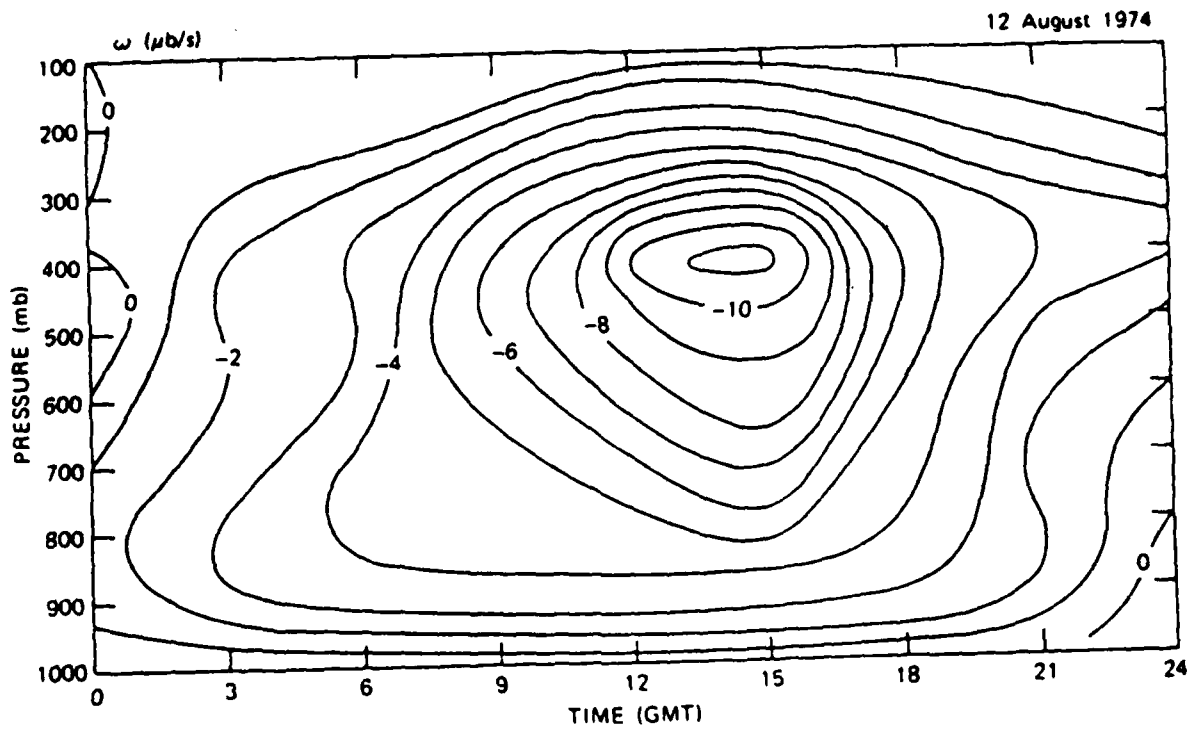
Fig. 5.13. (Continued)

Fig. 5.14. Time-pressure section of the vertical p-velocity (ω) at the center of the cloud band in units of μb s^{-1} (Ogura et al., 1979).

motion was present while weak subsidence was present at middle and upper levels. As convection developed, ω increased in intensity and upward motion was present throughout a deep layer. The local maximum was located around the 400 mb level during the mature stage of the cloud band at 15 GMT. The decaying stage was characterized by rapid weakening of the ascending motion at low levels followed by the development of descending motion, while the ascending motion with a substantial intensity remained at upper levels. Figure 5.15 shows the evolution of the model-predicted w field horizontally averaged over 160 km in the central portion of the domain, which is considered the width of the cloud band simulated by the model. It can be seen that the model result generally agrees well with the observation shown in Fig. 5.14. The area averaged w ($\bar{w}$) shown in Fig. 5.15 also increases in intensity with time and reaches the maximum of about 15 cm s^{-1} at 9 hr, which is somewhat smaller than the maximum shown in Fig. 5.14. The observation indicates that the height of the local maximum of ω increases with time from 0 to 9 GMT. If we define this 9 hour period to be the developing stage of the cloud band, then that of the model results only takes 4 hours. As discussed previously, this is because the A-S scheme generates high clouds much faster than the real atmosphere. For the decaying stage, the characteristics of the low-level downward motion are also clearly observed in Fig. 5.15.

Figure 5.16 shows the model-predicted surface precipitation as a function of time and distance from the center. The width and distribution of significant precipitation almost coincide with those of upward motion as they should be. The maximum intensity, about 3 mm hr^{-1}, is located at the center of the domain at 8 hr. Figure 5.17 shows the observed precipitation accumulation
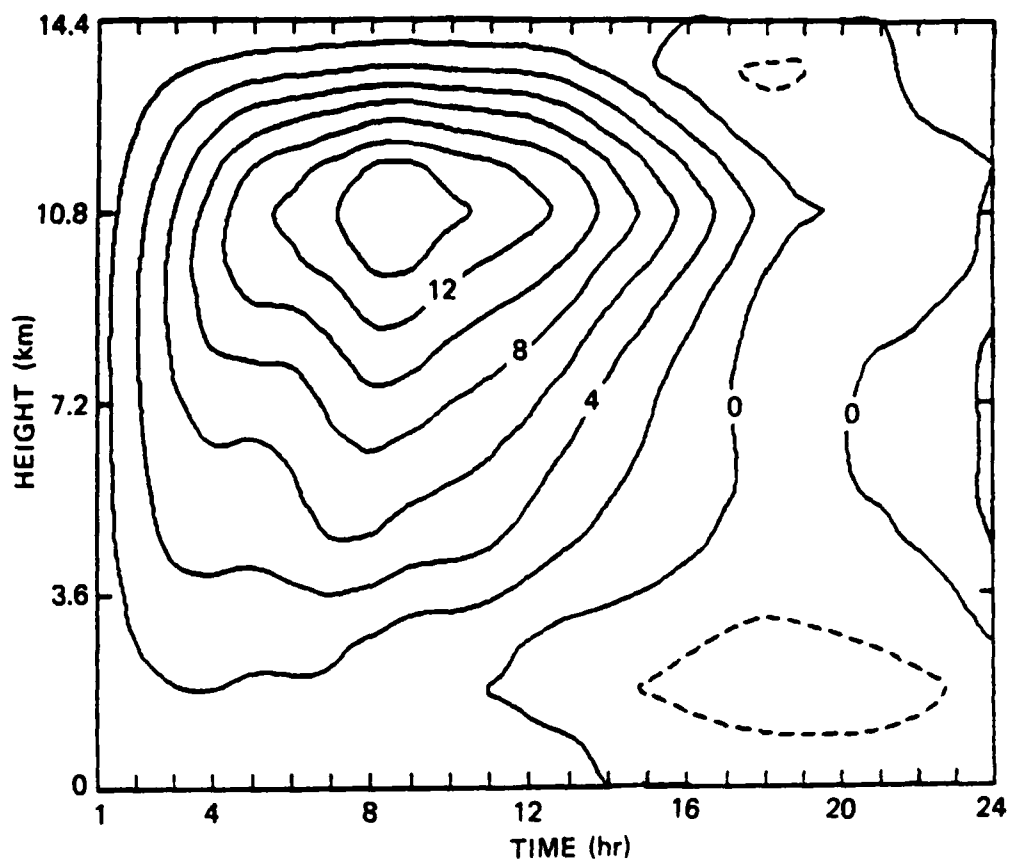
Fig. 5.15. Time-height section of the model-predicted vertical velocity in the control run averaged over the central 160 km of the model domain in units of cm s^{-1} with contour interval of 2.0.
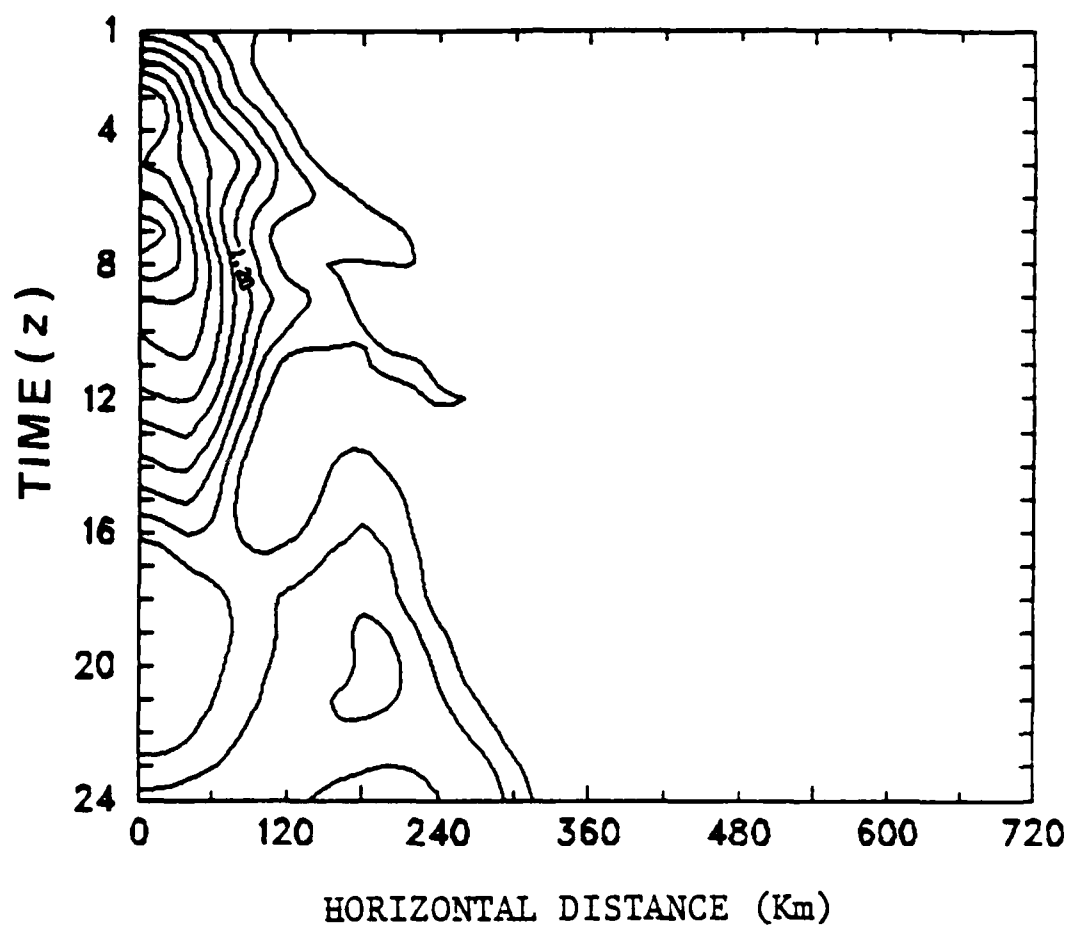
Fig. 5.16. Model-predicted rainfall accumulation in the control run as a function of time and distance from the center in units of mm hr^{-1} with contour interval of 0.3.
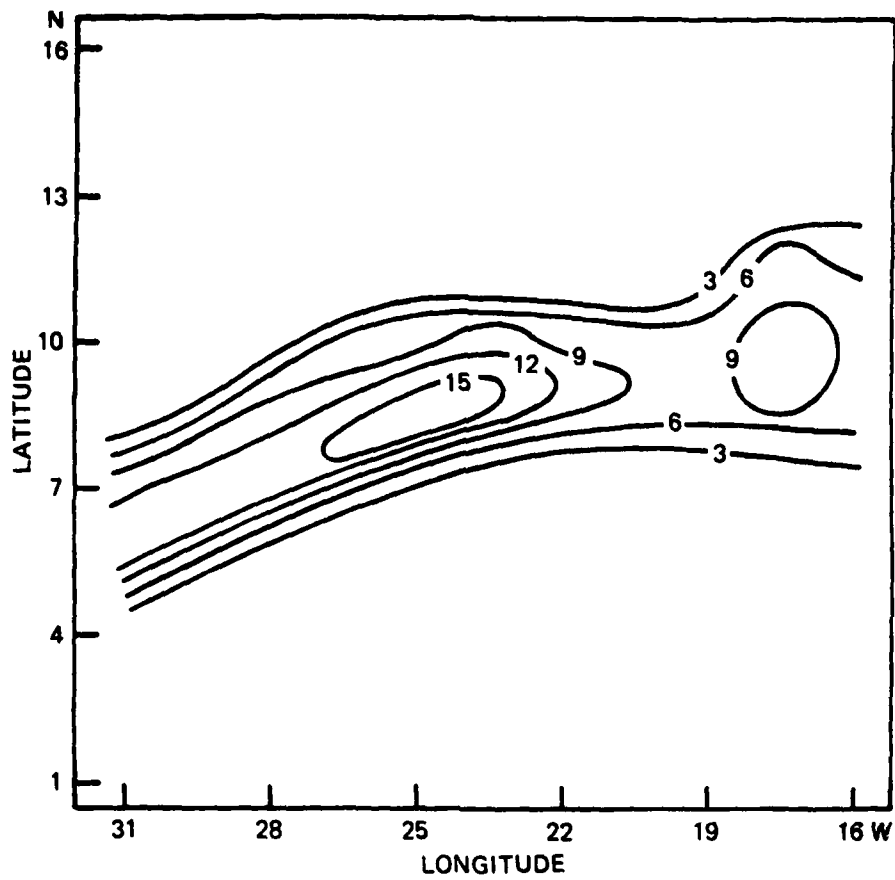
Fig. 5.17. The observed rainfall accumulation for the period from 12 GMT to 18 GMT 12 August 1974 in units of mm.

for the cloud band from 12 to 18 GMT 12 August 1974. It is found that the model result agrees well with the observation both in width scale and intensity of the precipitation.

The observational studies indicate that both the net heating rate by a well-developed cloud cluster and the adiabatic cooling rate by the large-scale lifting are typically 10 K day^{-1} in order of magnitude. In other words, the temperature change $\left(\frac{\partial \theta}{\partial t}\right)$ in the tropical region is a small residue between the two large terms of cooling by the large-scale lifting and heating by the clouds and is 1 K day^{-1} in order of magnitude. The model presented here appears to be capable of simulating this very unique feature in the tropics as illustrated in Table 5.1 which presents the deviation of area-averaged potential temperature and mixing ratio at 9 hr from the initial states. This implies that the A-S scheme does have a potential usefulness in predicting tropical phenomena.

5.2 Sensitivity tests:

5.2.1 The deletion of the imposed large-scale lifting:

The model results presented in the preceding section confirm the observational fact that the low-level large-scale lifting is necessary to trigger the formation of an organized convective system even if the atmospheric stratification is conditionally unstable. Here we shall undertake an experiment by deleting the imposed low-level lifting after 9 hours of simulation time to investigate the possible situation that the large-scale

Height (Km)	$\bar{\theta}'$ (k)	$\bar{q}'$ (g Kg)
0.45	0.04	0.15
1.35	-0.22	0.42
2.25	-0.16	0.24
3.15	0.21	0.15
4.05	0.75	0.25
4.95	0.66	0.73
5.85	0.61	0.03
6.75	0.64	-0.06
7.65	0.95	-0.02
8.55	1.15	-0.05
9.45	1.14	-0.10
10.35	1.38	-0.07
11.25	1.36	-0.03
12.15	0.82	0.07
13.05	0.07	0.05
13.95	0.09	0.01

Table 5.1. The deviation of area-averaged potential temperature and mixing ratio from the initial conditions in the control run.

lifting goes out of the convective area (or dies out) after the development of the cloud cluster.

Figure 5.18 shows the w fields at 11, 13, and 15 hr after the deletion of w_0 at 9 hr. The result clearly indicates a drastic decrease in the maximum of w from 17 cm s^{-1} at 9 hr (see Fig. 5.7b) to 3 cm s^{-1} at 15 hr. It is also clearly observed from Fig. 5.18 that the original convective area is cut into halves by the intrusion of downward motion from the low levels. One of them rapidly decays and the other propagates laterally. Figure 5.19 shows θ' fields at 11, 13, and 15 hr. The magnitudes of the positive anomalies around the center are smaller while new maxima are generated far away from the center. The original negative anomaly at the low levels around the center, as shown in Fig. 5.8b, disappears because of the deletion of w_0 and its associated adiabatic cooling. The negative anomaly at the upper levels around the center, shown in Fig. 5.19, is due to the smaller heating ability of the A-S scheme, since the deletion of w_0 decreases the population of the high clouds. In fact, the basic reason for initiating the rapid dissipitation in this run can be explained by Fig. 5.20 which bears a similar rationale with that of Fig. 5.11 for the decaying stage in the control run. The deletion of the w_0 makes the lower maximum of the total vertical velocity disappear, as shown in Fig. 5.20b, and the adiabatic cooling rate exceed the convective heating rate for the middle and upper atmosphere, as shown in Fig. 5.20a. Meanwhile, since the adiabatic cooling rate due to w_0 at the low levels does not exist any longer, a large excess of convective heating over adiabatic cooling at the low levels is observed. Obviously, this implies that the atmospheric static stability is destabilized. Nonetheless, from the viewpoint of the coupling or interactions
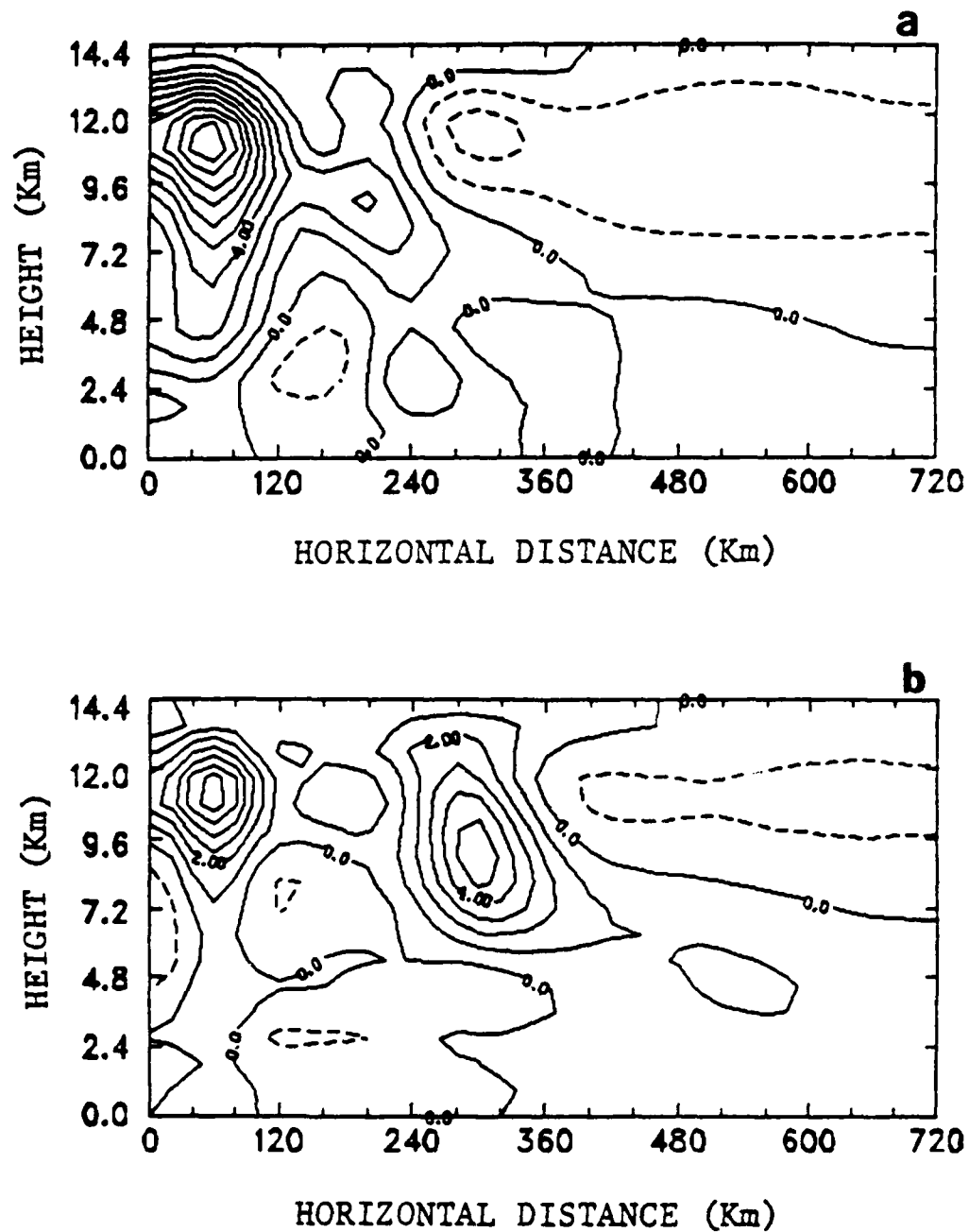
Fig. 5.18. Cross sections of vertical velocity (w) in units of cm s^{-1} in Run 2: (a) at 11 hr with contour interval of 1.0, (b) at 13 hr with contour interval of 1.0, and (c) at 15 hr with contour interval of 0.7.
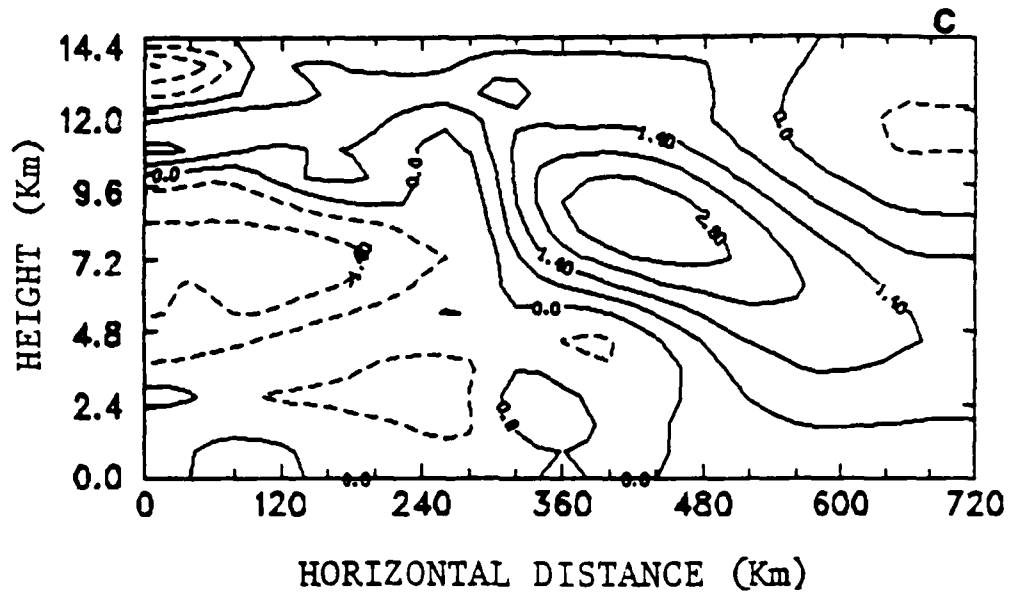
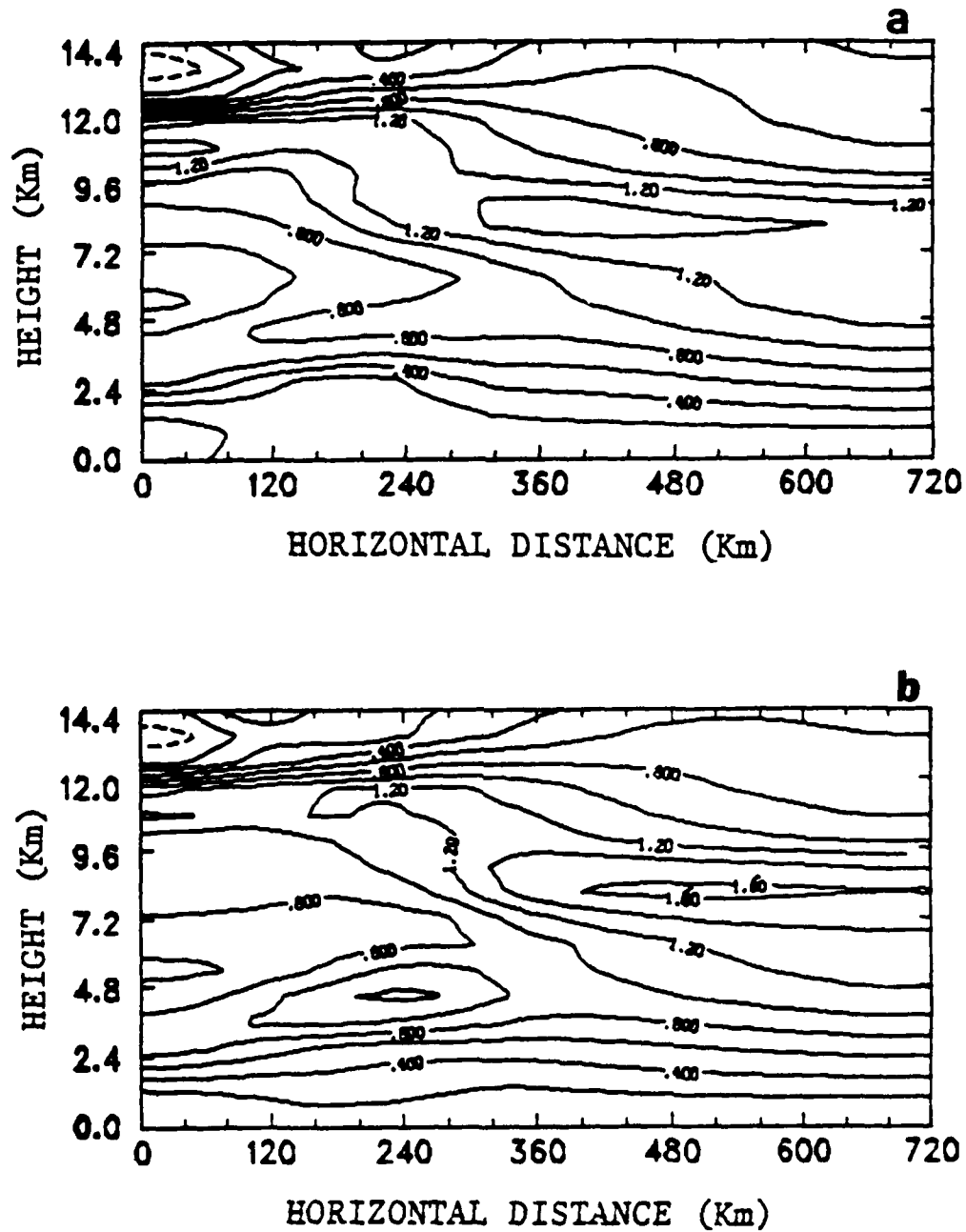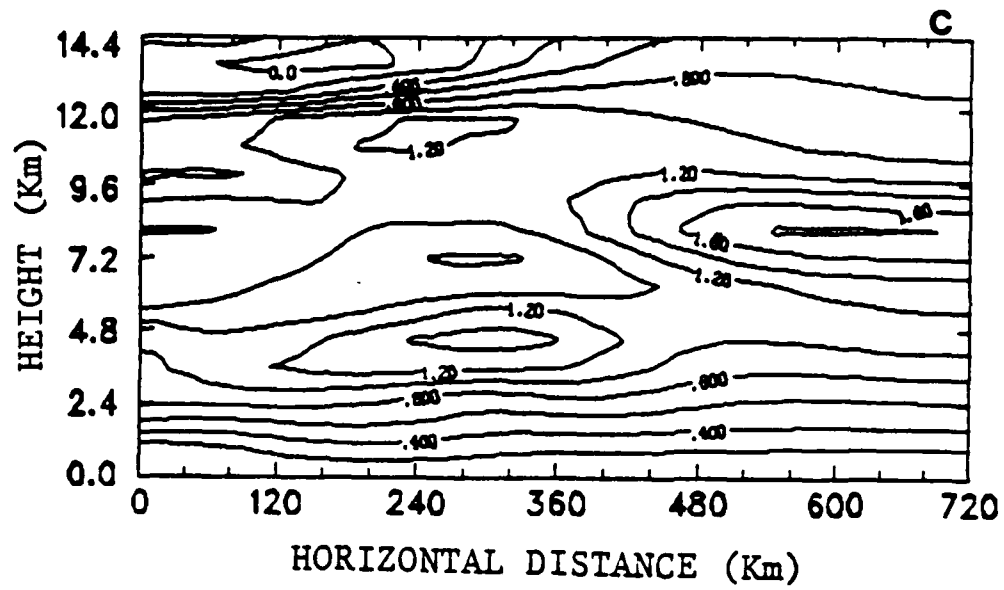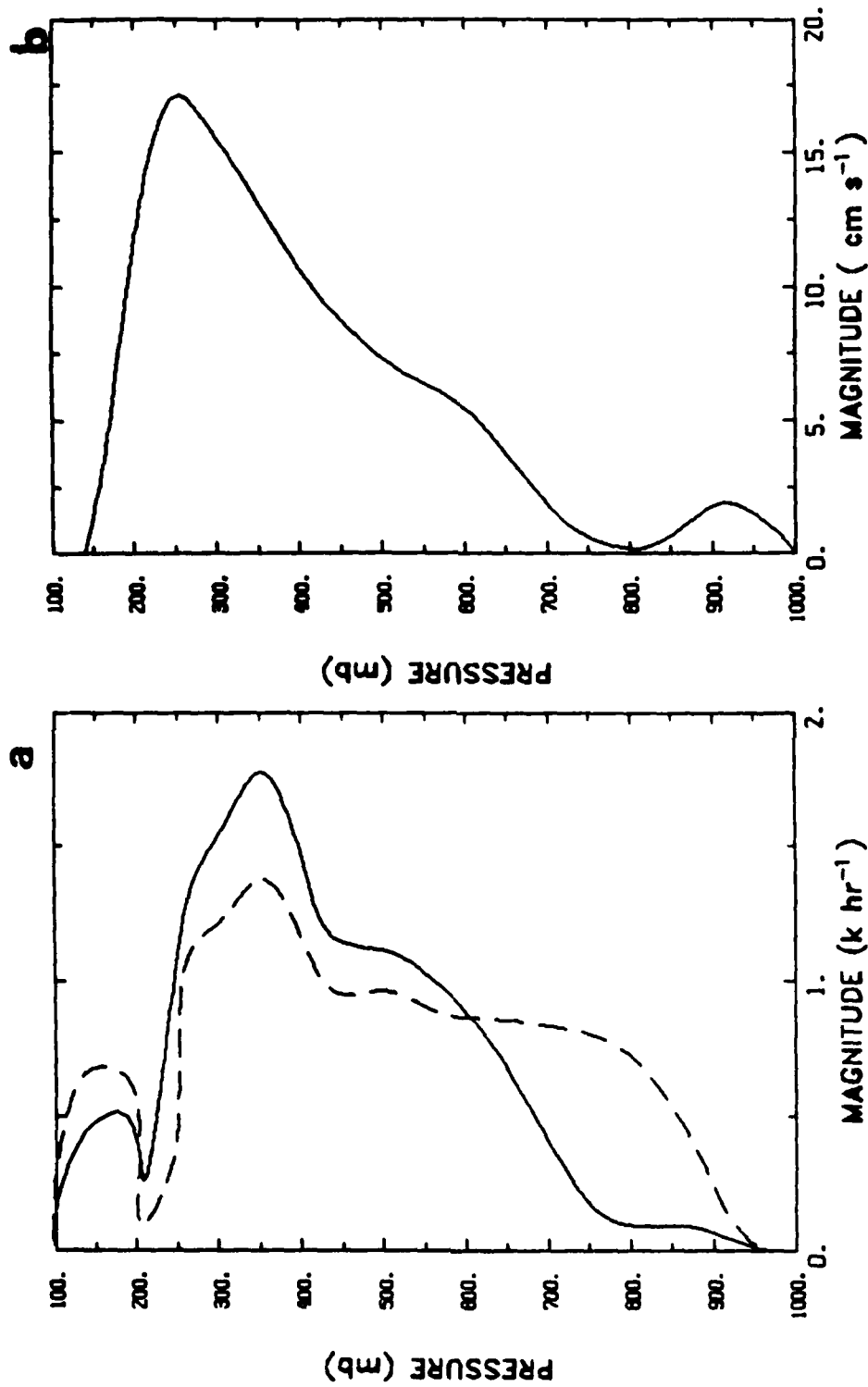HORIZONTAL DISTANCE (Km)

Fig. 5.18. (Continued)

Fig. 5.19. Cross sections of the deviation of potential temperature (θ′) from the initial condition in units of K in Run 2: (a) at 11 hr with contour interval of 0.2, (b) at 13 hr with contour interval of 0.2, and (c) at 15 hr with contour interval of 0.2.

Fig. 5.19. (Continued)

-151-

Fig. 5.20. (a) Profiles of convective heating (dashed line) and adiabatic cooling (solid line) of the center column at 9 hr in Run 2 and (b) profile of the total vertical velocity $(w + w_0)$ of the center column at 9 hr in Run 2.

between the mesoscale circulation and cumulus convection, the original horizontal temperature gradient around the center is reduced because of the distributions of heating and cooling, shown in Fig. 5.20a, and its corresponding upward motion is consequently weakened. It should be noted that several aspects of the decaying stages of the two runs are different. Other than the difference of the time scales of dissipation, there is no distinct propagation of w fields in the control run, as shown in Fig. 5.10, while rapid propagation is evident in Fig. 5.18. This is because in the control run the imposed w_0 is always present. Although the imposed w_0 is partially compensated by the downward motion in the decaying stage, the net effect of w_0 is still to release the potential instability of the lower atmosphere and practically serves as a continuous heating source through the A-S scheme. It is believed that suddenly deleting this heating source can result in the rapid lateral propagation of the convective system. More relevant discussion along the problem of system propagation will be given in Section 5.2.4 where Kuo's scheme is incorporated into the model. Figure 5.21 shows the vector fields at 13 hr for the two different runs. In the control run, a low-level reverse circulation is present with fairly strong inflows lying above, as shown in Fig. 5.21a, which introduces a possible moisture supply for the secondary upward motion area. Obviously, this feature cannot be observed from Fig. 5.21b. Generally speaking, the experiment presented in this section reveals another possible decaying situation whose time scale is much shorter and in which physical processes are much more straightforward.
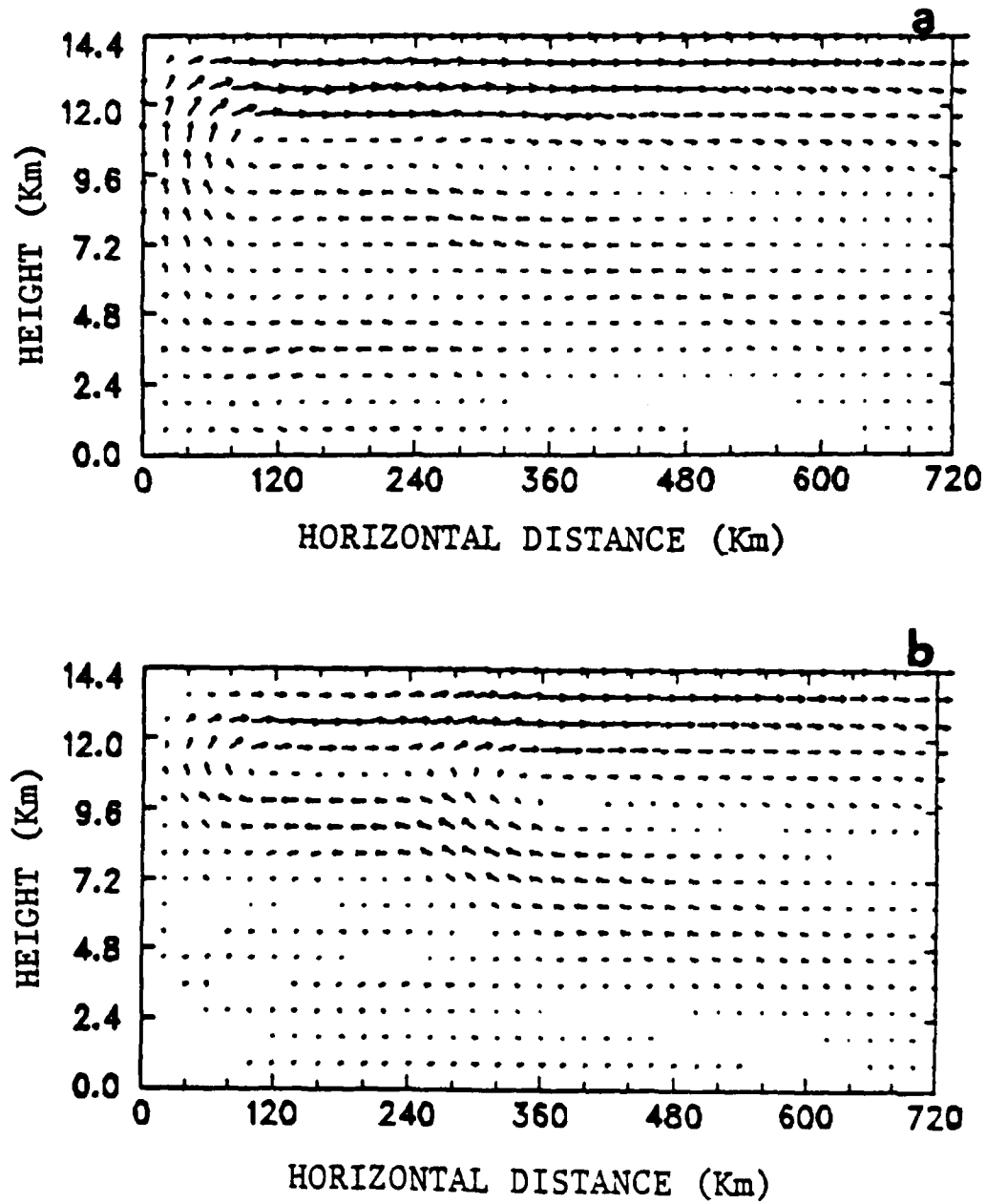
Fig. 5.21. Cross sections of vector field of [u,w]: (a) at 13 hr in the control run and (b) at 13 hr in Run 2. The magnitudes of w have been enlarged by 10 times.

5.2.2 The effects of vertical wind shear:

The initial horizontal wind (u_g) profile used in this run is shown in Fig. 5.22. According to Eq. (4.8), the corresponding meridional temperature gradient $\left(\frac{\partial \theta_g}{\partial y}\right)$ is about -0.4×10^{-3} K km^{-1} and this value will be used as a constant throughout the integration. First of all, it should be expected that the model results would not stay symmetric about the center line of the domain. Figure 5.23 shows the w fields for the whole domain at the different stages. It is seen that the convection does shift to form in the downwind area but not very distant from the center, with the width of the convective area about the same as that of the control run shown in Fig. 5.7. The main difference between Figs. 5.23 and 5.7 lies in the distributions of downward motion. Combining Figs. 5.23b and 5.23c with the intermediate w fields at 11, 13, and 15 hr shown in Fig. 5.24, it appears that the gradual intrusion of the downward motion from the low levels at 9 hr into the right half of the domain characterizes the dissipation of the system. Figures 5.25 and 5.26 show the fields of θ' and its horizontal gradient at the different stages. Small negative temperature anomalies are found at the top of the convective portion, shown in Fig. 5.25, which implies that the heating due to high clouds is less than that in the control simulation. This difference is caused by the fact that the low-level large-scale lifting does not shift with the horizontal wind so that the magnitudes of w_0 under the convective portion in the present experiment are smaller than those in the control run. The temperature gradient, shown in Fig. 5.26, in conjunction with the ageostrophic wind (v_{ag}) shown, in Fig. 5.27, explains the evolution of w fields shown in Fig. 5.23. Figure 5.28 shows the
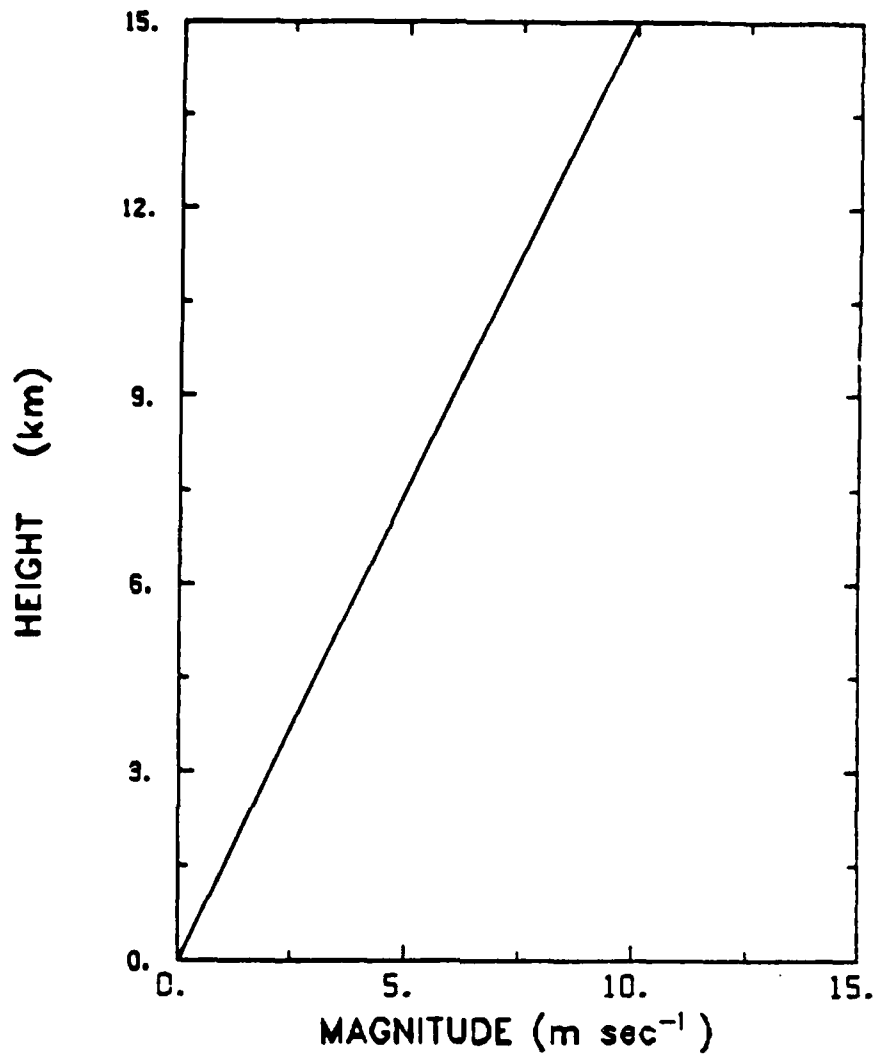
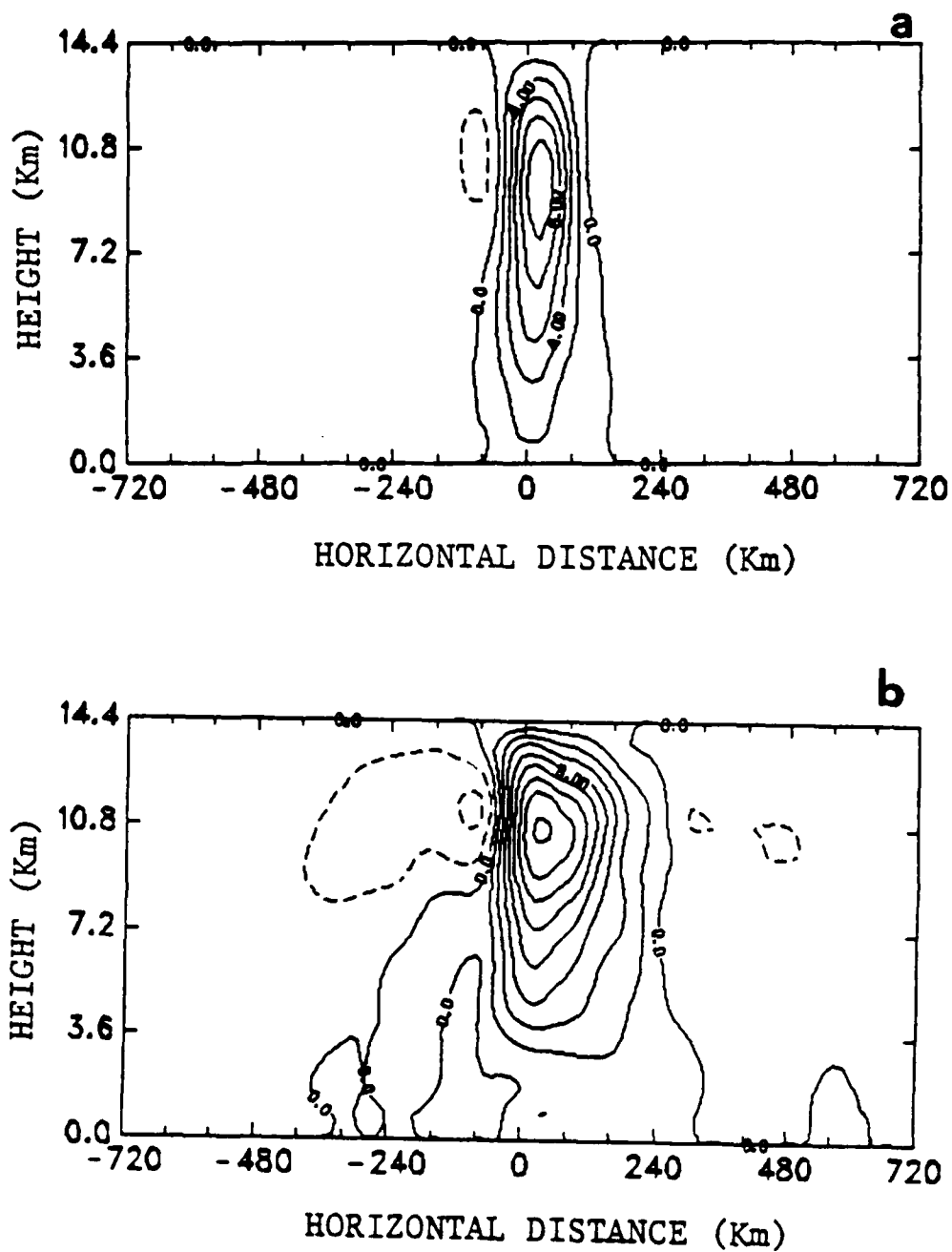Fig. 5.22. The profile of initial wind (u_g) in Run 3.

Fig. 5.23. Cross Sections of vertical velocity (w) in units of cm s^{-1} in Run 3: (a) at 3 hr with contour interval of 2.0, (b) at 9 hr with contour interval of 2.0, and (c) at 17 hr with ocntour interval of 1.0.
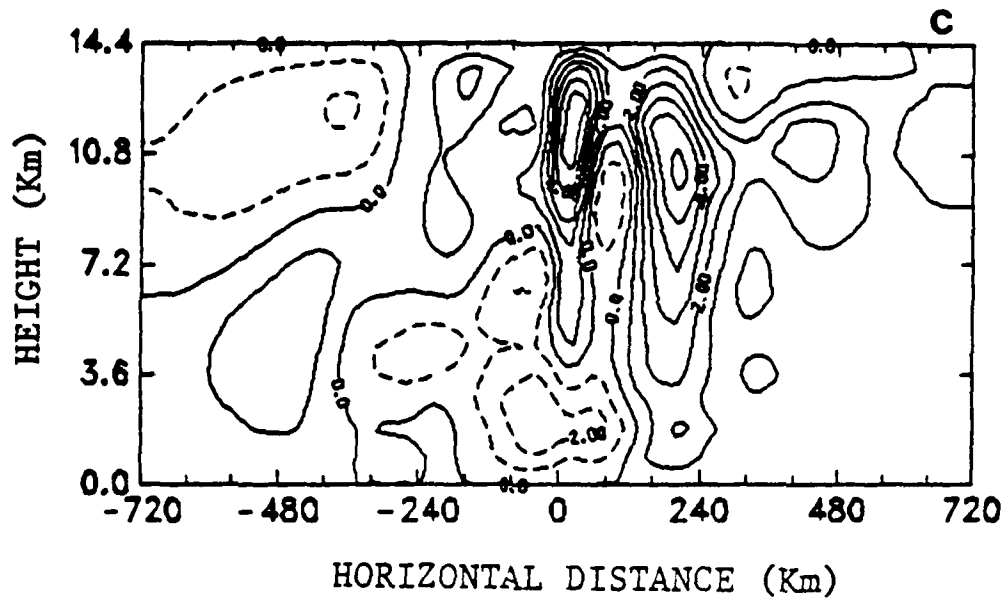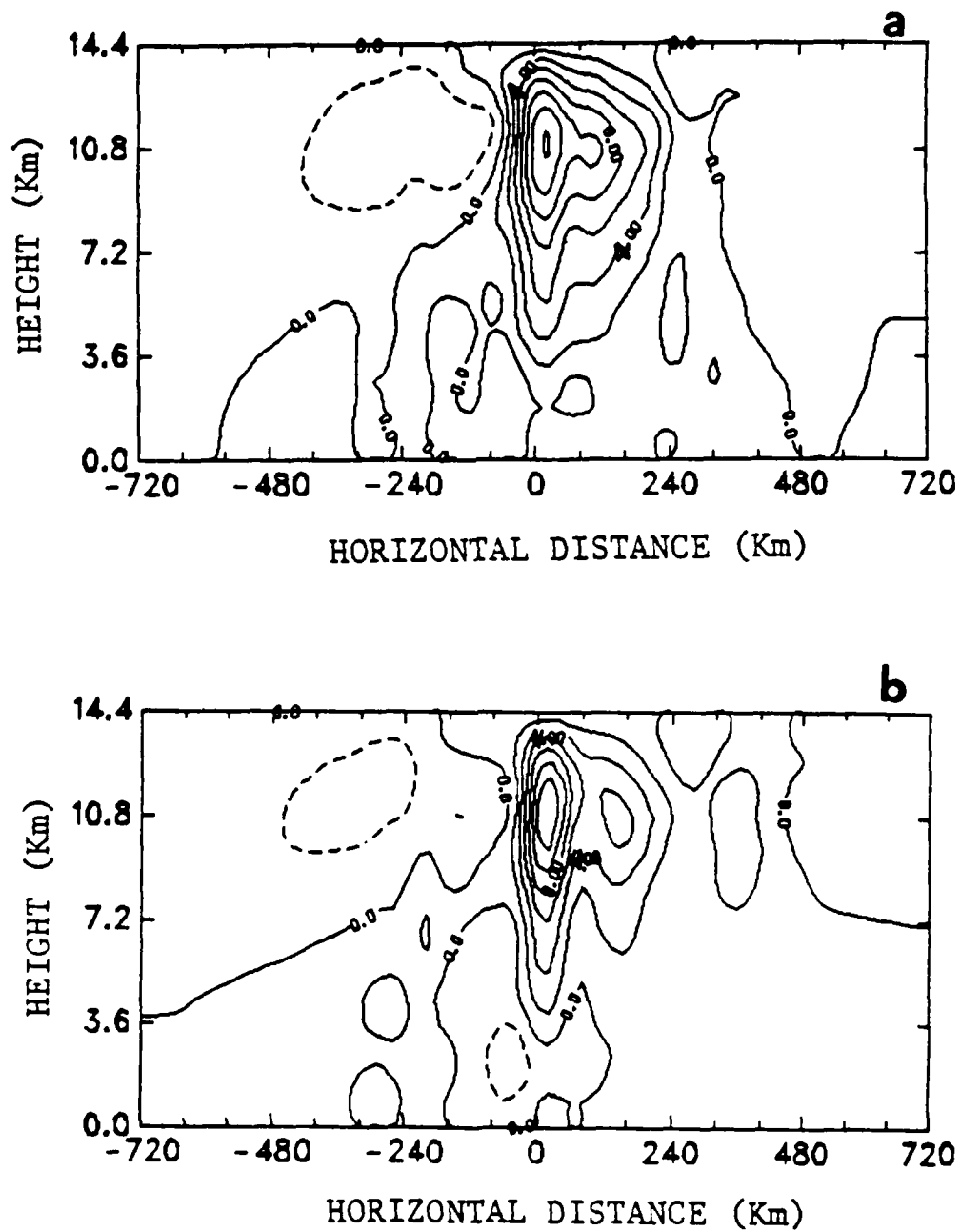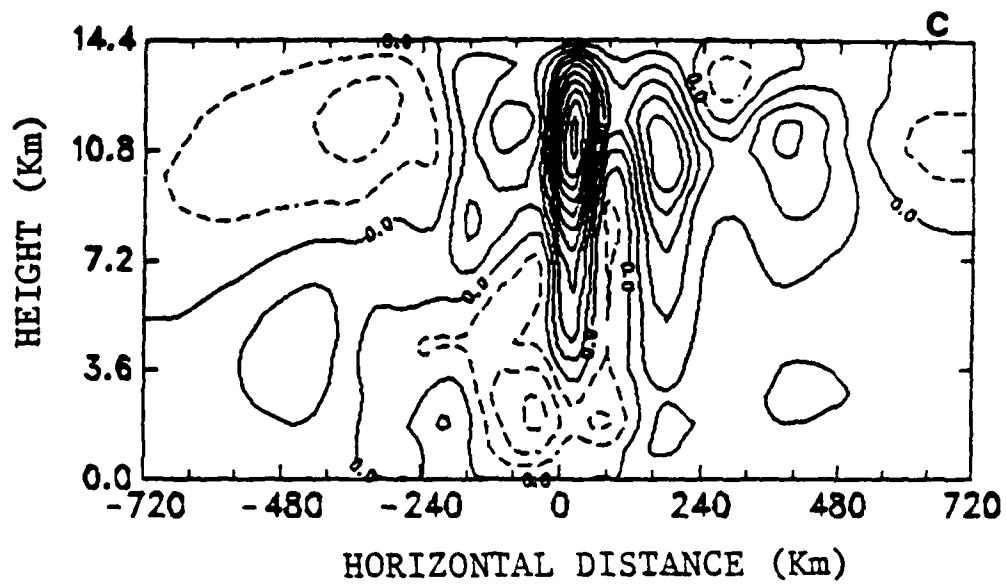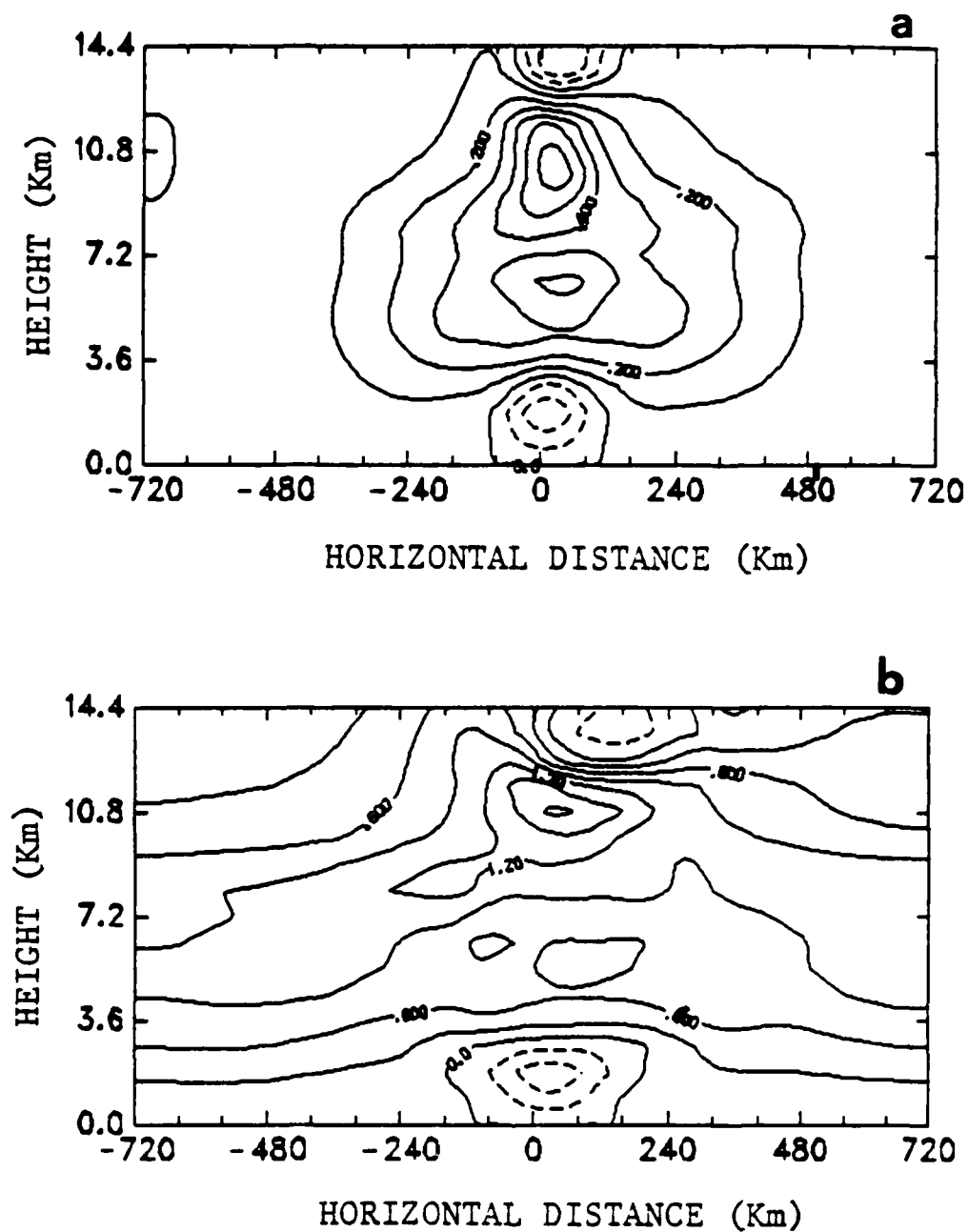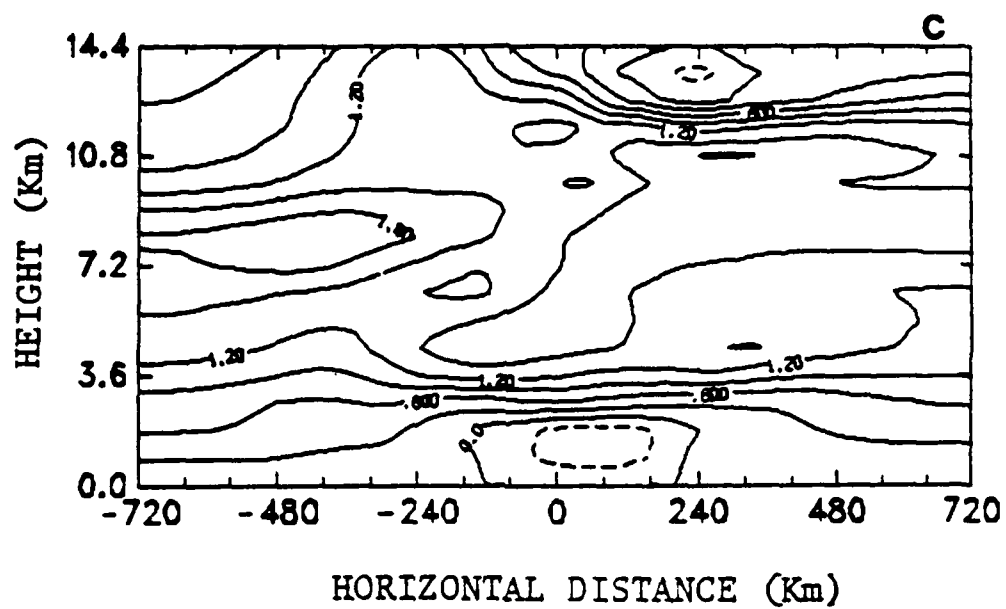
Fig. 5.23. (Continued)

Fig. 5.24. Cross sections of vertical velocity (w) in units of cm s^{-1} in Run 3: (a) at 11 hr with contour interval of 2.0, (b) at 13 hr with contour interval of 2.0, and (c) at 15 hr with contour interval of 1.0.

Fig. 5.24. (Continued)

Fig. 5.25. Cross sections of the deviation of potential temperature (θ') from the initial condition in units of K in Run 3: (a) at 3 hr with contour interval of 1.0, (b) at 9 hr with contour interval of 0.3, and (c) at 17 hr with contour interval of 0.3.
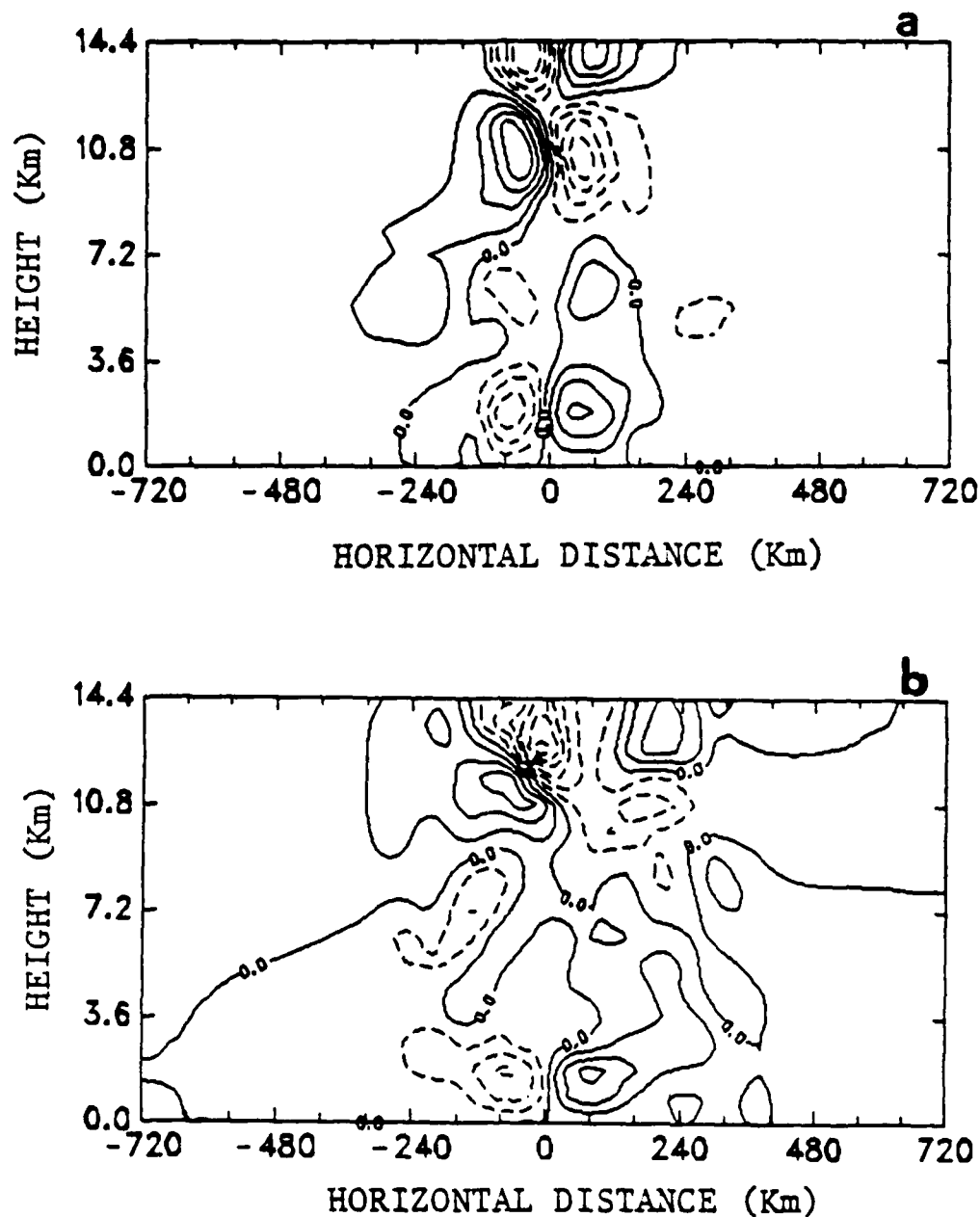
Fig. 5.25. (Continued)

Fig. 5.26. Cross sections of the horizontal gradient of potential temperature $(\frac{\partial \theta}{\partial x})$ in units of K 100 km^{-1} in Run 3: (a) at 3 hr with contour interval of 0.1, (b) at 9 hr with contour interval of 0.2, and (c) at 17 hr with contour interval of 0.3.
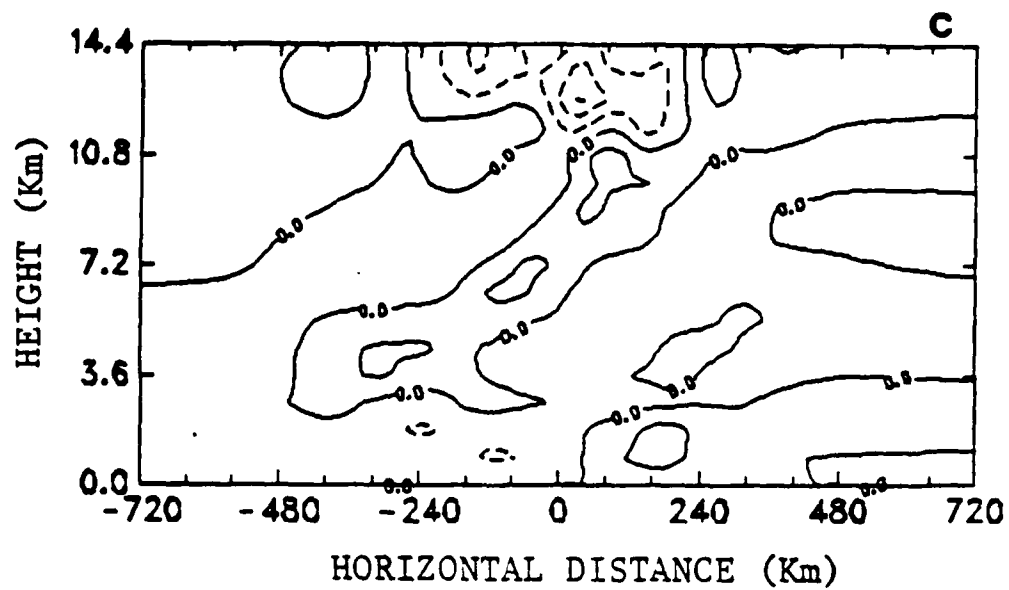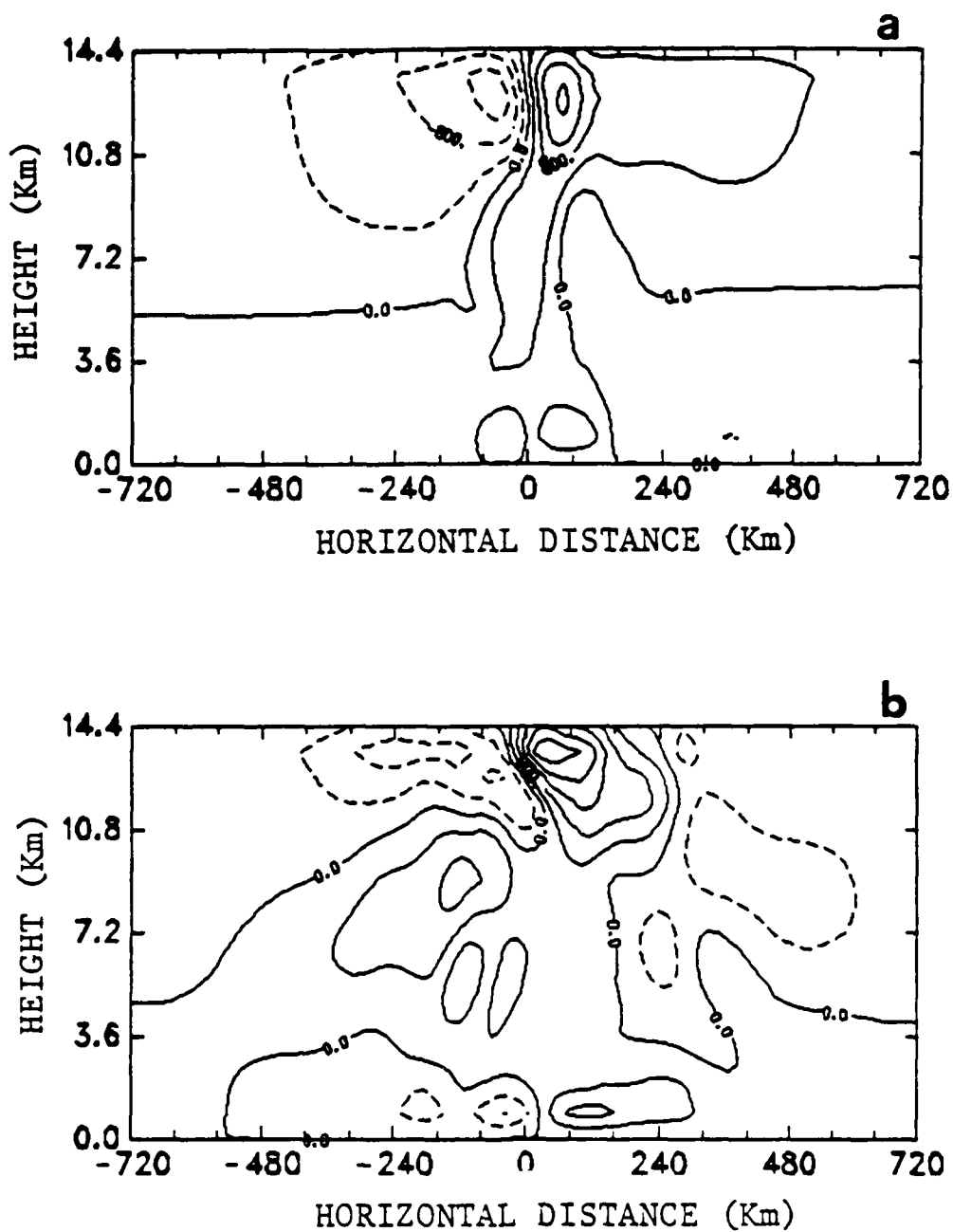
Fig. 5.26. (Continued)

Fig. 5.27. Cross sections of the v ageostrophic wind (v_{ag}) in units of cm s^{-1} in Run 3: (a) at 3 hr with contour interval of 400, (b) at 9 hr with contour interval of 400, and (c) at 17 hr with contour interval of 300.
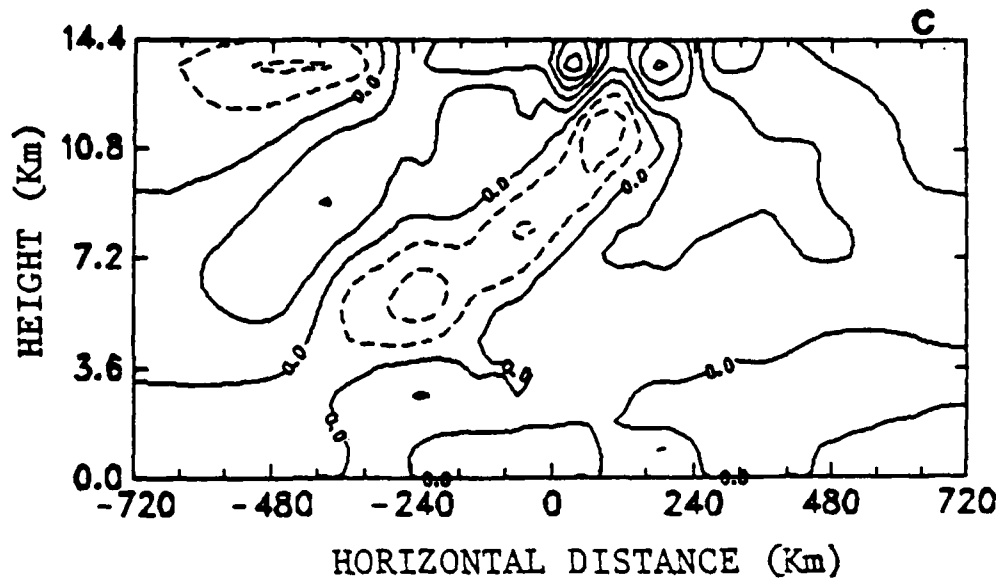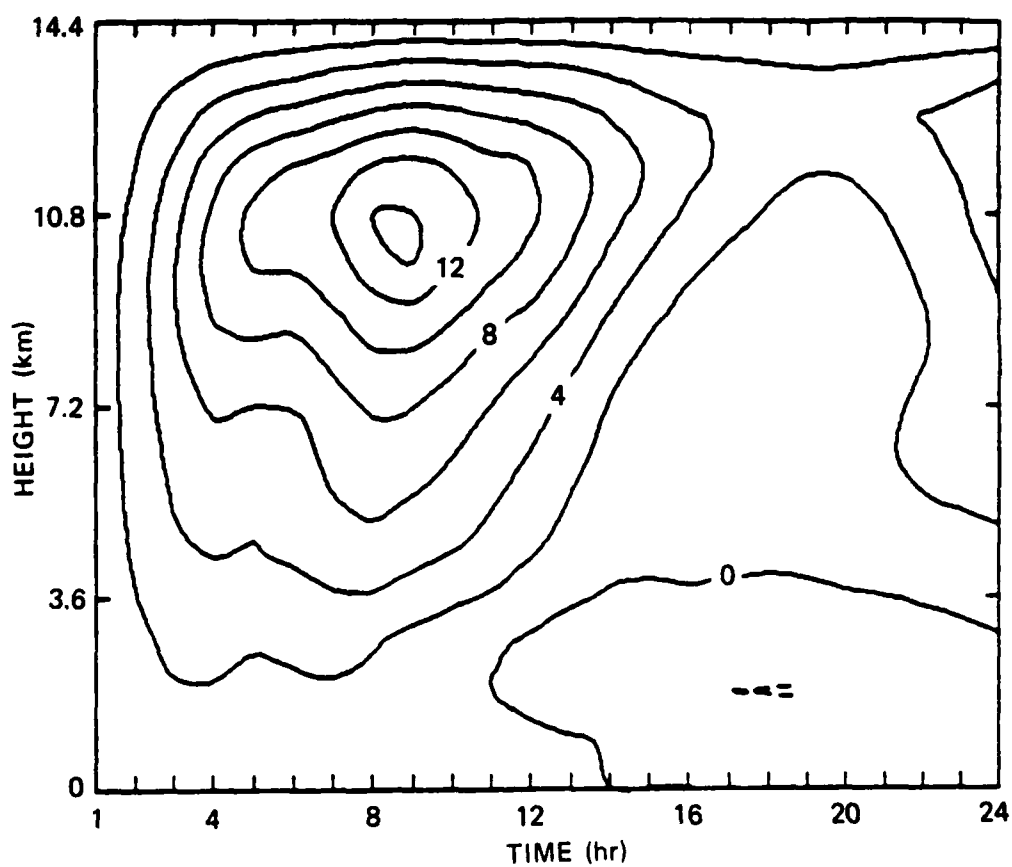
Fig. 5.27 (Continued)

Fig. 5.28. Time-height section of the model-predicted vertical velocity in Run 3 averaged over 160 km around the center of the model domain in units of cm s^{-1} with contour interval of 2.0.

horizontally averaged w ($\bar{w}$) over 160 km around the central portion of the domain, which covers 40 km in the left half and 120 km in the right half. No substantial differences are found in the life cycle and intensity of $\bar{w}$ when compared with the result of the control run shown in Fig. 5.15. Generally speaking, the effects of vertical wind shear may be of no importance in this model framework.

Many cloud modeling studies (Schlessinger, 1973; Wilhelmson, 1974; Thorpe et al., 1982; and many others) have concluded that the vertical wind shear is responsible for the long-lived, multi-cell thunderstorms. The shortness of the life span of individual thunderstorms results from the process that the downdrafts, which develop inside the cell due to water loading, cut off the supporting upward motion. In contrast, the vertically-sheared flow can effectively dislocate the water particles from the updraft area. This effect makes the thunderstorms live longer or turn into the multi-cell storms. With this recognition, the insensitivity of this model to the vertical wind shear is not surprising, since no precipitating particles are included in the present model.

5.2.3 The effects of cumulus downdrafts:

The semi-prognostic studies with the inclusion of cumulus downdrafts have been presented in Section 3.4. The results indicated that the agreement between the predicted and observed cloud heating effects is as good as that in the case without the downdrafts. Nevertheless, it is not guaranteed that the

results of the mesoscale model would be insensitive to the downdraft effects because of the following reasons. First, from the discussion in Section 5.1, it is recognized that in this mesoscale model the development of the convective system is exclusively initiated by the small difference between the convective heating and adiabatic cooling. The inclusion of the cumulus downdraft effects may significantly alter this "small difference" and consequently result in very different mesoscale fields. Secondly, the feedback mechanism between the cloud layer and subcloud layer through the cumulus downdrafts may play an important role in the simulation. As discussed earlier, the detrainment of downdrafts into the mixed layer and the evaporation of the precipitation in the mixed layer can introduce the modification of the mixed layer thermodynamic properties (θ_M and q_M), which are important factors in determining the cloud properties. Here it is worthwhile to mention that, in the control run, the mixed layer properties are only governed by the large-scale horizontal advection and turbulent eddy fluxes so that the time rate of change of θ_M is as small as 10^{-1} K day^{-1} in order of magnitude.

It should be mentioned that $\epsilon = -0.3$ (see Eq. (3.19)) is used in the present experiment. Figure 5.29 shows the potential temperature deviation (θ') from the initial state at 3, 6, 9, and 12 hr. As compared with Fig. 5.8, it is seen that the maximum temperature drop in the mixed layer is as large as 0.7 K at 3 hr due to the downdrafts. It is also found that a considerable temperature decrease is present in the low levels around the center above the mixed layer, which can be expected to induce the low-level reverse circulation more quickly and strongly than in the control run. Furthermore, the maximum temperature increase due to convective heating is only about 0.9 K at 9 hr.
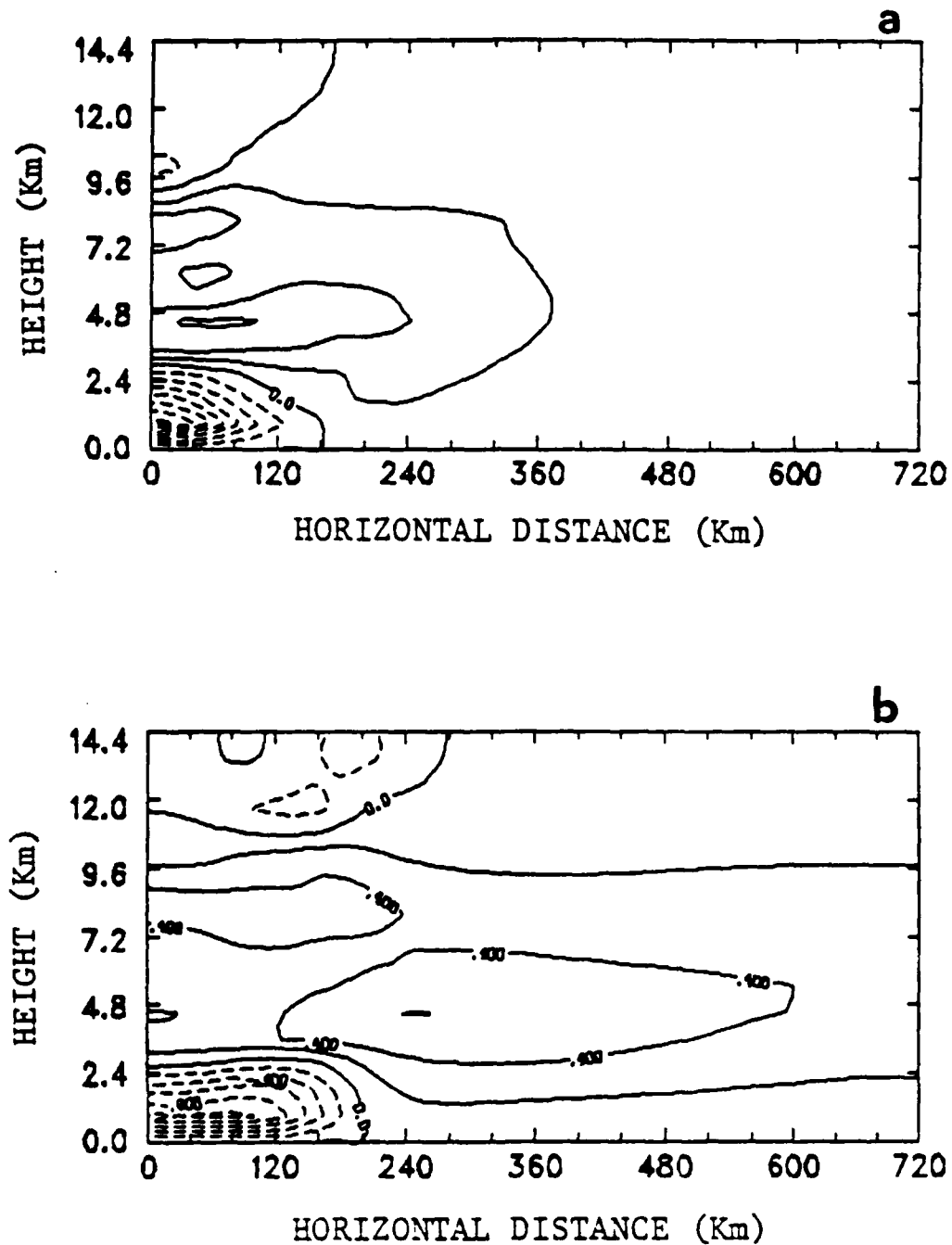
-169-

Fig. 5.29. Cross sections of the deviation of potential temperature (θ′) from the initial condition in units of K in Run 4: (a) at 3 hr with contour interval of 0.1, (b) at 6 hr with contour interval of 0.2, (c) at 9 hr with contour interval of 0.2, and (d) at 12 hr with contour interval of 0.3.
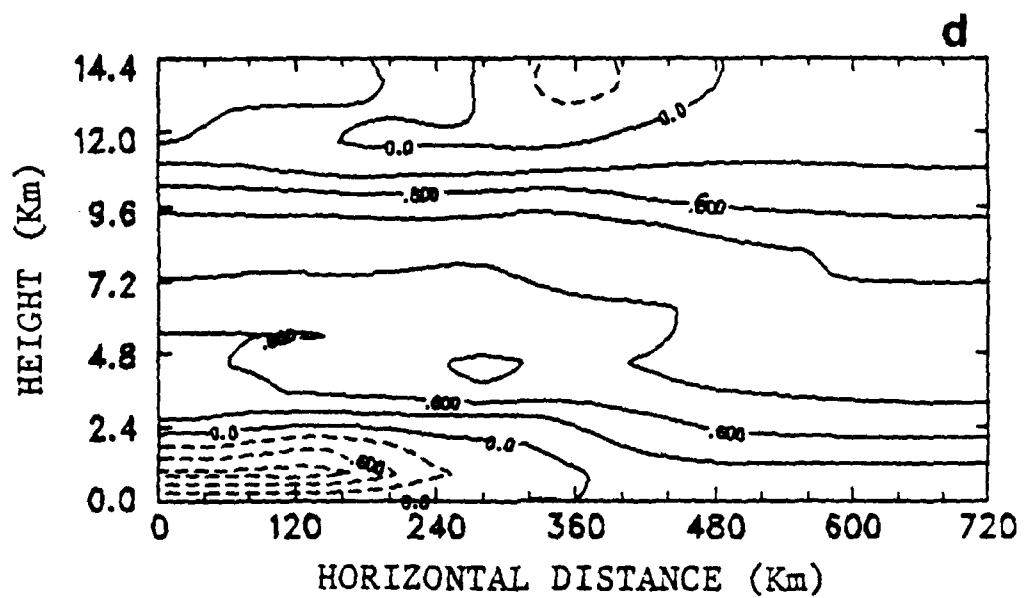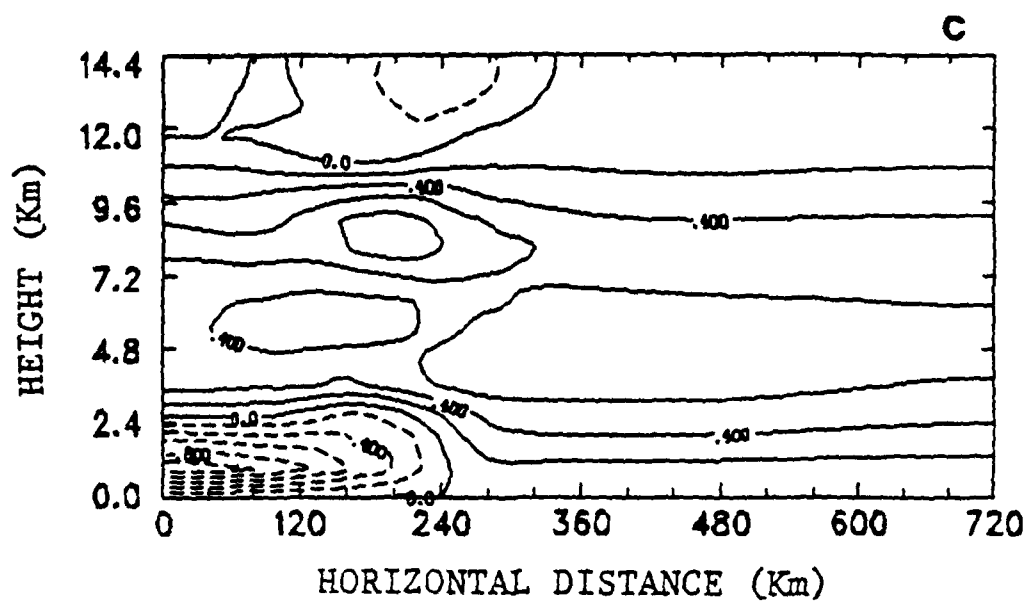
Fig. 5.29. (Continued)

The basic reason for the situation described above can be demonstrated in Fig. 5.30, which is the counterpart of Fig. 5.5, showing the difference in magnitudes between the convective heating and adiabatic cooling for the very beginning of the simulation. It is found in Fig. 5.30 that the excess of the adiabatic cooling over the convective heating in the lower atmosphere is slightly larger than that in Fig. 5.5 while the excess of the convective heating over the adiabatic cooling in the upper atmosphere is slightly smaller. Obviously, these differences are attributed to the modification of the A-S scheme due to the inclusion of the downdraft effects in the cloud layer. Based on the discussion of Figs. 5.5 and 5.30, two important lessons are learned. First, in the present mesoscale model, the early development of the convective system greatly depends upon the difference between the magnitudes of the convective heating and adiabatic cooling. Secondly, we may further confirm our previous statement about the different purposes between the semi-prognostic approach and fully prognostic model in testing a cumulus parameterization scheme. The small difference between the two profiles in Fig. 5.30 or Fig. 5.5 may be of no concern in the semi-prognostic approach but can be extremely crucial in a fully prognostic model, especially in simulating the development of a mesoscale convective system.

It is obvious that the weaker convective activities in this run are also attributed to the temperature drop of the mixed layer resulting from the downdraft effects in terms of the downdraft heat flux and the evaporation of precipitation (see Eq. (4.28)). The result shows that the contributions of these two factors to the decrease of θ_M are about the same in magnitude. As indicated by Frank (1980) in an observational study of GATE convective systems,
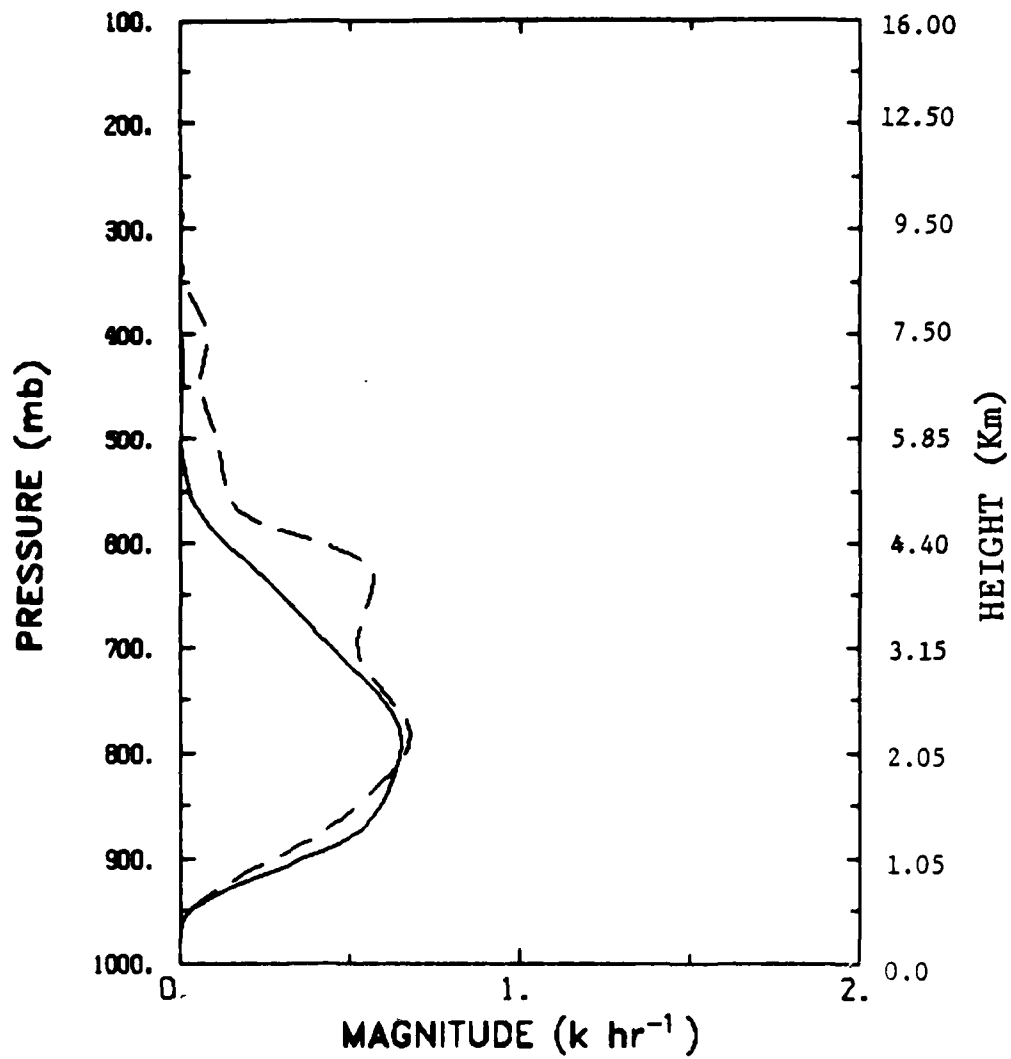
Fig. 5.30. Profiles of convective heating (dashed line) in response to the imposed w_0 and adiabatic cooling (solid line) due to the imposed w_0 in Run 4.

when the boundary layer is disturbed by downdrafts, the convective heating in
the middle and upper troposphere is generally weaker than the boundary layer
cooling and plays a minor role in stabilizing the atmosphere. Observations
also indicate that the stabilization resulting from downdrafts is sufficient to
inhibit further convective development until the boundary layer recovers
(Fitzjarrald and Garstang, 1981). In the preceding paragraph, we have shown
the effect of the modification of the A-S scheme due to the inclusion of
cumulus downdrafts on the heating profile. Here we shall illustrate the
sensitivity of the heating profile to the temperature in the mixed layer. To
do so, we select the center column at 3 hr and compare its heating profile with
the one which is computed from the same atmospheric conditions except for the
mixed layer temperature, which is 1 K higher. The result shown in Fig. 5.31
indicates that a significant difference is apparently present between 750 to
550 mb and below 850 mb and that the case with the lower mixed layer
temperature provides less convective heating. With the recognition that the
model results are sensitive to the difference between the convective heating
and adiabatic cooling at the initial stage, as discussed earlier, another
implication of the result shown in Fig. 5.31 is that the evolution of the
mesoscale fields is sensitive to the initial mixed layer thermodynamic
properties.

Figure 5.32 shows the corresponding w fields at 3, 6, 9, and 12 hr. As
compared with Fig. 5.7, significant differences are found in that (a) the
magnitudes of w are smaller and the maximum of w in the entire simulation is
only about 10 cm s^{-1} at 9 hr, (b) the upward motion area slightly shifts
outward with time, and (c) intense downward motion occupies all of the central
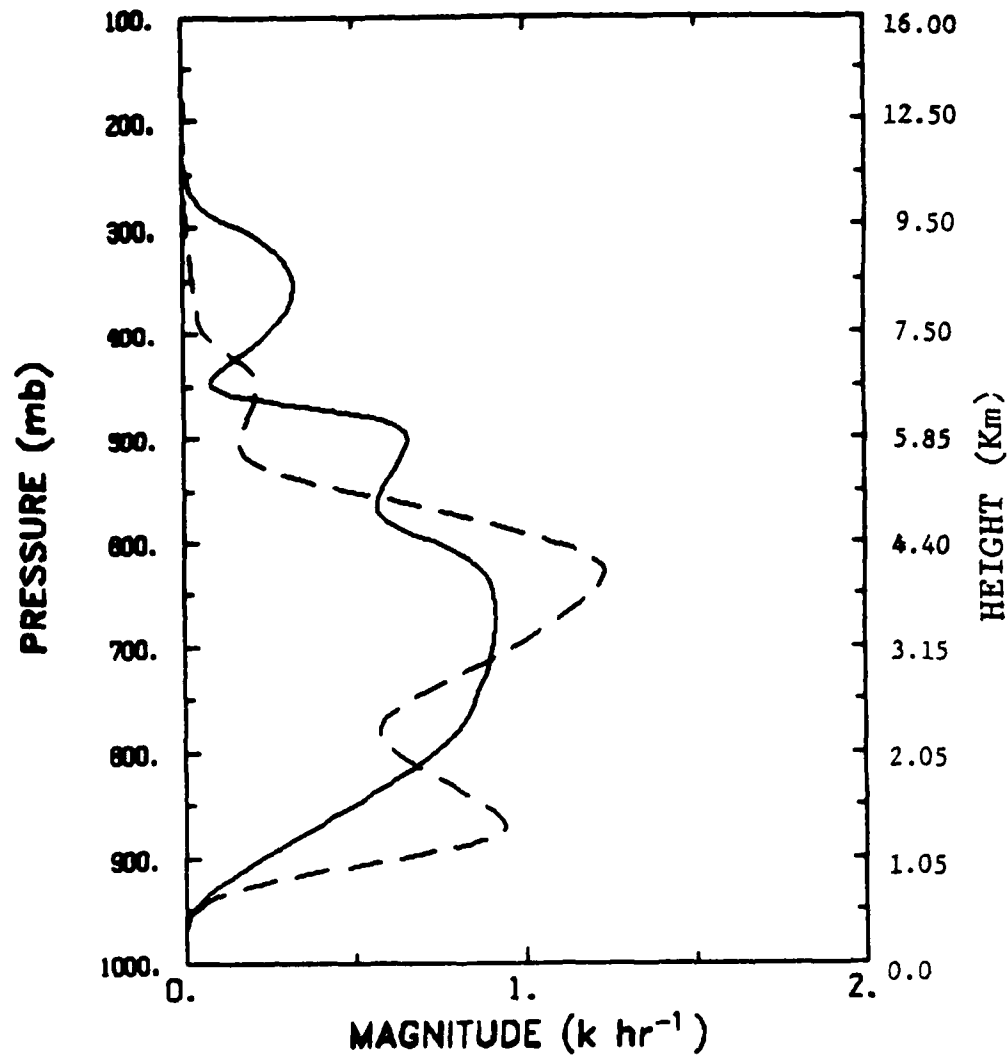
Fig. 5.31. The profiles of convective heating rates. The solid line represents the convective heating rate of the center column at 3 hr in Run 4. The dashed line represents the convective heating rate corresponding to the warmer mixed layer.
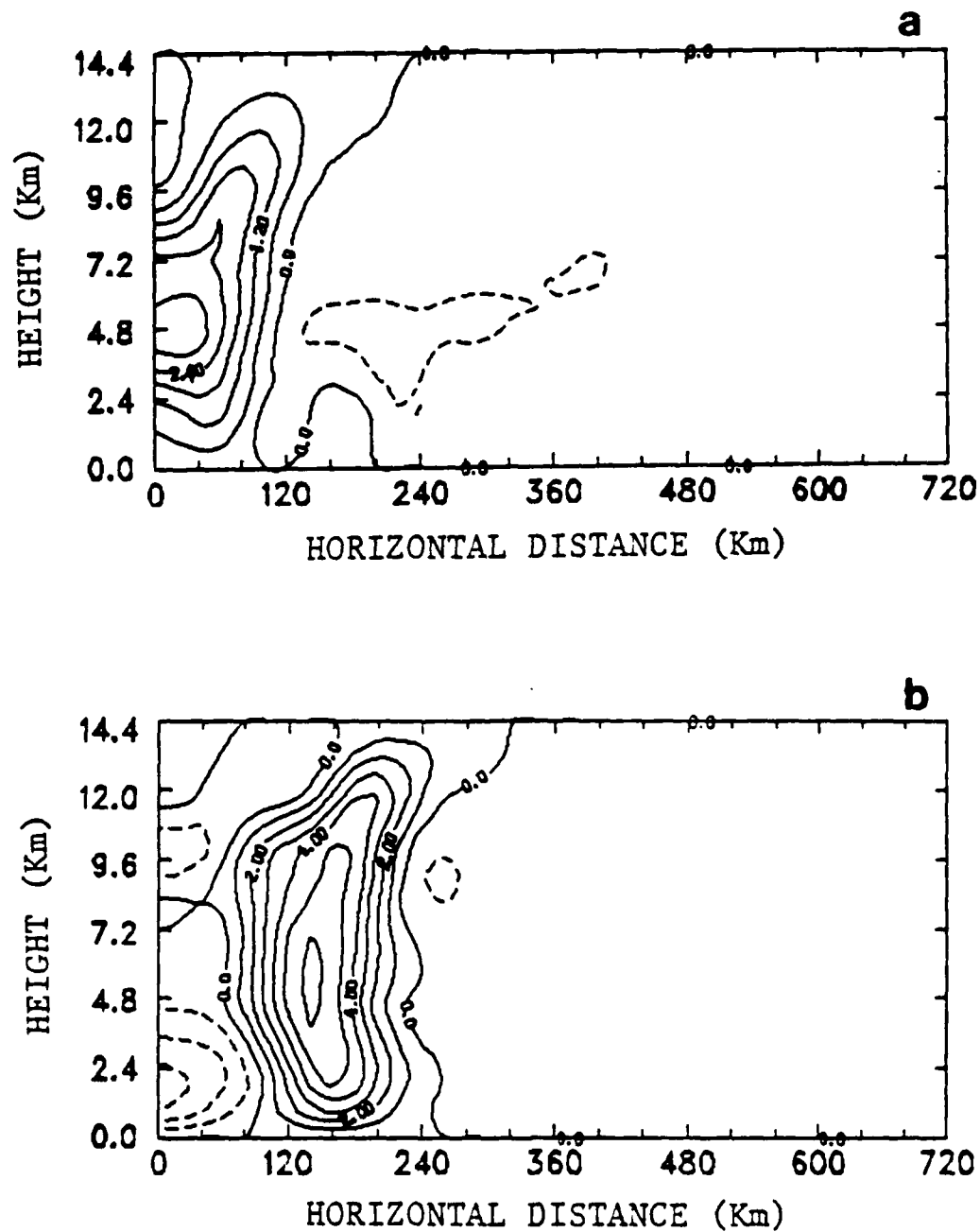
Fig. 5.32. Cross sections of the vertical velocity (w) in units of cm s^{-1} in Run 4: (a) at 3 hr with contour interval of 0.6, (b) at 6 hr with contour interval of 1.0, (c) at 9 hr with contour interval of 1.0, and (d) at 12 hr with contour interval of 1.0.
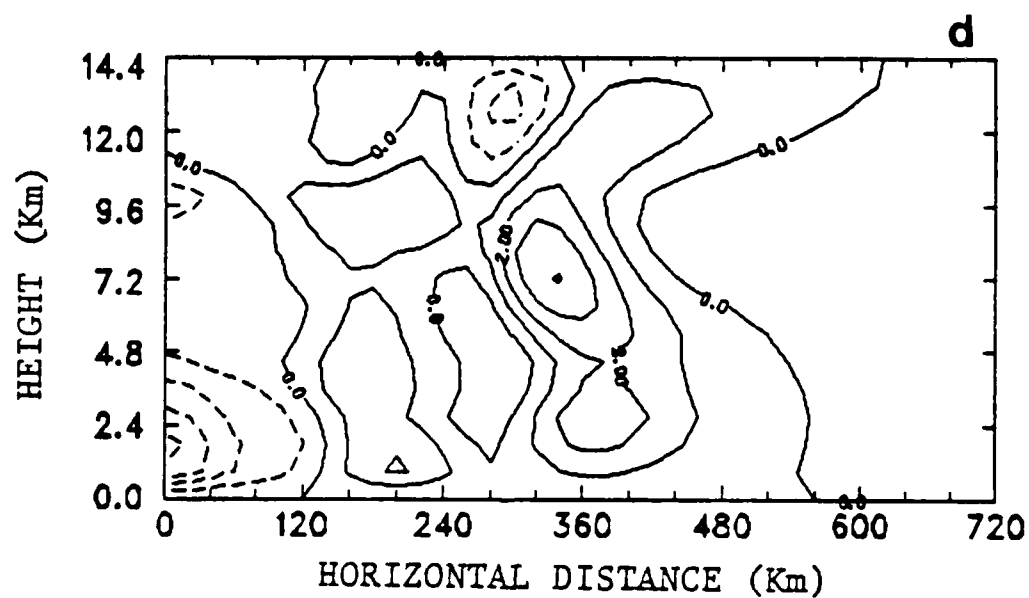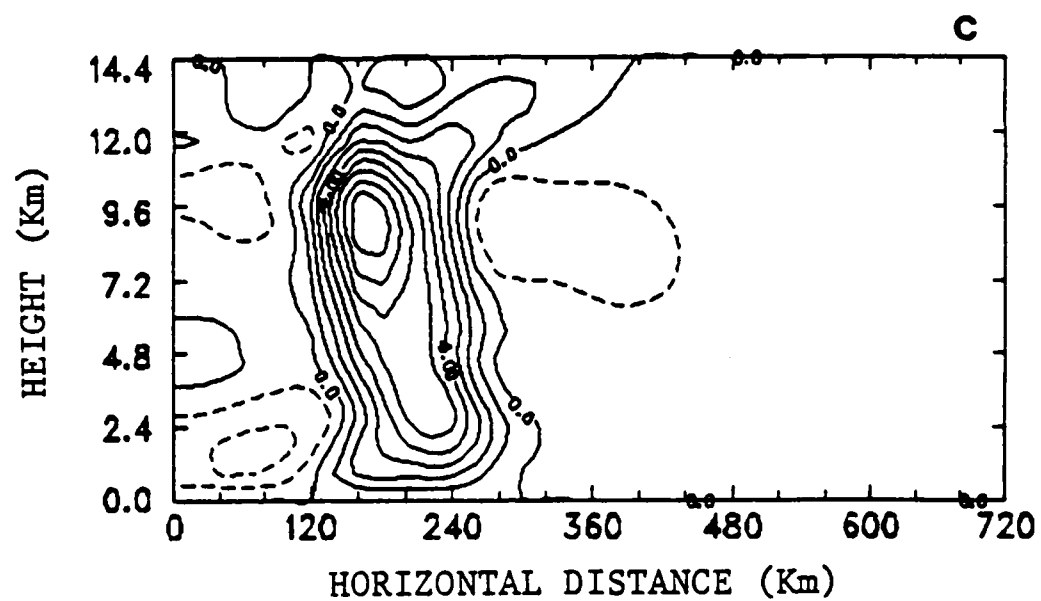
Fig. 5.32. (Continued)

columns at 9 and 12 hr. In passing, it should be mentioned that no distinct change in the mixing ratio in the mixed layer (q_M) is observed because as the downdrafts bring the drier air into the mixed layer, the precipitation evaporates to moisten the mixed layer. Evidently, the experiment with the cumulus downdraft effects presented above has provided less realistic results than the case without the downdrafts. Nevertheless, serving as a conceptional experiment, this simulation does reveal several aspects of the cumulus downdraft effects not only in conjunction with the A-S scheme but also with the simulation of a mesoscale convective system.

5.2.4 The test of Kuo's scheme:

Soong and Tao (1980) made a comparison between the results from explicit calculations for clouds and that derived from Kuo's 1965 cumulus parameterization scheme within the framework of the cumulus ensemble model discussed previously. They found that the cloud heating profile computed by Kuo's scheme had a maximum in the upper atmosphere while the heating rate below 700 mb was negligibly small, which does not agree with the observed heating profile at all. In the present experiment, we shall replace the A-S scheme by Kuo's 1974 scheme (Kuo, 1974) with the parameter b set to 0, as suggested by Kuo (1974) for highly convective regions. Setting b to 0 implies that all of the moisture convergence into an atmospheric column will precipitate to heat the atmosphere. It would be interesting to see whether or not, or to what extent, Kuo's scheme is able to simulate the development of a mesoscale convective system in the present model framework.

The detailed derivation of Kuo's scheme has been given in Kuo (1965, 1974). Here, we briefly summarize the scheme as follows. The total rate of moisture accession per unit horizontal area (M_t) is given by:

$$M_t = \int_0^{z_T} \nabla \cdot (q\vec{V}) \, \rho \, dz + \text{surface evaporation rate} \qquad (5.3)$$

where z_T is the top of the domain and the surface evaporation rate can be expressed by (4.37) or another bulk formula. Having assumed that all of the moisture convergence is for heating the atmosphere, we can determine the rate of cloud production per unit time (Q_c) as:

$$Q_c = M_t / W_h \qquad (5.4)$$

where W_h is expressed by:

$$W_h = \frac{c_p}{L} \int_{z_B}^{z_{ct}} (T_c - T_e) \, \rho \, dz \qquad (5.5)$$

where z_{ct} represents the height of cloud top. Equation (5.5) represents the amount of moisture which will condense and precipitate to raise the environmental temperature (T_e) to cloud temperature (T_c). T_c has the moist adiabatic value and can be obtained by the saturation technique. Now assume that the prediction is made for a time-step Δt giving a temperature T^* without the effects of cumuli at $t + \Delta t$ as:

$$T^* = T(t - \Delta t) + 2\Delta t \cdot F_t \qquad (5.6)$$

where F_t represents the advection terms in the thermodynamic equation. Using T^* and its corresponding T_c to obtain W_h and using the current $\vec{V} \cdot q\vec{V}$ and surface evaporation to obtain M_t, we can determine Q_c by (5.4). Then, an adjusted temperature $T(t + \Delta t)$ is determined by:

$$T(t + \Delta t) = T^* + Q_c \Delta t(T_c - T^*) \tag{5.7}$$

Note that, since the value of M_t is at time t, only one Δt is multiplied in (5.7). Accordingly, the rate of precipitation per unit time per unit volume in the column is $Q_c c_p (T_c - T^*)/L$. Since b is set to 0, there is no increase or decrease of humidity as the convection takes place. During the integration of the model, if the computed amount of M_t exceeds the specified value of 0.3×10^{-4}, the convection is assumed to take place.

It should be mentioned that in this model T_c in (5.7) is determined from the non-entraining plume such that only the highest clouds are allowed to form. Figure 5.33 shows the evolution of w fields for the period from 1 to 5 hr at every 1 hr interval. At 3 hr, the intensity of w reaches its maximum with the magnitude about 10 cm s^{-1}, which is considered significantly smaller in comparison with the observation and the result simulated in the control run. The corresponding θ' fields are shown in Fig. 5.34. The most distinct feature in Figs. 5.33 and 5.34 is the rapid lateral propagation of the convective system with the speed about 30 m s^{-1}. As compared with the results in the control run, it is felt that the fast lateral propagation in the present experiment is mainly due to the heating profile generated by Kuo's scheme. As indicated previously, in the developing stage of the control run, the vertical
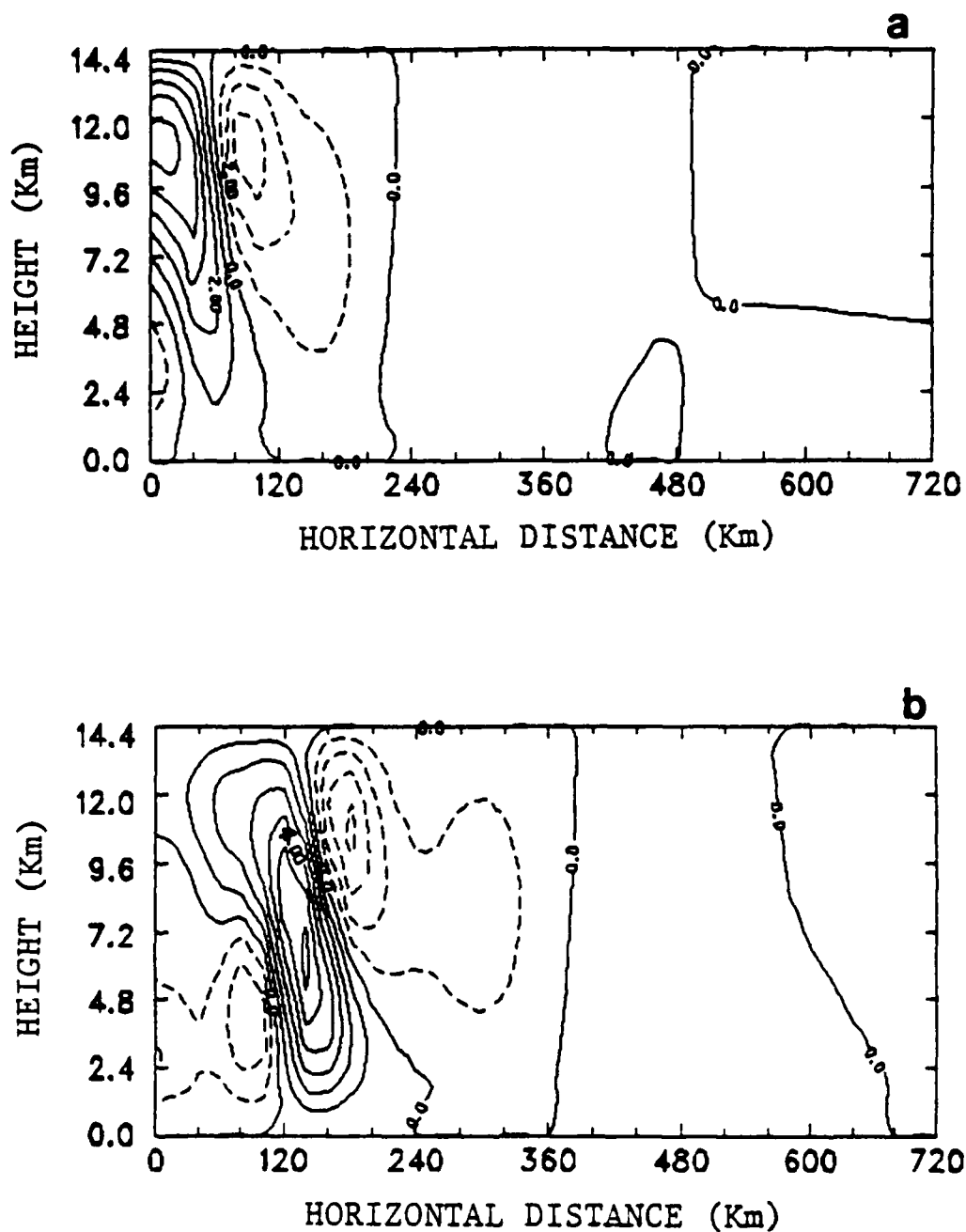
Fig. 5.33. Cross sections of the vertical velocity (w) in units of cm s^{-1} in Run 5 using Kuo's scheme: (a) at 1 hr with contour interval of 1.0, (b) at 2 hr with contour interval of 1.0, (c) at 3 hr with contour interval of 1.0, (d) at 4 hr with contour interval of 1.0, and (e) at 5 hr with contour interval of 1.0.
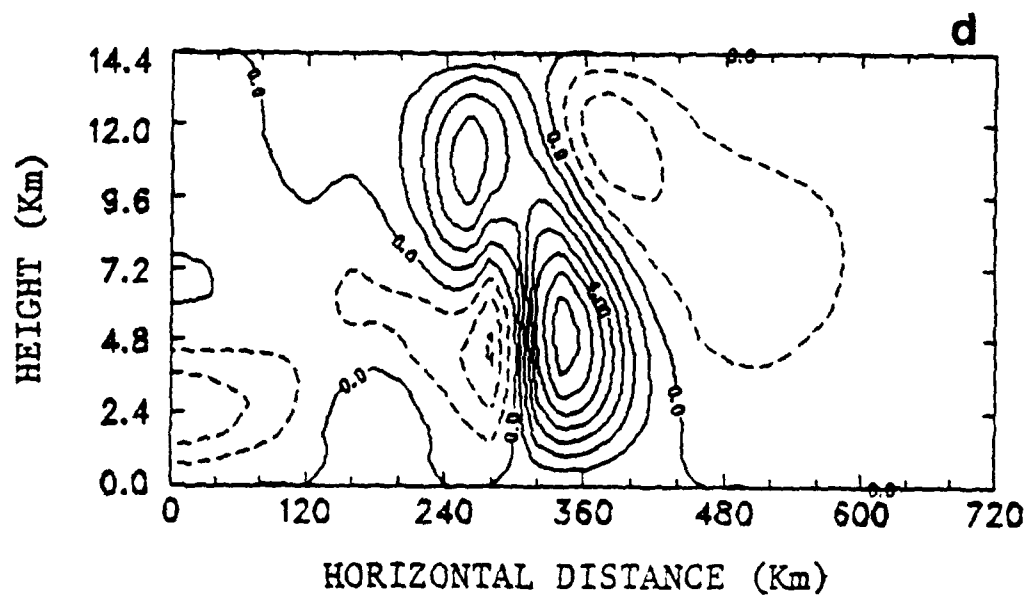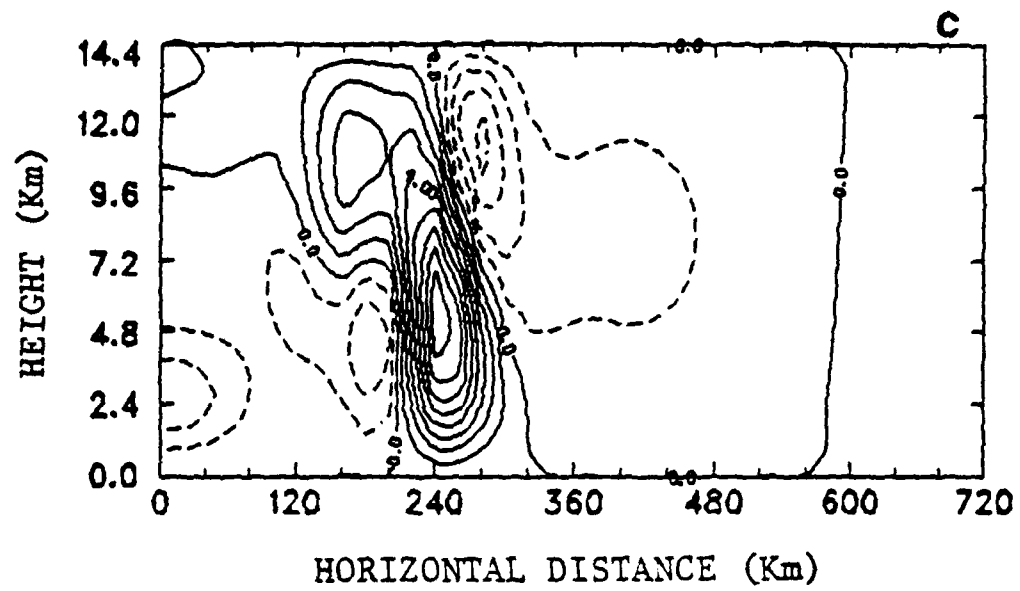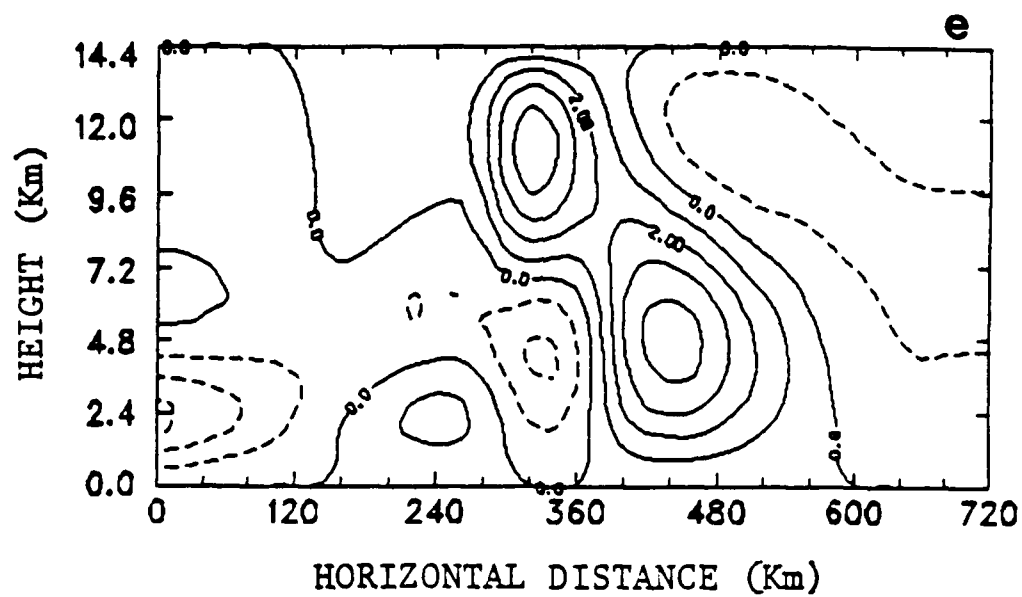
c

d

Fig. 5.33. (Continued)

Fig. 5.33. (Continued)

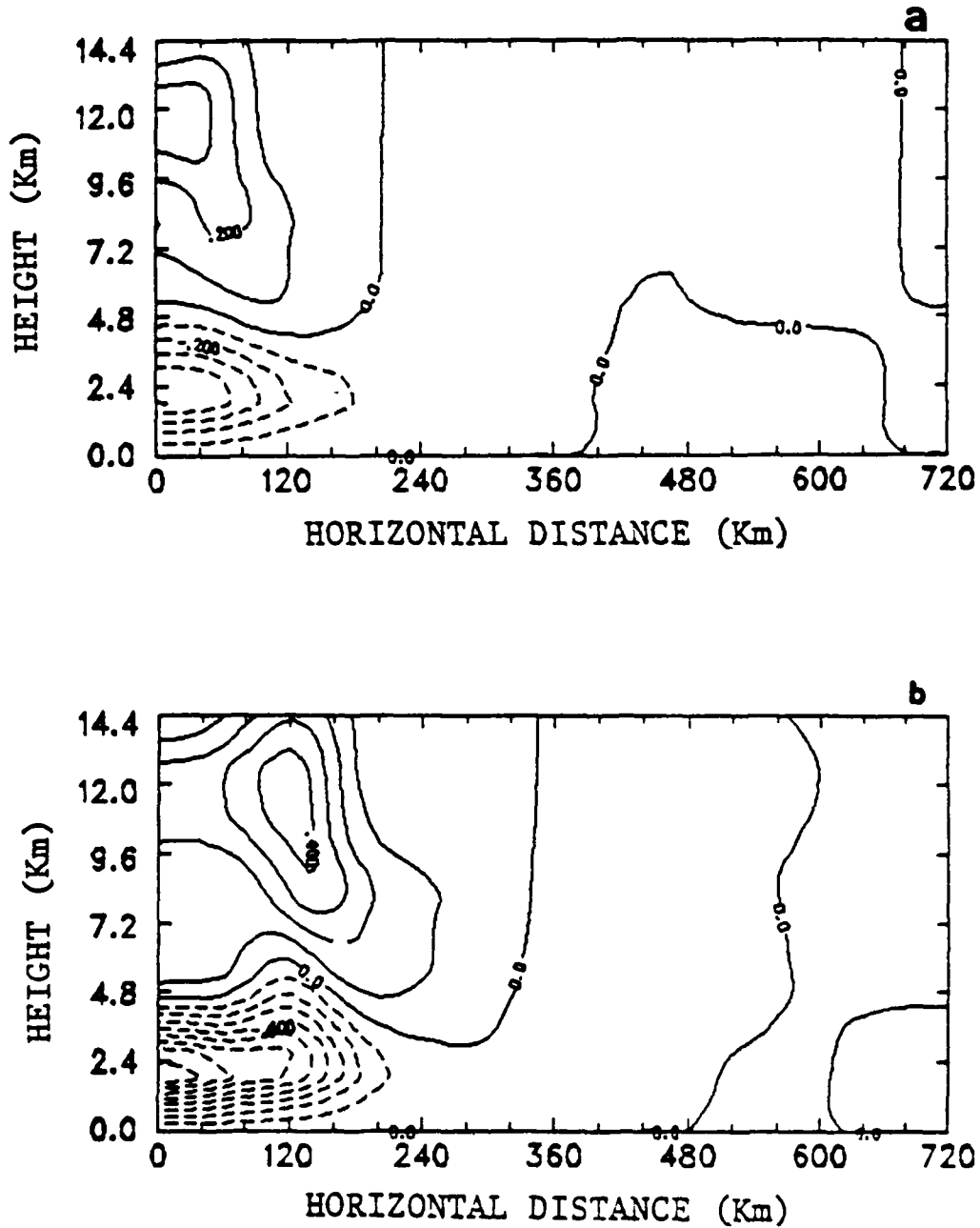Fig. 5.34. Cross sections of the deviation of potential temperature (θ′) in units of K in Run 5 using Kuo's scheme: (a) at 1 hr with contour interval of 0.1, (b) at 2 hr with contour interval of 0.1, (c) at 3 hr with contour interval of 0.2, (d) at 4 hr with contour interval of 0.2, and (e) at 5 hr with contour interval of 0.2.
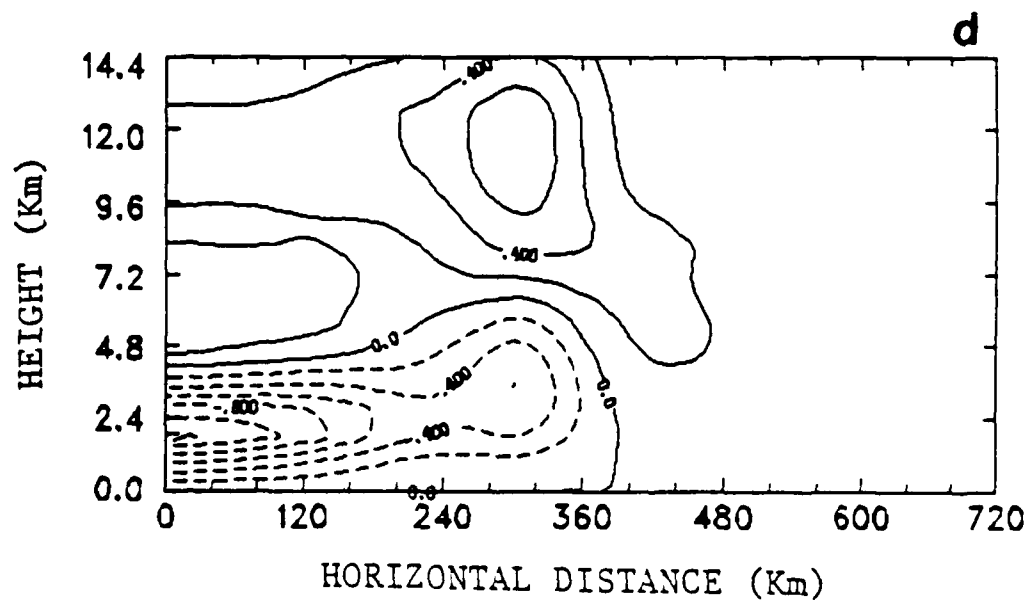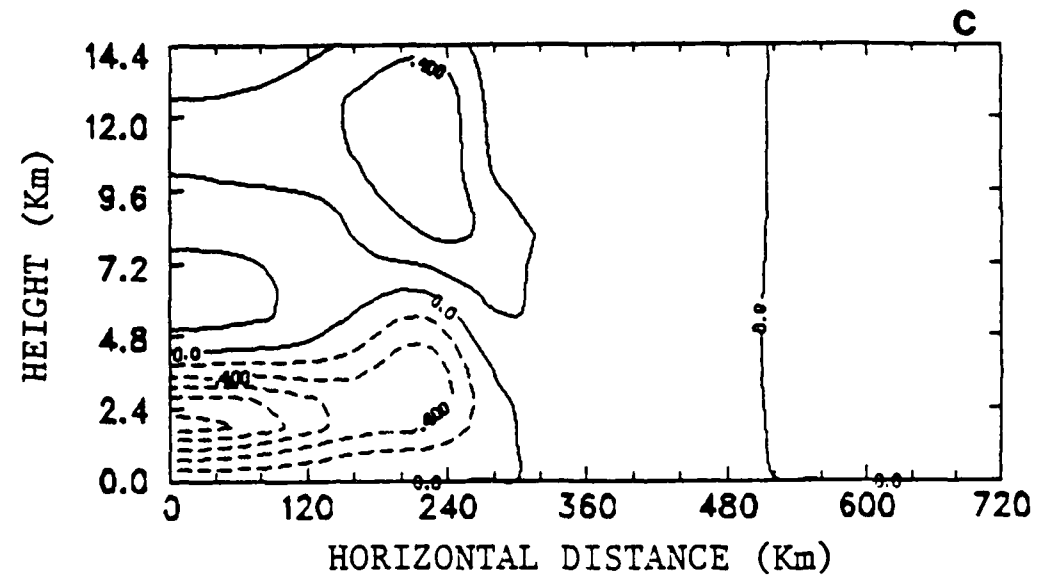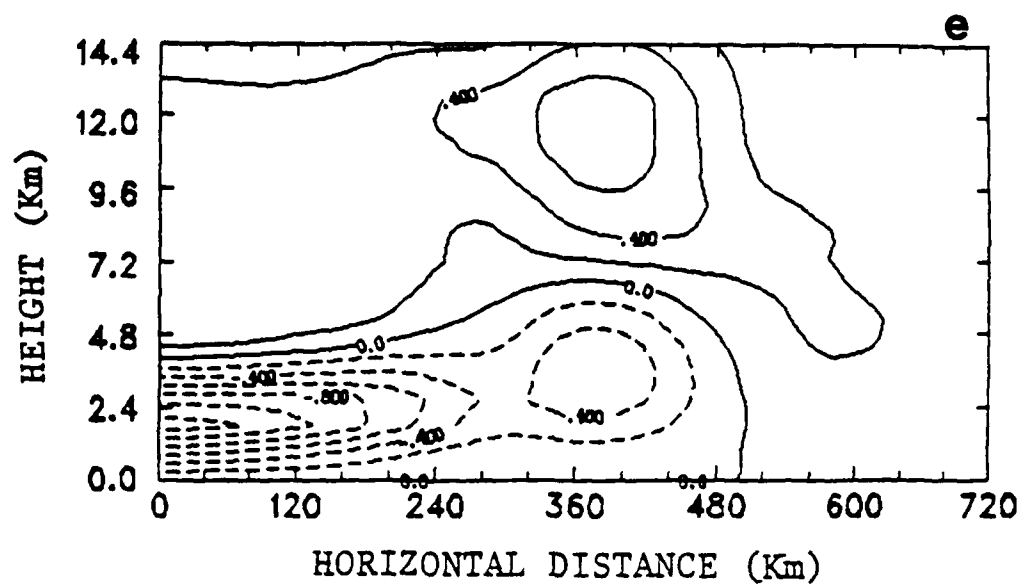
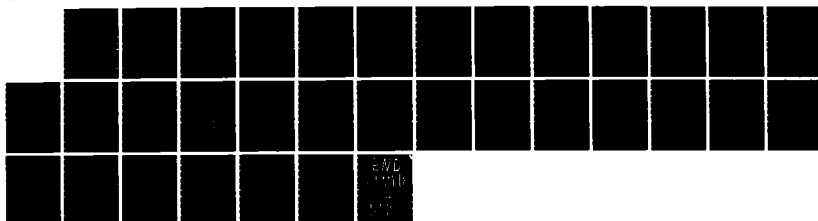Fig. 5.34. (Continued)

Fig. 5.34. (Continued)
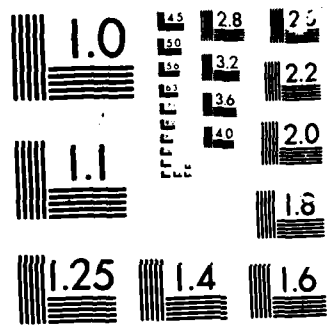
MICROCOPY   CHART

heating profiles have the double maximum distribution, as shown in Fig. 5.9a. Figure 5.35 shows the vertical profile of the convective heating rate for the central column at 1 hr. From Eq. (5.7), it is seen that the amount of convective heating is proportional to $(T_c - T^*)$ which ordinarily has the maximum at upper levels, as illustrated by Fig. 5.35. On the other hand, the negligibly small heating in the lower atmosphere cannot compensate the adiabatic cooling due to the imposed vertical motion (w_0). Accordingly, this results in the large amount of negative temperature anomalies around the lower central portion, as shown in Fig. 5.34.

It is generally believed that a large amount of upper level heating tends to excite gravity waves and causes the lateral propagation. The fast lateral dispersal of the convective heating has been discussed in a review paper by Frank (1983). He indicated that when the atmosphere is heated on a dynamically small scale (i.e., the spatial horizontal scale is smaller than the Rossby radius of deformation), such as the release of latent heat in a convective mesoscale system, the divergence field is usually not significantly constrained due to the lack of stiffness of rotational flow resulting from the weakness of inertial instability. Thus, one net result is the lateral propagation of the induced warming. Now recall that the experiment presented in Section 5.2.1 also demonstrates similar propagation after the low-level forcing (w_0) is deleted (and, consequently, so is the low-level heating), as shown in Fig. 5.18, while no such propagation is observed in the control simulation. Thus, it is felt that sufficient low-level heating may be indispensable to prevent the convective system from propagating.
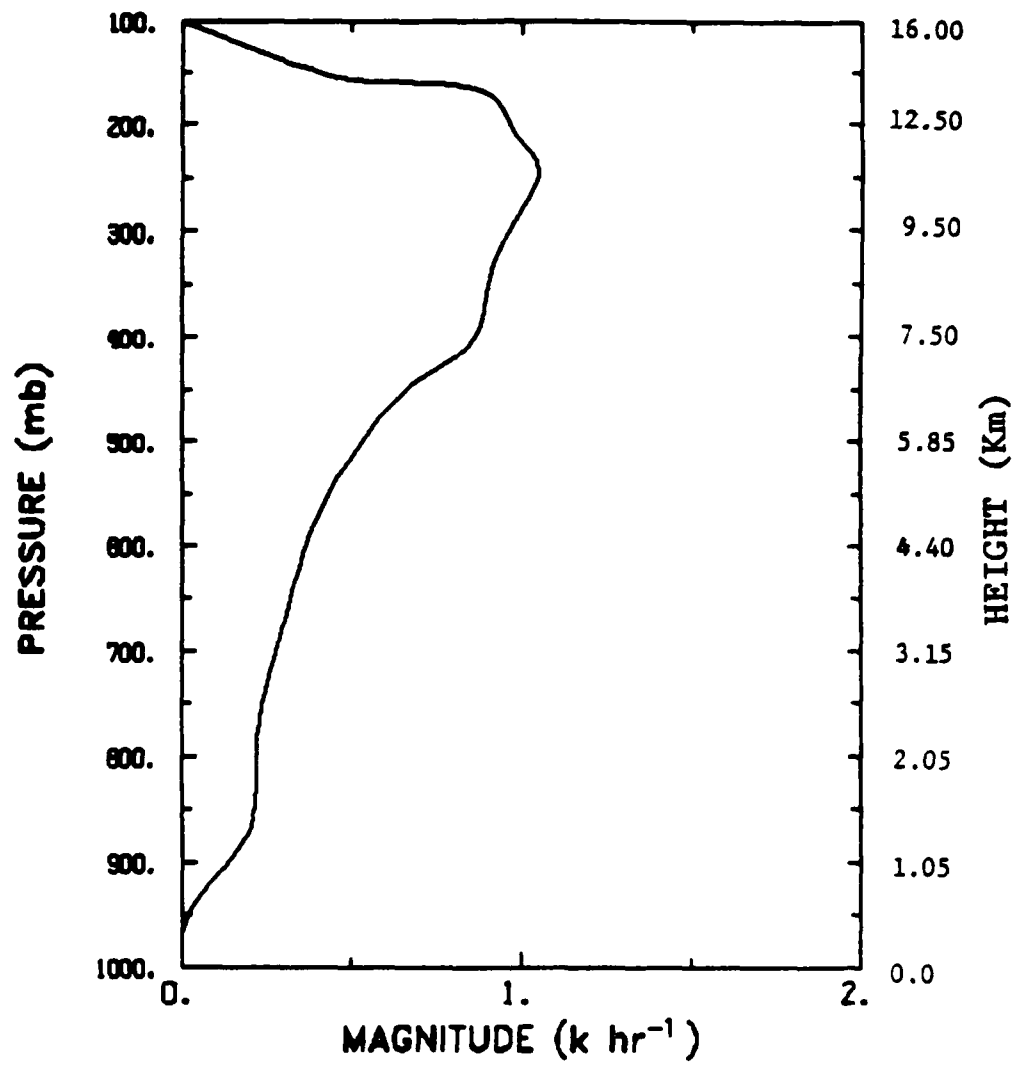
Fig. 5.35. The vertical profile of convective heating of the center column at 1 hr in Run 5 using Kuo's scheme.

CHAPTER VI

SUMMARY AND CONCLUSION

In this report, we first reviewed the Arakawa-Schubert cumulus parameterization scheme in a framework that conceptually divides the mutual interaction of the cumulus convection and larger-scale disturbances into the categories of the large-scale budget requirements and the quasi-equilibrium assumption of the cloud work function as presented in Chapter 2. The quasi-equilibrium assumption asserts a near balance between the generation of moist convective instability due to large-scale processes and its destruction due to the clouds. Since the A-S scheme bears considerable complexity and, thereby, different implementations may produce quite different results, we have been cautious in selecting the computational algorithm, as reported in Section 3.2. The algorithm employed in this report is different from that used by Lord (1978, 1982) and appears to be capable of providing more accurate results. We also reviewed the technical aspects involved in solving the cloud base mass flux distribution equation, which has been restated by a linear programming problem. A software package was found to be very efficient in solving the problem.

We first applied the A-S scheme through the semi-prognostic approach to two different data sets: one for the tropical cloud band event and the other for the composite data for GATE Phases II and III. Basically, the semi-prognostic approach is designed to investigate the capability of a cumulus parameterization scheme in reproducing the observed cloud heating and drying

profiles. The performance of the A-S scheme presented in Section 3.3 appears quite successful in serving the purpose. More importantly, the results confirm the potential advantages of the quasi-equilibrium assumption, which is considered the core of the A-S scheme. Nevertheless, a deficiency of the A-S scheme was found to lie in the underestimation of the condensation and evaporation rates when the semi-prognostic results were compared with those derived from the cloud ensemble model. Even though, from a practical point of view, this deficiency can be considered minor, the results and the discussion of the cumulus downdraft effects in Section 3.4 have pointed out a way to improve the A-S scheme. In doing so, we have modified the A-S scheme by incorporating the downdraft model formulated by Johnson (1976) but with a different parameter ϵ which is a measure of the downdraft intensity relative to the updraft intensity. The results showed that the modified A-S scheme not only substantially improved the condensation and evaporation rates but also predicted a downdraft mass flux which agreed fairly well with the result of the cloud ensemble model. A drawback introduced by this downdraft model lies in the overestimation of the moistening effect resulting from the detrainment of the cloud air at the cloud tops. Because of the lack of a sound scientific basis to determine ϵ, it is felt that this downdraft study through the semi-prognostic approach is only an initial step toward a more complete examination of the role played by the cumulus downdrafts in the cumulus parameterization problem for prognostic purposes.

A more severe test of the A-S scheme was subsequently made by incorporating the scheme into a two-dimensional primitive mesoscale model to simulate the tropical cloud band event that was considered in the previous

paragraph. The details of the mesoscale model have been presented in Chapter 4. The principal goals have been to investigate (a) the development of the mesoscale convective system resulting from the convective heating as estimated by the A-S scheme, (b) the evolution of the mesoscale fields and its associated physical processes, (c) the sensitivity of the model to different environmental conditions, and (d) the response of the A-S scheme to the mesoscale circulation.

Section 5.1 presented the results of a 24-hour integration for the control simulation in which the effects of cumulus downdrafts and the vertical shear of the ambient wind were not included. The evolution of the mesoscale circulation in conjunction with the convective heating due to cumulus convection, the adiabatic cooling due to total upward vertical motion, and the adiabatic warming due to mesoscale downward motion was examined. Initial conditions were calm except for the imposed large-scale, low-level circulation $[w_0, u_0]$ that releases the potential instability through the applications of the A-S scheme. The first 6-hour period was dominated by the convective heating located in the central portion of the domain where the imposed w_0 was located. The second 6-hour period was still basically dominated by the convective heating. During this period, however, the accumulation of the adiabatic warming outside the cloud cluster area gradually became appreciable. This subsequently generated a reverse circulation at the low levels and the decaying stage set in for the third 6-hour period. The last 6-hour period was more or less in a steady state. One gratifying aspect is that the model results bear considerable resemblance to many aspects of the observations including (a) the evolution of area-averaged vertical velocity ($\bar{w}$), (b) the intensity and distribution of

surface precipitation, (c) the width of the mesoscale convective system, and (d) the development of low-level downward motion during the decaying stage.

Although the model can provide the characteristics of the decay of the system in terms of the rapid weakening of upward motion and the development of downward motion at the lower atmosphere with self-consistent physical processes, the realism of this decaying situation may be uncertain when one recalls the following fact. It is commonly documented that the decay of individual thunderstorms is caused by the low-level water particles which reduce the buoyancy force around the cloud base and consequently induce precipitating downdrafts to cool and dry the sub-cloud layer. Obviously, all of these effects are not included in this particular simulation. Nevertheless, the statement described above is mostly deduced from the cloud simulation with explicit calculation for the cloud-scale properties for an individual convective entity. To date, the complete physical reasons for the dissipation of the mesoscale convective systems are not well understood. If we take a more macroscopic point of view, the physical processes of the decaying stage deduced from our mesoscale model, as discussed in Sections 5.1 and 5.2.1, may be valid to some extent. This argument appears especially significant when the decaying processes presented in Section 5.2.1 for run 2 are considered, where we dealt with a decaying situation by suddenly deleting the large-scale, low-level forcing.

A test on the effects of the vertical wind shear was presented in Section 5.2.2. Since the water loading is not included in this mesoscale model, no

substantial differences from the control run are observed except for the slight shift of the convective activities to the downwind area.

A test on the effects of the cumulus downdrafts was presented in Section 5.2.3. It was found that the A-S scheme with the incorporation of the downdrafts tended to stabilize the atmosphere by the relatively large excess of the adiabatic cooling over the convective heating in the lower atmosphere at the initial stage. In addition, the cooling of the mixed layer due to the detrainment of downdrafts and the evaporation of precipitation also reduced the convective heating significantly. Thus, less realistic results were obtained when compared with the control simulation. This experiment also revealed that the evolution of the mesoscale fields is highly contingent upon the initial mixed layer thermodynamic properties and the difference between the magnitudes of the convective heating and adiabatic cooling at the beginning of the simulation. However, this sensitivity by no means implies that the mesoscale model presented in this dissertation is a susceptible one. As indicated by Frank (1983), in "dynamically small" circulations such as a mesoscale convective system, the timing and magnitude of the latent heat release are dominant factors in determining the life cycle and structure of the convective system because the divergent wind field is relatively strong in such a system and is very sensitive to the convective heating.

An experiment was carried out in Section 5.2.4 by replacing the A-S scheme by Kuo's 1974 scheme. The results indicated that Kuo's scheme gave a much less favorable comparison, lying in the rapid lateral propagation of the convective system. We attributed this phenomenon to the large amount of convective

heating in the upper atmosphere and the negligibly small amount in the lower atmosphere since Kuo's scheme assumes that the vertical heating is proportional to the temperature difference between the cloud and its environment. In combination with the effect of the relatively strong adiabatic cooling at the low levels due to the imposed w_0, the net result was the rapid lateral dispersal of the convective system.

In essence, this study examined the Arakawa-Schubert cumulus parameterization scheme through the semi-prognostic approach and the mesoscale simulation of a tropical convective system. Both applications demonstrated quite encouraging results. The former served as a basic test in evaluating the scheme. Without its satisfactory performance, it would have been meaningless to further incorporate the scheme into any fully prognostic model. The mesoscale simulation presented here seems to be the first attempt to investigate the evolution of a tropical cloud cluster with the inclusion of the A-S scheme in the primitive prognostic equations. We are pleased not only that the simulated results bear considerable resemblance to the observations but also that this study reveals some intrinsic nature of the A-S scheme as the convective system evolves.

As far as future research is concerned, we divide our intention into four steps. The first one is to apply the same semi-prognostic method to a midlatitude data set to examine whether or not, or to what extent, the quasi-equilibrium hypothesis works in the extratropical atmosphere. The second step, which certainly depends upon the performance of the first one, is to use the same mesoscale model to simulate extratropical mesoscale convective systems.

The third step is to apply the framework of the mesoscale model but with coarser grids to easterly wave disturbances to investigate the ability of the model in reproducing the tropical large-scale phenomena. The fourth step is to incorporate the A-S scheme into a regional prediction model or general circulation model to test the ability of the scheme in simulating the observed synoptic-scale or global distributions of cloud effects and precipitation. As should be expected, the accomplishment of this task is also contingent upon other physical processes, especially the boundary layer parameterization, which must be able to resolve well the coupling processes between the cloud layer and boundary layer (Suarez et al., 1983).

APPENDIX A

CLOUD EQUATIONS

A.1 The cloud model for cumulus sub-ensembles:

The one-dimensional steady-state entraining cloud model used in the A-S scheme can be represented by the following budget equations:

mass:

$$\frac{\partial \eta(z,\lambda)}{\partial z} = \lambda \eta(z,\lambda) \qquad \text{(A.1)}$$

static energy:

$$\frac{\partial}{\partial z} [\eta(z,\lambda)s_c(z,\lambda)] = \frac{\partial \eta(z,\lambda)}{\partial z} \bar{s}(z) + L\eta(z,\lambda)c(z,\lambda) \qquad \text{(A.2)}$$

moist static energy:

$$\frac{\partial}{\partial z} [\eta(z,\lambda)h_c(z,\lambda)] = \frac{\partial \eta(z,\lambda)}{\partial z} \bar{h}(z) \qquad \text{(A.3)}$$

water content:

$$\frac{\partial}{\partial z} [(q_c(z,\lambda) + \ell(z,\lambda))] = \frac{\partial \eta(z,\lambda)}{\partial z} \bar{q}(z) - \eta(z,\lambda)r(z,\lambda) \qquad \text{(A.4)}$$

where $c(z,\lambda)$ is the condensation rate, serving as a source for the static

energy and a sink for water vapor and $r(z,\lambda)$ is the rainwater converted from the liquid water $\ell(z,\lambda)$ by:

$$r(z,\lambda) = c_0 \ell(z,\lambda) \tag{A.5}$$

where c_0 is the conversion coefficient and is specified by the value of 2×10^{-5} cm^{-1}. The total rainwater per unit height (R) can be calculated by:

$$R(z) = \int_0^{\lambda_D(z)} m_B(\lambda)\eta(z,\lambda)r(z,\lambda)d\lambda \tag{A.6}$$

Solving (A.1), we obtain the normalized mass flux:

$$\eta(z,\lambda) = \exp\{\lambda(z - z_B)\} \tag{A.7}$$

With the use of (A.1), we can solve h_c from (A.3):

$$h_c(z,\lambda) = \frac{1}{\eta(z,\lambda)} \left[h_c(z_B,\lambda) + \lambda \int_{z_B}^{z} \eta(z',\lambda)\bar{h}(z')dz' \right] \tag{A.8}$$

Assuming that the air is saturated in the clouds and the pressure difference between the cloud and environment is neglected, we obtain two approximations (Arakawa and Schubert, 1974):

$$s_c(z,\lambda) - \bar{s}(z) = \frac{1}{1+\gamma} (h_c(z,\lambda) - \bar{h}^*) \tag{A.9}$$

$$q_c(z,\lambda) - \bar{q}^*(z) = \frac{\gamma}{1+\gamma} \frac{1}{L} (h_c(z,\lambda) - \bar{h}^*) \qquad (A.10)$$

$$\gamma = \frac{L}{c_p} \left(\frac{\partial \bar{q}^*}{\partial \bar{T}}\right)_{\bar{p}} \qquad (A.11)$$

substituting (A.8) into (A.9) and (A.10), we can respectively obtain s_c and q_c, and subsequently substituting q_c into (A.4), $\ell(z,\lambda)$ can be solved. With the known $\ell(z,\lambda)$, we can determine $\hat{\ell}(z)$ in (2.7) and (2.8) by:

$$\hat{\ell}(z) = \ell(z,\lambda_D(z)) \qquad (A.12)$$

where $\lambda_D(z)$ represents the fractional entrainment rate of the sub-ensemble which has the detrainment level at z. The schematic d..agram of the vertical structure of a sub-ensemble and the arrangement of the cloud variables is shown in Fig. A.1.

A.2 The determination of λ:

Figure A.2 shows the schematic diagram of the distribution of the cloud spectrum for a cumulus ensemble. To determine λ for each sub-ensemble, we first prescribe the cloud top nonbuoyancy condition by:

$$\hat{h}_c(i) = \bar{h}^*(i) \qquad (A.13)$$

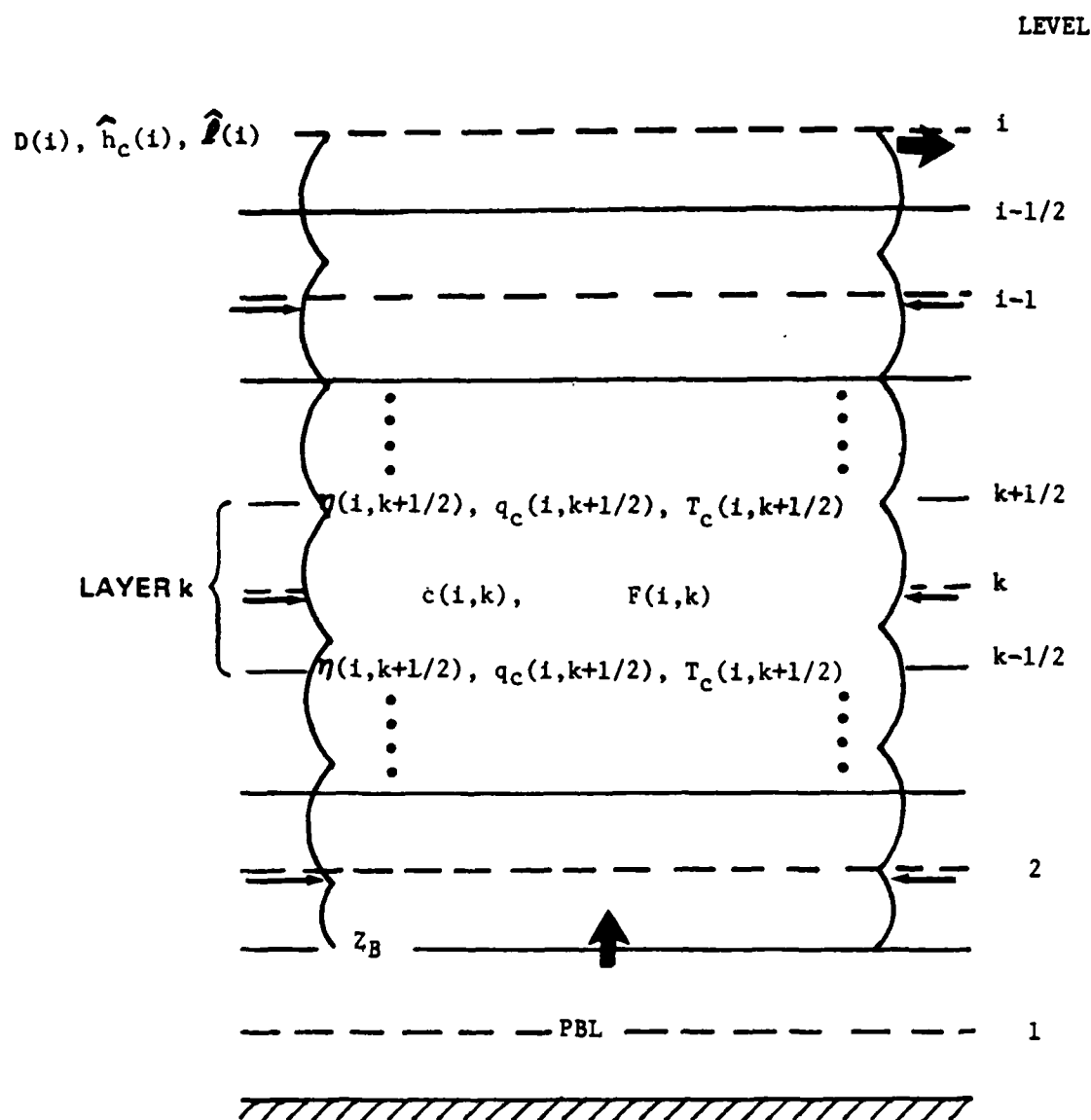where $\hat{h}_c(i)$ represents the h_c at the top of the ith sub-ensemble which detrains

Fig. A.1: The schematic diagram of the vertical structure of the sub-ensemble cloud i where η, q_c, and T_c are located at half-integer levels and condensation rate (c) and vertical convergence of heat and moisture fluxes (F) located at integer levels. The cloud top conditions $D(i)$, $h_c(i)$, and $\ell(i)$ are located at level i. The thin arrows denote the entrainment from the environment. The vertical thick arrow denotes the cloud base mass flux originating from the PBL. The horizontal thick arrow denotes the detrainment of cloud air.
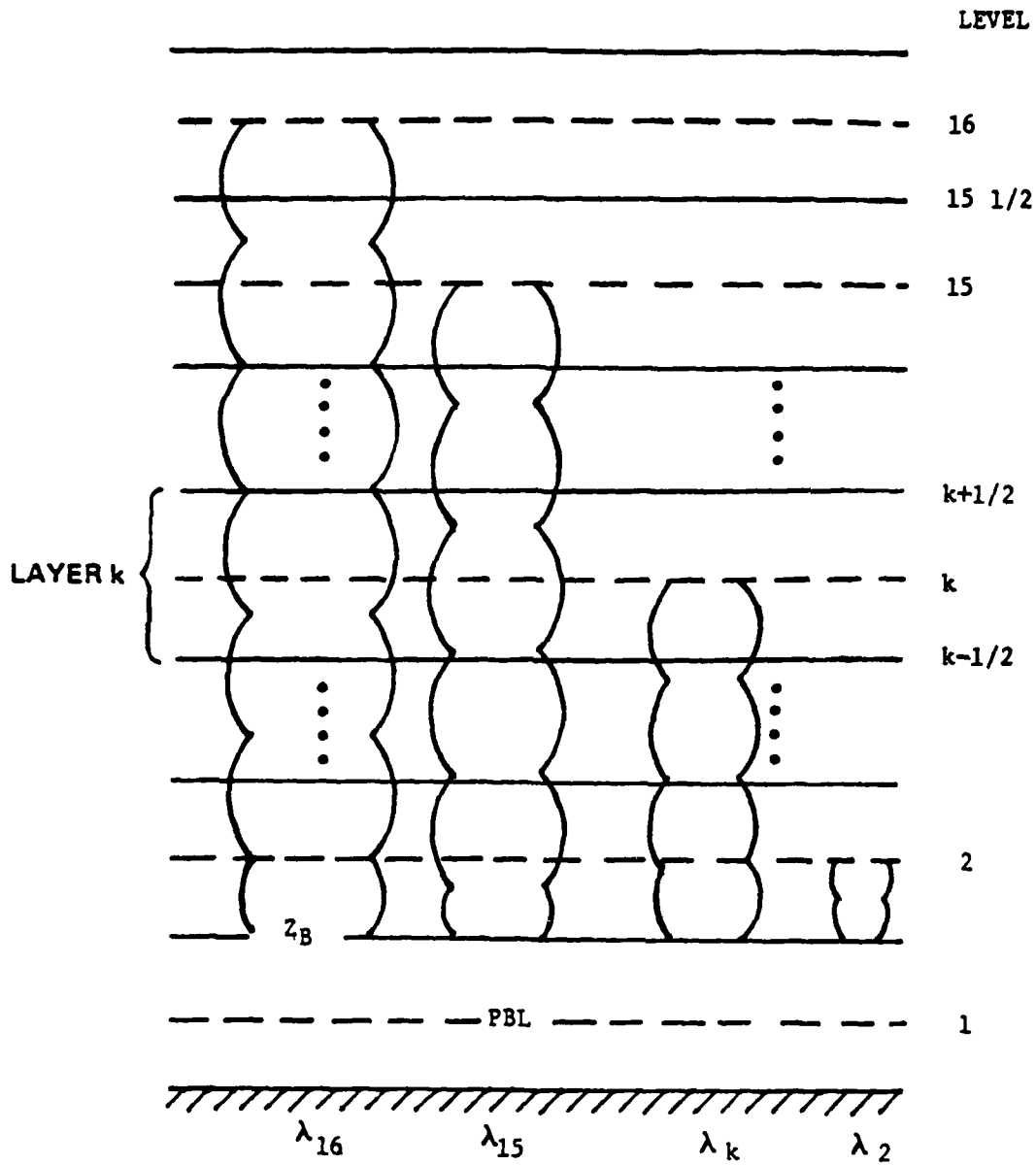
Fig. A.2: The schematic diagram of the distribution of cloud spectrum for a cumulus ensemble in which the entrainment rates have the relation as $\lambda_{16} < \lambda_{15} < \ldots < \lambda_k \ldots < \lambda_2$. It is also indicated that the smaller λ has the larger cross section of the cloud.

at the level i and $\bar{h}^{*}(i)$ is the large-scale saturated moist static energy at the level i. Then, using (A.13) and (A.8) and inserting the cloud base condition

$$h_c(z_B,\lambda) = h_M \qquad\qquad (A.14)$$

into (A.8), we can iteratively determine the fractional entrainment rate for the ith sub-ensemble (λ_i) with the use of (A.7). Thus, it is evident that the value of h_M in (A.14) is very crucial in determining the properties of sub-ensembles.

A.3 The cloud model for cumulus downdrafts:

Since we model the cumulus downdraft practically as an "inverted" updraft (see Fig. A.3), the cloud equations for downdrafts can be easily deduced from those for updrafts presented in Section A.1:

mass:

$$\frac{\partial \eta_d(z,\lambda)}{\partial z} = -\lambda \eta_d(z,\lambda) \qquad\qquad (A.15)$$

static energy:

$$\frac{\partial}{\partial z} [\eta_d(z,\lambda)s_{cd}(z,\lambda)] = \frac{\partial \eta_d(z,\lambda)}{\partial z}\,\bar{s}(z) - \eta_d(z,\lambda)E(z,\lambda) \qquad (A.16)$$
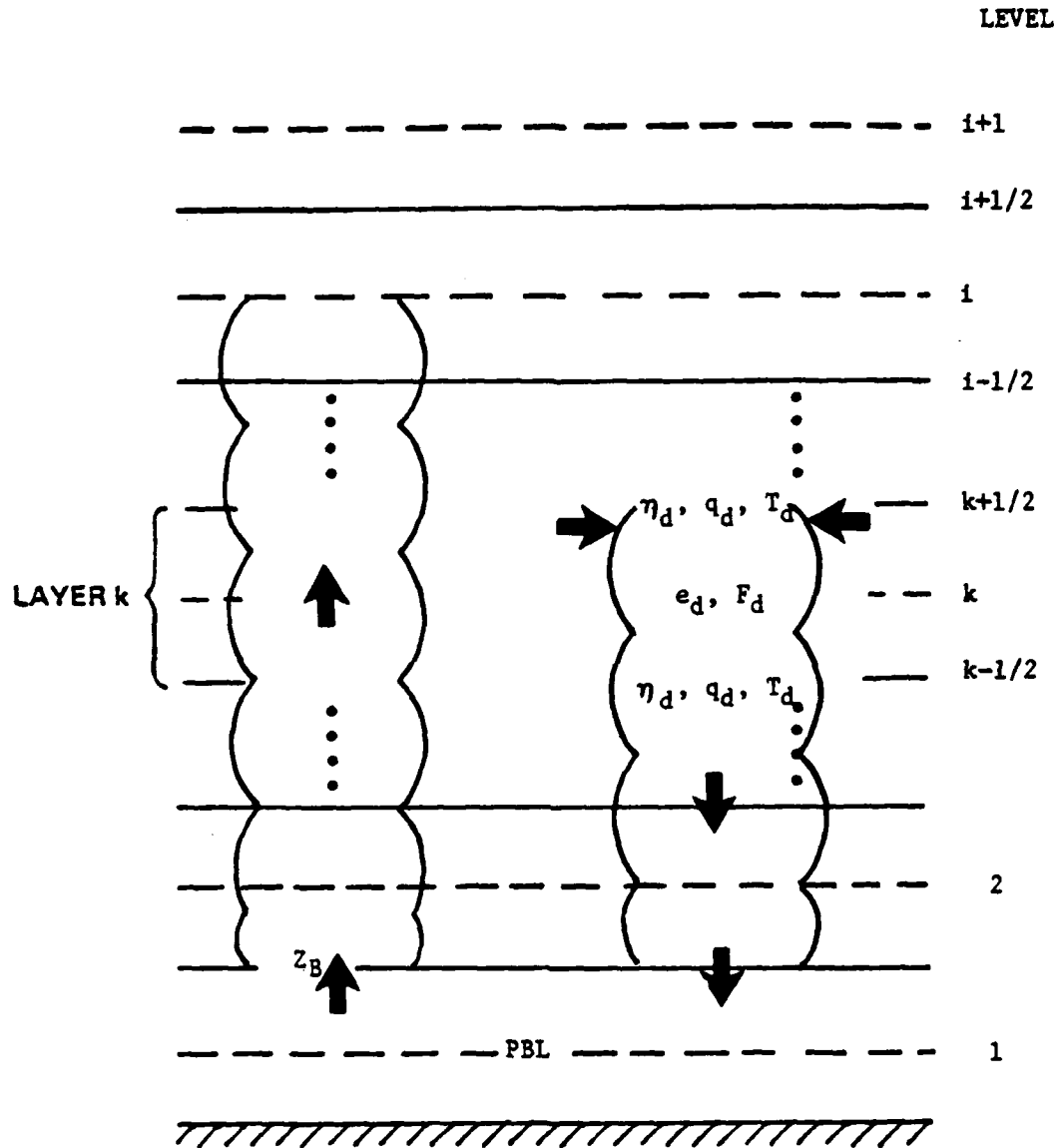
moist static energy:

LEVEL

Fig. A.3: The schematic diagram of the vertical structure of a downdraft element. The details of the accompanying updraft have been illustrated in Fig. A.1. e_c denotes the evaporation rate in the downdraft.

$$\frac{\partial}{\partial z} [\eta_d(z,\lambda) h_{cd}(z,\lambda)] = \frac{\partial \eta_d(z,\lambda)}{\partial z} \bar{h}(z) \qquad (A.17)$$

water vapor:

$$\frac{\partial}{\partial z} [\eta_d(z,\lambda) q_{cd}(z,\lambda)] = \frac{\partial \eta_d(z,\lambda)}{\partial z} \bar{q}(z) + \eta_d(z,\lambda) E(z,\lambda) \qquad (A.18)$$

where $E(z,\lambda)$ is the evaporation rate from the falling precipitation and is a sink for static energy and a source for water vapor. It is seen that a negative sign is in front of λ in (A.15), which illustrates the nature of the "inverted plume." It is also seen that there is no liquid water term (ℓ) in (A.18) because no condensation takes place in the downdrafts. Since the downdrafts are also assumed to be saturated, (A.9) and (A.10) are still valid in determining s_{cd} and q_{cd} from h_{cd}.

APPENDIX B

DERIVATIONS OF $K(\lambda, \lambda')$ and $F(\lambda)$

Starting from the definition of cloud work function:

$$A(\lambda) = \int_{z_B}^{z_D(\lambda)} \frac{g}{c_p \bar{T}(z)} \eta(z,\lambda) [s_c(z,\lambda) - \bar{s}(z)] dz \qquad (B.1)$$

and taking the time derivative of (B.1), we have:

$$\frac{\partial A(\lambda)}{\partial t} = \int_{z_B}^{z_D(\lambda)} \frac{g}{c_p \bar{T}(z)} \eta(z,\lambda) \frac{\partial}{\partial t} [s_c(z,\lambda) - \bar{s}(z)] dz \qquad (B.2)$$

Using (A.9), we obtain:

$$\frac{\partial A(\lambda)}{\partial t} = \int_{z_B}^{z_D(\lambda)} \frac{g}{c_p \bar{T}(z)} \eta(z,\lambda) \frac{\partial}{\partial t} [\frac{1}{1+\gamma(z)} (h_c(z,\lambda) - \bar{h}(z)] dz \qquad (B.3)$$

Using (A.8) and (A.14) yields:

$$\frac{\partial A(\lambda)}{\partial t} = \int_{z_B}^{z_D(\lambda)} \frac{g}{c_p \bar{T}(z)} \frac{1}{1+\gamma(z)} \frac{\partial}{\partial t} [h_M + \lambda \int_{z_B}^{z} \eta(z',\lambda)\bar{h}(z)dz'$$

$$- \eta(z,\lambda)\bar{h}^*(z)] dz \qquad (B.4)$$

By the relation of

$$L \frac{\partial \overline{q}^{*}}{\partial t} = \gamma \frac{\partial \overline{s}}{\partial t} \tag{B.5}$$

where γ has been defined in (A.11), (B.4) can be expressed as:

$$\frac{\partial A(\lambda)}{\partial t} = \int_{z_B}^{z_D(\lambda)} \frac{g}{c_p \overline{T}(z)} \frac{1}{1+\gamma(z)}$$

$$[\frac{\partial h_M}{\partial t} + \lambda \int_{z_B}^{z} \eta(z,\lambda') \frac{\partial \overline{h}(z')}{\partial t} dz'$$

$$- \eta(z,\lambda)(1 + \gamma(z)) \frac{\partial \overline{s}(z)}{\partial t}] dz \tag{B.6}$$

Reversing the order of integration of the double integral in (B.6), we have:

$$\frac{\partial A(\lambda)}{\partial t} = \frac{\partial h_M}{\partial t} \int_{z_B}^{z_D(\lambda)} \frac{g}{c_p \overline{T}(z)} \frac{1}{1+\gamma(z)} dz$$

$$+ \int_{z_B}^{z_D(\lambda)} \{ \int_{z}^{z_D(\lambda)} \frac{g}{c_p \overline{T}(z')} \frac{1}{1+\gamma(z')} dz' \} \lambda \eta(z,\lambda) \frac{\partial \overline{h}(z)}{\partial t} dz$$

$$- \int_{z_B}^{z_D(\lambda)} \frac{g}{c_p \overline{T}(z)} \eta(z,\lambda) \frac{\partial \overline{s}(z)}{\partial t} dz \tag{B.7}$$

Now, by defining:

$$\frac{g}{c_p \overline{T}(z)} \frac{1}{1+\gamma(z)} \equiv \rho(z)\beta(z) \tag{B.8}$$

$$\rho(z)b(z,\lambda) \equiv \int_{z}^{z_D(\lambda)} \rho(z')\beta(z')dz' \qquad (B.9)$$

$$\frac{g}{c_p \bar{T}(z)} \equiv \rho(z)\alpha(z) \qquad (B.10)$$

(B.7) can be expressed as:

$$\frac{\partial A(\lambda)}{\partial t} = \frac{\partial h_M}{\partial t} \int_{z_B}^{z_D(\lambda)} \frac{g}{c_p \bar{T}(z)} \frac{1}{1+\gamma(z)} dz$$

$$+ \int_{z_B}^{z_D(\lambda)} \rho(z)b(z,\lambda)\lambda\eta(z,\lambda) \frac{\partial \bar{h}(z)}{\partial t} dz \qquad (B.11)$$

$$- \int_{z_B}^{z_D(\lambda)} \rho(z)\alpha(z)\eta(z,\lambda) \frac{\partial \bar{s}(z)}{\partial t} dz$$

Substituting $\frac{\partial \bar{s}}{\partial t}$ and $\frac{\partial \bar{h}}{\partial t}$ from (2.7) and (2.9) into (B.11), we have:

$$\frac{\partial A(\lambda)}{\partial t} = \frac{\partial h_M}{\partial t} \int_{z_B}^{z_D(\lambda)} \frac{g}{c_p \bar{T}(z)} \frac{1}{1+\gamma(z)} dz$$

$$+ \int_{z_B}^{z_D(\lambda)} \eta(z,\lambda) \left\{ \lambda b(z,\lambda)L(\bar{q}^* - \bar{q}) + \alpha(z)L\hat{\ell} \right\} D(z)dz$$

$$+ \int_{z_B}^{z_D(\lambda)} \eta(z,\lambda) \left\{ \lambda b(z,\lambda) \frac{\partial \bar{h}}{\partial z} - \alpha(z) \frac{\partial \bar{s}}{\partial z} \right\} M_c(z)dz \qquad (B.12)$$

$$+ \int_{z_B}^{z_D(\lambda)} \eta(z,\lambda) \left\{ \lambda b(z,\lambda) \left(\frac{\partial \bar{h}}{\partial t}\right)_{LS} - \alpha(z) \left(\frac{\partial \bar{s}}{\partial t}\right)_{LS} \right\} \rho(z)dz$$

where

$$\rho\left(\frac{\partial \bar{h}}{\partial t}\right)_{LS} \equiv -\rho \bar{w}\frac{\partial \bar{h}}{\partial z} - \rho \bar{\vec{V}}\cdot \nabla \bar{h} + \bar{Q}_R \tag{B.13}$$

$$\rho\left(\frac{\partial \bar{s}}{\partial t}\right)_{LS} \equiv -\rho \bar{w}\frac{\partial \bar{s}}{\partial z} - \rho \bar{\vec{V}}\cdot \nabla \bar{s} + \bar{Q}_R \tag{B.14}$$

Substituting $M_c(z)$ and $D(z)$ from (2.10) and (2.16) into (B.12), we obtain:

$$\frac{\partial A(\lambda)}{\partial t} = F_M(\lambda) + F_c(\lambda) + \int_0^{\lambda_{max}}[K_V(\lambda,\lambda') + K_D(\lambda,\lambda')]m_B(\lambda')d\lambda' \tag{B.15}$$

where

$$F_c(\lambda) = \int_{z_B}^{z_D(\lambda)} \eta(z,\lambda)\{\lambda b(z,\lambda)[-w\frac{\partial \bar{h}}{\partial z} - \bar{\vec{V}}\cdot \nabla \bar{h} + \bar{Q}_R]$$

$$- \alpha(z)(-\bar{w}\frac{\partial \bar{s}}{\partial z} - \bar{\vec{V}}\cdot \nabla \bar{s} + \bar{Q}_R)\}\ \rho(z)dz \tag{B.16}$$

$$F_M(\lambda) = \frac{\partial h_M}{\partial t} \int_{z_B}^{z_D(\lambda)} \rho(z)\beta(z)dz \tag{B.17}$$

$$K_V(\lambda,\lambda') = \int_{z_B}^{z_D(\lambda)} \eta(z,\lambda)\eta(z,\lambda')\{\lambda b(z,\lambda)\frac{\partial \bar{h}}{\partial z} - \alpha(z)\frac{\partial \bar{s}}{\partial z}\}\ dz \tag{B.18}$$

$$K_D(\lambda,\lambda') = n(z_D',\lambda)n(z_D',\lambda')\{\lambda b(z_D',\lambda)\ L(\bar{q}^*(z_D') - \bar{q}(z_D')) \tag{B.19}$$

$$+ \alpha(z_D')L\hat{\ell}(z_D')\}$$

APPENDIX C

FINITE DIFFERENCE EQUATIONS

Continuity equation:

$$\frac{u^n_{i+1/2,k} - u^n_{i-1/2,k}}{\Delta x_i} + \frac{1}{\rho_k}\frac{\rho_{k+1/2}w^n_{k+1/2,i} - \rho_{k-1/2}w^n_{k-1/2,i}}{\Delta a_k} = 0 \qquad (C.1)$$

U-momentum equation:

$$\frac{u^{n+1}_{i+1/2,k} - u^{n-1}_{i+1/2,k}}{2\Delta t} = -\left[\left(\frac{u^n_{i+1/2,k} + u^n_{i+3/2,k}}{2}\right)^2 - \right.$$

$$\left(\frac{u^n_{i+1/2,k} + u^n_{i-1/2,k}}{2}\right)^2 / \Delta x_{i+1/2}$$

$$-\left\{\rho_{k+1/2}\left[\left(\frac{w^n_{i,k+1/2} + w^n_{i+1,k+1/2}}{2}\right)\left(\frac{u^n_{i+1/2,k} + u^n_{i+1/2,k+1}}{2}\right)\right]\right.$$

$$\left.- \rho_{k-1/2}\left[\left(\frac{w^n_{i,k-1/2} + w^n_{i+1,k-1/2}}{2}\right)\left(\frac{u^n_{i+1/2,k} + u^n_{i+1/2,k-1}}{2}\right)\right\}/\rho_k\Delta z_k\right.$$

$$+ fv^n_{i+1/2,k} - c_p\bar{\theta}_k(\pi^n_{i+1,k} - \pi^n_{i,k})/\Delta x_{i+1/2} \qquad (C.2)$$

v-momentum equation:

$$\frac{v_{i+1/2,k}^{n+1} - v_{i+1/2,k}^{n-1}}{2\Delta t} = -\left[\left(\frac{u_{i+1/2,k}^n + u_{i+3/2,k}^n}{2}\right)\left(\frac{v_{i+1/2,k}^n + v_{i+3/2,k}^n}{2}\right)\right.$$

$$\left. - \left(\frac{u_{i+1/2,k}^n + u_{i-1/2,k}^n}{2}\right)\left(\frac{v_{i+1/2,k}^n + v_{i-1/2,k}^n}{2}\right)\right]/\Delta x_{i+1/2}$$

$$- \left\{\rho_{k+1/2}\left[\left(\frac{w_{i,k+1/2}^n + w_{i+1,k+1/2}^n}{2}\right)\left(\frac{v_{i+1/2,k}^n + v_{i+1/2,k+1}^n}{2}\right)\right]\right.$$

$$\left. - \rho_{k-1/2}\left[\left(\frac{w_{i,k-1/2}^n + w_{i+1,k-1/2}^n}{2}\right)\left(\frac{v_{i+1/2,k}^n + v_{i+1/2,k-1}^n}{2}\right)\right]\right\}/\rho_k\Delta z_k$$

$$- f\,(u_{i+1/2,k}^n - u_{g_k}) \qquad\qquad (C.3)$$

thermodynamic equation:

$$\frac{\theta_{i,k}^{n+1} - \theta_{i,k}^{n-1}}{2\Delta t} = -\left[\frac{u_{i+1,k}^n(\theta_{i+1,k}^{'n}+\theta_{i,k}^{'n})}{2} - \frac{u_{i-1/2,k}^n(\theta_{i,k}^{'n}+\theta_{i-1,k}^{'n})}{2}\right]/\Delta x_i$$

$$- \left[\frac{\rho_{k+1/2}w_{i,k+1/2}^n(\theta_{i,k+1}^{'n}+\theta_{i,k}^{'n})}{2} - \frac{\rho_{k-1/2}w_{i,k-1/2}^n(\theta_{i,k}^{'n}+\theta_{i,k-1}^{'n})}{2}\right]/\rho_k\Delta z_k$$

$$- \left[w_{i,k+1/2}^n\frac{(\bar{\theta}_{k+1}^n-\bar{\theta}_k^n)}{\Delta z_{k+1/2}} + w_{i,k-1/2}^n\frac{(\bar{\theta}_k^n-\bar{\theta}_{k-1}^n)}{\Delta z_{k-1/2}}\right]/2 + Q_{L_{i,k}}^n \qquad (C.4)$$

where n denotes the time step, i and k respectively denote the horizontal and
vertical grid points, and

$$\Delta x_{i+1/2} = (\Delta x_i + \Delta x_{i+1})/2 \qquad\qquad\qquad (C.5)$$

$$\Delta z_{k+1/2} = (\Delta z_k + \Delta z_{k+1})/2 \qquad\qquad\qquad (C.6)$$

Note that the time-independent imposed u_0 and w_0 are not included in the above
equations for simplicity and the moisture equation is also not included since
it has the same form as (C.4).

Crum, F. X., and D. E. Stevens, 1983: A comparison of two cumulus parameterization schemes in a linear model of wave-CISK. J. Atmos. Sci., 40, 2671-2688.

Dantzig, G. B., 1963: Linear programming and extensions, Princeton University Press, Princeton, 631 pp.

Deardorff, J. W., 1972: Parameterization of the planetary boundary layer for use in general circulation models. Mon. Wea. Rev., 100, 93-106.

Dopplick, T. G., 1970: Global radiative heating of the earth's atmosphere. Rept. No. 24, Planet. Circ. Project, Dept. of Meteor., MIT, 128 pp.

Frank, W. M., 1980: Modulation of the net tropospheric temperature during GATE. J. Atmos. Sci., 37, 1056-1064.

Frank, W. M., 1983: The cumulus parameterization problem. Mon. Wea. Rev., 111, 1859-1871.

Fitzjarrald, D. R., and M. Garstang, 1981: Vertical structure of the tropical boundary layer. Mon. Wea. Rev., 109, 1512-1526.

Gass, S., 1975: Linear Programming: Methods and Applications. McGraw-Hill, New York, 406 pp.

Hack, J. J., and W. H. Schubert, 1980: The role of convective-scale processes in tropical cyclone development. Atmos. Sci. Pap. No. 330. Colorado State University, 206 pp.

Hack, J. J., W. H. Schubert, and P. L. Silva Dias, 1984: A spectral cumulus parameterization for use in numerical models of the tropical atmosphere. Mon. Wea. Rev., 112, 704-716.

Hanson, R. J., and J. A. Wisniewski, 1979: A revised simplex code for LP problem using orthogonal decomposition - A user's guide. Sandia Lab. Rept., SAND 78-2322.

Haltiner, G. J., and R. T. Williams, 1979: Numerical prediction and dynamic meteorology. John Wiley and Sons, Inc., 477 pp.

Johnson, R. H., 1976: The role of convective-scale precipitation downdrafts in cumulus and synoptic-scale interactions. J. Atmos. Sci., 33, 1890-1910.

Johnson, R. H., 1978: Cumulus transport in a tropical wave composite for phase III of GATE. J. Atmos. Sci., 35, 484-494.

Johnson, R. H., 1980: Diagnosis of convective and mesoscale motions during phase III of GATE. J. Atmos. Sci., 37, 733-753.

Klemp, J. B., and R. B. Wilhelmson, 1978: The simulation of three-dimensional convective storm dynamics. J. Atmos. Sci., 35, 1070-1093.

Kreitzberg, C. W., and D. J. Perkey, 1977: Release of potential instability, Part II: The mechanism of convective/mesoscale interaction. J. Atmos. Sci., 34, 1569-1596.

Krishnamurti, T. N., Y. Ramanathan, H.-L. Pan, R. J. Rasch, and J. Molinari, 1980: cumulus parameterization and rainfall rates I. Mon. Wea. Rev., 108, 465-472.

Kuo, H. L., 1965: On the formation and intensification of tropical cyclones through latent heat release by cumulus convection. J. Atmos. Sci., 22, 40-63.

Kuo, H. L., 1974: Further studies of the parameterization of the influence of cumulus convection on large-scale flow. J. Atmos. Sci., 31, 1232-1240.

Kurihara, Y., 1973: A scheme of moist convective adjustment. Mon. Wea. Rev., 101, 547-553.

Kurihara, Y., and R. E. Tuleya, 1974: Structure of a tropical cyclone developed in a three-dimensional numerical simulation model. J. Atmos. Sci., 31, 893-919.

Lilly, D. K., 1968: Models of cloud-topped mixed layers under a strong inversion. Quart. J. Roy. Meteor. Soc., 94, 292-309.

Lindzen, R. S., 1974: Wave-CISK in the tropics. J. Atmos. Sci., 31, 156-179.

Lord, S. J., 1978: Development and observational verification of a cumulus cloud parameterization. Ph.D. dissertation, UCLA, 359 pp.

Lord, S. J., and A. Arakawa, 1980: Interaction of a cumulus cloud ensemble with the large-scale environment, Part II. J. Atmos. Sci., 37, 2677-2692.

Lord, S. J., 1982: Interaction of cumulus cloud ensemble with the large-scale environment. Part III: Semi-prognostic test of the Arakawa-Schubert cumulus parameterization. J. Atmos. Sci., 39, 88-103.

Lord, S. J., W. C. Chao, and A. Arakawa, 1982: Interaction of a cumulus cloud ensemble with the large-scale environment. Part IV: The discrete model. J. Atmos. Sci., 39, 104-113.

Manabe, S., J. Smagorinsky, and R. F. Strickler, 1965: Simulated climatology of a general circulation model with a hydrological cycle. Mon. Wea. Rev., 93, 769-791.

Miyakoda, K., and J. Sirutis, 1977: Comparative integration of global models with various parameterized processes of subgrid-scale vertical transports: description of the parameterization. Beitr. Phys. Atmos., 50, 445-487.

Nitta, T., 1975: Observational determination of cloud mass flux distribution. J. Atmos. Sci., 32, 73-91.

Ogura, Y., and N. A. Phillips, 1962: A scale analysis of deep and shallow convection in the atmosphere. J. Atmos. Sci., 19, 173-179.

Ogura, Y., and H.-R. Cho, 1973: Diagnostic determination of cumulus cloud population from large-scale variables. J. Atmos. Sci., 30, 1276-1286.

Ogura, Y., and H.-R. Cho, 1974: On the interaction between the subcloud and cloud layers in tropical regions. J. Atmos. Sci., 31, 1850-1859.

Ogura, Y., Y.-L. Chen, J. Russel, and S.-T. Soong, 1979: On the formation of organized convective systems observed over the eastern Atlantic. Mon. Wea. Rev., 107, 426-441.

Ooyama, K., 1971: A theory on parameterization of cumulus convection. J. Meteor. Soc. Japan, 39, 744-756.

Ooyama, K., 1982: Conceptual evolution of the theory and modeling of the tropical cyclone. J. Meteor. Soc. Japan, 60, 369-379.

Orlanski, I., and B. B. Ross, 1977: The circulation associated with a cold front, part I: dry case. J. Atmos. Sci., 34, 1619-1633.

Reed, R. J., and E. E. Recker, 1971: Structure and properties of synoptic-scale wave disturbances in the equatorial western Pacific. J. Atmos. Sci., 28, 1117-1133.

Robert, A. J., 1966: The integration of a low order spectral form of the primitive meteorological equation. J. Atmos. Soc. Japan, 44, 237-245.

Rosenthal, S. L., 1969: Numerical experiments with a multilevel primitive equation model designed to simulate the development of tropical cyclones, Experiment I. ESSA Tech. Memo. ERLTM-NHRL 82, Nat. Hurr. Res. Lab., Miami, FL 36 pp.

Rosenthal, S. L., 1970: A circularly symmetric primitive equation model of tropical cyclone development containing an explicit water vapor cycle. Mon. Wea. Rev., 98, 643-663.

Schlessinger, R. E., 1973: A numerical model of deep moist convection: Part I. Comparative experiments for variable ambient moisture and wind-shear. J. Atmos. Sci., 30, 835-856.

Schubert, W. H., 1973: The interaction of a cumulus cloud ensemble with the large-scale environment. Ph.D. dissertation. Dept. of Meteorology, UCLA, 168 pp.

Shukla, J., 1978: CISK-baratropic-baroclinic instability and the growth of monsoon depressions. J. Atmos. Sci., 35, 495-508.

Silva Dias, P. L., and W. H. Schubert, 1977: Experiment with a spectral cumulus parameterization theory. Atmos. Sci. Pap. No. 275, Colorado State University, 132 pp.

Simpson, J., G. Van Helvoirt, 1980: GATE cloud-subcloud layer interactions examined using a three-dimensional cumulus model. Beitr. Phys. Atmos., 53, 106-134.

So, S. S., 1982: An observational study of the role of convection in the Baiu situation with special attention to the Arakawa-Schubert cumulus parameterization. Ph.D. dissertation, Geophysical Institute, Univ. of Tokyo, Tokyo, Japan, 133 pp.

Soong, S.-T., and Y. Ogura, 1980: Response of trade-wind cumuli to large-scale processes. J. Atmos. Sci., 37, 2016-2034.

Soong, S.-T., and W.-T. Tao, 1984: A numerical study of the vertical transport of momentum in a tropical rainband. J. Atmos. Sci., 41, 1049-1061.

Stark, T. E., 1976: Wave-CISK and cumulus parameterization. J. Atmos. Sci., 33, 2383-2391.

Suarez, M. J., A. Arakawa, and D. A. Randall, 1983: The parameterization of the planetary boundary layer in the UCLA general circulation model: Formulation and results. Mon. Wea. Rev., 111, 2224-2243.

Tapp, M. C., and P. W. White, 1976: A nonhydrostatic mesoscale model. Quart. J. Roy. Meteor. Soc., 102, 277-296.

Tao, W.-K., 1983: A numerical study of the structure and vertical transport properties of a tropical convective system. Ph.D. dissertation, Dept. of Atmos. Sci., Univ. of Ill. at Urbana-Champaign, 228 pp.

Thorpe, A. J., M. J. Miller, and M. W. Moncrieff, 1982: Two-dimensional convection in nonconstant shear: a model of mid-latitude squall lines. Quart. J. Roy. Meteor. Soc., 108, 739-761.

Wilhelmson, R. B., and Y. Ogura, 1972: The pressure perturbation and the numerical modeling of a cloud. J. Atmos. Sci., 29, 1295-1307.

Wilhelmson, R. B., 1974: The life cycle of a thunderstorm in three dimensions. J. Atmos. Sci., 31, 1629-1651.

Yanai, M., S. Esbensen, and J.-H. Chu, 1973: Determination of bulk properties of tropical cloud clusters from large-scale heat and moisture budgets. J. Atmos. Sci., 30, 611-627.

END

FILMED

5-86

DTIC